SEISMIC EVALUATION OF GROUTED SPLICE SLEEVE CONNECTIONS FOR BRIDGE PIERS IN ACCELERATED BRIDGE CONSTRUCTION

by

Mohammad Javad Ameli Renani

A dissertation submitted to the faculty of
The University of Utah
in partial fulfillment of the requirements for the degree of

Doctor of Philosophy

Department of Civil and Environmental Engineering

The University of Utah

August 2016

The University of Utah Graduate School

STATEMENT OF DISSERTATION APPROVAL

The dissertation of **Mohammad Javad Ameli Renani**

has been approved by the following supervisory committee members:

Chris P. Pantelides	, Chair	**5/2/2016** Date Approved
Lawrence D. Reaveley	, Member	**5/2/2016** Date Approved
Daniel O. Adams	, Member	**5/2/2016** Date Approved
Luis F. Ibarra	, Member	**5/2/2016** Date Approved
Jerod G. Johnson	, Member	**5/2/2016** Date Approved

and by **Michael E. Barber**, Chair/Dean of

the Department/College/School of **Civil and Environmental Engineering**

and by David B. Kieda, Dean of The Graduate School.

ABSTRACT

Accelerated bridge construction (ABC) has been practiced in the United States because of the efficiency it offers as a bridge construction method. Prefabricated reinforced concrete components have been frequently used as part of ABC. The connections between such precast components may be subjected to large earthquake-induced deformations resulting in a considerable permanent damage. The present study investigates the seismic performance of grouted splice sleeve (GSS) connections with the connectors placed in the column, footing, or cap beam of bridge subassemblies. Quasi-static cyclic loads were used to test five half-scale precast subassemblies and two cast-in-place control specimens. Two different GSS connectors were used; the column-to-footing connections incorporated one type of GSS with the bars grouted at both ends, whereas the column-to-cap beam connections used another type where one bar was threaded into one end and the other bar was grouted into the opposite end. Experimental results show that the precast subassemblies had similar strength but lower displacement capacity compared to the control specimens. Improved seismic response was observed when the location of the connectors was changed or when debonding was applied to dowel bars adjacent to the connectors.

Computational models were developed and validated with the experiments to further investigate the application of such precast connections in bridge bents with full-size configurations. Force-based beam-column elements with fiber sections were used to

construct the computational models based on plastic hinge weighted integration. The modeling strategy is based on transformation of the model for the precast column with GSS connectors, to an idealized equivalent cast-in-place column with a fictitious plastic hinge length that is capable of simulating both the global and local response. Bond-slip effects as well as low-cycle fatigue were included to address the performance differences between the precast and cast-in-place alternatives. Prototype precast bridge bent models designed with GSS connections were subjected to scaled ground motion records compatible with the earthquake demand in downtown Salt Lake City. Comparing the capacity and demand levels, the GSS connection was found to be promising for applications in high-seismic areas.

Dedicated to my parents, Roya and Ahmad;

and to my wife, Ellie.

TABLE OF CONTENTS

ABSTRACT iii

ACKNOWLEDGEMENTS x

1. INTRODUCTION 1

Development and Splicing of Reinforcement for Bridge Components 2
Lap Splices in Tension 3
Splice of Column Reinforcement in Seismic Zones 3
Research Motivation 4
Common ABC Connection Types for Seismic Regions 4
Grouted Duct Connection 5
Pocket Connection 8
Socket Connection 9
Grouted Splice Sleeve Connection 14
Layout of Dissertation 19
References 21

2. SEISMIC EVALUATION OF GROUTED SPLICE SLEEVE CONNECTIONS FOR REINFORCED PRECAST CONCRETE COLUMN–TO–CAP BEAM JOINTS IN ACCELERATED BRIDGE CONSTRUCTION 26

Abstract 27
Introduction 28
Previous Research 29
Monotonic Tensile Tests on Individual Connectors 32
Design and Construction of Specimens 33
Specimen Design 33
Fabrication of Test Specimens 35
Test Procedure 38
Instrumentation 38
Experimental Setup 39
Displacement History 40
Test Results 40
Hysteretic Response 40
Hysteresis Response of Specimen FGSS-1 40
Hysteresis Response of Specimen FGSS-2 41

Hysteresis Response of Specimen CIP 42
Experimental Observations and Damage States 42
Visual Observations for Specimen FGSS-1 43
Visual Observations for Specimen FGSS-2 43
Visual Observations for Specimen CIP 45
Displacement Ductility 46
Energy Dissipation 48
Column Curvature and Dowel Bar Yielding Patterns 49
Residual Drift 52
Conclusion 52
Acknowledgements 55
Notation 55
References 56

3. SEISMIC COLUMN-TO-FOOTING CONNECTIONS USING GROUTED SPLICE SLEEVES 79

Abstract 80
Introduction 81
Research Significance 83
Tensile Tests of Grouted Splice Sleeve Connectors 84
Specimen Design and Fabrication 86
Experimental Procedure 88
Instrumentation 88
Test Setup and Loading Protocol 89
Test Results 90
Hysteretic Response and Damage Progression 90
Precast Specimen GGSS-1 90
Precast Specimen GGSS-2 91
Precast Specimen GGSS-3 92
Cast-in-place Specimen CIP 93
Displacement Ductility 94
Energy Dissipation 95
Column Base Curvature and Dowel Bar Strain 97
Bond-Slip Rotation and Column Displacement Components 98
Conclusions 100
Acknowledgements 102
Notation 103
References 103

4. SEISMIC ANALYSIS OF PRECAST CONCRETE BRIDGE COLUMNS CONNECTED WITH GROUTED SPLICE SLEEVE CONNECTORS 118

Abstract 118
Introduction 119
Experimental Study 121

Design and Fabrication of Half-scale Specimens 121
Test Setup and Instrumentation 123
Summary of Test Results 124
Test-day Material Properties 124
Hysteretic Performance 124
Computational Study 126
Analysis Objective 127
Description of Proposed Computational Model 127
Bond-slip 130
Low-cycle Fatigue 134
Model Layout 134
Analysis Results and Comparison 136
Global Response 136
Local Response 137
Conclusions 138
Acknowledgements 140
Notation 141
References 141

5. PARAMETRIC STUDY 156

Introduction 156
Design and Details of the Column Models 157
Design Procedure 157
Material Properties 159
Plastic Hinge Length for Models with Precast-2 Detailing 160
Pseudo Stress-strain Relationship for Reinforcing Bars 160
Details of Model Alternatives 161
Model Layout 163
Analysis Results 164
Analysis Termination Criteria and Mode of Failure 164
Comparison of CIP and Precast-2 Alternatives 165
Column Model 1 and 2 165
Column Model 3 and 4 167
Column Model 5 and 6 168
Column Model 7 and 8 169
Column Model 9 and 10 169
Column Model 11 and 12 170
Column Model 13 and 14 171
Column Model 15 and 16 172
Column Model 17 and 18 173
Column Model 19 and 20 173
Column Model 21 and 22 174
Column Model 23 and 24 175
Column Model 25 and 26 176
Column Model 27 and 28 177

Column Model 29 and 30 177
Column Model 31 and 32 178
Effect of Parameters on Response of Column Models 179
Design Displacement Ductility 181
Axial Load 182
Column Height 183
Column Longitudinal Reinforcing Bars 184
Effects of P-Δ 184
P-Δ Effects on Half-Scale Column Experiments 185
P-Δ Effects on Column Model 29 and 30 186
Effects of Plastic Hinge Length Variation 187
Conclusions 188
References 192

6. NONLINEAR TIME-HISTORY ANALYSIS OF A BRIDGE BENT SYSTEM 268

Introduction 268
Design and Details of the Bridge Bents 269
Selection of a Baseline Bridge Bent 269
Layout of the Bridge Bent Model 271
Analysis of the Bridge Bents 272
Static Cyclic Analysis 272
Analysis Results for Bent CIP 273
Analysis Results for Bent Precast-1 274
Analysis Results for Bent Precast-2 275
Comparison of the Three Bent Systems 276
Nonlinear Time-History Analysis 277
Selection of Ground Motions 277
Analysis Results for Bent CIP 279
Analysis Results for Bent Precast-1 280
Analysis Results for Bent Precast-2 281
Comparison of the Three Bent Systems 282
Conclusions 284
References 286

7. CONCLUSIONS 328

Experiments 328
Computational Study 330
Parametric Study 331
Prototype Bridge Bents 332

8. RECOMMENDATIONS FOR FUTURE RESEARCH 334

ACKNOWLEDGEMENTS

I would like to sincerely thank my advisor and mentor Dr. Chris Pantelides for his continuous guidance, dedication, and support. Without him, this work would not have been possible. I am honored to have the opportunity of being his student forever, and continue to learn not only about technical lessons in research but also about important life lessons.

I would like to extend my gratitude to Dr. Reaveley for being on my supervisory committee and providing invaluable insight into the fundamental aspects of this research. I appreciate fruitful discussions we occasionally had on effective experimental data interpretation methods, leading me towards a comprehensive understanding of the topics.

I was honored to have Dr. Daniel Adams, Dr. Luis Ibarra, and Dr. Jerod Johnson on my supervisory committee. I greatly appreciate their time and input which made this research a better work. It was a privilege to have such a distinguished supervisory committee, I could not ask for a better one.

I am grateful to UDOT, NYDOT, TxDOT, and Mountain Plains Consortium for providing financial support for the experiments. Splice Sleeve North America and Erico donated materials and mechanical splicing devices; their donation is appreciated.

I wish to thank the Graduate School of the University of Utah for the prestigious Graduate Research Fellowship they offered to me. I was able to devote my time and efforts to the analytical sections of this research during the course of this fellowship in

academic year 2015-16.

My two good friends and colleagues, Joel Parks and Dylan Brown, contributed greatly to the experimental phase of this research; we built, instrumented, tested, and repaired several large-scale subassemblies between year 2012 and 2014. Their help is greatly acknowledged. I also appreciate Mark Bryant and his team: Wade Stinson, Zant Doty, and Trevor Nye for their untiring efforts and support during the experiments.

I would like to extend my gratitude to Dr. Bordelon, Dr. Bartlett, and my friend Sharad Dangol for teaching me skills I needed to complete this work. I really appreciate their kindness and prompt responses during their busy time of the semester.

I wish to thank my friend Dr. Mostafa Tazarv, Assistant Professor at SDSU, for his invaluable input to this research. He offered important advice and suggestions which were critical to improving the quality of my work.

My good friends Amir Mohaghegh, Catherine Tucker, Birhanu Bishaw, Rouzbeh Gholizadeh, Wenjing Xu, Hamid Sarmadi, Anurag Upadhyay, Andrew Wu, Matt Wang, Rishav Poudel, Raul Uribe, and Elmar Eidelpes made my stay here at the U very pleasant. Thank you for your support and encouragement.

Words cannot describe how grateful I am to my family. I would not have had the motivation to succeed without their support, love, and prayers. My parents, Ahmad and Roya, would always follow up with my progress anxiously, and provide technical (both being experts in engineering) and moral advice. My brother Alireza, PhD student in Computer Science at the MSU, helped me a lot during the initial stage of the test data interpretation when I was overwhelmed with millions of rows of data. My dear sister Zahra, graduate student in Counseling at WMU, was a great help with stabilizing my

emotional state during this cumbersome endeavor. I am very thankful for having such a supportive family who are truly a source of love, peace, and tranquility; Mehdi, Elaheh, Noosha, Morteza, Hoda, Abbas, Hossein, Mahdi, Kaveh, and Mojtaba, thank you all very much.

My deepest gratitude goes out to my beloved wife, Ellie, who was also my patient companion throughout this long journey. She selflessly kept up with me and my long work days, at the end of which I was greeted by her most beautiful smile. Ellie, I hope I deserve all the sacrifices you made.

CHAPTER 1

INTRODUCTION

Accelerated bridge construction (ABC) refers to a bridge construction type that incorporates innovative techniques, methodologies, and materials to efficiently reduce construction time and traffic disruptions. ABC also provides a higher level of work-zone safety for workers and commuters, and improves environmental-friendly procedures. Prefabrication of bridge structural components is highly effective and is one of the ABC methods under the category of prefabricated bridge elements and systems (PBES) promoted by the Federal Highway Administration (FHWA).

Many bridges have been built or rehabilitated following ABC standards. Local examples include the I-15 CORE Provo Center Street Interchange, the Riverdale Road over I-84, and the I-15 South Layton Interchange. Precast concrete deck panels, substructures, and superstructures have been frequently utilized as effective ABC methods. Connections between such precast elements are among the most critical components of the structure. Researchers are in the process of investigating the suitability of various connection configurations, especially in moderate-to-high seismic regions. These connections not only have to conform to ABC standards in terms of the overall construction delivery time, but also must resist high levels of earthquake-induced deformations and stresses. Lateral load capacity, ductility capacity, and reparability are

three significant acceptance criteria for any bridge connection considered in earthquake-prone regions.

To achieve a moment-resisting column connection, continuity of column reinforcing bars is essential for the integrity of the structure. Therefore, splicing of reinforcement is used following one of the conventional splicing techniques available in the construction industry.

Development and Splicing of Reinforcement for Bridge Components

Reinforcing bars are spliced to achieve structural continuity or a greater length when maximum available length of reinforcement is limited due to transportation restrictions. According to AASHTO LRFD Bridge Design Specifications (2012), splicing of reinforcement may be implemented using lap splices, mechanical connections, and welded splices, as long as respective code provisions are met. Tension lap splices are not permitted for bars larger than No. 11. Therefore, a full-mechanical connection or full-welded splice may be used for No. 14 and No. 18 bars. A full-mechanical connection must develop 125% of the specified yield strength of the bar in tension or compression; moreover, the slip of bar within the splice region after loading to 30.0 ksi and unloading to 3.0 ksi should not be more than 0.01 in. for bars up to No. 14, and 0.03 in. for No. 18 bars. A full-welded splice must develop 125% of the specified yield strength of the bar in tension; welding needs to comply with the Structural Welding Code—Reinforcing Steel (AWS 2011).

Lap Splices in Tension

The length of a lap splice in tension specified by the AASHTO LRFD is the larger of 12.0 in. or the tension development length for a Class A splice, 1.3 times the tension development length for a Class B splice, or 1.7 times the tension development length for a Class C splice. The splice class is determined using the ratio of provided to required reinforcement and percent of spliced bars at a particular section. The basic tension development length (l_{db}) is defined in Eq (1.1) for No. 11 bars and smaller, Eq (1.2) for No.14 bars, and Eq (1.3) for No. 18 bars. The basic tension development length should be multiplied by proper increasing and decreasing modification factors as instructed by the AASHTO LRFD.

$$l_{db} = \frac{1.25 A_b f_y}{\sqrt{f'_c}} \geq 0.4 d_b f_y \quad (1.1)$$

$$l_{db} = \frac{2.7 f_y}{\sqrt{f'_c}} \quad (1.2)$$

$$l_{db} = \frac{3.5 f_y}{\sqrt{f'_c}} \quad (1.3)$$

where, A_b is the cross-sectional area of bar (in.^{2}), f_y is the specified yield strength (ksi), and f'_c is the 28-day specified compressive strength of concrete.

Splice of Column Reinforcement in Seismic Zones

Seismic bridge design guides such as AASHTO Guide Specification (2011) and Caltrans Seismic Design Criteria (2010) prohibit splicing of column longitudinal bars in plastic hinge regions of bridge columns located in seismic zones. This corresponds to Seismic Design Category (SDC) C for which the 1-sec period design spectral acceleration for the design earthquake is equal or greater than 0.3 and smaller than 0.5, along with

SDC D with a 1-sec period design spectral acceleration equal to or greater than 0.5. It is noted that the design earthquake is characterized using a probabilistic ground motion and the spectral response for 7% probability of exceedance in 75 years.

The plastic hinge region within which splicing of reinforcement is prohibited is the larger of 1.5 times the gross cross-sectional dimension in the direction of loading, the region of column with a moment demand larger than 75% of the plastic moment, or the analytical plastic hinge length (L_P) as defined in Eq (1.4) (Priestley et al. 1996):

$$L_P = 0.08L + 0.15f_{ye}d_{bl} \geq 0.3f_{ye}d_{bl} \quad (1.4)$$

where, L is the length of column from the point of maximum moment to the point of moment contraflexure (in.), f_{ye} is the expected yield strength of longitudinal column steel bars (ksi), and d_{bl} is the nominal diameter of longitudinal column steel bars (in.).

Research Motivation

Considering the current no-splice zone provisions for ductile columns in high-seismic regions, prefabrication of bridge substructure components as part of ABC cannot be implemented easily. Hence, numerous research studies have been investigating various forms of moment-resisting connections between precast bridge substructure components. One such connection type, grouted splice sleeve connection, was studied experimentally and analytically as presented in subsequent chapters.

Common ABC Connection Types for Seismic Regions

Various emulative connections have been studied for potential application in seismic regions. An emulative connection is a connection type that results in a precast

structural system with equivalent performance to the conventional monolithic construction (ACI 550).

Grouted Duct Connection

The grouted duct connection has been introduced as a viable ABC technique for both column-to-footing and column-to-cap beam connections. In this method corrugated steel ducts are accommodated in a footing or cap beam, and column reinforcement dowels are inserted and grouted inside the ducts.

A series of monotonic and cyclic tests on No. 8 bars grouted in ducts was reported in the work of Raynor et al. (2002). The experimental study investigated the bond-slip behavior of the confined bars, and provided data for further analytical and parametric studies. Failure of each specimen initiated by crushing of the grout adjacent to the reinforcing bar lugs, with no radial bond-related cracking as observed for bars embedded in unconfined reinforced concrete.

Brenes et al. (2006) investigated the response of reinforcing bars grouted in galvanized steel and plastic ducts under monotonic tension loading. The effect of different embedment length of bars grouted in the ducts was studied in addition to the group effect on the overall response. The duct clear spacing in the group tests, bar eccentricity, and epoxy coating were among the experimental parameters investigated in this research. No. 11 reinforcing bars were grouted in 4-in. diameter ducts for 32 experiments. Test results indicated that the response was not highly dependent on the variation of the embedment depth considered in the experimental program ($8d_b$, $12d_b$, and $16d_b$). On the other hand, the duct material was found to affect the failure mode of the

test specimens.

Steuck et al. (2009) described a series of pullout tests on 14 large-size reinforcing bars grouted into 8-in. diameter corrugated steel ducts. An anchorage length range of 2 to 14 bar diameters was considered in the experimental program. A monotonic displacement protocol was applied up to failure of each specimen. Polypropylene fibers which were utilized in the grout mix of only four specimens were not found to be advantageous in the overall response. A grout cone failure was observed for each test at the opening end of the duct due to an unsupported strut formation in the vicinity of the unconfined rebar outside the duct. The test results were used to develop a nonlinear model for this type of connector. According to both the test results and the analytical model, the required anchorage length in the grouted ducts was found to be 6 and 10 times the bar diameter to achieve bar yielding and fracture, respectively.

Pang et al. (2010) investigated the cyclic response of four 40% scale column-to-cap beam specimens in which the precast columns and cap beams were connected using grouted ducts. The corrugated steel ducts were located in the precast cap beam. The control specimen was constructed monolithically with 16 No. 5 longitudinal reinforcing bars in the column and no grouted duct, while the three precast specimens had 6 No. 8 column longitudinal bars and 12 No. 3 discontinuous bars which did not extend into the cap beam. The response of all models was comparable in terms of initial stiffness and lateral load capacity. A pinched hysteretic behavior was evident for the precast specimens. This resulted in a slightly lower energy dissipation capacity when compared to the control specimen. The intentional partial debonding of bars which was implemented over a length of 8 times the bar diameter within the ducts was found to be

ineffective under the applied cyclic loading. Bar fracture occurred for all four test alternatives due to low-cycle fatigue.

An experimental research study on one grouted duct connection was carried out by Matsumoto (2009a). The 20-in. diameter column was reinforced with 16 No. 5 longitudinal bars and No. 3 transverse hoops at 2 in. in the plastic hinge zone. The dowel bars protruding from the column end were grouted into ducts which were cast previously in the cap beam. Comparing the cyclic quasi-static test results from the grouted duct specimen with those of the cast-in-place specimen, the grouted duct connection was emulative of the monolithic construction in terms of strength, but a compromised displacement capacity was noted from the load-displacement response.

Tazarv and Saiidi (2015a, b) conducted experimental and analytical studies on two half-scale precast bridge column-to-footing subassemblies connected by means of grouted ducts. The 4-in. diameter corrugated steel ducts were cast 28 in. into the footing, and column dowel bars were grouted inside the ducts using ultra-high performance concrete (UHPC). A partial debonded bar region was considered for both test models to provide a superior strain distribution and prevent the concentration of strain at the column-to-footing interface. Shape memory alloy (SMA) bars were incorporated in the plastic hinge zone of one of the test specimens to study the self-centering effects and consequent minimal residual drift. The response of both test models under cyclic quasi-static lateral loading suggested that the grouted duct connection with the implemented detailing was viable in terms of strength, displacement capacity, and hysteretic performance.

Pocket Connection

The pocket connection was studied and implemented to connect bridge columns to cap beams. It is constructed by placing a circular corrugated steel duct inside the cap beam. Projected column bars are inserted into the pocket that is filled with concrete at the end.

Matsumoto (2009b-2009d) conducted an experimental study on two 42% scale precast column-to-cap beam joints utilizing the pocket connection method. One of the specimens had a higher level of joint detailing and was expected to achieve full ductility under quasi-static lateral loading, while the second test model was designed for a limited ductility by eliminating the stirrups within the joint and reducing the cap beam main and transverse reinforcing bars to a minimum required amount. An identical column configuration was incorporated in both tests, that is, 20-in. diameter column with 16 No. 5 longitudinal bars and No. 3 hoops at 2 in. on center. Compared to the control cast-in-place specimen, the performance of both precast test models was acceptable and met the objectives of the design. The control specimen had a nominal displacement ductility of 10 while the two precast specimens with pocket connections reached a nominal displacement ductility of 8. Plastic hinging was dominant for the full ductility specimen and column bar slip was similar to the control specimen. On the other hand, considerable joint shear cracking developed for the limited ductility specimen which resulted in softening of the joint. Also, decomposition of displacement revealed that the bar slip contribution was 11 times larger than the control and the full ductility test specimens.

Weinert (2011) evaluated several ABC connection types for precast bridges in seismic regions. According to this study, the pocket connection was considered feasible

for column-to-cap beam joints, while it could be utilized for the column-to-footing and pile-to-pile cap connections as well. However, this connection type achieved the lowest rank among all other precast connection types of bar coupler, grouted duct, socket connection, and hybrid connection. This was mainly because the time saving feature offered by this method was not great due to a relatively long curing time for the pocket concrete. In addition, there has not been sufficient research on the seismic performance of the pocket connection.

Socket Connection

The socket connection is another type of ABC connection that has recently become popular. A socket foundation was studied at the University of Washington and later used to connect columns to spread footings in a bridge constructed in the State of Washington over I-5 (Khaleghi et al., 2012). In this method, the bottom end of the precast column is roughened and embedded in the footing which is commonly cast-in-place, after which the footing concrete is cast around the column base. This connection type could be incorporated for column-to-cap beam joints as well as pile-to-pile cap joints, while it has mostly been utilized for column-to-footing joints (Weinert, 2011). Special detailing is required for column-to-cap beam and pile-to-pile cap joints connected with the socket connection. A comprehensive evaluation of this connection type was carried out in the work of Weinert (2011). The socket connection achieved the highest rank among other common precast connection types for applications in seismic zones, including the bar coupler, grouted duct, pocket connection, and hybrid connection. All connection types were evaluated relative to equivalent cast-in-place construction based on constructability

advantages, seismic performance and reparability, durability, technology readiness, and time savings potential. There have been many seismic experimental studies on this connection type which greatly helped to develop the fundamental understanding of the load transfer mechanism and the overall response under simulated seismic loads. Some of the most relevant experiments are briefly discussed in the following.

The force transfer mechanism in a socket was studied in the work of Osanai et al. (1996) using eight half-scale specimens along with an analysis based on the equilibrium of forces generated under combined axial and lateral loading. The two most significant test parameters were: (1) socket embedment depth, and (2) application of shear keys to the surface of the column base and socket. The authors found that an embedment depth of 1.5 times the dimension of the column was required for a rigid connection, in case shear keys were not used. When shear keys were used on the surface of the two connecting components, an embedment depth equal to the dimension of the precast column was found adequate because of higher friction forces at the interface plane.

Belleri and Riva (2012) conducted experimental tests on connections of four precast subassemblies, one of which was a socket connection for a 15 ¾-in. square column and a 23 5/8-in. deep footing. The column was reinforced with four No. 7 longitudinal bars and No. 3 closed hoops at 2 in. and at 4 in. up to 47 in. above the column base. The surface of the column base and interior surface of the socket were not roughened. Column main bars were bent inward at the base of the column. The socket connection showed a stable force-displacement response, compared to the control specimen which was a cast-in-place component. A slight strength deterioration was observed for the socket specimen at the 3% drift ratio, only for the pull direction. The

energy dissipation capacity of the socket connection was found slightly higher than the dissipation capacity of the control specimen in almost every drift ratio. Overall, the performance of the socket connection was found promising to be used as a connection between precast components.

Haraldsson et al. (2013) studied three socket foundations with varying test parameters including the socket depth and footing reinforcement. The precast specimens were scaled to 42% scale of the prototype bridge with headed longitudinal bars used for the column main reinforcement. The column and socket interface were roughened to achieve a higher level of shear-friction force transfer. An embedment depth equal to 1.1 times the column diameter was used for two specimens, while the third specimen had a socket depth equal to 0.5 times the column diameter to force failure to occur in the column-footing joint instead of the column base. The second specimen had a more simplified footing reinforcement layout than the first specimen. This was carried out by reducing the number of shear-friction reinforcement in addition to reduction of the footing ties down to 50% of the code specified numbers. This reduction was implemented as previous studies revealed that the original number of footing ties would have been needed if the main bars were bent outward. Cyclic quasi-static lateral loading was applied to the column under a constant axial load representing the gravity load effect on the subassemblies. Spalling occurred at drift ratios of 2.2% to 2.6%, and bar buckling occurred at the 7% drift ratio for all three specimens. Column bars fractured at 10.5% drift ratio for the first two specimens with the same footing depth, while the third specimen failed due to punching shear at 10.7% drift ratio, which implies an overall ductile performance for all three subassemblies. The first two specimens underwent pure

axial load up to failure, after completion of testing. Axial load test results showed that the axial load capacity of the columns was 3.5 times the factored tributary gravity load. Measurements obtained from strain gauges indicated that the heads of the column bars were most effective in the specimen with shallower footing, compared to the other two specimens. In addition, the low strain values in the shear-friction reinforcement plus the undamaged footing for the first two specimens implied that the diagonal shear-friction reinforcement was ineffective in the force transfer mechanism.

As part of experimental research on substructure connections for precast bridges, White (2014) discussed the response of four half-scale specimens, denoted as high damage (HD) connection type. This designation was used because a plastic hinging mechanism in the column base was expected to be severe in such a connection type; in another category of experiments, White (2014) presented the results of a controlled damage (CD) connection in which posttensioning and energy dissipative devices were incorporated to mitigate damage progression in the system. Two half-scale test specimens (out of four HD specimens), comprised of a precast column and a precast footing, were constructed and later connected during installation of the subassemblies using the socket connection. Both specimens had an identical dimension and configuration, but one was tested under uniaxial lateral loading and the other specimen was tested under biaxial lateral loading protocol. The footing depth was set to 20 in. which was equal to the diameter of the circular precast column. Since both column and footing were precast, the gap between the roughened column base and socket was filled with grout. A posttensioned bar was cast in a corrugated duct in the center of the column to apply the scaled axial load on the test assembly. Both specimens were tested until failure which

occurred because of column bar fracture during the 6% drift ratio. Well-distributed flexural cracks, concrete spalling, and buckling of the column bars were observed during application of lateral loads.

An application of the socket connection could be found under the category of concrete-filled steel tube (CFST) research studies, where a socket connection was utilized to achieve a moment-resisting base connection. One such study was presented in the work of Marson and Bruneau (2004). Four CFST columns were tested under constant axial and cyclic lateral loading. The column diameter and tube thickness were different to study the effect of diameter-to-thickness ratio on the response. The socket foundation was made by welding the steel tube end of the column to steel plates and channels. The socket was then encased in the concrete foundation. Test results showed that the foundation details were adequate and damage progressed away from the foundation. All four specimens performed well up to a 7% drift ratio which implies a ductile response under reversed cyclic quasi-static loads.

Lehman and Roeder (2012), and Moon et al. (2013) evaluated a series of experimental studies on CFST columns which were conducted at the University of Washington and presented in technical manuscripts from 2005 to present. The results of such experiments were used to evaluate the base connection for such components in seismic regions. As a result of this investigation, a simple design procedure was proposed for the base connection including all significant parameters such as embedment depth and required depth of concrete underneath the column to resist punching shear. A finite element model was developed and validated with the experiments, in the aforementioned study.

Grouted Splice Sleeve Connection

The grouted splice sleeve (GSS) connection and other types of bar splicing devices are considered to be an effective connection type for ABC. Such connections have been frequently used, specifically in nonseismic regions, because they offer ease and speed of construction. In this connection type each individual reinforcing bar in connecting precast components is spliced by means of a mechanical coupler which is located within one of the components, normally the precast component that is built at the precast plant. Two common types of the GSS connectors which are used in this research are shown in Fig. 1.1. The shorter GSS connector is referred to as FGSS in which the threaded factory dowel is fastened to one end while the field dowel is grouted in the other end of the sleeve (fastened/grouted splice sleeve). The longer GSS connector is referred to as GGSS indicating that reinforcing bars are grouted at both ends of the sleeve (grouted/grouted splice sleeve). Tensile and compressive force transfer between the two spliced bars occurs by means of bond stress between the bars, the high-strength grout, and the grouted splice sleeve connector. Fig. 1.2 shows a schematic of the interaction between reinforcing bar, grout, and connector. Sources of bond stress are: (1) chemical adhesion between bar and grout; (2) frictional forces due to roughness of the interface, forces transverse to the bar surface, and relative slip between the bar and the surrounding grout; and (3) mechanical anchorage or bearing of the ribs against the concrete surface, which is the main component after initial slip (ACI 408 2003). The relatively high level of confinement provided by sleeve connectors prevents splitting failure by restraining dilation of the splitting cracks. Therefore, reinforcing bars will develop sufficient strength in much shorter embedment lengths compared to the unconfined anchorage condition.

For instance, the embedment length required for spliced bars using the GGSS connector is about 25% of the code prescribed development length, for materials with typical properties. Bar embedment length, bar deformations (ribs), and grout strength are the most effective parameters for achieving a viable GSS connection.

The evaluation of several ABC connections in moderate-to-high seismic regions was conducted and summarized in NCHRP Report 698 (Marsh et al. 2011). Verified connection types include bar couplers, grouted ducts, pocket connections, socket connections, hybrid connections, integral connections, and emerging technologies, such as shape memory alloys and elastomeric bearings. These connections were either utilized in actual practice, or are being developed in research studies. The aforementioned ABC connections were then ranked according to technology readiness, performance, and time savings potential, relative to cast-in-place construction for the same connection type. One of the significant outcomes of this synthesis study was the prioritization of more research studies essential for each connection type in order to fully understand their behavior under seismic actions.

A bar coupler was defined as a mechanical coupler used to splice two bars together. This synthesis report addressed several types of couplers, such as threaded sleeves, headed bars with separate sleeves, external clamping screws, and GSS connectors. Application of the GSS connector, which is typically used in bridges, provides the benefit of larger tolerances in comparison with other types of couplers. Despite extensive use of such connections in regions of moderate seismicity, in-depth knowledge of their inelastic behavior has not been achieved, necessitating more research and experimental investigation. The need for further studies discussed in NCHRP Report

698 was based on the urgency level of the unknown aspects of this connection type. First priority was given to the cyclic performance of the couplers with the bars in their plastic range of stress, and strain distribution for the bars being spliced; second priority studies included the investigation of strength details, such as magnitude of stress that each bar can develop, together with verification of bar coupler placement. The latter refers to the proper location of the coupler (e.g., in the column or footing), so it does not affect the overall response to earthquake loads, but could still be a constructible detail. The effect of surrounding concrete and level of provided confinement on the coupler is the third category of priorities, as the last necessary study to be conducted on this type of ABC connection.

As part of a comprehensive research study on the seismic performance of next generation bridge components for ABC, researchers at the University of Nevada, Reno, investigated the behavior of four column-to-footing connections under cyclic lateral loading, utilizing two different proprietary couplers (Haber et al. 2014). The research program also considered a cast-in-place specimen as the control test. GSS connectors and HRC 500 Up-Set Headed Couplers (HC) were used to connect the longitudinal reinforcement in the column and footing. For each coupler, two specimens were constructed and tested under cyclic quasi-static load. A precast pedestal was incorporated in one specimen for each category to reduce the moment demand over the coupler region. Considering the hysteretic behavior of all specimens, it was noted that the HC connection showed a similar response to the cast-in-place detail and withstood a relatively large amount of drift. In spite the ease of construction achieved by the grouted couplers, their ductility capacity was found to be less than both the cast-in-place and HC connections.

Comparing the results of the cyclic tests, it was noted that all specimens exhibited similar performance in terms of ultimate load capacity and energy dissipation, but the ductility capacity was different. Tazarv and Saiidi (2014) described a remedial procedure to improve the ductility capacity of the columns with the GSS connectors embedded in the pedestal. The footing dowel bars were debonded within the pedestal to allow for spread of plasticity along the bars and to postpone rebar fracture.

Haber et al. (2015) described a series of connector tests on the two aforementioned splicing systems. The tests were conducted to obtain results necessary for numerical modeling focusing on the connector region. To study the stress-strain behavior, strain gages were used on the spliced bars and mid-section of the coupler. Results showed that the bar fractured away from the coupler region. Results also showed that the imposed displacement rate made a slight difference in the overall performance of the systems.

Jansson (2008) performed a series of connector tests on FGSS and GGSS connectors and studied their performance under slip, fatigue, ultimate load, and creep. As a result of this study, both connectors were approved for bridge applications in the State of Michigan, by meeting the requirements set by the AASHTO LRFD Bridge Design Specifications. The results showed that both GGSS and FGSS connectors conformed to the Type 2 connection requirements of ACI 550, enabling their application even in the plastic hinge regions of building elements in Michigan.

Aida et al. (2005) reported on experimental testing of three ¾-scale specimens in Japan, two of which used GGSS connectors to connect columns to footings. The specimens, representing railroad bridge column-to-footing connections, were heavily reinforced and tested under cyclic loading to investigate their inelastic performance. The

precast specimens showed acceptable inelastic behavior under cyclic loads compared to the cast-in-place specimen. The maximum load resisted by the two precast subassemblies was 7% to 11% greater than that of the cast-in-place specimen.

Yoshino et al. (1996) had proposed an innovative shear reinforcing configuration called the intensive shear reinforcing (ISR) method, for precast concrete elements connected by means of GGSS connectors. Transverse reinforcement in this configuration was concentrated at both ends of the sleeves, contrary to the conventional method in which hoops are placed at a particular spacing everywhere along the member. The ISR method offers the advantage of better constructability as there is no need to change the dimensions and arrangement of the transverse reinforcement. According to results from the experimental phase of the study, including monotonic and cyclic loading of both systems, the ISR method is comparable with the conventional detail. A strut-and-tie model was also developed in the analytical phase of the study, depicting load transfer in the connector zone. This patented technique is used in building construction in Japan. The Splice Sleeve Company carried out cyclic tests on building column specimens that incorporated GGSS connectors to splice the column longitudinal bars. Different levels of axial load, shear reinforcement, existence of shear keys, and ultimately the location of connectors, were considered as test variables and investigated in this experimental study that included a total number of nine specimens. Test results indicated acceptable performance of the connectors in terms of both strength and ductility properties. It was, however, observed that both the test setup and test specimens were not typical of bridge substructures.

Matsuzaki et al. (1987) conducted research studies on individual GGSS

connectors as well as test subassemblies connected by means of such devices. The results of monotonic and cyclic tests on various sleeve sizes connecting different size steel bars were presented. A significant contribution of this investigation was the characterization of slip and pull-out properties of the system, in addition to illustration of the stress transfer between bars and grouted splice sleeves. Results of this study were utilized in an analytical effort to replicate the response of precast components connected by means of such devices, under reversed cyclic load. All specimens showed a similar response under the applied loading, in terms of strength and displacement capacity up to a displacement ductility of 6.0.

Layout of Dissertation

The research presented in this dissertation investigates the seismic performance of GSS connections for reinforced precast concrete bridge piers. The dissertation includes two main sections: experimental program and computational study. The experimental section is presented in Chapter 2 and Chapter 3 and describes a series of quasi-static cyclic tests on three half-scale column-to-cap beam and four column-to-footing subassemblies, respectively. In addition, tension test results are discussed for both FGSS and GGSS connectors in respective chapters. The two experimental chapters present design and detailing of the subassemblies. Cyclic performance of the specimens is discussed in terms of strength, displacement capacity, and spread of nonlinearity. A cast-in-place monolithically constructed specimen is included for each category of experiments to provide a baseline for comparisons. The results show distinct performance benefits when the location of the GSS connectors is changed.

The first part of the computational study, which describes the development of a modeling strategy for monolithic and precast columns, is presented in Chapter 4. This modeling strategy is based on transformation of the precast column to an equivalent idealized monolithic column using distributed plasticity elements with a plastic hinge integration scheme. The computational model is validated with the experiments discussed in Chapter 3 through both local and global response comparisons. The objective of the computational study is to develop a predictive model capable of accounting for the differences between precast and monolithic bridge subassemblies.

Chapter 5 focuses on a parametric study conducted to ascertain the response sensitivity of the proposed computational model to varying parameters. A monolithic and a precast cantilever column with similar configuration were studied with two different levels of reinforcing bar ratio, column height, axial load, and displacement ductility capacity. Overall, 32 columns were investigated and results are discussed in terms of strength, displacement capacity, global response, and local response; moreover, comparisons are made between the monolithic and precast alternatives.

Chapter 6 presents the design and analysis of a prototype multicolumn bridge bent system in accordance with AASHTO Guide Specifications. The proposed model which was validated in Chapter 4 and later verified using a parametric study in Chapter 5 is used to model one monolithic and two precast concrete bridge bents with different GSS connection configurations. The objective of Chapter 6 is to study the application of GSS connectors in multicolumn bents and investigate the effects of such a connection on the response of bridge bents. Furthermore, the strength and displacement capacity of each bent is obtained by performing static cyclic analyses; subsequently, drift demands are

discussed using a series of nonlinear time-history analyses.

Concluding remarks on the present research and recommendations for future research are presented in Chapter 7 and Chapter 8, respectively.

References

AASHTO. (2012). AASHTO LRFD *bridge design specification*, Washington, DC.

AASHTO. (2011). AASHTO *guide specifications for LRFD seismic bridge design*, Washington, DC.

Aida, H., Tanimura, Y., Tadokoro, T., and Takimoto, K. (2005). "Cyclic loading experiment of precast columns of railway rigid-frame viaduct installed with NMB splice sleeves." *Proceedings of the Japan Concrete Institute*, 27(2).

American Concrete Institute (ACI). (2003). "Bond and development of straight reinforcing bars in tension." *ACI 408*, Farmington Hills, MI.

American Concrete Institute (ACI). (2009). "Guide to emulating cast-in-place detailing for seismic design of precast concrete structures." *ACI-ASCE Committee 550*, Farmington Hills, MI.

American Welding Society (AWS). (2011). *Structural welding code—reinforcing steel*, Miami, FL.

Belleri, A., and Riva, P. (2012). "Seismic performance and retrofit of precast concrete grouted sleeve connections." *PCI J.,* 57 (1), 97–109.

Brenes, F.J., Wood, S. L., and Kreger, M. E., (2006). "Anchorage requirements for grouted vertical-duct connectors in precast bent cap systems." *FHWA/TX-06/0-4176-1*, Center for Transportation Research, University of Texas at Austin.

Caltrans. (2010). *Seismic design criteria (SDC), version 1.6*, Sacramento, CA.

Haber, Z. B., Saiidi, M. S., and Sanders, D. H. (2014). "Seismic performance of precast columns with mechanically spliced column-footing connections." *ACI Struct. J.*, 111(3), 639–650.

Haber, Z. B., Saiidi, M. S., and Sanders, D. H. (2015). "Behavior and simplified modeling of mechanical reinforcing bar splices." *ACI Struct. J.*, 112(2), 179–188.

Haraldsson, O. S., Janes, T. M., Eberhard, M. O., and Stanton, J. F. (2013). "Seismic

resistance of socket connection between footing and precast column." *J. Bridge Eng.*, 18 (9): 910–919.

Jansson, P. O. (2008). "Evaluation of grout-filled mechanical splices for precast concrete construction." Report R-1512, Michigan Department of Transportation, Lansing, MI.

Khaleghi, B., Schultz, E., Seguirant, S., Marsh, M. L., Haraldsson, O. S., Eberhard, M. O., and Stanton, J. F. (2012). "Accelerated bridge construction in Washington State: From research to practice." *PCI J.*, 57(4), 34–49.

Lehman, D. E., and Roeder, C. W. (2012). "Foundation connections for circular concrete-filled tubes." *J. of Construct. Steel Research*, 78, 212–225.

Marsh, M. L., Wernly, M., Garett, B. E., Stanton, J. F., Eberhard, M. O., and Weinert M. D. (2011) "Application of accelerated bridge construction connections in moderate-to-high seismic regions." *NCHRP Report 698*, National Cooperative Highway Research Program, Washington, DC.

Marson, J., and Bruneau, M. (2004). "Cyclic testing of concrete-filled circular steel bridge piers having encased fixed-based detail." *J. Bridge Eng.*,9 (1), 14–23.

Matsumoto, E. E. (2009a). "Emulative precast bent cap connections for seismic regions: component tests—grouted duct specimen (unit 2)." *ECS Report No. ECS-CSUS-2009-02*, Sacramento, CA: California State University, Sacramento.

Matsumoto, E. E. (2009b). "Emulative precast bent cap connections for seismic regions: component tests—cast-in-place specimen (unit 1)." *ECS Report No. ECS-CSUS-2009-01*. Sacramento, CA: California State University, Sacramento.

Matsumoto, E. E. (2009c). "Emulative precast bent cap connections for seismic regions: component tests—cap pocket full ductility specimen (unit 3)." *ECS Report No. ECS-CSUS-2009-03*. Sacramento, CA: California State University, Sacramento.

Matsumoto, E. E. (2009d). "Emulative precast bent cap connections for seismic regions: component tests—cap pocket limited ductility specimen (unit 4)." *ECS Report No. ECS-CSUS-2009-04*. Sacramento, CA: California State University, Sacramento.

Matsuzaki, Y., et al. (1987). "Effects of sleeves on member properties, study on the behavior of reinforced concrete beams with grout-filled steel splice sleeves." Architectural Institute of Japan.

Moon, J., Lehman, D. E., Roeder, C. W., and Lee, H. (2013). "Evaluation of embedded concrete-filled tube (CFT) column-to-foundation connections*." Engineering Structures*, 56, 22–35.

Osanai, Y., Watanabe, F., Okamoto, S. (1996). "Stress transfer mechanism of socket base connections with precast concrete columns." ACI Struct. J., 93(3), 1–11.

Pang, J. B. K., Eberhard M. O., and Stanton J. F. (2010). "Large-bar connection for precast bridge bents in seismic regions." *J. Bridge Eng.,* 15 (3), 231–239.

Priestley, M. J. N., Seible, F., and Calvi, G. M. (1996). *Seismic design and retrofit of bridges*. John Wiley & Sons, Inc., New York, NY.

Raynor, D. J., Lehman, D. E., and Stanton J. F. (2002). "Bond-slip response of reinforcing bars grouted in ducts." *ACI Struct. J.,* 99 (5), 568–576.

Splice Sleeve Japan, Ltd, "Tests on re-bar splices in reinforced concrete columns using NMB splice sleeves." *Report NPD-024*, Splice Sleeve Japan, Ltd., Tokyo, Japan.

Steuck, K. P., Eberhard, M. O., and Stanton, J. F. (2009). "Anchorage of large-diameter reinforcing bars in ducts." *ACI Struct. J.*, 106(4), 506–513.

Tazarv, M., and Saiidi, M. S. (2014). "Next generation of bridge columns for accelerated bridge construction in high seismic zones." *Rep. No. CCEER 14-06*, Center for Civil Engineering Earthquake Research, Dept. of Civil and Environmental Engineering, Univ. of Nevada, Reno, NV.

Tazarv, M., and Saiidi, M. S. (2015a) "UHPC-filled duct connections for accelerated bridge construction of RC columns in high seismic zones." *Eng. Struct.,* (99), 413–422.

Tazarv, M., and Saiidi, M. S. (2015b) "Low-damage precast columns for accelerated bridge construction in high seismic zones." *J. Bridge Eng.,* 10.1061/(ASCE)BE.1943 5592.0000806, 04015056.

Weinert, M. D. (2011). "Substructure connections for accelerated bridge construction in seismic regions." MS Thesis, University of Washington.

White, S. (2014). "Controlled damage rocking systems for accelerated bridge construction." MS Thesis, University of Canterbury.

Yoshino, T., Kobayashi, K., and Ase, M. (1996). "Intensive shear reinforcing method for PCA members with splice sleeve joint." *Proceedings of the 11th World Conference on Earthquake Engineering*, Acapulco, Mexico.

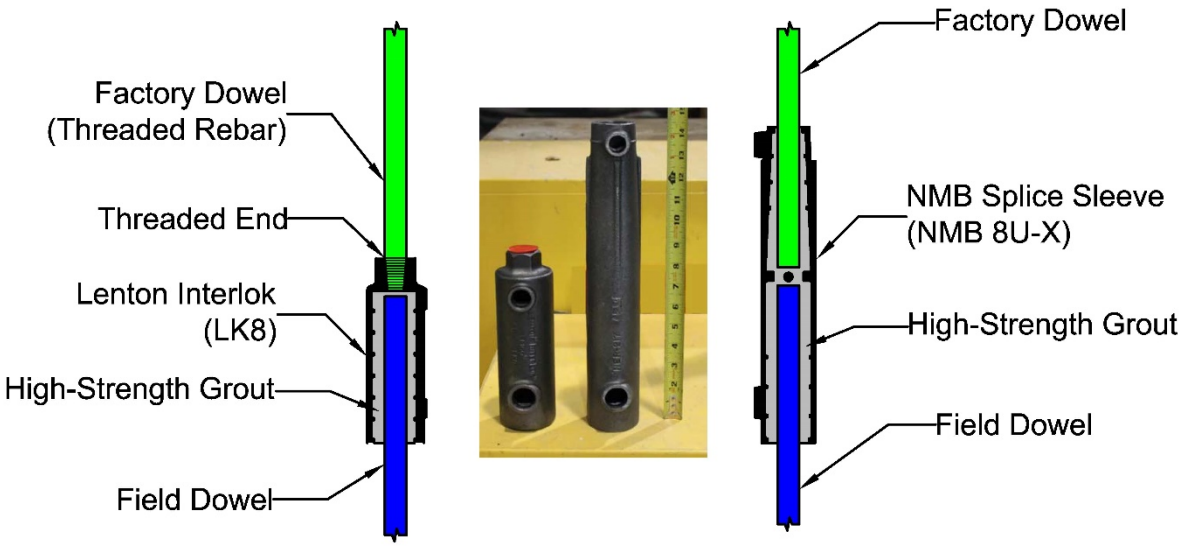

Fig. 1.1. Two types of grouted splice sleeve connectors used in this research, FGSS on the left and GGSS on the right.

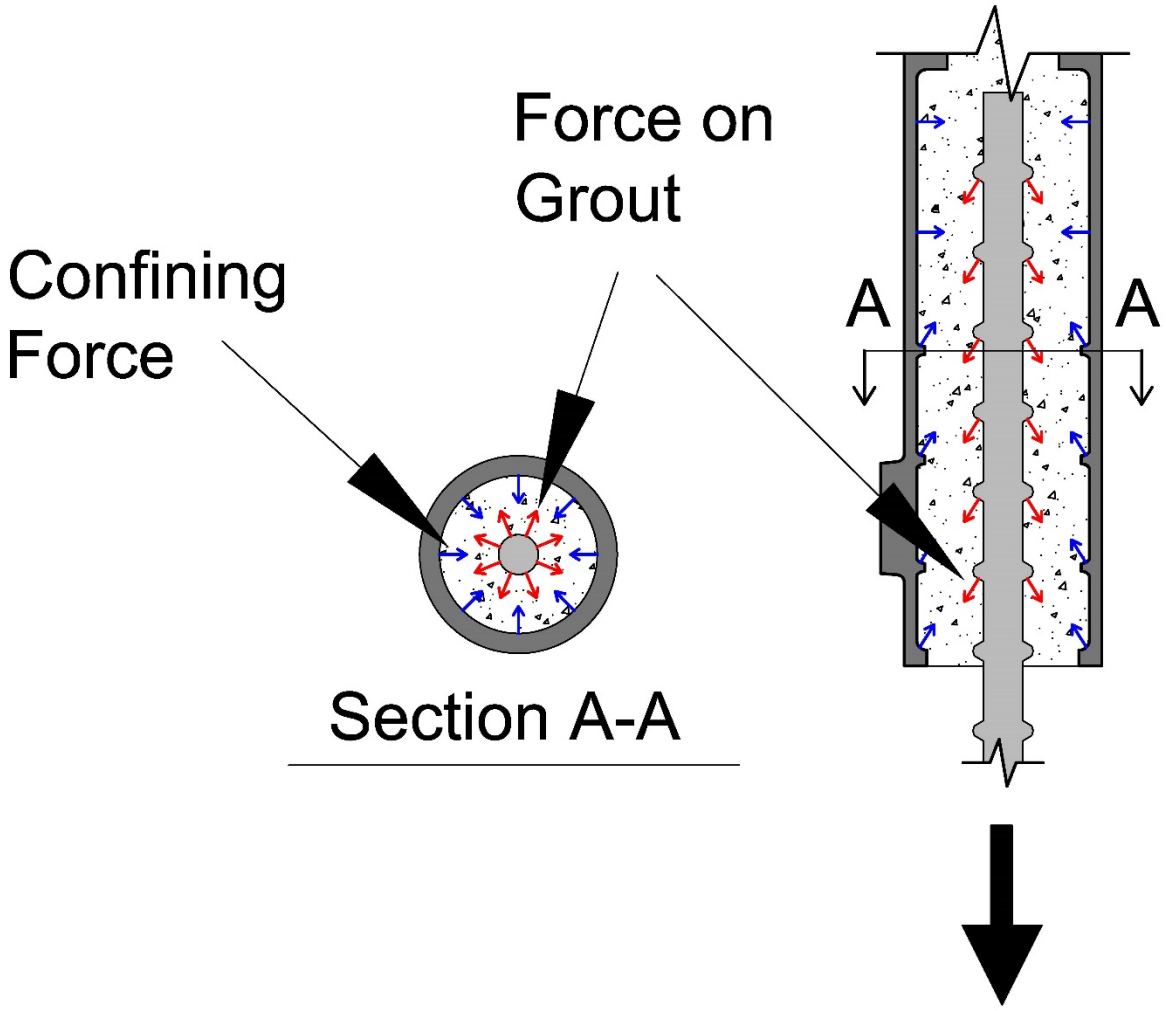

Fig. 1.2. Force transfer for a GSS connector.

CHAPTER 2

SEISMIC EVALUATION OF GROUTED SPLICE SLEEVE CONNECTIONS FOR REINFORCED PRECAST CONCRETE COLUMN–TO–CAP BEAM JOINTS IN ACCELERATED BRIDGE CONSTRUCTION

M. J. Ameli, Joel E. Parks, Dylan N. Brown, and Chris P. Pantelides

Reprinted with permission from the PCI Journal

M. J. Ameli is a PhD candidate in the Civil and Environmental Engineering Department of the University of Utah in Salt Lake City, Utah, where he also received his MSc. His research interests include large-scale testing of structural components, nonlinear design and analysis of reinforced concrete structures, and application of composites in repair and retrofit of concrete components.

Joel E. Parks is a PhD candidate in the Civil and Environmental Engineering Department of the University of Utah, where he also received his MSc. His research interests include nonlinear design and analysis of reinforced concrete structures, and application of composites in repair and retrofit.

Dylan N. Brown earned his MSc in structural engineering from the Civil and Environmental Engineering Department at the University of Utah. His research interests include testing, evaluation, and modeling of repaired precast concrete bridge components designed for accelerated bridge construction in seismic regions.

Chris P. Pantelides is a professor in the Civil and Environmental Engineering Department of the University of Utah. His research interests include seismic design and rehabilitation of reinforced concrete, precast and prestressed concrete buildings and bridges, and the application of fiber-reinforced-polymer composites.

Abstract

Connections between precast concrete elements must be able to withstand significant stresses and deformations in earthquakes. The grouted splice sleeve connector is being considered for use in accelerated bridge construction. Although the application of grouted splice sleeve connectors facilitates the construction of precast concrete bridges and accelerates construction work, seismic bridge design codes inhibit their use in column plastic hinges. Half-scale bridge column–to–cap beam assemblies were tested to investigate their response under cyclic quasi-static load. The grouted splice sleeve connectors were located in the column plastic hinge zone for the first alternative and in the cap beam for the second. A monolithic cast-in-place concrete specimen with identical details served as a control. Satisfactory drift capacity and displacement ductility were achieved when the grouted splice sleeve connectors were inside the cap beam joint. The research shows that precast concrete joints constructed with the specific type of grouted splice sleeve connectors in the cap beam should perform adequately in moderate to high

seismic regions.

Keywords: Accelerated bridge construction; column; connection; cyclic load test; grouted splice sleeve; joint; mechanical coupler.

Introduction

Accelerated bridge construction is a method that incorporates innovative techniques and materials to efficiently reduce construction time and traffic disruption. It also improves work-zone safety for workers and commuters. Prefabrication of bridge structural components is a highly effective technique and is one of the accelerated bridge construction methods under the category of prefabricated bridge elements and systems promoted by the Federal Highway Administration. Several bridges have been built or rehabilitated with accelerated bridge construction methods. Examples in Utah include the Interstate 15 (I-15) Core Provo Center Street interchange, the Riverdale Road over Interstate 84 (I-84) bridge, and the I-15 South Layton interchange. Precast concrete deck panels, substructures, and superstructures have been frequently used in accelerated bridge construction. Connections between such reinforced precast concrete elements are among the most critical components of the structure. Researchers are investigating the adequacy of various connection configurations, especially in moderate to high seismic regions. These connections not only have to conform to accelerated bridge construction standards in terms of construction delivery time but must also resist earthquake-induced deformations and stresses. Lateral load capacity, displacement ductility, and reparability are three significant criteria for any connection considered in seismic regions. In this paper, a column–to–cap beam joint is investigated using grouted splice sleeve connectors

in either the column or the cap beam to construct precast concrete column–to–cap beam joints; the performance of the precast concrete joints is compared with an identical cast-in-place column–to–cap beam joint.

Previous Research

The grouted duct connection is a typical accelerated bridge construction connection for reinforced precast concrete column–to–cap beam joints; corrugated steel ducts are cast in the cap beam, and column reinforcement dowels are inserted and grouted inside the ducts. This connection was found to be a viable technique for accelerated bridge construction in seismic regions.[1–3]

Pocket connections were used to connect bridge columns to cap beams. These are constructed by placing a circular corrugated steel duct inside the cap beam; projected column bars are inserted into the pocket that is filled with concrete. Matsumoto reported that the pocket connection was emulative of conventional monolithic construction in terms of the overall hysteretic performance, force-displacement response, and plastic hinging mechanism.[4]

Prestressing has been incorporated in research studies to improve seismic performance of bridge subassemblies by providing self-centering. This connection is identified as a hybrid connection because both prestressing and mild steel reinforcing bars are used. Residual displacements and overall damage are reduced compared with nonprestressed connections.[5,6]

Grouted splice sleeve connectors and other reinforcing bar splicing devices are also effective accelerated bridge construction methods. Such connectors have been used

in bridge construction in nonseismic regions because they accelerate the construction process. Each individual reinforcing bar connecting precast concrete components is spliced by means of a mechanical coupler located within one of the components. The response of such connections to cyclic loading was studied to investigate their performance in high-seismic regions.[7,8]

Grouted splice sleeve or mechanical reinforcing bar splices are hollow steel cylinders made of ductile iron. Figure 2.1 shows the grouted splice sleeve used in this research. One of the steel reinforcing bars from the two components to be connected is grouted at one end and fastened to the opposite threaded end. Hence, the connector is denoted here as fastened and grouted splice sleeve (FGSS) (Fig. 2.1 and 2.2).

NCHRP report 698 includes an evaluation of several accelerated bridge construction connections in moderate to high seismic regions.[9] Verified connection types include bar couplers, grouted ducts, pocket connections, socket connections, hybrid connections, integral connections, and emerging technologies, such as shape memory alloys. These connections were either used in actual projects or were being developed in research studies. One of the outcomes of this study was the prioritization of more research, considered essential for each connection type, to fully understand its behavior under seismic actions. For the bar coupler which is in the general category of mechanical couplers, including the grouted splice sleeve connectors, NCHRP report 698 recommended further experimental studies to ascertain strength properties of the grouted splice sleeve along with the displacement ductility of components joined with such connectors.

Experimental studies have been conducted on various types of mechanical

couplers comprising only two connecting bars, cast iron sleeves, and high-strength grout.[10–12] Such experiments, referred to as air tests, were conducted to study the strength, reinforcing bar slip, bond characteristics, and fatigue life of the mechanical couplers. Jansson (2008) reported a series of air tests on fastened and grouted splice sleeve connectors for no. 6 (19M) and no. 11 (36M) steel bars.[10] Test results showed acceptable performance in terms of reinforcing bar slip and fatigue life. Tensile test results indicated that all no. 6 assemblies failed due to fracture of the reinforcing bar in the threaded region, thereby reaching the nominal tensile strength of the bars.

Cyclic tests were conducted on large-scale precast concrete specimens joined by means of various grouted splice sleeve connectors.[12–17] The presence of grouted splice sleeve connectors in the plastic hinge region did not considerably change the lateral force capacity of the assembly. However, the displacement capacity was found to be smaller than that of monolithic specimens. Damage progression and the plastic hinge mechanism were also different relative to monolithic specimens.

This paper presents experimental results of three quasi-static cyclic tests of half-scale column–to–cap beam specimens, two of which used fastened and grouted splice sleeve connectors, to investigate their performance compared with the third specimen, which was built using cast-in-place concrete construction. Table 2.1 shows the test matrix, and Fig. 2.3 demonstrates the test configuration alternatives. All specimens were assembled and tested in an inverted position compared with actual construction for ease of construction and testing. A second objective of the study was to investigate the influence of the location of the fastened and grouted splice sleeve connectors within the precast concrete specimens. Specimen FGSS-1 was composed of a precast concrete

column and cap beam with the connectors in the column end, whereas specimen FGSS-2 was composed of a precast concrete column and cap beam with the connectors in the cap beam. Specimen CIP was the cast-in-place concrete alternative, or control specimen, a monolithic construction without any connectors or bar lap splices.

Monotonic Tensile Tests on Individual Connectors

A series of tensile tests were conducted on six individual fastened and grouted splice sleeve connectors, referred to as air tests, to ascertain essential information on the performance of the connectors under monotonic tensile loads. Results from the air tests were used to assess the strength capacity and failure mode of the fastened and grouted splice sleeve connectors, in addition to providing an insight into the overall performance, specifically the stress transfer within the connector.

Two no. 8 (25M) reinforcing bars were connected using a proper size fastened and grouted splice sleeve connector for each air test specimen. The reinforcing bars had a nominal yield strength of 60 ksi (400 MPa) and an actual yield strength of 76 ksi (525 MPa). The test-day compressive strength of the high strength grout was 9.4 ksi (65 MPa). This grout was used to confine the reinforcing bar grouted inside the connector. Monotonic tensile loading was applied until failure occurred when the bottom reinforcing bar pulled out from the connector due to bond failure. Strains were monitored on the rebar portion outside the connector, the rebar portion inside the connector, and on the connector itself. The average strength achieved by the air test specimens was 1.44 ± 0.0488 (SD, n=6) times the nominal yield strength of the reinforcing bar. The strain gauge located 5 in. (127 mm) from the end of the reinforcing bar grouted inside the

connector showed that the rebar yielded at that section.

The gradual pull out failure was initiated by a grout cone failure at the opening end of the connector (Fig. 2.4). A subsequent crushing of the grout in front of the reinforcing bar deformations formed a shear failure surface with a diameter slightly larger than the diameter of the reinforcing bar, and therefore the reinforcing bar pulled out from the connector. Table 2.2 includes the results of the air tests. No sign of damage was noted on the threaded reinforcing bar and it was well developed beyond the yield point.

Design and Construction of Specimens

Specimen Design

The specimens were designed and detailed to simulate prototype bridges constructed in Utah, following the American Association of State Highway and Transportation Officials' AASHTO LRFD Bridge Design Specifications[18] and the AASHTO Guide Specifications for LRFD Seismic Bridge Design[19] in accordance with capacity-based design principles. A circular configuration of column longitudinal bars and an octagonal column cross section were adopted for precasting the columns because this is the method of choice in Utah. The aforementioned design codes in addition to the Caltrans Seismic Design Criteria (SDC)[20] inhibit the splicing of reinforcing bar, including mechanical anchorage devices, in the plastic hinge region of ductile members for bridges located in moderate to high seismic regions. In the AASHTO LRFD seismic bridge design, this would apply to seismic design categories C and D. Thus, the preliminary design and detailing were developed for specimens without fastened and grouted splice sleeve connectors (the cast-in-place concrete specimen). The design was then adjusted to

accommodate the fastened and grouted splice sleeve connectors inside the precast concrete specimens, and essential modifications were considered accordingly.

The specimens were half-scale models of common prototype highway bridges, specifically the Riverdale Road bridge over I-84 in Utah. The column and cap beam dimensions and main longitudinal bars and their configuration were acquired by considering 50% of the actual properties. The column height for all specimens was 8 ft 6 in. (2.6 m) with a 21 in. (530 mm) octagonal cross section to facilitate casting of the concrete. The top 18 in. (460 mm) of the column was changed to a 21 in. (530 mm) square for testing purposes. Six no. 8 (25M) bars in a circular arrangement and a no. 4 (13M) spiral with a pitch of 2½ in. (64 mm) made up the column reinforcement. The longitudinal and volumetric transverse reinforcement ratios were 1.3% and 1.9%, respectively.

A preliminary nonlinear static analysis and a series of sectional analyses were conducted to estimate the maximum lateral load and displacement of the CIP test model and to design the cap beam accordingly. Probable material properties for steel and concrete were used in addition to beam-column elements to perform the preliminary analysis. Detailed nonlinear analyses are currently ongoing which include the effect of the connectors in the system. The cap beam was designed as a 9 ft long × 2 ft wide × 2 ft deep (2.8 m × 0.6 m × 0.6 m) precast concrete member with no. 8 (25M) longitudinal bars enclosed by no. 4 (13M) double hoops. The cap beam was designed to remain linearly elastic and not undergo plastic deformations. The design inhibits shear failure from occurring in the column by using a shear span-to-depth ratio of more than 5.0 (corresponding to slender columns) along with closely spaced adequate shear

reinforcement. The desirable column failure mode was set to be either flexural or splice failure.

Figure 2.5 shows the steel reinforcement without the fastened and grouted splice sleeve connectors. This could be considered the monolithic joint design for cast-in-place concrete construction. The design details for each specimen are summarized in the next section. Dowel bar tails were bent inward to achieve a better performance under lateral cyclic loads as required for seismic design category D in accordance with AASHTO LRFD seismic bridge design.

Fabrication of Test Specimens

The three specimens had identical geometric properties and similar details in the plastic hinge region. Figure 2.6 shows the details of specimen FGSS-1 in addition to the column and cap beam reinforcing bar cages. Specimen FGSS-1 comprised a precast concrete column with the fastened and grouted splice sleeve connectors embedded in the column end and a precast concrete cap beam with dowel bars projecting 7 in. (180 mm). In the first step of the construction phase, column longitudinal bars were fastened to the threaded end of the fastened and grouted splice sleeve connectors. All bars were initially hand tightened to the connectors before being fully tightened using a pipe wrench. A form mounting fixture was used to fasten the grouted splice sleeve connectors to a wooden template arranging the column bars in the desired configuration. The spiral over the fastened and grouted splice sleeve connector region had a 1 5/8 in. (42 mm) larger diameter than the spiral for the rest of the column due to the larger diameter of the fastened and grouted splice sleeve connector compared with reinforcing bar. This resulted

in an overlapping spiral region right above the fastened and grouted splice sleeve connectors.

Figure 2.7 shows the details of specimen FGSS-2 along with the column and cap beam reinforcing bar cages. The location of the fastened and grouted splice sleeve connectors was changed from the column end to inside the cap beam. Such a modification would make the specimen conform to the bridge design code because the fastened and grouted splice sleeve connectors would not be located inside the column plastic hinge region.[19,20] A second reason for examining this alternative was to investigate the reduced disruption to the column plastic hinge region compared with specimen FGSS-1. Such a connection configuration was successfully implemented in the Provo to Salt Lake Frontrunner rail bridge construction using an alternative grouted splice sleeve connector in which both connecting bars were grouted inside the splice sleeve. The precast concrete column reinforcing bar cage was built first for specimen FGSS-2. Dowel bars measuring 7 in. (180 mm) long protruded from the column end. The joint core was built and centered in the cap beam. Threaded hooked bars were previously fastened onto the fastened and grouted splice sleeve connectors by means of a pipe wrench and arranged in a circular fashion using a template. Horizontal joint reinforcement consisting of a closely spaced spiral was tied to both the vertical fastened bars and the fastened and grouted splice sleeve connectors. The tails of the fastened bars were oriented into the joint core and had a length of 2 ft 4 in. (0.7 m).

Specimen CIP represents monolithic construction without any fastened and grouted splice sleeve connectors. Figure 2.8 shows the details of specimen CIP and the reinforcing bar cage before casting the concrete. The column longitudinal bars had no lap

splice. The spiral reinforcement did not have any splice and extended from the column top to the cap beam bottom as continuous helical steel reinforcement around the longitudinal bars. The diameter of the spiral was kept the same as for the spiral around the column bars in the other two specimens, thus ensuring an identical moment arm for column longitudinal bars.

A proprietary high-strength and ready-to-mix grout formulated for this particular grouted splice sleeve was used. One 50 lb (23 kg) bag of grout mixed with 0.7 gal. (2.6 L) of water was sufficient to fill all six fastened and grouted splice sleeve connectors and cast the ¼ in. (6 mm) bed grout. An electric mortar mixer with a jiffler paddle attachment was used to continuously mix the grout with water for 5 min. The flow test conducted after mixing indicated that the grout had a good consistency with an acceptable spread diameter of 5 in. (130 mm) for specimen FGSS-1. The high-strength grout was used to complete the installation. A postgrout technique was implemented for specimen FGSS-1 in which the grout was pumped into the bottom nozzle of the connector. The grout traveled up against gravity and filled the inside space of the connector using a hand pump. Both inlet and outlet ports were plugged when the connector was completely filled with grout. A pregrout technique was conducted for specimen FGSS-2 to facilitate installation. Both inlet and outlet ports of the six connectors were sealed during construction of the cap beam reinforcing bar cage. During erection of specimen FGSS-2 and before lowering and positioning the column, the high-strength grout was pumped into the wide end opening (Fig. 2.9). The flow test showed an acceptable grout consistency with a spread diameter of 5.25 in. (133 mm) for specimen FGSS-2.

Tension tests of reinforcing bars were conducted along with compression tests on concrete cylinders and grout cubes for each specimen.[21–23] Table 2.3 presents the results of tension tests on reinforcing bars. The column bars for specimen FGSS-1 and the cap beam dowel bars for specimen FGSS-2 had different material properties than the rest of the steel bars because these were obtained from the manufacturer as threaded bars. Table 2.4 contains the compression test results for the concrete and grout reported for both the 28th day of curing and the day of the specific test.

Test Procedure

Instrumentation

Test specimens were instrumented with strain gauges in the plastic hinge region and the joint area on both longitudinal and transverse steel. For the precast concrete specimens, strain gauges were placed in the middle section of the fastened and grouted splice sleeve connectors to obtain the strain on the sleeves. String potentiometers were used to measure column displacements during the test. They were attached to the column head at the actuator centerline. The two potentiometers were oriented in two opposite directions. Column displacements were obtained by taking the average of the two potentiometer readings. Linear variable differential transformers (LVDTs) were used to study the curvature distribution and base rotation, bond slip, and global vertical and horizontal movement of the specimens.

Ten LVDTs were mounted to the column end, over a 30 in. long region to measure the relative vertical displacements and provide data for curvature analysis. Figure 2.10 shows an example of strain gauges installed on both longitudinal and

transverse reinforcement of specimen CIP along with LVDTs attached to fixtures on the east side of the column.

Experimental Setup

Each specimen was connected to the floor by means of eight high-strength threaded rods on each side, half of which ran through PVC pipes embedded in the cap beam. The rods were then bolted to the strong floor to prevent the specimens from moving or slipping. This support condition was designed to provide limited rotational restraint simulating a hinged support condition.

The axial load system consisted of a cylindrical 500 kip (2200 kN) hydraulic actuator, a 4 ft (1.2 m) long stiffened W14 × 90 (W360 × 134) spreader beam, a 3 in. (76 mm) thick A36 (248 MPa) steel plate, and two 14 ft 6 in. (4.4 m) long 150 ksi (1030 MPa) all-thread rods. The actuator rested on the column top and applied a compression force to the steel beam above it, causing the all-thread rods to pull on the steel plate underneath the cap beam. An axial compressive load of 6% of column axial capacity was applied to simulate gravity loads. Figure 2.11 shows a schematic and a picture of the specimen fastened to the floor girders.

A 120 kip (530 kN) servo-controlled actuator with an overall stroke of 18 in. (440 mm) was used to apply the quasi-static displacement history; however, specimen CIP was tested using a 250 kip (1100 kN) servo-controlled actuator with an overall stroke of 24 in. (610 mm).

Displacement History

A reversed cyclic quasi-static displacement-controlled protocol was applied to the column at an elevation of 8 ft (2.4 m) above the cap beam. The history comprised increasing amplitudes as multiples of the predicted yield displacement of the column.[24] Two cycles were employed for each displacement cycle to the east and west (Fig. 2.11). The displacement rate was set to 1.2 in./min (30 mm/min) up to the end of the 3 in. (76 mm) displacement cycle, after which it was changed to 4 in./min (100 mm/min) and was kept constant until test completion.

Test Results

Hysteretic Response

Figure 2.12 shows the hysteresis curves of the specimens. They include four major damage states: concrete cracking and spalling, reinforcing bar pullout, yield penetration, and reinforcing bar fracture.

Hysteresis Response of Specimen FGSS-1

The pinched hysteresis loops for specimen FGSS-1 (Fig. 2.12) indicate that the overall force-displacement performance was controlled by the bond-slip characteristics of the fastened and grouted splice sleeve connectors. In addition to pinching from excessive slippage of the cap beam dowel bars inside the fastened and grouted splice sleeve connectors, reinforcing bar slippage introduced another type of disruption in the unloading branch of the response in the east direction. This was attributed to closure of the gap originally formed as a result of bond deterioration and bar slip. This gap closure

phenomenon at the column–to–cap beam interface is visible for the unloading branch of the hysteresis loops at the 4% to 6% drift ratio in the east direction. The lateral force peaked at the 5% and 3% drift ratio in the east and west direction, respectively. A gradual strength reduction or cyclic strength deterioration was noted as a result of bond degradation between the dowel bar and grout inside the fastened and grouted splice sleeve connectors. The test was terminated at the end of the 6% drift ratio due to a load reduction of 20% and 30% for the east and west directions, respectively. Failure of specimen FGSS-1 was caused by excessive bar slippage and pullout of reinforcing bar from the fastened and grouted splice sleeve connectors. It is noted that the axial load applied to this specimen was unintentionally 40% higher than the height of the other two test specimens. This introduced a slight increase in the lateral force capacity for FGSS-1.

Hysteresis Response of Specimen FGSS-2

Hysteresis loops of specimen FGSS-2 (Fig. 2.12) were relatively wide and stable compared with specimen FGSS-1, without any considerable strength degradation before reinforcing bar fracture or pullout, in the last drift ratio of 7%. The peak lateral force of 34.7 kip (154 kN) and 36.3 kip (161 kN) occurred at the 4% and 5% drift ratio, in the east and west directions, respectively. The column west reinforcing bar fractured in the first cycle of the 7% drift ratio, while column east bars underwent excessive slippage, which resulted in considerable strength reduction. Ultimately, the test was terminated after completion of the 7% drift ratio because a strength drop of 42% and 45% occurred in the lateral force capacity as a result of west reinforcing bar fracture and east reinforcing bar pullout. This was a unique failure mode because it included both a ductile failure and a

bond-slip failure. The gap closure phenomenon at the column–to–cap beam interface described for specimen FGSS-1 was also observed for this specimen, an indication of excessive reinforcing bar slip at the 4% drift ratio.

Hysteresis Response of Specimen CIP

The overall response of specimen CIP was satisfactory, and the wide and stable hysteresis loops implied a high energy dissipation capacity. This desirable performance represents a ductile response of a well-detailed reinforced concrete flexural component, under both axial and lateral loading. The peak lateral force was 37.8 kip (168 kN) during the 2% drift ratio and 33.9 kip (151 kN) during the 3% drift ratio for the east and west direction, respectively.

This test was terminated at the end of the 10% drift ratio due to the fracture of both extreme east and west column longitudinal steel bars. The west reinforcing bar fractured when the column top was close to the peak displacement during the first cycle of the 10% drift ratio. Subsequently, the bar on the east side of the column fractured during the first cycle of the 10% drift ratio. The superior hysteretic response of the control specimen is evident when compared with both precast concrete alternatives in Fig. 2.12.

Experimental Observations and Damage States

Visual observations made during testing of the precast concrete and control specimens are summarized in Fig. 2.13 to 2.15. This includes damage progression along with damage states of the most significant events throughout the response.

Visual Observations for Specimen FGSS-1

All major cracks developed by the end of the 3% drift ratio. Spalling initiated at the corners of the octagonal column during the first cycle of the 3% drift ratio. The largest crack, which had formed previously at the bed grout section, turned into a gap at the column–to–cap beam interface during the 3% drift ratio. This is evident in Fig. 2.13, which shows the gap opening while the column was at the peak displacement of the 3% drift ratio.

Cracks widened and concrete spalling progressed at higher drift ratios. During the 6% drift ratio, the cone shape of the expelled grout became visible; this condition is presented in Fig. 2.13. This grout failure resembles the air test results shown in Fig. 2.4. The test was terminated after completion of the 6% drift ratio due to bond deterioration, and subsequent reinforcing bar pullout. The height of the spalled concrete was 8 in. (200 mm) and 12 in. (300 mm) on the west and east sides of the column, respectively. The spiral was partially exposed, and the bed grout was crushed at the column peripheral. The permanent opening at the bed grout had a residual gap equal to 0.1 in. (2.5 mm). The cap beam remained intact with only a few scattered hairline cracks in the joint region.

Visual Observations for Specimen FGSS-2

A hairline flexural crack formed at a section 12 in. (300 mm) above the column base during the 0.5% drift ratio. During the next drift ratio of 1%, this crack had a width of 0.002 in. (0.05 mm). Two more flexural cracks developed at 20 in. (510 mm) and 28 in. (710 mm) above the column end during the same drift ratio. More cracks developed during the 2% and 3% drift ratio including one at the bed grout. There were

overall seven major flexural cracks that formed along the column by the end of the 3% drift ratio. The width of the crack formed during the 2% drift ratio at a section 8 in. (200 mm) from the column base measured 0.03 in. (0.8 mm) at the end of the 3% drift ratio. Concrete cover spalling initiated during this drift ratio with a height of 8 in. on the column east side (Fig. 2.14). Cracks opened further and concrete spalling intensified after the 3% drift ratio up to test termination. Flexure-shear cracks formed on the north and south sides of the column during the 5% drift ratio, and the representative crack at 8 in. above the column base had a width of 0.04 in. (1 mm). Spalling became deeper and wider during the 6% drift ratio, and a strength reduction was noted at the end of the second cycle in the west direction. This was attributed to bond deterioration between the grout and the embedded column dowel. The column extreme west bar broke at the end of the first cycle in the 7% drift ratio, whereas the east bar did not fracture; however, the drop in the lateral force capacity for the west direction implied that a bond-related phenomenon had caused a sudden reduction in strength. Post-test observations showed that the spiral became exposed near the column end, and the largest flexural crack was found 4 in. (100 mm) above the column base measuring 0.06 in. (1.5 mm) wide. The location of the reinforcing bar fracture was 1 in. (25 mm) above the column base, right below the spiral. Low cycle fatigue was the cause of reinforcing bar fracture as a result of successive bending and straightening of the column extreme bars. A permanent gap equal to 0.125 and 0.0625 in. (3.18 and 1.59 mm) remained at the bed grout section on the east and west sides of the column, respectively. Figure 2.13 shows the damage condition at the 3% and 7% drift ratio for specimen FGSS-2.

Visual Observations for Specimen CIP

A few hairline flexural cracks appeared at the end of the 0.5% drift ratio over a 40 in. (1020 mm) long region up from the column end. More hairline flexural cracks developed during the 1% drift ratio, up to 60 in. (1500 mm) above the column end. The cracks, which had formed within the lowermost 12 in. (300 mm) portion of the column, grew larger in width during the 2% drift ratio. Also, a 0.03 in. (0.8 mm) wide crack formed at the column–to–cap beam interface. The crack at 12 in. from the column end had a width of 0.005 in. (0.1 mm) at this drift ratio. All major flexural cracks developed by the end of the 3% drift ratio, and concrete cover spalling began at the column corners. The crack at the column–to–cap beam interface remained unchanged, while the crack at 12 in. (300 mm) from the column end was 0.01 in. (0.3 mm) wide. Figure 2.15 shows the damage condition at the end of the 3% drift ratio.

Inclined cracks formed on the north and south sides of the column base in the 4% drift ratio. By the end of the 4% drift ratio, the largest three cracks measured 0.04, 0.06, and 0.013 in. (1, 1.5, and 0.30 mm) wide for the crack at the column–to–cap beam interface, 6 in. (150 mm) from the column end, and 12 in. (300 mm) from the column end, respectively.

Yield penetration was noted around the two column extreme bars at the end of the 6% drift ratio. Spalling became wider and deeper, covering the cracks that developed in the previous cycles. Figure 2.14 shows the state of damage to the column at the end of the 6% drift ratio. In the 7% drift ratio, the column spiral became visible and the depth of yield penetration increased to 1 1/8 in. (29 mm). The column extreme longitudinal reinforcing bar was visible during the 8% drift ratio. The concrete cover was crushed,

which led to buckling of the reinforcing bar during the next drift ratio.

Low cycle fatigue caused fracture of the column extreme bars on both sides in the first cycle of the 10% drift ratio. The west column bar fractured first when the load was applied in the east direction, and then the east column bar fractured when the load was applied in the west direction. Reinforcing bar fracture occurred in the column end, at 1 and 1 ½ in. (25 and 38 mm) from the cap beam surface for the west and east column bars, respectively. The spalled region had an effective width of 21 in. (530 mm) and height of 8 in. (200 mm), though the maximum height of the spalled area was 16 and 20 in. (400 and 510 mm) for the east and west column sides, respectively. The cap beam horizontal reinforcing bar was revealed as a result of continuous yield penetration of the column reinforcing bar. Figure 2.14 shows the damage state for this specimen at the end of the test. The cap beam remained intact with only two hairline cracks developed in the joint region during the 2% drift ratio.

Displacement Ductility

Displacement ductility capacity is the ability of a structural component to perform beyond the yield point without excessive strength deterioration; this was computed based on the concept of equal energy of an idealized elasto-plastic system.[25] The average backbone curve was first constructed using the peak values of the first cycle for each drift ratio. To obtain the effective yield displacement of the system, it was assumed that the ideal elasto-plastic curve intersects the average backbone curve at a force equal to 70% of the effective yield force.[24] The ultimate displacement was taken as the displacement corresponding to a 20% drop in lateral load capacity.[26] Displacement ductility is the ratio

of the ultimate displacement to the yield displacement. Table 2.5 shows the displacement ductility of all specimens.

The displacement ductility of specimen FGSS-1 was 4.9, while specimen FGSS-2 had an improved value equal to 5.8 due to a more pronounced bending action along the entire column height. Specimen CIP had a ductile performance and a displacement ductility of 9.9, which was superior to the precast concrete specimens. The displacement ductility capacity obtained for the precast concrete specimens exceeded the minimum displacement ductility capacity of 3.0 for ductile components specified in Caltrans SDC.[20] According to the AASHTO seismic bridge design provisions, the local ductility demand for ductile members in high seismic zones is limited to 5.0 for single-column bents and 6.0 for multiple-column bents.[19] The backbone curve of the force-displacement response or cyclic envelope was constructed by joining the peak values of the load for the first cycle at each drift ratio. Figure 2.16 presents the cyclic envelopes for the three specimens. The response is similar up to 0.5% drift ratio, after which there were differences in the nonlinear response, especially in terms of displacement capacity. The lateral load capacity was similar for specimens FGSS-2 and CIP, whereas specimen FGSS-1 had a relatively higher strength. This is attributed to the fact that the axial load applied to specimen FGSS-1 was unintentionally 40% higher than the other two specimens. In addition, based on previous experiments, when the bulky cast-iron grouted splice sleeve connectors are incorporated in the column plastic hinge, there is a 7% to 13% increase in the lateral force capacity due to a partial transition of the flexural action to the section right above the grouted splice sleeve.[12,16,27] A third reason is the additional compression component from the cast-iron connectors, which provide some resistance

against the applied lateral forces. Hence, the lateral force capacity of specimen FGSS-1 was 11% greater than that of specimen CIP.

Energy Dissipation

One of the desirable features of ductile elements in high seismic regions is their ability to dissipate energy through inelastic deformations. This is an indication of the quality of the hysteretic response. The area enclosed by the hysteresis loops, referred to as the hysteretic energy, was computed cumulatively for each specimen to obtain the energy dissipation capacity.

Figure 2.17 shows the cumulative hysteretic energy capacity. The three specimens had similar hysteretic energy dissipation up to 3% drift ratio, after which specimens CIP and FGSS-2 had a slightly better performance. Specimen FGSS-2 with the fastened and grouted splice sleeve connectors inside the cap beam had wide and stable hysteresis loops that compared well with specimen CIP.

Equivalent viscous damping is another quantity used to evaluate relative energy dissipation capacity under cyclic loads. The equivalent viscous damping offers more information about the hysteretic response of the system because both hysteretic and strain energy are considered. The equivalent viscous damping ratio ξ_{eq} was obtained as the ratio of the hysteretic energy to the energy of the equivalent viscous system as defined in Eq. (2.1).[28]

$$\xi_{eq} = \frac{E_D}{4\pi E_{S0}} \tag{2.1}$$

where

E_D = hysteretic energy (area inside hysteresis loop)

E_{S0} = strain energy

Figure 2.18 presents the average ξ_{eq} of both cycles for each drift ratio. Specimen FGSS-2 had the closest hysteretic performance to specimen CIP. Specimen CIP had a ξ_{eq} of 35% at the 10% drift ratio, which is a desirable value for ductile components. The equivalent viscous damping ratio at 6% drift ratio was 14%, 22%, and 24% for specimens FGSS-1, FGSS-2, and CIP, respectively. This implies that the hysteretic response was improved when the fastened and grouted splice sleeve connectors were located inside the cap beam because of a reduced level of flexural demand in the fastened and grouted splice sleeve region.

Column Curvature and Dowel Bar Yielding Patterns

LVDTs installed on both the east and west sides of the column were used to study curvature distribution. Four curvature segments were specified by using four LVDTs on each side of the column. The average curvature was computed using Eq. (2.2):

$$\phi = \frac{A - B}{wh} \tag{2.2}$$

where

ϕ = average curvature

A = west LVDT reading

B = east LVDT reading

w = width of curvature segment

h = height of curvature segment

The average curvature profile was constructed over a 30 in. (760 mm) column height above the column end. The average curvature values were normalized by

multiplying by the column dimension of 21 in. (530 mm), and the curvature segment heights were divided by the column overall height of 96 in. (2440 mm). Positive curvature was associated with the load applied in the east direction. The calculated curvature was assumed to be an average over the segment height. Figure 2.19 presents the normalized curvature distribution along the column for all specimens. Curvatures were included up to a 6% drift ratio, which was the last common drift ratio. Dashed lines mark the top of the fastened and grouted splice sleeve connectors in the column for specimen FGSS-1.

The normalized curvature profile of specimen FGSS-1 indicates that curvature capacity was a minimum over the FGSS connectors and that flexural action was concentrated at sections above and below the fastened and grouted splice sleeve connectors. An examination of this curvature profile reveals that the fastened and grouted splice sleeve connectors did not develop considerable stresses. The asymmetric curvature profile of specimen FGSS-1 was attributed to early bond deterioration of the east cap beam dowels inside the connectors. Considering the hysteretic response of this specimen (Fig. 2.12), a drastic strength drop was noted after the 3% drift ratio, when the load was applied in the west direction. This implies gradual strength degradation as a result of severe bond deterioration, which caused a more pronounced rocking behavior than bending, and thus smaller curvature values when the column was in the west direction.

A satisfactory curvature distribution was achieved for specimen FGSS-2 (Fig. 2.19). This is similar to the curvature distribution for cast-in-place concrete bridge bents with either well-detailed standard lapped splices or monolithic construction. Neglecting the asymmetric curvature distribution for the load applied in the west and east

directions, this curvature profile resembles an acceptable distribution of curvature demand along the column, with the highest curvature values at the column end where moment is also a maximum and a gradual decrease in curvature away from the joint. The asymmetric curvature profile was caused mainly because of a movement of one of the LVDT fixtures located on the column east side as a result of damage occurring in the plastic hinge zone during the 3% drift ratio.

Specimen CIP had a desirable curvature distribution along the column base. This was attributed to the well-detailed column plastic hinge region without fastened and grouted splice sleeve connectors.

Strain gauges located on the two extreme longitudinal bars in the column end within the joint core of specimen FGSS-1, covered an area with a depth of 7 in. (180 mm) into the cap beam and 16 ¼ in. (413 mm) above the column end. Both extreme bars yielded over the whole range covered by strain gauges, except for the initial 5 in. (125 mm) portion of the field dowels, which was embedded and confined inside the fastened and grouted splice sleeve connectors.

For specimen FGSS-2, strain gauges were installed over an area with a depth of 13 in. (330 mm) into the cap beam and 18 in. (460 mm) above the column end. The extreme column dowels yielded starting at 5 in. (125 mm) from the tip of the column dowel bars, which were confined within the fastened and grouted splice sleeve connectors, or 2 in. (50 mm) into the cap beam from the column–to–cap beam interface. The cap beam dowel bars did not yield.

Strain gauges located on the extreme longitudinal bars, in the column end, and within the joint core of specimen CIP showed that the extreme bars yielded over an area

with a depth of 9 ½ in. (240 mm) into the cap beam and 38 in. (970 mm) above the column end.

Residual Drift

During a major seismic event it is highly probable for bridge piers to have a permanent residual displacement (drift), indicating the system is in the inelastic range of response without the ability to return to its original position. A reduced residual drift is more desirable in regions of high seismicity as it implies a lower level of significant damage to the plastic hinge region of bridge columns. To compare the residual drift of the three test specimens, this parameter was obtained by collecting the drift values associated with zero lateral force for each drift ratio. The average residual drift of the push and pull response was considered from the second cycle of each drift ratio.

Figure 2.20 shows that specimen CIP had larger residual drift values within the inelastic range of response starting at 1% drift ratio. The response of FGSS-2 is similar to CIP as anticipated, since the connectors were outside the column. Specimen FGSS-1 had the smallest residual drift values for every cycle. This was mainly attributed to the pinched hysteretic response of FGSS-1.

Conclusion

The experimental evaluation of the column–to–cap beam joint tests conducted in this research provided qualitative and quantitative measures to evaluate the specimens under quasi-static lateral cyclic loads. A summary of findings is offered:

1. Specimen CIP had a good hysteretic response with ductile failure (reinforcing bar

fracture on opposite sides of the column). Well-distributed flexural cracks formed along the column height and the concrete cover spalled completely at the column end. The overall performance of specimen CIP was dominated by flexural action and formation of a plastic hinge at the column end. More localized damage was observed for precast concrete specimen FGSS-1 with the fastened and grouted splice sleeve connectors in the column. This involved fewer flexural cracks along the column height compared to specimen CIP. The spalled region was also smaller as a result of the presence of the fastened and grouted splice sleeve connectors in the column end. Precast concrete specimen FGSS-2 with the fastened and grouted splice sleeve connectors in the cap beam had a damage state similar to specimen CIP because there were no sleeve connectors in the column. More flexural cracks formed along the column compared with specimen FGSS-1, and the spalled region had a similar height, width, and depth to that of specimen CIP.

2. Reinforcing bar fracture for specimen CIP occurred at a 10% drift ratio due to low cycle fatigue. Premature reinforcing bar fracture occurred in the west column bar of specimen FGSS-2 at a 7% drift ratio, which was accompanied by pullout failure of the east column bar. Specimen FGSS-1 failed early at a drift of 6% because of reinforcing bar pullout due to excessive bond slip.
3. Specimen CIP had a displacement ductility of 9.9 with hysteresis loops that were wide and stable, implying excellent energy dissipation. A displacement ductility of 5.8 was achieved for specimen FGSS-2 for which the fastened and grouted splice sleeve connectors were inside the cap beam. Compared with specimen

FGSS-1, with a displacement ductility of 4.9, a more ductile response along with a better hysteretic performance was obtained by placing the fastened and grouted splice sleeve connectors in the cap beam. The displacement ductility obtained for all alternatives exceeded the minimum component displacement ductility of 3.0 specified in the Caltrans SDC. The displacement ductility for specimen FGSS-2 was greater than the maximum ductility of 5.0 for single-column bridge bents but less than the maximum ductility of 6.0 for multiple-column bridge bents specified in the AASHTO seismic guide for ductile members in high seismic zones.

4. The distribution of inelasticity at the column end for precast concrete specimen FGSS-2 was similar to that of specimen CIP because there was no disruption of the natural stress transfer in the column end; however, for specimen FGSS-1 a different distribution of inelasticity was observed. This was attributed to the presence of the fastened and grouted splice sleeve connectors in the column end and the inelastic action shifting to locations at the top and bottom of the connectors. Strain gauge data for specimen FGSS-1 showed that dowel bars developed their yield strength both in the column and cap beam. By contrast, for specimen FGSS-2, the bars in the column yielded, but the bars in the cap beam did not yield. This is desirable and closely emulates cast-in-place concrete construction.
5. Column–to–cap beam specimen FGSS-2, constructed with fastened and grouted splice sleeve connectors in the cap beam, achieved a drift capacity of 7.0%, which exceeds the drift demand expected in large earthquakes. Specimen FGSS-2 achieved satisfactory hysteretic performance and energy dissipation. In addition it

achieved a displacement ductility of 5.8 and a curvature distribution that closely emulates cast-in-place construction. Precast concrete joints constructed with the specific details of specimen FGSS-2 are expected to perform adequately in moderate to high seismic regions.

Acknowledgements

The authors would like to acknowledge the financial support of the Utah, New York State, and Texas departments of transportation. The authors wish to thank Lawrence D. Reaveley, a professor at the University of Utah, for his invaluable input throughout the project. Special thanks are extended to Mark Bryant of the University of Utah for his untiring efforts and support. The authors are also grateful for the donation of materials by ERICO and the assistance of Hanson Structural Precast.

Notation

A = west linear variable differential transformers reading

B = east linear variable differential transformers reading

E_D = hysteretic energy (area inside hysteresis loop)

E_{S0} = strain energy

f_y = nominal yield strength of reinforcing bars

F = force

F_y = effective yield force

h = height of curvature segment

K_{eff} = effective stiffness

P = axial load

w = width of curvature segment

Δ_u = effective ultimate displacement

Δ_y = effective yield displacement

μ_Δ = displacement ductility

ξ_{eq} = equivalent viscous damping

ϕ = average curvature

References

1. Pang, J. B. K., M. O. Eberhard, and J. F. Stanton. 2010. "Large-Bar Connection for Precast Bridge Bents in Seismic Regions." *Journal of Bridge Engineering* 15 (3): 231–239.

2. Matsumoto, E. E. 2009. "Emulative Precast Bent Cap Connections for Seismic Regions: Component Tests—Grouted Duct Specimen (Unit 2)." ECS report ECS-CSUS-2009-02. Sacramento, CA: California State University, Sacramento.

3. Mashal, M., and A. Palermo. 2014. "Experimental Investigation into the Seismic Performance of Half-Scale Fully Precast Bridge Bent Incorporating Emulative Solution." In *10th National Conference in Earthquake Engineering: Frontiers of Earthquake Engineering, Proceedings*, CD Rom, Earthquake Engineering Research Institute, Oakland, CA.

4. Matsumoto, E. E. 2009. "Emulative Precast Bent Cap Connections for Seismic Regions: Component Tests—Cap Pocket Full Ductility Specimen (Unit 3)." ECS report ECS-CSUS-2009-03. Sacramento, CA: California State University, Sacramento.

5. Restrepo J. I., M. J. Tobolski, E. E. Matsumoto. 2011. "Development of a Precast Bent Cap System for Seismic Regions." NCHRP (National Cooperative Highway Research Program) 681.Washington, DC: NCHRP.

6. Haraldsson, O. S., M. J. Schoettler, G. Finnsson, P. M. Davis, J. F. Stanton, and M. O. Eberhard. 2013. "Seismic Resistance of Precast Concrete Bridge Columns Made with Unbonded Pre-Tensioning and Hybrid Fiber Reinforced Concrete." In *Proceedings of the Seventh National Seismic Conference on Bridges & Highways, Bridge Resilience for Earthquakes & Other Natural Hazards, Eds., Kapur, J. and Ostrom, T., CD Rom, MCEER, University at Buffalo, State University of New York, Buffalo, New York. Paper*

A3-5.

7. Haber, Z. B., M. S. Saiidi, and D. H. Sanders. 2014. "Seismic Performance of Precast Columns with Mechanically Spliced Column-Footing Connections." *ACI Structural Journal* 111 (3): 639–650.

8. Tazarv, M., and M. S. Saiidi. 2014. "Next Generation of Bridge Columns for Accelerated Bridge Construction in High Seismic Zones." CCEER (Center for Civil Engineering Earthquake Research) 14-06. Reno, NV: Department of Civil and Environmental Engineering, University of Nevada, Reno.

9. Marsh, M. L., M. Wernly, B. E. Garett, J. F. Stanton, M. O. Eberhard, and M. D. Weinert. 2011. "Application of Accelerated Bridge Construction Connections in Moderate-to-High Seismic Regions." NCHRP (National Cooperative Highway Research Program) 698.Washington, DC :NCHRP.

10. Jansson, P. O. 2008. "Evaluation of Grout-Filled Mechanical Splices for Precast Concrete Construction." Report R-1512. Lansing, MI: Michigan Department of Transportation.

11. Rowell, S. P., C. E. Grey, S. C. Woodson, and K. P. Hager. 2009. "High Strain Rate Testing of Mechanical Couplers." ERDC (Engineer Research and Development Center) TR-09-8. Vicksburg, MS: U.S. Army Corps of Engineers, Engineer Research and Development Center, Geotechnical and Structures Laboratory.

12. Haber, Z. B., M. S. Saiidi, and D.H. Sanders. 2013. "Precast Column-Footing Connections for Accelerated Bridge Construction in Seismic Zones." CCEER 13-08. Reno, NV: Center for Civil Engineering Earthquake Research, Department of Civil and Environmental Engineering, University of Nevada, Reno.

13. Matsuzaki, Y., et al. 1987. "Effects of Sleeves on Member Properties, Study on the Behavior of Reinforced Concrete Beams with Grout-Filled Steel Splice Sleeves." Architectural Institute of Japan, Tokyo, Japan.

14. Splice Sleeve Japan Ltd. "Tests on Re-Bar Splices in Reinforced Concrete Columns Using NMB Splice Sleeves." NPD-024, Splice Sleeve Japan, Ltd., Tokyo, Japan.

15. Yoshino, T., K. Kobayashi, and M. Ase. 1996. "Intensive Shear Reinforcing Method for PCA Members with Splice Sleeve Joint." In *Proceedings of the Eleventh World Conference on Earthquake Engineering June 23–28, Acapulco, Mexico, CD-Rom, Elsevier Science, Oxford.*

16. Aida, H., Y. Tanimura, T. Tadokoro, and K. Takimoto. 2005. "Reversed Cyclic Loading Test of Precast Columns with Grout-filled Sleeves for Railway Viaducts." Japan Concrete Institute, *Proceedings of the Japan Concrete Institute.* 27 (2).

17. Reetz, R. J., M. V. Ramin, and A. Matamoros. 2004. "Performance of Mechanical

Splices within the Plastic Hinge Region of Beams Subject to Cyclic Loading." Paper No. 1073, *Proceedings of 13th World Conference on Earthquake Engineering, 13 WCEE-Canada 2004,CD Rom, Canadian Association for Earthquake Engineering,* Vancouver, B.C., Canada.

18. AASHTO (American Association of State Highway and Transportation Officials). 2012. *AASHTO LRFD Bridge Design Specifications.* Washington, DC: AASHTO.

19. AASHTO. 2011. AASHTO Guide Specifications for LRFD Seismic Bridge Design. Washington, DC: AASHTO.

20. California Department of Transportation. 2010. *Seismic Design Criteria.* Sacramento, CA: Division of Engineering Services.

21. ASTM A370-09a. 2009. *Standard Test Method and Definitions for Mechanical Testing of Steel Products*. West Conshohocken, PA: ASTM International. doi: 10.1520/A0370-09A.

22. ASTM C39. 2012. *Standard Test Method for Compressive Strength of Cylindrical Concrete Specimens*. ASTM International, West Conshohocken, PA. doi: 10.1520/C0039_C0039M-12.

23. ASTM C109. 2012. Standard Test Method for Compressive Strength of Hydraulic Cement Mortars (Using 2-in. or [50-mm] Cube Specimens). ASTM International: West Conshohocken, PA. doi: 10.1520/C0109_C0109M-12.

24. ACI Committee 374. 2013. Guide for Testing Reinforced Concrete Structural Elements Under Slowly Applied Simulated Seismic Loads. ACI 374.2R-13. Farmington Hills, MI: ACI.

25. Park, R. 1989. "Evaluation of Ductility of Structures and Structural Assemblages from Laboratory Testing." *Bulletin of the New Zealand National Society for Earthquake Engineering* 22 (3): 155–166.

26. Priestley, M. J. N., and R. Park. 1987. "Strength and Ductility of Concrete Bridge Columns Under Seismic Loading." *ACI Structural Journal* 84 (1): 61–76.
27. Ameli, M. J., J. E. Parks, D. N. Brown, C. P. Pantelides. 2014. Seismic Evaluation of Grouted Splice Sleeve Connections for Precast RC Bridge Piers. Report UT-14.09 . Salt Lake City, UT: Utah Department of Transportation.

28. Chopra, A. 2007. *Dynamics of Structures, Theory and Applications to Earthquake Engineering*. 4th ed., Upper Saddle River, NJ: Pearson Prentice Hall.

Table 2.1. Test matrix for column–to–cap beam joints

Test identification	Specimen	Connector type	Connector location	Other
1	FGSS-1	LK-8	Column	n/a
2	FGSS-2	LK-8	Cap beam	n/a
3	CIP	n/a	n/a	Cast-in-place

Note: n/a = not applicable.

Table 2.2. Tension test results for air test specimens

Air test identification	Maximum load (kip)	Maximum bar stress (ksi)	Maximum bar stress normalized to f_y^*	Observed failure mode
Air test-1	69.7	88.2	1.47	Reinforcing bar pullout
Air test-2	71.5	90.5	1.51	Reinforcing bar pullout
Air test-3	66.4	84.1	1.40	Reinforcing bar pullout
Air test-4	68.0	86.1	1.43	Reinforcing bar pullout
Air test-5	64.6	81.8	1.36	Reinforcing bar pullout
Air test-6	69.1	87.5	1.46	Reinforcing bar pullout

*Nominal yield strength of reinforcing bar is used.

Table 2.3. Yield and ultimate strength of reinforcing bars

Specimen	Column reinforcing bar				Cap beam reinforcing bar			
	Longitudinal (no. 8)		Transverse (no. 4)		Dowel bar (no. 8)		Transverse (no. 4)	
	Yield, ksi	Ultimate, ksi	Yield, ksi	Ultimate, ksi	Yield, ksi	Ultimate, ksi	Yield, ksi	Ultimate, ksi
FGSS-1	77	102	63	103	68	93	63	103
FGSS-2	68	93	63	103	77	102	63	103
CIP	68	93	63	103	68	93	63	103

Note: no. 4 = 13M; no. 8 = 25M; 1 ksi = 6.89 MPa

Table 2.4. Compressive strength of concrete and grout, ksi

Specimen	Concrete		Grout	
	28-day, ksi	Test day, ksi	28-day, ksi	Test day, ksi
FGSS-1	5.3	6.2	12.5	13.3
FGSS-2	3.9	5.2	10.3	10.3
CIP	5.2	6.7	n/a	n/a

Note: n/a = not applicable. 1 ksi = 6.89 MPa.

Table 2.5. Effective yield properties and displacement ductility values

Specimen	Last drift ratio, %	$F_{y,}$ kip	Δ_y, in.	Δ_u, in.	K_{eff}, kip/in.	μ_Δ
FGSS-1	6	35.35	1.08	5.32	32.70	4.9
FGSS-2	7	33.29	1.11	6.50	29.92	5.8
CIP	10	32.33	0.90	8.95	35.84	9.9

Note: 1 kip = 4.448 kN; 1 in. = 25.4 mm; 1 kip/in. = 175.1 kN/m.

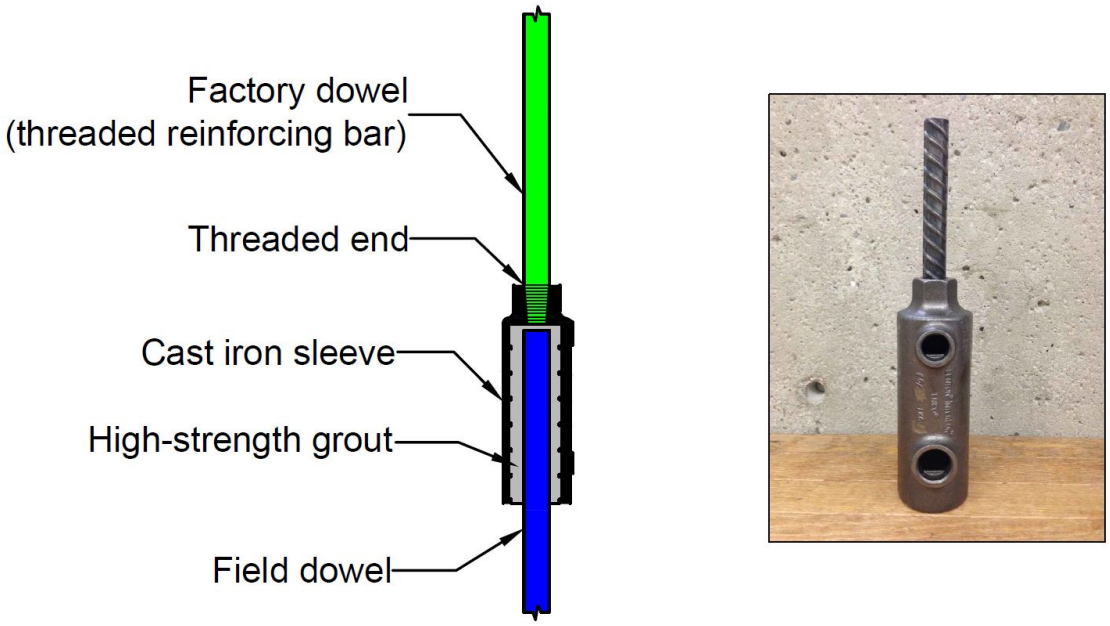

Fig. 2.1. Grouted splice sleeve incorporated in this research.

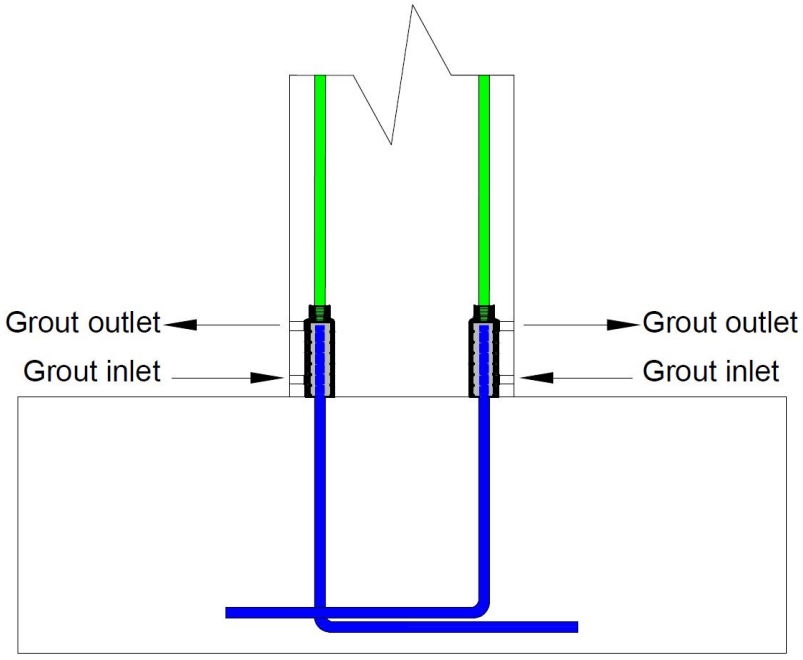

Fig. 2.2. Fastened and grouted splice sleeve connectors in precast concrete components.

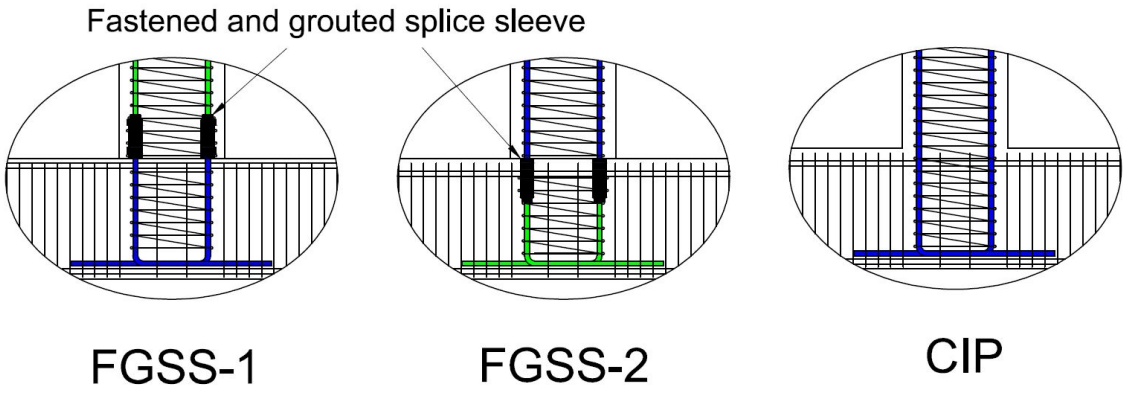

Fig. 2.3. Configuration of test alternatives.

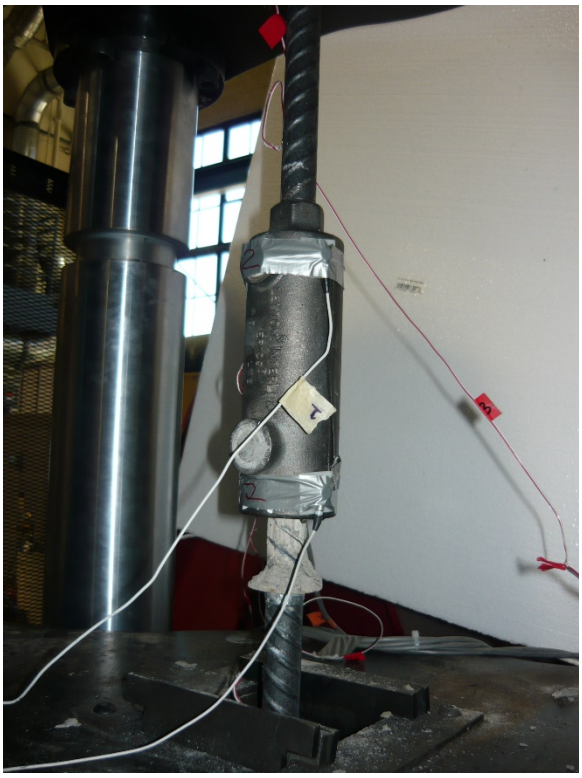

Failure of air test specimen in testing apparatus

Grout cone failure and reinforcing bar pullout

Fig. 2.4. Pullout failure of air test specimen.

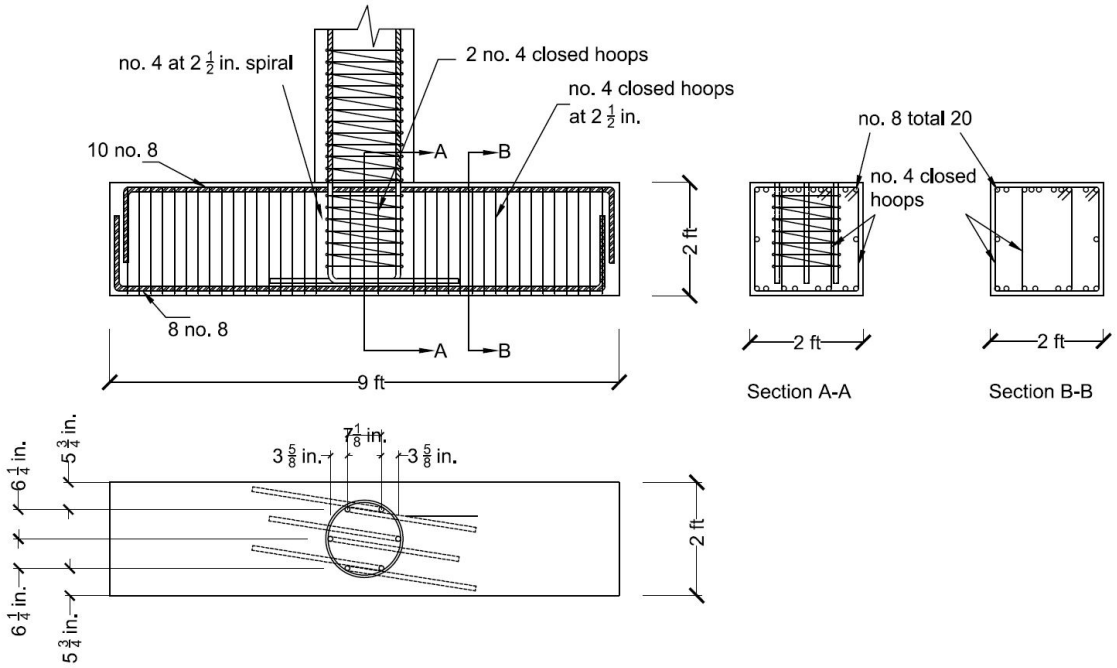

Fig. 2.5. General design and detailing of joint region for monolithic specimen. Note: no. 4 = 13M; no. 8 = 25M; 1 in. = 25.4 mm; 1 ft = 0.305 m.

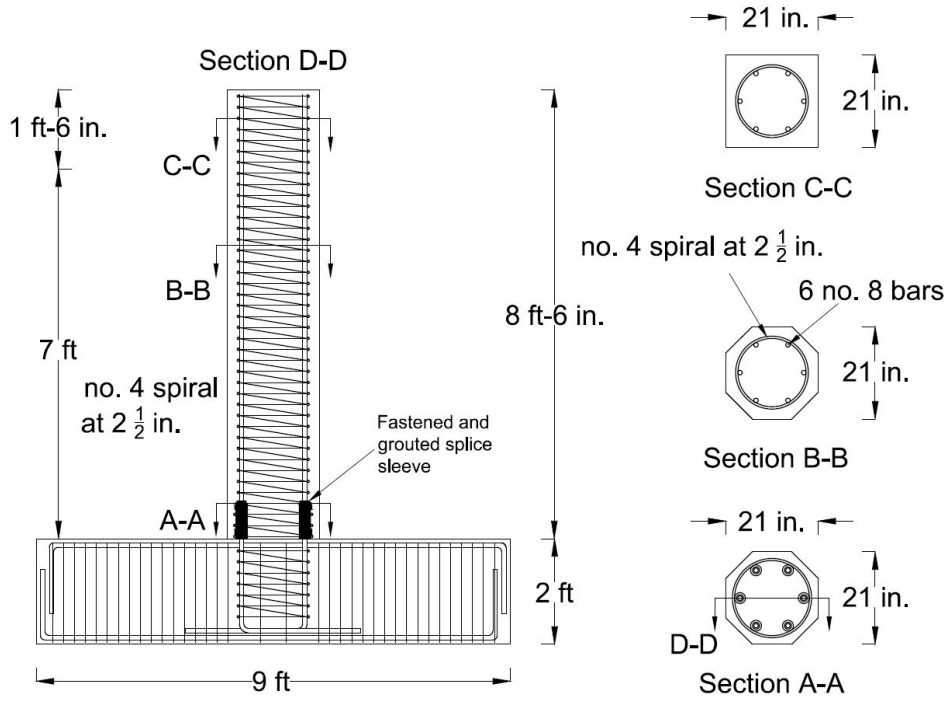

Specimen FGSS-1 details

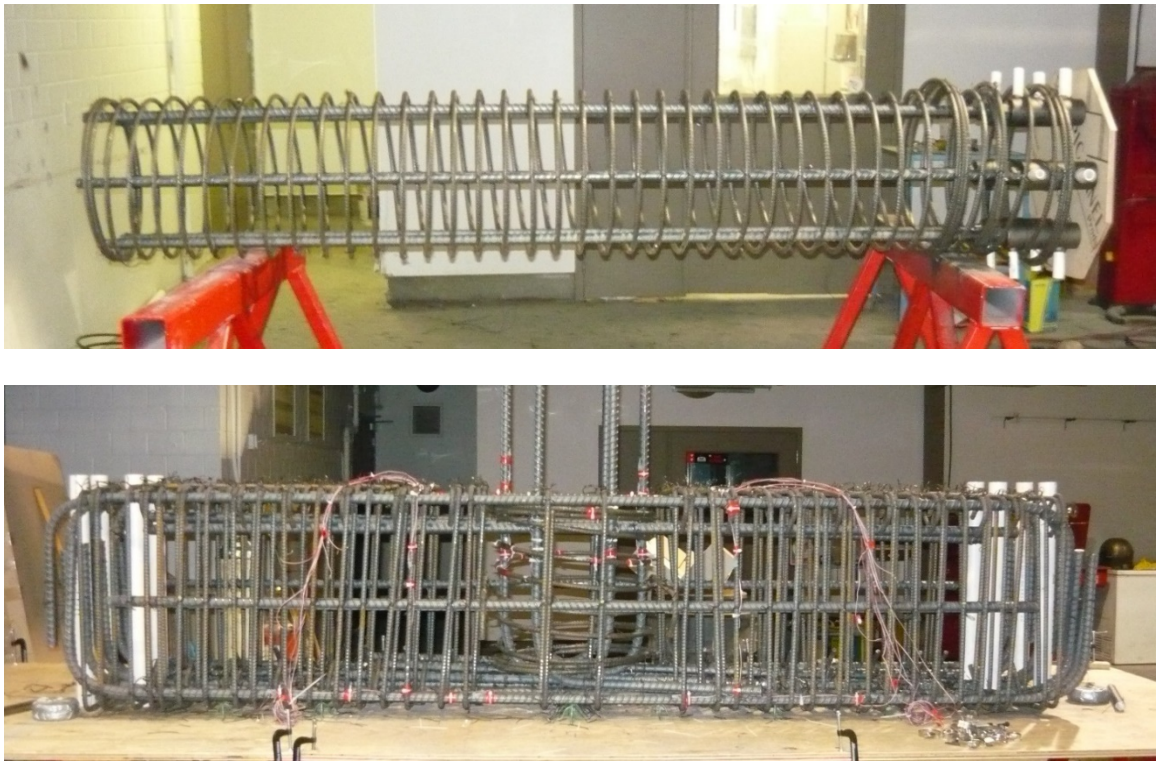

Specimen FGSS-1 reinforcing bar cages

Fig. 2.6. Specimen FGSS-1 construction details. Note: no. 4 = 13M; no. 8 = 25M; 1 in. = 25.4 mm; 1 ft = 0.305 m.

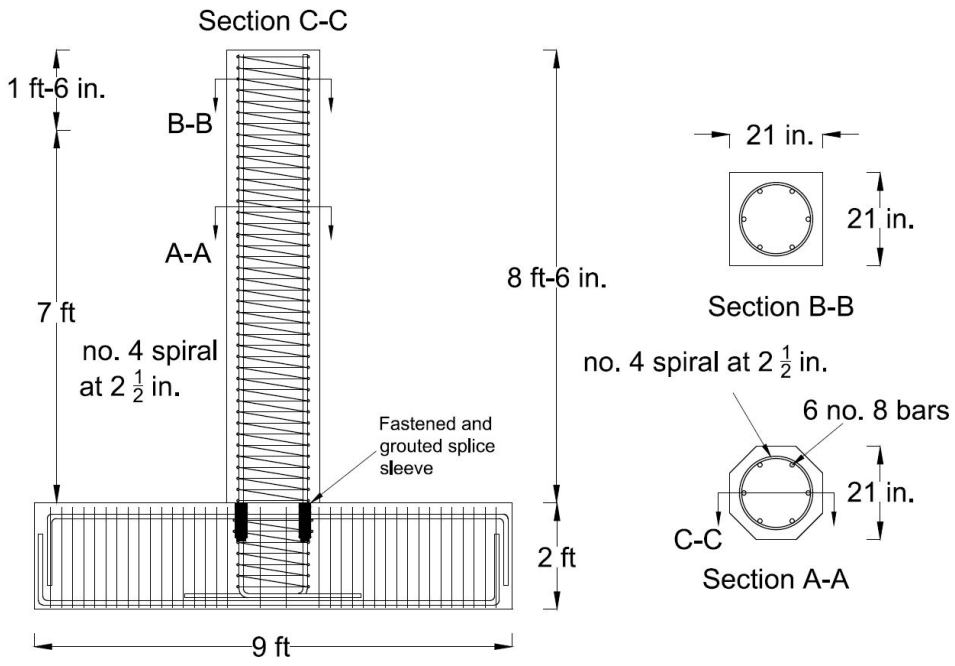

Specimen FGSS-2 details

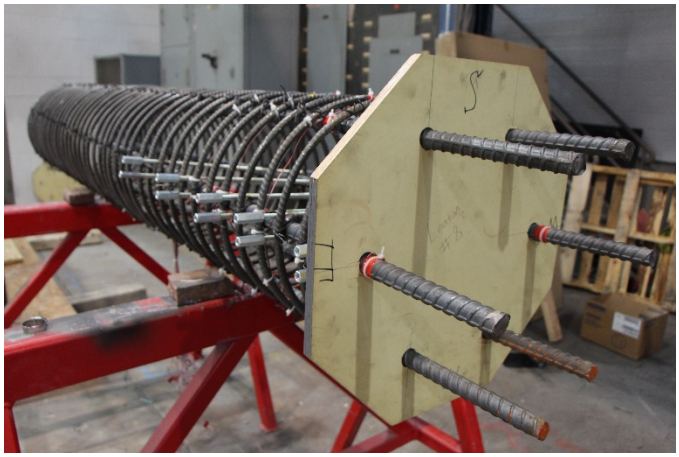

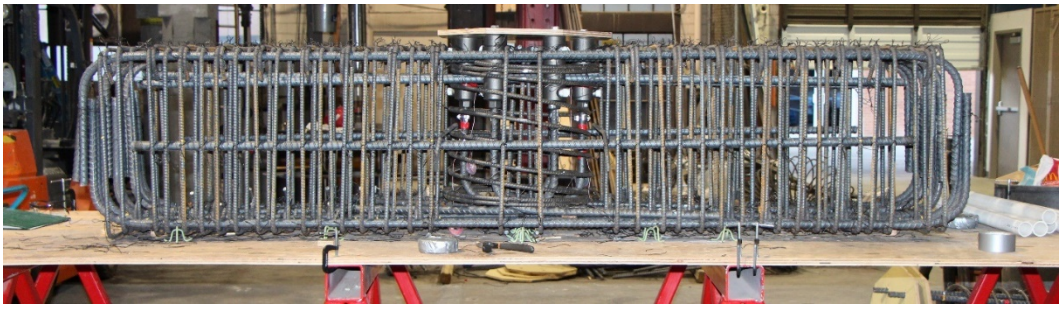

Specimen FGSS-2 reinforcing bar cages

Fig. 2.7. Specimen FGSS-2 construction details. Note: no. 4 = 13M; no. 8 = 25M; 1 in. = 25.4 mm; 1 ft = 0.305 m.

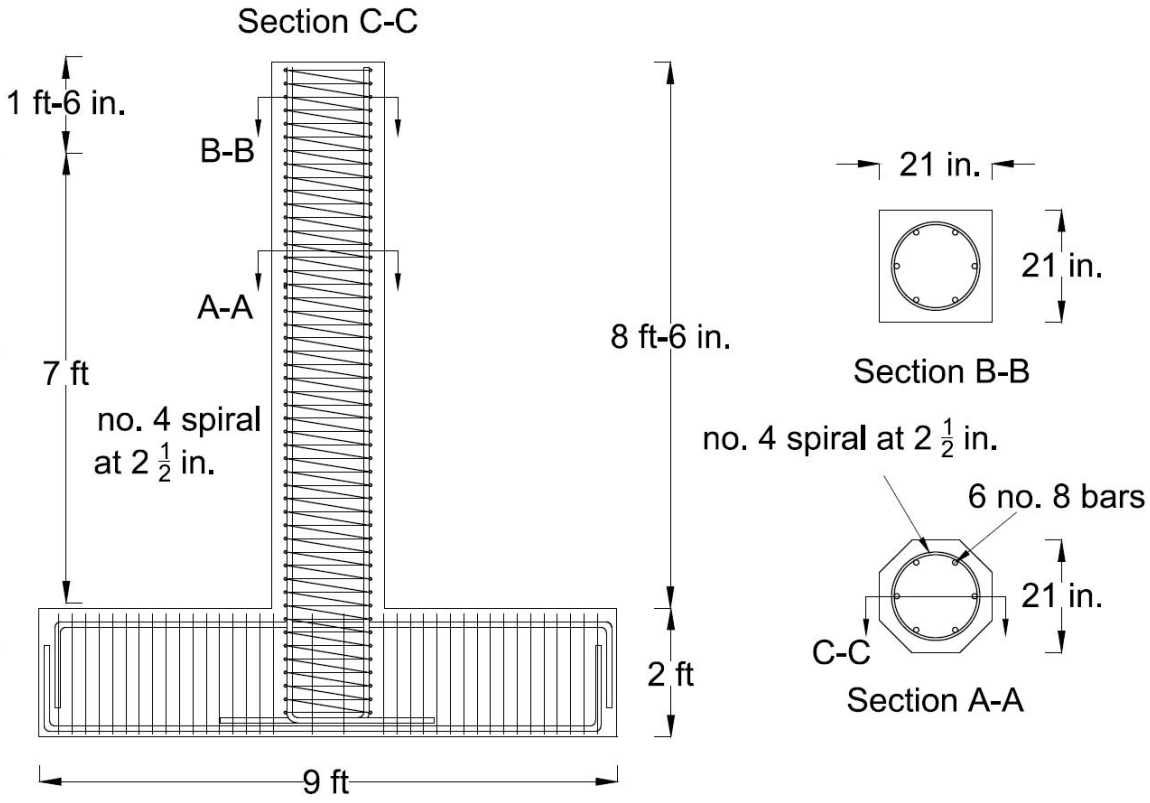

Specimen CIP details

Specimen CIP reinforcing bar cages

Fig. 2.8. Specimen CIP construction details. Note: no. 4 = 13M; no. 8 = 25M; 1 in. = 25.4 mm; 1 ft = 0.305 m.

Pregrout technique prior to installation

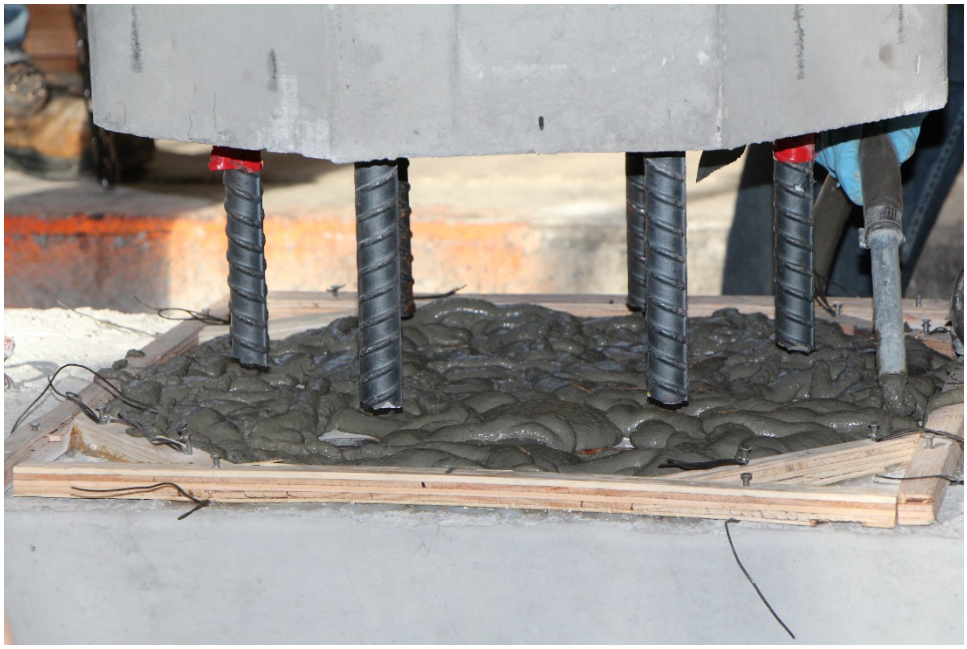

Bed grout at column-to-cap beam interface

Fig. 2.9. Grout operation for FGSS-2.

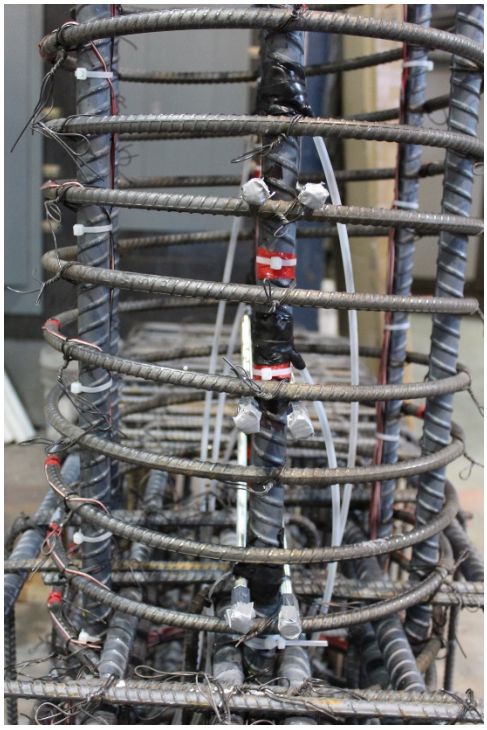

Strain gauges on reinforcing bars

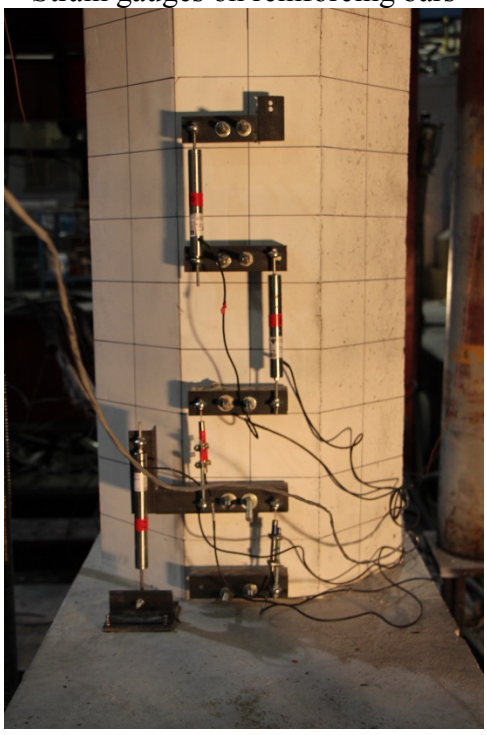

LVDTs adjacent to column end

Fig. 2.10. Instrumentation details.

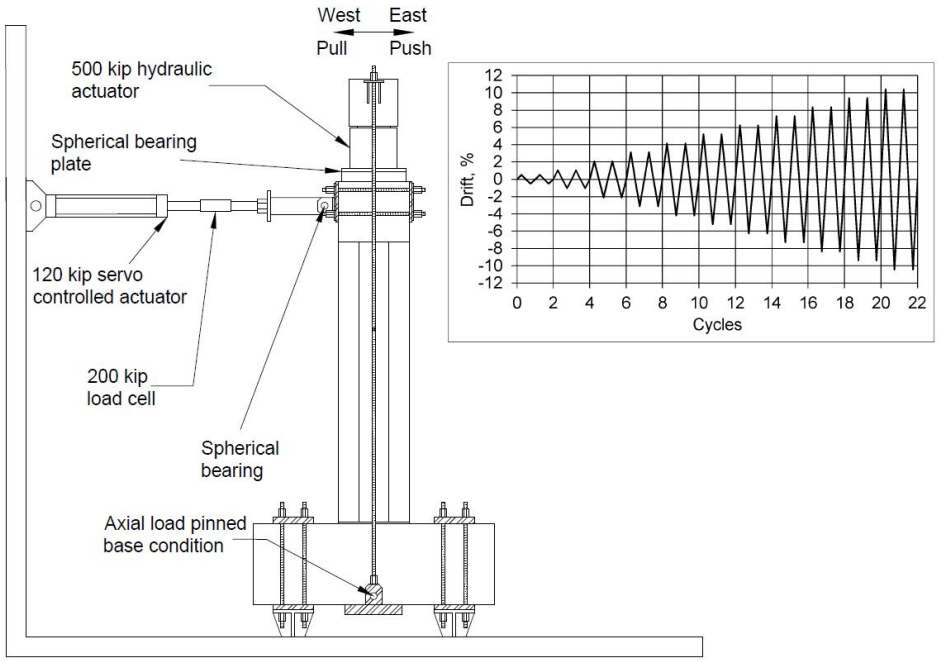

Schematic test setup

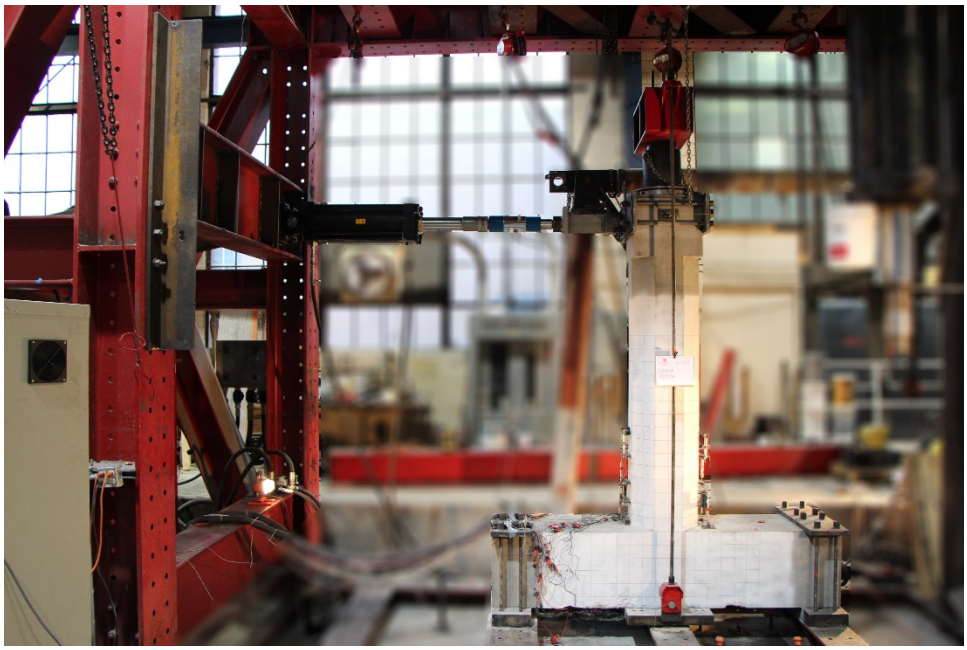

Actual test setup

Fig. 2.11. Experimental configuration and displacement history. Note: 1 kip = 4.448 kN.

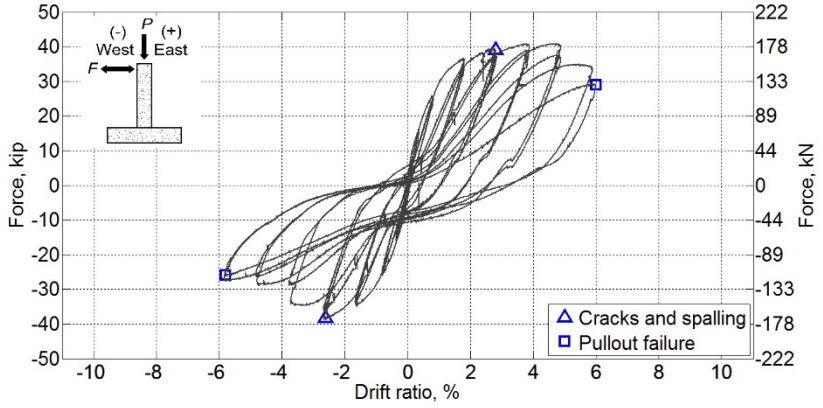

Specimen FGSS-1

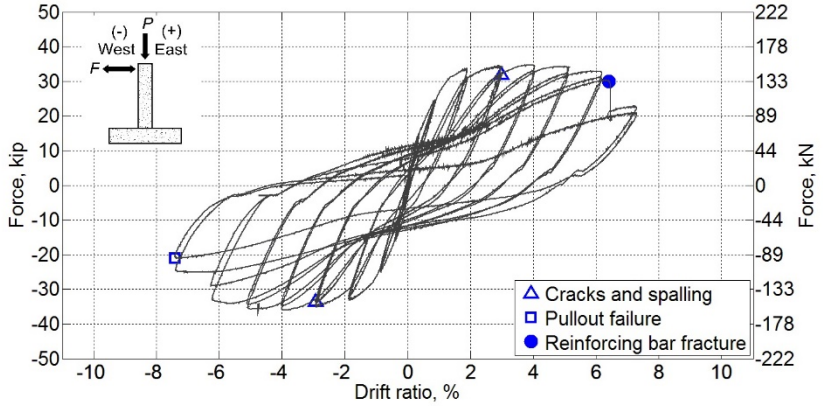

Specimen FGSS-2

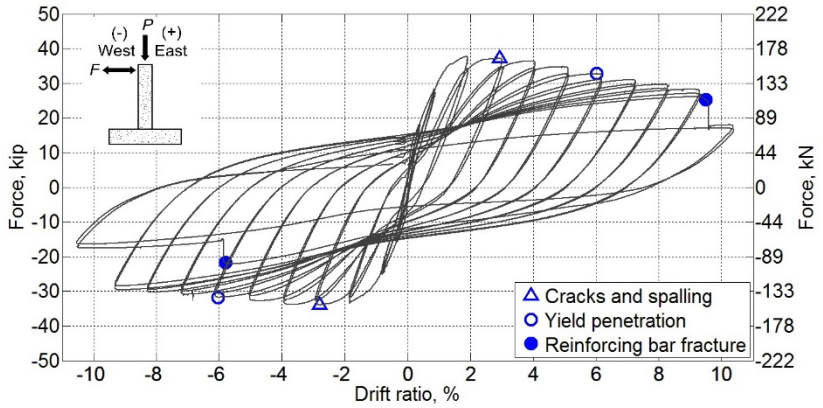

Specimen CIP

Fig. 2.12. Hysteresis response of precast concrete and control specimens. Note: F = force; P = axial load.

Bed grout opening at 3% drift ratio (peak)

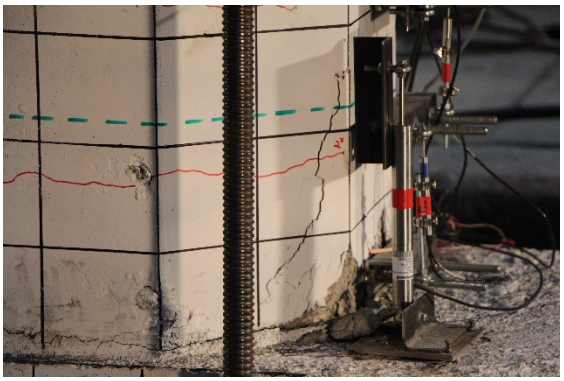

Damage state at 3% drift ratio

Bar pullout during 6% drift ratio

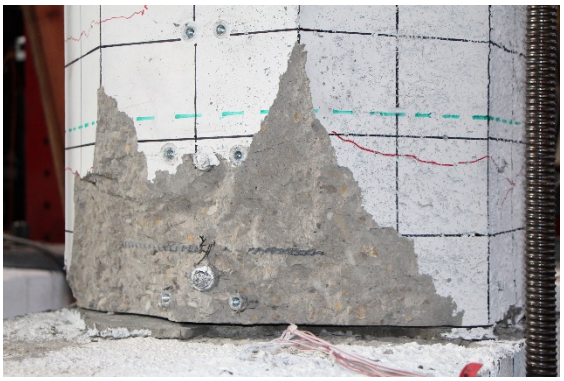

Damage state at end of test (6%)

Fig. 2.13. Specimen FGSS-1 visual observations.

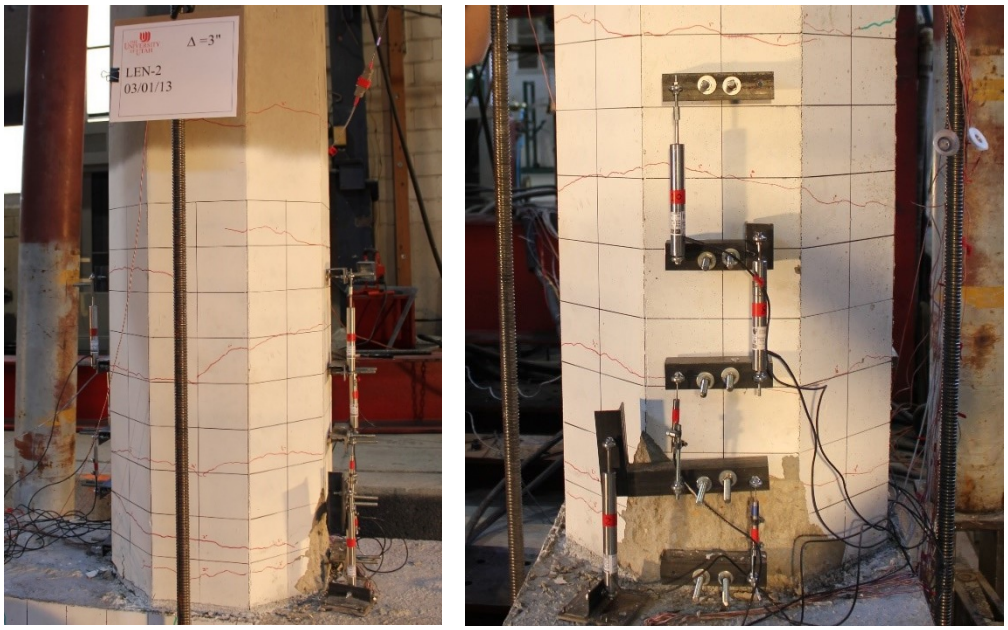

Damage state at 3% drift ratio: cracks and spalling

Damage state at 7% drift ratio: cracks, spalling, and exposed spiral

Fig. 2.14. Specimen FGSS-2 visual observations.

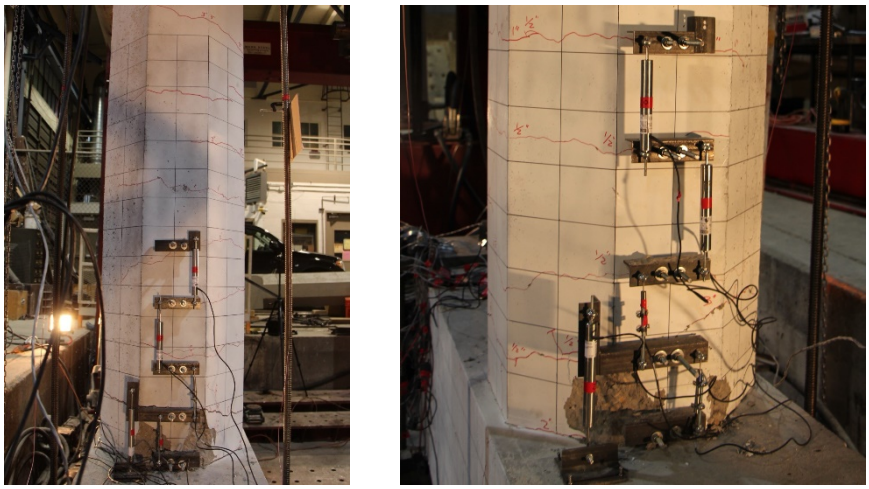

Damage state at 3% drift ratio

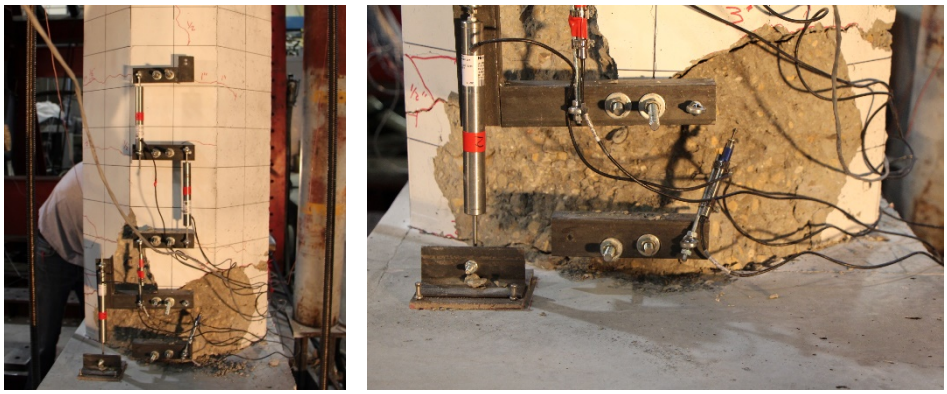

Damage state at 6% drift ratio: cracks and spalling, yield penetration

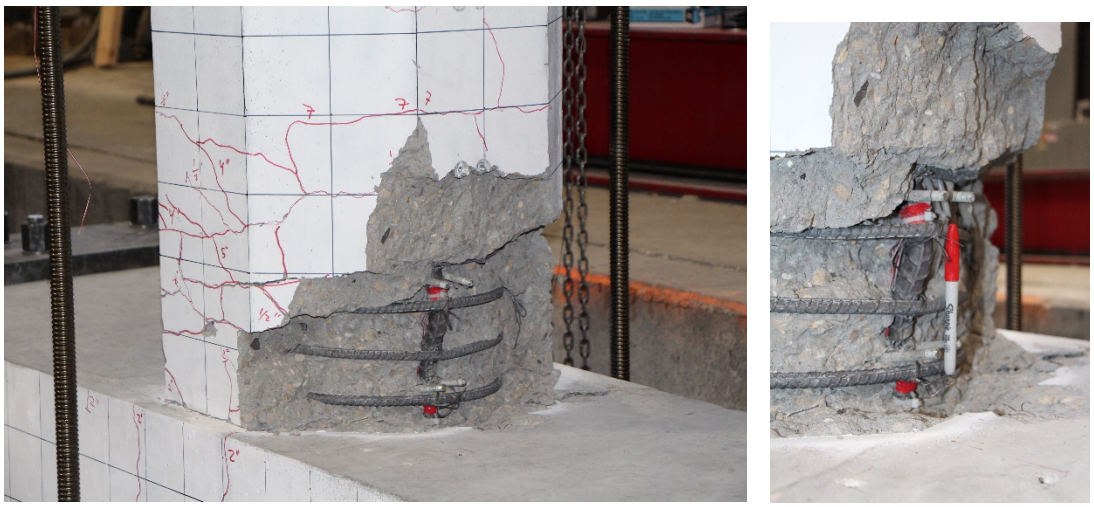

Damage state at end of test: cracks and spalling, reinforcing bar buckling and fracture

Fig. 2.15. Specimen CIP visual observations.

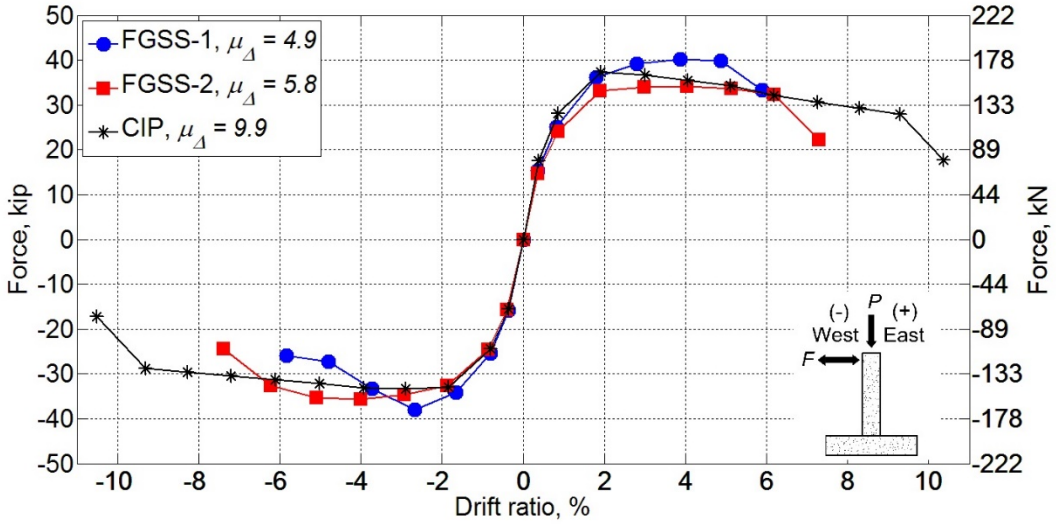

Fig. 2.16. Force-displacement response. Note: F = force; P = axial load; μ_Δ = displacement ductility.

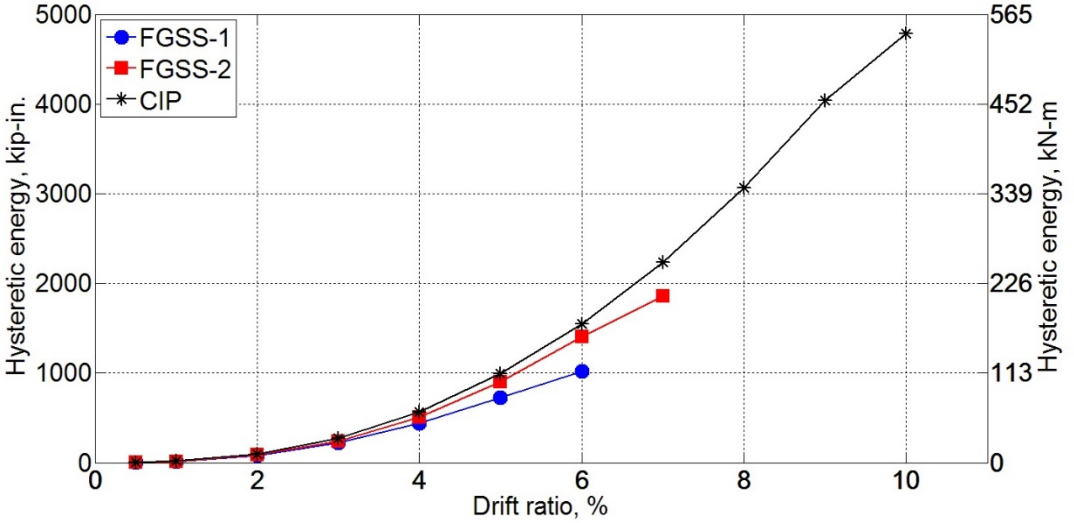

Fig. 2.17. Cumulative hysteretic energy.

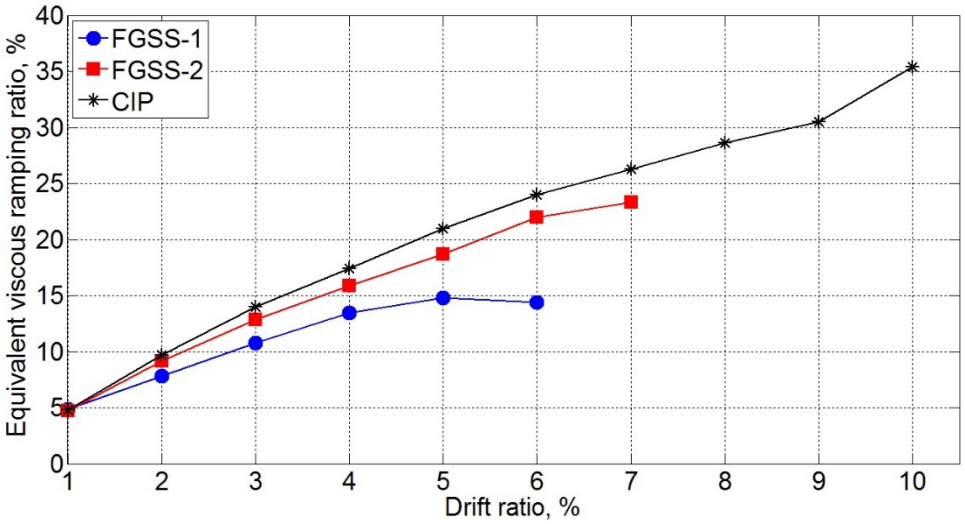

Fig. 2.18. Equivalent viscous damping.

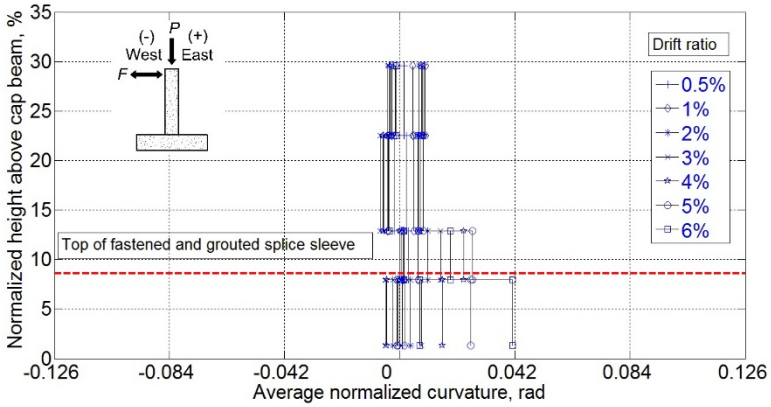

Curvature distribution for specimen FGSS-1

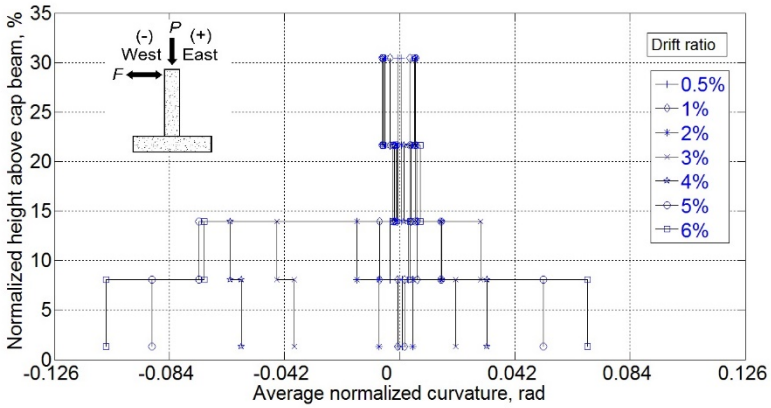

Curvature distribution for specimen FGSS-2

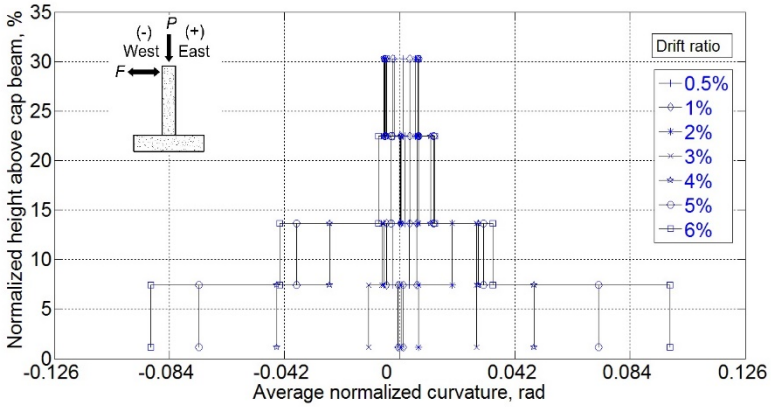

Curvature distribution for specimen CIP

Fig. 2.19. Normalized curvature distribution. Note: *F* = force; *P* = axial load; Average curvature values are multiplied by the column dimension (21 in.) for normalization.

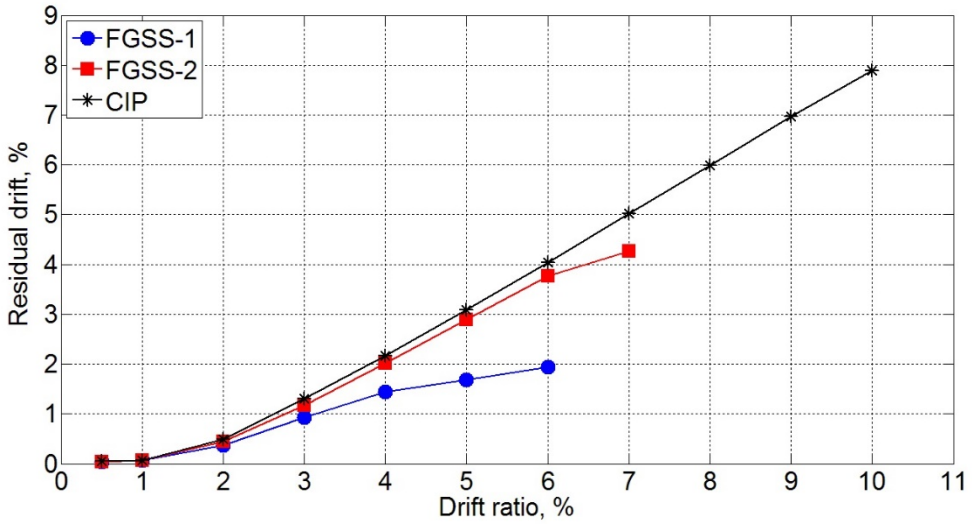

Fig. 2.20. Residual drift for all test specimens.

CHAPTER 3

SEISMIC COLUMN-TO-FOOTING CONNECTIONS USING GROUTED SPLICE SLEEVES

M. J. Ameli, Dylan N. Brown, Joel E. Parks, and Chris P. Pantelides

Accepted for publication in the ACI Structural Journal

ACI member M. J. Ameli is a PhD candidate at the Civil and Environmental Engineering Department of the University of Utah, where he also received his MS. He earned his BS from Sharif University of Technology, Tehran, Iran. His research interests include large scale testing of structural components, nonlinear design and analysis of reinforced concrete structures, and application of composites in repair and retrofit of concrete components.

Dylan N. Brown is a bridge engineer at Michael Baker International in Madison, Wis. He earned his MS in structural engineering from the Civil and Environmental Engineering Department at the University of Utah. His research interests include testing, evaluation, and modeling of precast concrete bridge components designed for accelerated bridge construction in seismic regions, and postseismic bridge repair.

Joel E. Parks is a PhD candidate at the Civil and Environmental Engineering

Department of the University of Utah, where he also received his MS. His research interests include nonlinear design and analysis of reinforced concrete structures, and application of composites in repair and retrofit.

ACI member Chris P. Pantelides is a Professor at the Civil and Environmental Engineering Department of the University of Utah. His research interests include seismic design and rehabilitation of reinforced concrete, precast and prestressed concrete buildings and bridges, and the application of fiber reinforced polymer composites.

Abstract

Mechanical couplers have been utilized in connections between prefabricated reinforced concrete elements. Grouted splice sleeves offer good construction tolerance and a bond-related load transfer mechanism between the connecting members. The present study investigates the seismic performance of grouted splice sleeve connections with the connectors placed in the column or footing of bridge subassemblies, and intentional debonding of the footing dowel bars. Quasi-static cyclic loads were used to test three half-scale precast column-to-footing specimens and one cast-in-place control specimen. The precast concrete specimens incorporated grouted splice sleeve connectors in which two bars were grouted at both ends. Experimental results show that the precast subassemblies had a lower displacement ductility capacity than the control specimen. Improved seismic response was observed when the splice sleeve connectors were located inside the footing rather than the column end. An intentional debonded rebar zone was used to further improve the displacement ductility capacity of the bridge subassembly.
Keywords: accelerated bridge construction; connection; joint; concrete column; cyclic

load test; grouted splice sleeve; mechanical coupler.

Introduction

Accelerated bridge construction (ABC) has been practiced in the United States because of the efficiency it offers as a bridge construction procedure. Prefabricated reinforced concrete components have been frequently used as part of ABC. In moderate-to-high seismic zones, special care must be taken in the design and detailing of moment-resisting connections of such precast components since they play a critical role in maintaining integrity of the whole structure. These connections may be subjected to large earthquake-induced deformations at the interface of precast members that could cause considerable permanent damage. Hence, there is a need to conduct research on potential precast connection types which offer improved constructability, increased construction speed, and enhanced reliability.

Many bridges have been constructed, retrofitted, or replaced using different ABC methods. Within regions of high seismicity several States including Washington, Utah, and California are adopting ABC. One recent application of ABC column-to-footing connection can be found in Washington over Interstate 5 where reinforced precast columns were connected to spread footings using a socket connection.[1] In this method, the bottom end of precast columns is roughened and embedded in footings, after which footing concrete is cast around the column bases. This connection type could be incorporated for column-to-cap beam joints as well as pile-to-pile cap joints; it has been utilized mostly in column-to-footing joints.[2] An experimental study conducted prior to application of the socket connection showed that the response of such a connection under

simulated seismic loads was acceptable.[3] Other studies revealed similar results on the overall response of such column-to-footing connections, for buildings and bridges.[4,5] Another viable connection type is the grouted duct connection. In this method, corrugated steel ducts are cast in a footing or cap beam, and column reinforcement dowels are inserted and grouted inside the ducts. In bridge construction applications, the grouted duct connection was originally developed for column-to-cap beam connections.[6,7] Experiments on large-scale column-to-footing subassemblies with grouted ducts embedded in the footing were conducted by Tazarv et al. (2015); the performance of this connection type was found to be promising and emulative of conventional monolithic construction.[8]

The grouted splice sleeve connection has been used in bridges located in low seismic regions since it accelerates construction while being a reliable method in terms of resisting gravity loads. A grouted splice sleeve connector is a type of reinforcing bar splicing device in which load transfers between the two connecting bars by means of stress transfer through bond between the reinforcing bar, high strength grout, and cast iron splice sleeve coupler. Recently, experimental and analytical studies were conducted on this precast connection type to investigate its application in high seismic zones. NCHRP report 698 recommended further investigation of the grouted splice sleeve connection, in terms of strength details and hysteretic performance.[9] To study the strength properties of individual splicing systems, researchers have performed experiments on assemblies composed of two connecting reinforcing bars, high strength grout, and a cast iron sleeve.[10-12] Jansson (2008) carried out such experiments on No. 6 (19M) and No. 11 (36M) subassemblies and studied bar slip, fatigue life, creep behavior, and ultimate load

capacity. Different ultimate failure modes were observed including fracture or pullout of both No. 6 (19M) and No. 11 (36M) reinforcing bars and fracture of No. 11 (36M) cast iron connectors. However, the nominal tensile strength of the reinforcing bar was achieved for all specimens.[10]

Reversed cyclic quasi-static tests were conducted on large-scale precast concrete specimens connected by means of grouted splice sleeve connectors at various locations along the precast column, footing or cap beam.[13-20] The results indicated that a different hysteretic performance, damage progression, and plastic hinging mechanism occurred when the splice sleeve connectors were used to splice reinforcing bars in precast concrete members. Strength and stiffness of the precast concrete specimens were found to be similar or slightly different than the corresponding monolithic specimens without grouted splice sleeve connectors.

This paper presents the results of four half-scale specimens, three of which were composed of precast concrete components connected using grouted splice sleeve connectors. The performance of the three precast specimens is compared to a fourth specimen without grouted splice sleeve connectors which represents cast-in-place concrete monolithic construction.

Research Significance

The research presented herein provides valuable information on the seismic performance of grouted splice sleeve connections with a focus on the location of the connectors within the column-to-footing joint. Currently, bridge design codes prohibit the application of any type of mechanical connectors in the column plastic hinge zone of

bridges located in high-seismic regions. This study presents findings from cyclic experiments in terms of load capacity, hysteretic response, ductility capacity, and spread of inelasticity along the column. The seismic performance was investigated for two connector location alternatives: (1) at the column plastic hinge zone with and without intentional debonding of reinforcing bars inside the footing, and (2) outside the column plastic hinge zone, i.e., in the footing.

Tensile Tests of Grouted Splice Sleeve Connectors

Fig. 3.1 shows the grouted splice sleeve used in this research. The spliced reinforcing bars are both grouted in the two ends of the connector, hence the connector is denoted as grouted/grouted splice sleeve or GGSS. A series of tensile tests were conducted on six individual grouted splice sleeve connectors to investigate the performance of the connectors under monotonic tensile load. Results from these tests were used to assess strength capacity and failure mode of this type of grouted splice sleeve connectors, in addition to providing insight to their overall performance under pure tensile loading.

Two No. 8 (25M) reinforcing bars were connected using a grouted splice sleeve connector for each connector specimen. The reinforcing bars had a nominal yield strength of 60 ksi (400 MPa) and an actual yield strength of 76 ksi (525 MPa). The test-day compressive strength of the high strength grout was 13.8 ksi (95 MPa).

A monotonic tensile load was applied to each connector assembly until failure which occurred when the reinforcing bars fractured outside the connector zone, 3 in. (76 mm) to 5 in. (127 mm) from the field end of the connector. The field end is the wide end

of the grouted splice sleeve connector which is positioned at the outermost edge of the precast component; this implies that the tensile strength of the connecting reinforcing bars was achieved. Other potential failure modes such as bar pullout or connector fracture did not occur for any of the test assemblies. The average ultimate strength achieved by the connector assemblies was 1.68 ± 0.0260 (SD, n=6) times the nominal yield strength of the reinforcing bar. Table 3.1 shows the results of the connector tests; the failure mode for all tests was bar fracture.

A grout cone was formed due to localized stresses at the unconfined ends of the connectors that resulted in an inferior bond between the reinforcing bar and surrounding grout, at the two ends. The depth of the grout cone ranged from ½ in. (13 mm) to ¾ in. (19 mm) for the larger end (field end). On the opposite end of the connector with the smaller opening (factory end), the grout cone depth was ¼ in. (6.5 mm) to ½ in. (13 mm). Fig. 3.2 shows a connector assembly with the fractured field dowel after the test was terminated, along with the grout cone. Acoustic emission (AE) monitoring was used to detect major performance benchmarks during the tensile tests. Interpretation of the AE event rate indicated that the formation of the grout cone occurred at approximately 1.2 times the actual yield strength of reinforcing bars. Further discussion on AE monitoring of the connector experiments is available in Parks (2014).[21]

Haber et al. (2015) discussed the stress-strain behavior of connector test subassemblies with reference to the stress-strain behavior of spliced bars, under monotonic tensile loads.[12] Within the connector region, defined as the connector length plus 1 11/16 in. (43 mm) from each connector end, the strain capacity was 65% smaller than that of the spliced bars; this was attributed to the presence of the cast-iron sleeve

connector. However, the overall trend of the stress-strain behavior of the subassembly and spliced bars was similar.

Previous tests on connector subassemblies with heavily-instrumented spliced bars showed that their yield strength was achieved at a section located 4 times the bar diameter from the end of the bar grouted inside the connector; beyond this point, the reinforcing bars underwent inelastic response.[19] Strains up to 2.5% were measured at both ends of the spliced bars.

Specimen Design and Fabrication

The design was first carried out for the cast-in-place specimen CIP; a design displacement ductility equal to 11.0 was used. Detailing of the remaining specimens was adjusted in accordance with the required change from specimen CIP. The AASHTO LRFD Bridge Design Specifications and the AASHTO Guide Specifications for LRFD Seismic Bridge Design were followed to implement capacity based design. [22, 23] The application of grouted splice sleeve connectors or bar lap splices is prohibited in the plastic hinge region of bridge columns located in moderate to high seismic zones.[23, 24] This applies to seismic design categories C and D per AASHTO Guide Specifications. The half-scale columns were composed of a 21 in. (533 mm) octagonal cross section with six No. 8 (25M) reinforcing bars arranged in a circular configuration and confined by a No. 4 (13M) spiral with a pitch of 2.5 in. (64 mm). A column with an octagonal cross-section was selected because it is easier to precast compared to a column with a circular cross-section. The longitudinal and volumetric transverse reinforcement ratios were 1.3% and 1.9%, respectively. The column height for all specimens was 8 ft 6 in. (2.6 m). The

precast footings were designed as 6-ft long x 3-ft wide x 2-ft deep (1.8 x 0.9 x 0.6 m) precast concrete elements; reinforcement consisted of No. 8 (25M) longitudinal bars with No. 4 (13M) double hoops. The footings were designed and detailed to remain in the linear elastic range, as capacity-protected members. Dowel bar tails were bent inward into the footing to achieve a better performance under lateral cyclic loads as required for seismic design category D in accordance with AASHTO Guide Specifications.[23]

Fig. 3.3 shows the design details of the four test alternatives, and Table 3.2 contains the test matrix. For specimens GGSS-1 and GGSS-3, the connectors were placed at the column base; No. 8 dowel bars with an extension of 7 in. (180 mm) protruded from the top of the footing. To investigate the displacement ductility enhancement provided by debonding reinforcing bars, the footing dowel bars of GGSS-3 were debonded for a length equal to eight times the diameter of the reinforcing bars, adjacent to the sleeve connectors, as shown in Fig. 3.3(c). Debonding is expected to reduce strain localization of footing dowel bars at the column-to- footing interface. Weinert (2011) described the effectiveness of partial debonding of connecting bars outside sleeve connectors.[2] For specimen GGSS-2, the grouted splice sleeve connectors were cast inside the footing and dowel bars protruded from the column. A postgrout operation was performed during erection of GGSS-1 and GGSS-3, during which, the column was lowered over the footing to match the dowel bars with the connector openings, and the grout was subsequently pressure pumped into the connectors. A pregrout operation was conducted for GGSS-2 in which the connectors were filled with grout before joining the two precast components. For ease of construction, the inlet and outlet grout ports of all connectors were sealed before casting the footing concrete. During installation, compressed air was blown into

the connectors to remove debris; grout was then poured into the connectors from the wide end opening. This configuration (except the grout operation) was implemented during the construction of a rail bridge in Salt Lake City in 2012; this is a practical alternative to commonly-used grouted splice sleeve connections. A ¼ in. (6 mm) bed grout was incorporated at the column-to-footing interface for all precast specimens.

No. 8 (25M) grade 60 (414 MPa) ASTM A706 reinforcing bars were used as column longitudinal bars. The results of tension tests showed that the yield and ultimate strength of these reinforcing bars was 68 ksi (469 MPa) and 93 ksi (641 MPa), respectively. The No. 4 (13 M) transverse reinforcing bars had a yield strength of 63 ksi (434 MPa) and an ultimate strength of 103 ksi (710 MPa). Compression tests were conducted using concrete cylinders and grout cubes for the 28-day and test-day compressive strength of the cementitious materials. Table 3.3 presents the compression test results for the cementitious materials used for all specimens.

Experimental Procedure

Instrumentation

The specimens were instrumented with strain gauges in the plastic hinge region and joint area. For the precast concrete specimens, strain gauges were placed on the dowel bars inside the connectors. Column displacements were obtained by taking the average of readings from two potentiometers installed at the actuator level. Linear variable differential transformers (LVDTs) were used to study the displacement increments and curvature distribution along the column base in addition to the global vertical and horizontal movement of the specimens. Ten LVDTs were mounted at the

column end zone, over a 30 in. (760 mm) high region to measure the relative vertical displacements and provide data for curvature analysis.

Test Setup and Loading Protocol

The specimens were attached to the test frame using high strength bolts; the lateral cyclic load and axial load were applied simultaneously at the column top. A 120-kip (530 kN) servo-controlled actuator, with an overall stroke of 18 in. (440 mm) was used to apply the cyclic load to the precast specimens; the control specimen was tested using a 250-kip (110 kN) servo-controlled actuator with an overall stroke of 24 in. (610 mm). An axial load of 6% of the column compressive capacity was applied to simulate gravity loads. The column compressive capacity was approximated as the column cross-sectional area multiplied by the 28-day compressive strength of the column for each specimen. An actuator placed on top of the column applied the compression force to a steel spreader beam which was connected to two high strength threaded rods pinned to a steel plate below the footing, as shown in the test setup of Fig. 3.4; the steel rods were used to apply the axial load.

Fig. 3.5 shows the horizontal drift history applied quasi-statically to the column at an elevation of 8 ft (2.4 m) above the footing. Drift is defined as the lateral displacement of the column top, where the actuator applied the lateral load, divided by the distance from top of the footing to center of the lateral load application, which was 8 ft (2.4 m). The drift history was composed of increasing amplitudes as multiples of the predicted yield drift of the column.[25] Two cycles were employed for each drift ratio in the east and west directions. The displacement rate was set to 1.2 in./min (30 mm/min) up to the end

of the 3% drift ratio, after which it was changed to 4 in./min (100 mm/min).

Test Results

Hysteretic Response and Damage Progression

Fig. 3.6 shows the lateral force-drift curves for all specimens including major damage states observed during the cyclic tests. Spalling of concrete initiated during the 3% drift ratio, and major flexural cracks formed by the end of the 3% drift ratio. Yield penetration was noted for precast specimen GGSS-1 and cast-in-place specimen CIP while this phenomenon was not observed for precast specimens GGSS-2 and GGSS-3 because of embedding the connectors in the footing, and debonding of footing bars, respectively. Fracture of reinforcing bars was the main cause of strength degradation for all specimens; no damage was observed due to bond deterioration between dowel bars and high-strength grout in the sleeve connectors. Fig. 3.6 identifies fracture of the reinforcing bars on each hysteresis curve. The hysteresis loops of the precast specimens were wide and stable, resembling the cast-in-place alternative CIP. This indicates a potentially satisfactory hysteretic performance for all precast specimens.

Precast Specimen GGSS-1

A minor hairline crack developed at the bed grout, at the column-to-footing interface of GGSS-1, during the 0.5% drift ratio. This crack became wider and was accompanied by another crack forming above the connectors during the first cycle of the 1% drift ratio. Spalling initiated during the first cycle of the 3% drift ratio and progressed near the corners of the octagonal column. Cracks widened and spalling progressed at

higher drift ratios (Fig. 3.7(a)). The crack, which had formed above the connectors, had a width of 0.013 in. (0.3 mm) at a drift ratio of 4%, 0.02 in. (0.5 mm) at a drift ratio of 5%, and 0.03 in. (0.8 mm) at a 6% drift ratio. There were only a few flexural cracks at the column base as damage was localized over the column-to-footing interface and the section above the connectors. Yield penetration was noted at the end of the 6% drift ratio up to a depth of 1.5 in. (38 mm) on the west and 1 in. (25 mm) on the east side of the column. The height of the spalled region was 8 in. (203 mm) on the west and 14 in. (356 mm) on the east side of the column. The column spiral became visible during the 7% drift ratio. The bed grout deteriorated around the perimeter of the column end, while the spalled region over the connectors became deeper and the GGSS connectors were visible at the end of the 8% drift ratio; the two extreme footing dowels fractured shortly after the 8% drift ratio at a location from 1.0 in. (25 mm) to 1.5 in. (38 mm) below the surface of the footing due to strain concentration. Fig. 3.7(b) shows the damage state of specimen GGSS-1 shortly after the 8% drift ratio.

Precast Specimen GGSS-2

Unlike GGSS-1, two hairline flexural cracks developed at sections 12 in. (305 mm) and 28 in. (711 mm) above the column base during the 0.5% drift ratio, prior to any crack formation at the interface. The interface gap between the precast column and footing became evident during the 1% drift ratio, while a total of nine flexural cracks formed along the column by the end of the 3% drift ratio. The widest crack, located 6 in. (152 mm) above the column base, had a width of 0.03 in. (0.8 mm) at the end of the 3% drift ratio, as shown in Fig. 3.7(a). Inclined cracks developed on the north and south side

of the column base during the 5% drift ratio due to increased tensile demand in the column plastic hinge zone. The extreme east column dowel ruptured during the first pull of the 7% drift ratio at a section 2 in. (51 mm) above the column base. At the end of the test, the concrete cover completely spalled at the column base which made the spiral visible over the bottom 8 in. (203 mm). The permanent gap at the column-to-footing interface had a width of 1/16 in. (1.6 mm). The state of damage for GGSS-2 is presented in Fig. 3.7(b) after the 7% drift ratio.

Precast Specimen GGSS-3

The damage state of GGSS-3 was similar to that of GGSS-1 with the exception of a slightly postponed spalling at the column section corners (Fig. 3.7(a)). The crack formation pattern was similar to GGSS-1. The crack, which had formed above the connectors, had a width of 0.013 in. (0.3 mm) and 0.02 in. (0.5 mm) after the 4% and 5% drift ratio, respectively. The spiral reinforcement was exposed during the 7% drift ratio when the concrete cover crushed completely over the bottom column segment. The gap created at the bed grout section was increased, when the column was at the extreme position, in such a way that the footing dowel bars became visible.

During first pull at the 8% drift ratio, the extreme column reinforcing bar fractured at the interface, and the test was terminated as the column strength dropped below 80% of the peak lateral force. Fracture of the bar was attributed to low cycle fatigue as a result of successive bending and restraightening. Posttest investigation revealed that the concrete cover deteriorated within the lowest 4-in. (102 mm) section of the column, and hence, one spiral hoop and the bottom end of the connectors were visible

(Fig. 3.7(b)). Damaged concrete was noted around the top portion of the debonded dowel bars in the footing. The crack, which had developed at the column-to-footing interface during the previous drift ratios, became a 3/32-in. (2.4 mm) permanent gap at the end of the test for specimen GGSS-3.

Cast-in-place Specimen CIP

Two hairline flexural cracks formed at two sections located 12 in. (305 mm) and 32 in. (813 mm) above the column-to-footing interface, by the end of the 0.5% drift ratio. Spalling initiated at the column corners and a total of nine flexural cracks developed by the end of the 3% drift ratio. The major crack, which had developed at 4 in. (102 mm) above the column base, had a width of 0.06 in. (1.5 mm) at the end of the 3% drift ratio. Another major crack which had formed 12 in. (305 mm) above the column base during the previous drift ratio widened and measured 0.007 in. (0.2 mm) at the end of the 3% drift ratio. During the 5% drift ratio, inclined or flexure-shear type cracks developed on the north and south sides of the column. During the 7% drift ratio, the spalled region grew in such a way that the spiral became visible in part. The extreme west column bar fractured 1.5 in. (38 mm) above the column base, as a result of low cycle fatigue, slightly before the peak displacement during the second push of the 8% drift ratio while the extreme east bar was still undamaged but visible; this bar fractured 2 in. (51 mm) above the column base, during the first cycle of the 9% drift ratio, after which the test was terminated. Figs. 3.7(a) and (b) show the damage state of specimen CIP after the 3% and 9% drift ratios, respectively.

The footing and joint region remained intact with only two minor cracks developing in

the joint region during the 2% drift ratio for all specimens.

Displacement Ductility

In seismic design of structures, displacement ductility capacity is the ability of a structural component to perform beyond the yield point without excessive strength deterioration. This parameter was computed for each specimen based on the concept of equal energy of an idealized elasto-plastic system.[26] The average cyclic envelope curve was first constructed using the peak values of the first cycle for each drift ratio; the idealized elasto-plastic curve was then generated in order to calculate the displacement ductility. To obtain the effective yield displacement of the system, it was assumed that the idealized elasto-plastic curve intersects the average cyclic envelope curve at a force equal to 70% of the effective yield force; ACI Committee 374 states that the point of intersection shall be between 65% and 75% of the effective yield force.[25] This method was selected in place of the method prescribed in bridge design codes in which the idealized curve shall intersect the actual envelope at first yielding of reinforcing bars.[23, 24] This was done mainly because strain gauges were not installed close to the critical sections of GGSS-1 and GGSS-3, due to accessibility constraints. The ultimate displacement (Δ_u) was taken as the displacement corresponding to a 20% drop in lateral load capacity.[27] Displacement ductility was subsequently obtained as the ratio of ultimate displacement (Δ_u) to effective yield displacement (Δ_y) of the system. The displacement ductility capacity of specimen CIP was 8.9, compared to displacement ductility values of 5.4, 6.1, and 6.8 achieved by GGSS-1, GGSS-2, and GGSS-3, respectively, as presented in Table 3.4 which includes the properties of the idealized elasto-plastic curves.

Fig. 3.8 shows the average cyclic envelope for all specimens, constructed by using average peak values of the push and pull cycles. The last point on each curve corresponds to a 20% strength reduction, which is the ultimate point considered for displacement ductility calculations. The average cyclic envelope revealed a noticeable distinction between precast and CIP specimens. The CIP specimen failed by rebar fracture of the column longitudinal bars, due to low cycle fatigue. Premature rebar fracture was observed for all precast specimens that resulted in a reduced ultimate displacement capacity of precast subassemblies; this was attributed to higher strain levels concentrated at the end of the GGSS located at the column-to-footing interface.

The overall force-displacement performance of all test specimens is similar up to the 1% drift ratio. Specimens GGSS-1 and GGSS-3 had the greatest strength capacity; this was attributed to a higher axial load that was unintentionally applied to precast specimen GGSS-1, and a relatively larger test-day concrete compressive strength of GGSS-3. The axial load for GGSS-1 was 16% larger than that of GGSS-3.

Energy Dissipation

The ability to dissipate energy during seismic events is considered a key feature of ductile bridge components in high seismic regions and an indication of the hysteretic response quality. The presence of mild steel in the plastic hinge region capable of undergoing inelastic behavior is important for achieving an acceptable amount of energy dissipation. The hysteretic energy was computed for each specimen to obtain the energy dissipation capacity. Fig. 3.9(a) shows the cumulative hysteretic energy dissipation of the test alternatives. As observed, the rate of this quantity increases with an increase in the

drift ratio up to failure, for all specimens. Fig. 3.9(a) shows that the four specimens had a similar hysteretic energy dissipation capacity up to a 3% drift ratio, after which the CIP and GGSS-3 specimens had a slightly better performance due to debonding effects.

Equivalent viscous damping is another quantity used to evaluate the relative energy dissipation capacity of systems under cyclic load. The equivalent viscous damping offers more information about the hysteretic response of the system since both the hysteretic and strain energy are included. The equivalent viscous damping ratio (ξ_{eq}) was obtained as the ratio of hysteretic energy to energy of the equivalent viscous system as defined in Equation (3.1) [28]:

$$\xi_{eq} = \frac{E_D}{4\pi E_{S0}} \tag{3.1}$$

where E_D and E_{S0} are the area inside the hysteresis loop and the strain energy, respectively.

Fig. 3.9(b) presents the average ξ_{eq} of both cycles for each drift ratio. In the inelastic region of the response, which begins after completion of the 1% drift ratio, ξ_{eq} for all specimens increases with drift ratio. At the 8% drift ratio, specimen CIP had a ξ_{eq} of 31% which indicates that this reinforced concrete component had good seismic detailing. It is evident that GGSS-2 and CIP had greater ξ_{eq} values than GGSS-1 and GGSS-3, during all drift ratios. For instance, ξ_{eq} at 6% drift ratio was 26% and 24% for GGSS-2 and CIP, respectively, compared to 17% and 20% for GGSS-1 and GGSS-3, respectively. A relatively superior energy dissipation capability is achieved when the GGSS connector is in the footing, rather than the column base. GGSS-3 had a better overall performance when compared to GGSS-1 indicating that the debonded reinforcing bar zone was an effective modification.

Column Base Curvature and Dowel Bar Strain

LVDTs installed on both extreme sides of the column base were used to study curvature distribution and capacity. Four curvature segments were specified by using four LVDTs on the east and west sides of the column. The average curvature (φ) was computed as:

$$\varphi = \frac{A - B}{wh} \tag{3.2}$$

where *A* and *B* are west and east LVDT measurements, respectively; *w* and *h* are the width and height of the curvature segment, respectively. Constructed over a 30-in. (762 mm) column height above the column base, the average curvature values were normalized by multiplying them by the column dimension of 21 in.(533 mm), and the curvature segment heights were divided by the column overall height of 96 in. (2338 mm), as shown in Fig. 3.10. Positive curvature values were associated with the push direction and negative values with the pull. The calculated curvature value was assumed to be an average over the whole segment height. Curvature values are included up to a 6% drift ratio after which the instrumentation had to be removed due to limited stroke. The top of GGSS connectors is identified by a dashed line for specimens GGSS-1 and GGSS-3. The curvature profile of GGSS-1 and GGSS-3, with the connectors in the column, implies that the curvature distribution was minimal over the connector length and inelastic response was redirected to the column-to-footing interface and the section above the connector. This indicates that sections with GGSS connectors were less ductile compared to sections without them, due to the size and stiffness of the connectors. A well-distributed curvature profile was achieved for GGSS-2 with the connectors cast in the footing; this curvature response was in a good agreement with that of specimen CIP

as no disruption was introduced to the plastic hinge zone of the column.

Data from strain gauges, located on the extreme two reinforcing bars, were used to study the yield pattern in the column plastic hinge zone and joint regions. For GGSS-1 and GGSS-3, extreme bars yielded within the covered area with a depth of 7 ½ in. (190 mm) into the footing, and 22 in. (559 mm) above the column base, except for the initial 5-in. (127 mm) portion of both the factory and field dowels embedded and confined inside the connector. For GGSS-2, the covered area was 16 in. (406 mm) into the footing and 20 in. (508 mm) above the column base, within which the factory dowels did not yield, while the field dowels yielded starting 2 in. (51 mm) inside the footing and throughout the 20-in. (508 mm) height in the column base. Strain gauges located on extreme reinforcing bars of specimen CIP showed that bars yielded up to 34 in. (864 mm) above the column base and 9 ½ in. (241 mm) into the footing.

Bond-Slip Rotation and Column Displacement Components

The end rotation of each column was obtained using the four bottom LVDTs located adjacent to the interface of the column and the footing. The end rotation is commonly referred to as the bond-slip rotation since it is caused by the localized slippage of the dowel bars passing through the interface. Fig. 3.11(a) shows the average of the peak bond-slip rotations at each drift ratio for all specimens. CIP had the smallest rotation at every drift ratio beyond the yield drift which indicates that the performance of CIP was dominated by flexure. On the other hand, GGSS-3 had the largest rotations implying that debonding of the dowel bars resulted in considerably more localized rotations at the interface. The bond-slip rotation was found to be 0.0267 rad, 0.0169 rad, 0.0282 rad, and

0.0114 rad for GGSS-1, GGSS-2, GGSS-3, and CIP, respectively, at 4% drift ratio, suggesting that the bond-slip rotation of the precast subassemblies was 2.3, 1.5, and 2.5 times that of CIP for GGSS-1, GGSS-2, and GGSS-3, respectively.

The horizontal displacement of a cantilever column (Δ_c) is made up of three main components, as shown in Eq. (3.3):

$$\Delta_c = \Delta_{fl} + \Delta_{bs} + \Delta_v \tag{3.3}$$

where, (Δ_{fl}) is the flexural component, (Δ_{bs}) is the bond-slip component, and (Δ_v) is the shear component. For the slender columns investigated in this study with a shear span-to-depth ratio of more than 5.0, shear contribution can be neglected. Lehman and Moehle (2000) showed that the bond-slip contribution can be as high as 50% and 30% of the overall column displacement capacity for monolithic columns with an aspect ratio equal to 4.0 and 8.0, respectively; this indicates the more slender the column is, the larger the flexural contribution.[29] Another study mentioned that the bond-slip contribution can be up to 35% of the total displacement for monolithic columns.[30]

Fig. 3.11(b) presents the average peak bond-slip displacement components for all specimens at each drift ratio. The largest bond-slip contribution for the monolithically built CIP was 42.8% of the overall column displacement which is comparable to the findings of the two aforementioned references. This quantity was found to be 73.2%, 60.6%, and 83.0% for GGSS-1, GGSS-2, and GGSS-3, respectively, implying that the intentional debonding bar zone for GGSS-3 resulted in a larger bond-slip displacement component and consequently smaller flexural displacement component. This justifies the rocking behavior of GGSS-3 under the cyclic loads.

Conclusions

Research was carried out to assess the overall performance of grouted splice sleeve connectors used to connect precast columns to precast footings. The experimental data provided both qualitative and quantitative measures to evaluate and study each specimen under quasi-static lateral cyclic loading. A summary of findings is offered:

1. The cast-in-place control specimen (CIP) had a good hysteretic response with ductile failure (reinforcing bar fracture on opposite sides of the column). Well-distributed flexural cracks formed along the column height of the specimen, and concrete cover spalled completely at the column base. The overall performance was dominated by flexural action and formation of a plastic hinge at the column base. The precast specimen with the connectors inside the footing (GGSS-2) had a damage state similar to the control specimen, because the connectors were located outside the column base. Hence, more flexural cracks formed along the column, and the spalled region was similar to specimen CIP in terms of height, width, and depth. Damage to the column base of precast specimens with the connectors in the column base (GGSS-1 and GGSS-3) was localized to the column-to-footing interface. This involved fewer flexural cracks along the column height compared to specimen CIP. The spalled region for GGSS-1 and GGSS-3 was also smaller than that of specimens CIP and GGSS-2.
2. Rebar fracture occurred for all precast alternatives and specimen CIP, which indicated that the bond between reinforcing bars and high-strength grout was good, as observed from individual connector tests. Hence, a ductile performance was achieved for all specimens until bar fracture. Fracture of reinforcing bars in

all specimens was due to low cycle fatigue.

3. Precast specimen GGSS-1 (connectors in column base) had a displacement ductility of 5.4. A more ductile response along with better hysteretic performance was achieved for precast specimen GGSS-2 with the connectors inside the footing which had a displacement ductility equal to 6.1. The eight bar diameter debonded rebar zone for the footing dowel bars implemented for specimen GGSS-3 (connectors in column base) resulted in a displacement ductility of 6.8. The cast-in-place control specimen had a displacement ductility of 8.9 with hysteresis loops that were wide and stable, implying good energy dissipation and hysteretic performance. The displacement ductility obtained for all test alternatives exceeded the minimum component displacement ductility of 3.0 specified in the Caltrans SDC. In addition, the displacement ductility values were greater than the maximum displacement ductility demand of 5.0 which was specified in the AASHTO Guide Specifications for single-column bridge bents.
4. The distribution of inelasticity in the column base of specimen GGSS-2 (connectors in the footing) was very similar to specimen CIP, as there was no disruption of the natural stress transfer in the column base. A different distribution of inelasticity was observed for specimens GGSS-1 and GGSS-3 (connectors in column). This was attributed to the presence of connectors in the column base in which the inelastic actions were shifted to locations at the bottom and top of the GGSS connectors.
5. A comparison between the columns overall displacement components revealed that the response of the control specimen CIP was governed by flexure, whereas

the response of the precast specimens was governed by bond-slip. The bond-slip contribution to the column displacement was up to 73.2%, 60.6%, 83.0%, and 42.8% of the total displacement capacity for GGSS-1, GGSS-2, GGSS-3, and CIP, respectively.

6. Precast specimen GGSS-2 (connectors in the footing) had a better overall performance compared to GGSS-1 (connectors in column). The former was found to be more emulative of specimen CIP in terms of energy dissipation capacity, damage sequence, and extent of damage.
7. All precast alternatives are expected to perform adequately in moderate-to-high seismic regions if the reduced displacement ductility is addressed accordingly; however, the precast specimen with debonded reinforcing bars in the footing is recommended because it achieved the highest displacement ductility among all precast specimens tested in this research.

Acknowledgements

The authors would like to acknowledge the financial support of the Utah, New York State, Texas departments of transportation, and the Mountain-Plains Consortium. The authors wish to thank Lawrence D. Reaveley, Professor at the University of Utah, for his invaluable input throughout the project. Special thanks are extended to Mark Bryant of the University of Utah for his untiring efforts and support. The authors greatly appreciate the valuable input offered by Carmen Swanwick and Joshua Sletten of UDOT, and Harry White of NYSDOT. The authors are also grateful for the donation of materials by Splice Sleeve North America and the assistance of Hanson Structural Precast. The

authors would like to acknowledge the helpful comments of the reviewers which improved the paper.

Notation

A = west linear variable differential transformers reading

B = east linear variable differential transformers reading

E_D = hysteretic energy (area inside hysteresis loop)

E_{S0} = strain energy

f_y = nominal yield strength of reinforcing bars

h = height of curvature segment

w = width of curvature segment

Δ_{bs} = displacement component due to bond-slip

Δ_c = total displacement of column

Δ_{fl} = displacement component due to flexure

Δ_u = ultimate displacement

Δ_v = displacement component due to shear

Δ_y = effective yield displacement

μ_Δ = displacement ductility

ξ_{eq} = equivalent viscous damping

φ = average curvature

References

1. Khaleghi, B., Schultz, E., Seguirant, S., Marsh, L., Haraldsson, O. S., Eberhard, M. O., and Stanton, J. F., "Accelerated Bridge Construction in Washington State: From

Research to Practice," *PCI Journal*, V. 57, No. 4, 2012, pp. 34–49.

2. Weinert, M. D., "Substructure Connections for Accelerated Bridge Construction in Seismic Regions," MS Thesis, University of Washington, Seattle, WA, 2011.

3. Haraldsson, O. S., Janes, T. M., Eberhard, M. O., and Stanton, J. F., "Seismic Resistance of Socket Connection between Footing and Precast Column," *Journal of Bridge Engineering,* V. 18, No. 9, 2013, pp. 910–919.

4. Belleri, A., and Riva, P., "Seismic Performance and Retrofit of Precast Concrete Grouted Sleeve Connections." *PCI Journal*, V. 57, No. 1, 2012, pp. 97–109.

5. White, S., "Controlled Damage Rocking Systems for Accelerated Bridge Construction," MS Thesis, University of Canterbury, Christchurch, New Zealand, 2014.

6. Matsumoto, E. E., "Emulative Precast Bent Cap Connections for Seismic Regions: Component Tests—Grouted Duct Specimen (Unit 2)," *ECS Report No. ECS-CSUS-2009-02*, California State University, Sacramento, CA, 2009.

7. Pang, J. B. K., Eberhard, M. O., and Stanton, J. F., "Large-Bar Connection for Precast Bridge Bents in Seismic Regions," *Journal of Bridge Engineering*, V. 15, No. 3, 2010, pp. 231–239.

8. Tazarv, M., and Saiidi, M. S., "UHPC-Filled Duct Connections for Accelerated Bridge Construction of RC Columns in High Seismic Zones." *Engineering Structures*, V. 99, 2015, pp. 413–422.

9. Marsh, M. L., Wernly, M., Garett, B. E., Stanton, J. F., Eberhard, M. O., and Weinert M. D., "Application of Accelerated Bridge Construction Connections in Moderate-to-High Seismic Regions," *NCHRP Report 698*, National Cooperative Highway Research Program, Washington, DC, 2011.

10. Jansson, P. O., "Evaluation of Grout-Filled Mechanical Splices for Precast Concrete Construction," *Report R-1512,* Michigan Department of Transportation, Lansing, MI, 2008.

11. Rowell, S. P., Grey, C. E., Woodson, S. C., and Hager, K. P., "High Strain Rate Testing of Mechanical Couplers," *Report ERDC TR-09-8*, Washington, DC, 2009.

12. Haber, Z. B., Saiidi, M. S., and Sanders. D. H., "Behavior and Simplified Modeling of Mechanical Reinforcing Bar Splices," *ACI Structural Journal*, V. 112, No. 2, 2015, pp. 179-188.

13. Ameli, M. J., Parks, J. E., Brown, D. N., and Pantelides, C. P., "Seismic Evaluation of Grouted Splice Sleeve Connections for Reinforced Precast Concrete Column-to-Cap beam Joints in Accelerated Bridge Construction," *PCI Journal*, V. 60, No. 2, 2015, pp.

80-103.

14. Tazarv, M., and Saiidi, M. S., "Next Generation of Bridge Columns for Accelerated Bridge Construction in High Seismic Zones," *Report No. CCEER 14-06*, Center for Civil Engineering Earthquake Research, Department of Civil and Environmental Engineering, University of Nevada, Reno, Reno, NV, 2014.

15. Haber, Z. B., Saiidi, M. S., and Sanders, D. H., "Seismic Performance of Precast Columns with Mechanically Spliced Column-Footing Connections," *ACI Structural Journal*, V. 111, No. 3, 2014, pp. 639-650.

16. Aida, H., Tanimura, Y., Tadokoro, T., and Takimoto, K., "Cyclic Loading Experiment of Precast Columns of Railway Rigid-Frame Viaduct Installed with NMB Splice Sleeves," *Proceedings of the Japan Concrete Institute*, V. 27, No. 2, 2005.

17. Reetz, R. J., Ramin, M. V., and Matamoros, A., "Performance of Mechanical Splices within the Plastic Hinge Region of Beams Subject to Cyclic Loading," *Proceedings of 13th World Conference on Earthquake Engineering*, Vancouver, B.C., Canada, 2004.

18. Yoshino, T., Kobayashi, K., and Ase, M., "Intensive Shear Reinforcing Method for PCA Members with Splice Sleeve Joint," *Proceedings of the 11th World Conference on Earthquake Engineering*, Acapulco, Mexico, 1996.

19. Matsuzaki, Y., et al., "Effects of Sleeves on Member Properties, Study on the Behavior of Reinforced Concrete Beams with Grout-Filled Steel Splice Sleeves," Architectural Institute of Japan, 1987.

20. Splice Sleeve Japan, Ltd, "Tests on Re-Bar Splices in Reinforced Concrete Columns Using NMB Splice Sleeves," *Report NPD-024*, Splice Sleeve Japan, Ltd., Tokyo, Japan.

21. Parks, J. E., "Seismic Rehabilitation of Column to Pier Cap Accelerated Bridge Construction Connections and Acoustic Emission Monitoring Assessment," MS Thesis, University of Utah, Salt Lake City, UT, 2014.

22. American Association of State Highway and Transportation Officials (AASHTO). "AASHTO LRFD Bridge Design Specifications," Washington, DC, 2012.

23. American Association of State Highway and Transportation Officials (AASHTO). "AASHTO Guide Specifications for LRFD Seismic Bridge Design," Washington, DC, 2011.

24. California Department of Transportation, "Seismic Design Criteria," Division of Engineering Services, Sacramento, CA, 2010.

25. ACI Committee 374, "Guide for Testing Reinforced Concrete Structural Elements Under Slowly Applied Simulated Seismic Loads," American Concrete Institute,

Farmington Hills, MI, 2013.

26. Park, R., "Evaluation of Ductility of Structures and Structural Assemblages from Laboratory Testing," *Bulletin of the New Zealand National Society for Earthquake Engineering*, V. 22, No. 3, 1989, pp. 155–166.

27. Priestley, M. J. N., and Park, R., "Strength and Ductility of Concrete Bridge Columns under Seismic Loading," *ACI Structural Journal*, V. 84, No. 1, 1987, pp. 61–76.

28. Chopra, A, "Dynamics of Structures, Theory and Applications to Earthquake Engineering," 4th ed., Pearson Prentice Hall, Upper Saddle River, NJ, 2007.

29. Lehman, D. E., and Moehle, J. P, "Seismic Performance of Well-confined Bridge Columns," *PEER Report 1998/01*, Pacific Earthquake Engineering Research Center, University of California, Berkeley, Berkeley, CA, 2000.

30. Zhao, J., and Sritharan, S, "Modeling of Strain Penetration Effects in Fiber-Based Analysis of Reinforced Concrete Structures," *ACI Structural Journal*, V. 104, No. 2, 2007, pp. 133–141.

Table 3.1. Tension test results for connector test assemblies

Connector test identifier	Maximum load (kip)	Maximum bar stress (ksi)	Maximum bar stress normalized to f_y	Failure mode
Connector test-1	81.2	102.8	1.71	Bar fracture
Connector test-2	80.7	102.2	1.70	Bar fracture
Connector test-3	80.1	101.4	1.69	Bar fracture
Connector test-4	79.9	101.1	1.69	Bar fracture
Connector test-5	80.0	101.3	1.69	Bar fracture
Connector test-6	77.3	97.8	1.63	Bar fracture

Note: f_y = nominal yield strength of reinforcing bars. 1 kip = 4.448 kN; 1 ksi = 6.895 MPa.

Table 3.2. Test matrix

Test ID	Specimen	Connector Location	Description
1	GGSS-1	Column base	NA
2	GGSS-2	Footing	NA
3	GGSS-3	Column base	Debonded reinforcing bars inside footing
4	CIP	NA	Control specimen

Table 3.3. Compressive strength of concrete and grout (ksi)

Specimen	Concrete		Grout	
	28-day	Test day	28-day	Test day
GGSS-1	5.3	5.9	14.4	14.4
GGSS-2	3.9	5.5	11.1	13.5
GGSS-3	6.7	8.4	15.6	14.6
CIP	5.2	6.7	NA	NA

Note: 1 ksi = 6.895 MPa.

Table 3.4. Displacement ductility

Specimen	First yield point (idealized)*		Effective yield point		Ultimate point		Displacement ductility
	Displacement (in.)	Force (kip)	Displacement (in.)	Force (kip)	Displacement (in.)	Force (kip)	
GGSS-1	0.94	29.3	1.34	41.8	7.32	41.8	5.4
GGSS-2	0.74	22.8	1.05	32.6	6.42	32.6	6.1
GGSS-3	0.78	26.7	1.11	38.2	7.58	38.2	6.8
CIP	0.66	23.5	0.95	33.6	8.45	33.6	8.9

*Force values are set equal to 70% of effective yield force values.
Note: 1 in. = 25.4 mm; 1 kip = 4.448 kN.

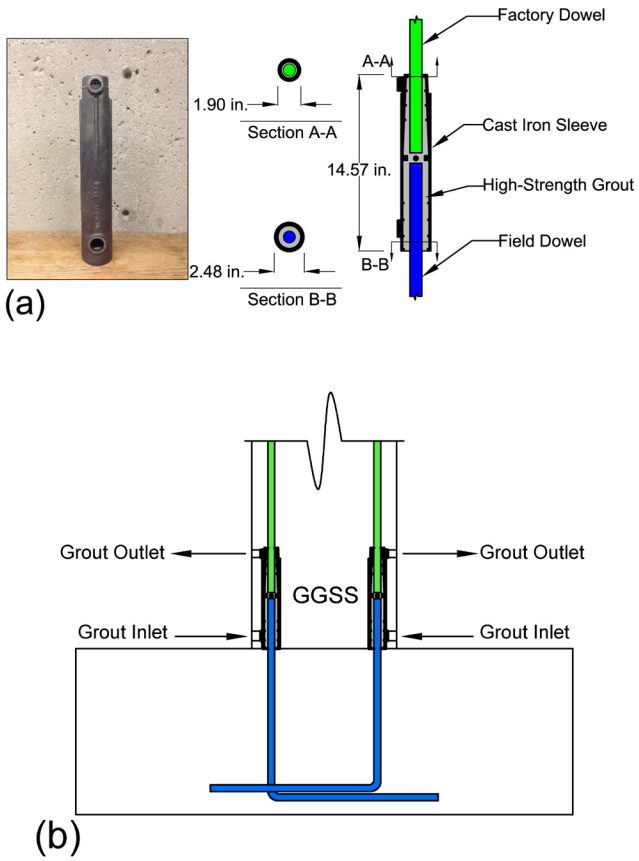

Fig. 3.1. Grouted splice sleeve connector: (a) Details of connector with No. 8 (25M) bars; (b) Connectors in precast components. (Note: 1 in. = 25.4 mm).

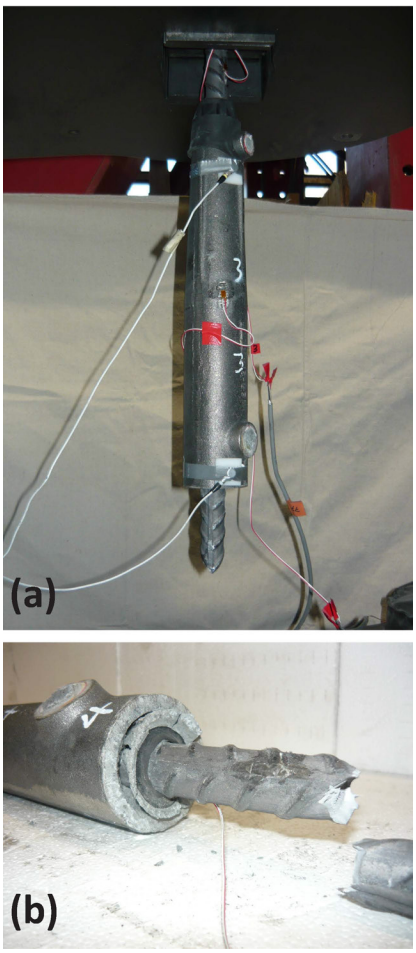

Fig. 3.2. Failure of connector assembly due to reinforcing bar fracture: (a) Failure of connector assembly in testing apparatus; (b) Formation of grout cone.

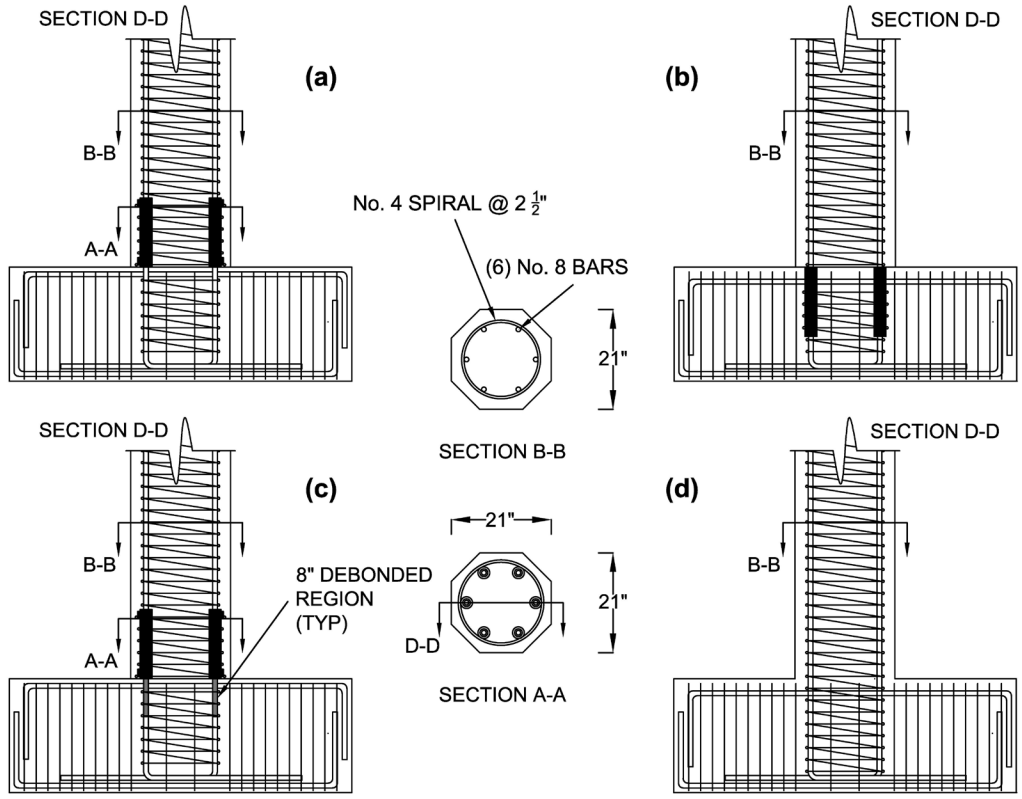

Fig. 3.3. Details of specimens: (a) GGSS-1; (b) GGSS-2; (c) GGSS-3; and (d) CIP (Note: No. 4 = 13M; No. 8 = 25M; 1 in. = 25.4 mm).

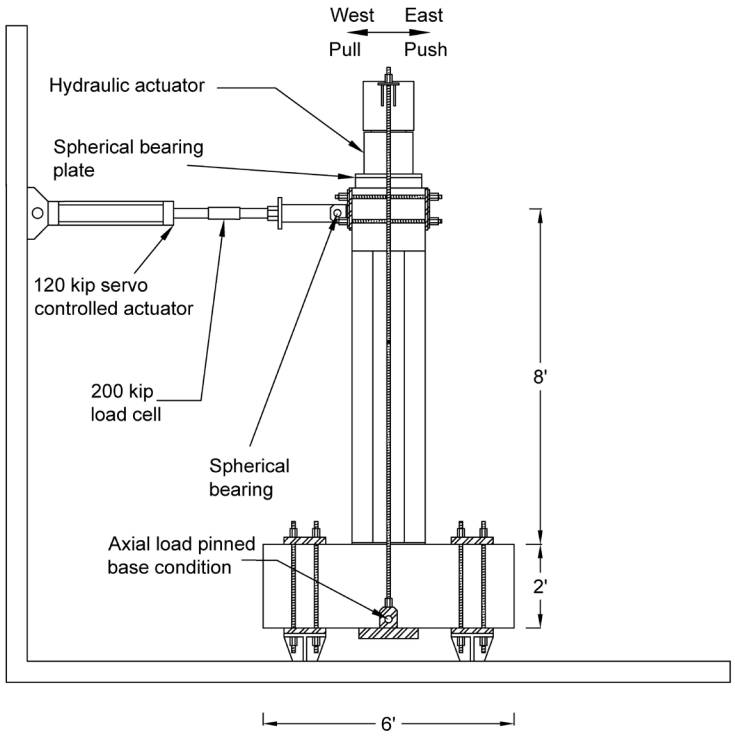

Fig. 3.4. Schematic test setup (Note: 1 ft = 0.305 m; 1 kip = 4.448 kN).

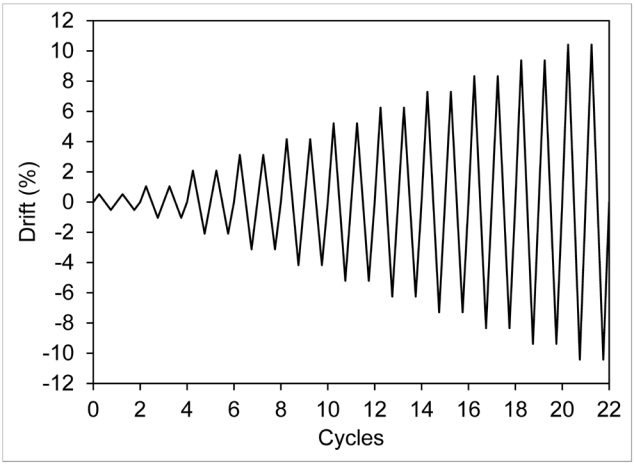

Fig. 3.5. Drift history.

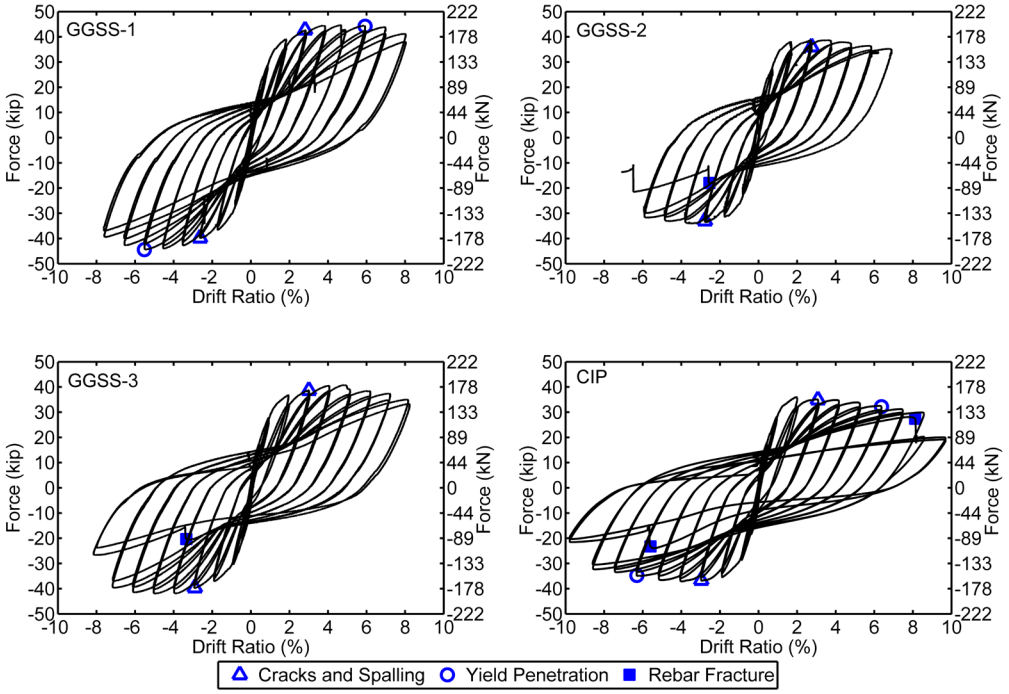

Fig. 3.6. Hysteretic response.

(a) *Cracks and spalling at end of the 3% drift ratio.*

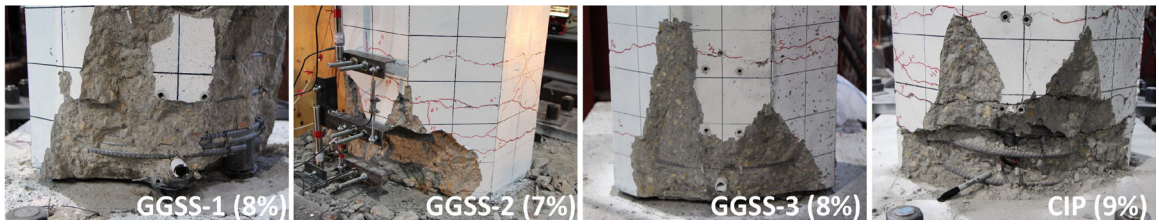

(b) *End of experiment.*

Fig. 3.7. Visual observations and damage states.

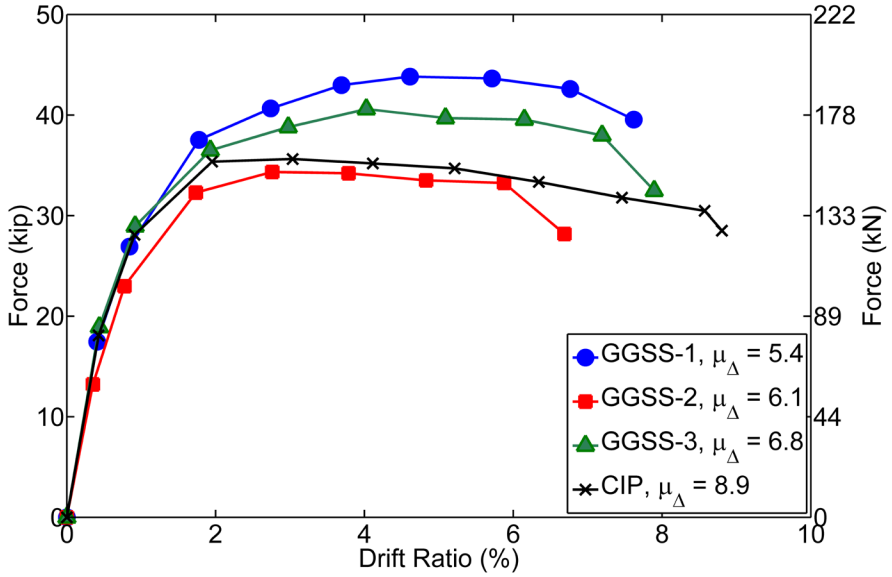

Fig. 3.8. Average cyclic envelope.

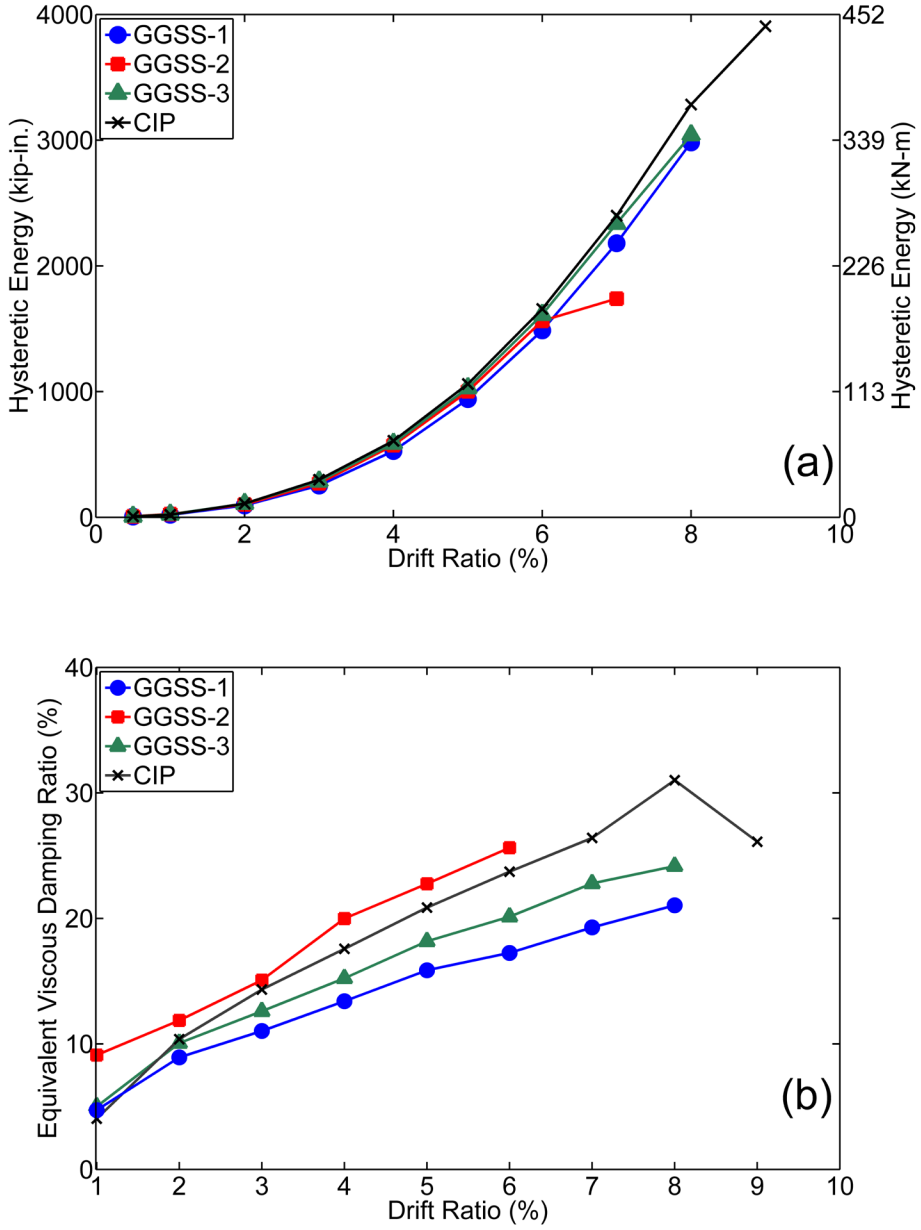

Fig. 3.9. Energy dissipation capacity: (a) Cumulative hysteretic energy; (b) Equivalent viscous damping ratio.

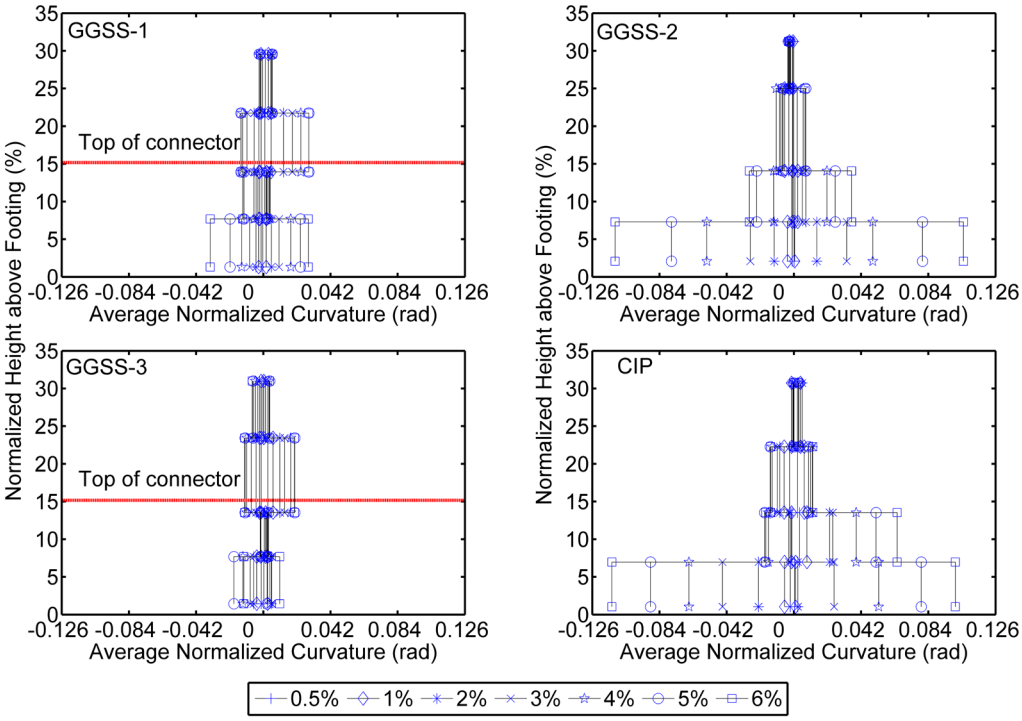

Fig. 3.10. Column base curvature distribution (Average curvature values are multiplied by the column dimension [21 in.] for normalization).

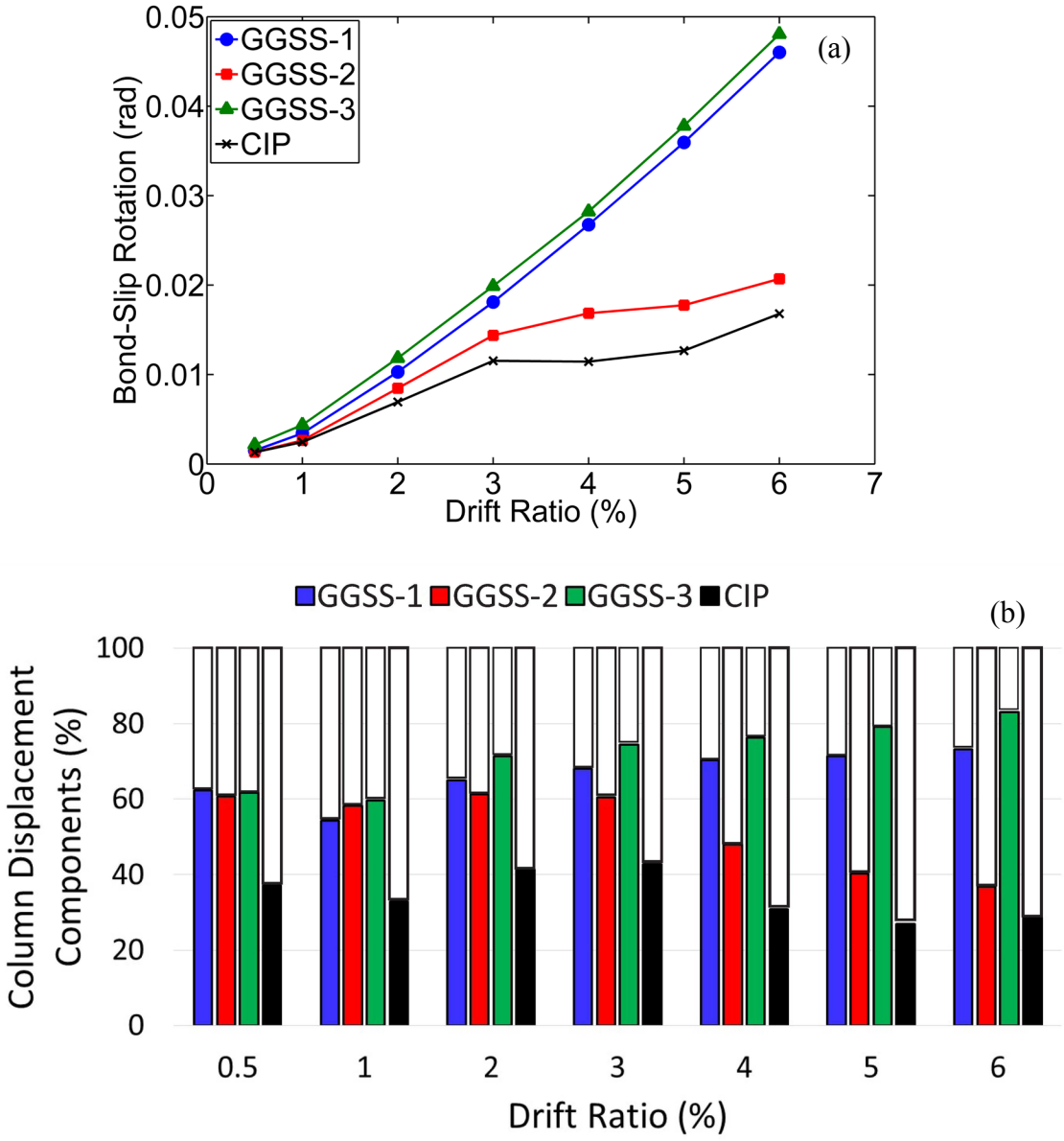

Fig. 3.11. Effect of bond-slip on the performance: (a) Column end rotation; (b) Column displacement components (colored bars show bond-slip components, white bars show flexural components).

CHAPTER 4

SEISMIC ANALYSIS OF PRECAST CONCRETE BRIDGE COLUMNS CONNECTED WITH GROUTED SPLICE SLEEVE CONNECTORS

M. J. Ameli[1], and Chris P. Pantelides[2]

Submitted to the ASCE Journal of Structural Engineering

Abstract

Reinforcing bar couplers are used in prefabricated bridge elements and bridge systems for accelerated bridge construction. Grouted splice sleeve connectors are used in bridge substructures because of the enhanced construction tolerances they offer. This paper presents a simplified acomputational model for seismic assessment of precast bridge columns connected to precast footings using grouted splice sleeve connectors. The proposed model was developed and validated using three half-scale bridge subassemblies

[1] Graduate Research Fellow, Dept. of Civil and Environmental Eng., Univ. of Utah, SLC, UT 84112 (corresponding author). E-mail: m.ameli@utah.edu
[2] Professor, Dept. of Civil and Environmental Eng., Univ. of Utah, SLC, UT 84112, E-mail: c.pantelides@utah.edu

tested to failure. Cyclic quasi-static loading was applied to two precast specimens and one cast-in-place specimen. The connectors were located in the footing, for the first precast alternative, and in the column end for the second precast alternative along with debonding of reinforcing bars in the footing. Force-based beam-column elements with fiber sections were used to construct the model based on plastic hinge weighted integration; the model included low-cycle fatigue and bond-slip. The computational model was validated with the experiments through both local and global response comparisons. The results from the proposed computational model were found to be in a close agreement with the experiments.

Keywords: Accelerated bridge construction; Connection; Cyclic load test; Grouted splice sleeve; Computational study; Precast concrete; Reinforcing bar coupler; Seismic.

Introduction

Recent advancements in bridge design and construction include innovative methodologies that bring about ease of construction and significant acceleration of project completion time. Prefabrication of bridge elements contributes to acceleration of construction and better quality control. Accelerated bridge construction (ABC) is an effective method for improving the bridge construction process in terms of speed, quality, safety, and reduction of environmental impacts. As part of ABC, precast concrete substructure components have been used in seismic regions in the US (Khaleghi et al. 2012). A Grouted splice sleeve (GSS) connector is a type of reinforcing bar splicing device that is composed of a ductile iron sleeve and high-strength grout; two connecting bars are spliced that extend from the two ends of the connector. These connectors have

found applications because of the enhanced construction tolerances they offer. Connections between precast elements in bridge substructures could experience high levels of earthquake-induced deformations and stresses. When GSS connectors are used in precast concrete components concentrated damage accumulates in a limited and localized area.

Experimental studies have been conducted on flexural precast columns to assess strength and deformability properties of bridge substructure subassemblies connected with GSS connectors. The experiments revealed that precast and corresponding cast-in-place subassemblies have comparable strength capacity; however, the displacement capacity of precast subassemblies was found to be lower than that of the cast-in-place control specimens (Haber et al. 2014; Pantelides et al. 2014). Further research studies showed that the displacement capacity can be improved by implementing proper detailing, such as debonding of reinforcing bars outside the GSS connectors (Tazarv and Saiidi 2014; Pantelides et al. 2014). Haber et al. (2015) investigated the stress-strain behavior of GSS connector subassemblies with reference to the stress-strain behavior of spliced bars, under monotonic tensile loads; it was found that strain capacity of the GSS connector was 35% of the strain capacity of the spliced bars; this was attributed to the presence of the splicing device.

Analytical models are needed for a more thorough and holistic investigation of the overall aspects of cyclic performance of precast concrete substructures with GSS connectors. Analytical models have been developed for precast bridge piers with GSS connectors (Tazarv and Saiidi 2014; Haber et al. 2015); these analytical models were successful in reproducing the corresponding experimental results.

As part of a comprehensive research program, three half-scale column-to-footing concrete specimens were tested under a quasi-static cyclic displacement history (Pantelides et al. 2014). Two precast specimens incorporated one type of GSS connector where the bars were grouted at both ends of the connector; the third specimen was built monolithically as the control. This paper highlights the experimental results and the research conducted to develop a computational model for the tested subassemblies.

Experimental Study

Quasi-static cyclic tests were conducted on three half-scale concrete specimens, two of which were constructed using precast components joined by means of GSS connectors, as shown in Fig. 4.1. The connectors were incorporated in the footing of specimen Precast-1, with dowel bars protruding from the column end. The second precast specimen, Precast-2, was composed of a precast column and precast footing connected by GSS connectors cast at the column base; dowel reinforcing bars protruded from the footing which were debonded from the concrete over a 203-mm (8.0-in.) region just below the footing surface. Control specimen CIP was constructed monolithically without any GSS connectors. Table 4.1 shows the test matrix and test configuration alternatives.

Design and Fabrication of Half-scale Specimens

The specimens were designed and detailed to simulate typical prototype bridges constructed in the State of Utah, according to the AASHTO LRFD Bridge Design Specifications (2012), and AASHTO Guide Specifications for LRFD Seismic Bridge Design (2011). A circular configuration of column longitudinal bars and an octagonal

column cross-section were implemented to facilitate precasting of the columns. The aforementioned design codes in addition to the Caltrans Seismic Design Criteria (2010) prohibit splicing of reinforcement, including mechanical anchorage devices, in the plastic hinge region of ductile members, for bridges located in moderate-to-high seismic areas. In the AASHTO Guide Specifications, this would apply to Seismic Design Categories C and D. Thus, the initial design and detailing was developed for an assembly without any GSS connectors, i.e., the cast-in-place control specimen. The design was then adjusted to accommodate GSS connectors within the precast subassemblies and necessary modifications were considered accordingly (Pantelides et al. 2014).

The specimens were half-scale models of common prototype highway bridges, specifically the Riverdale Road Bridge over I-84 in Utah. Fig. 4.2 shows the details and configuration of the three specimens. The column height was 2.59 m (8 ft 6 in.) with a 533-mm (21-in.) octagonal cross-section to facilitate casting. The top 457-mm (18-in.) length of the column was changed from an octagon to a 533-mm (21-in.) square for ease of testing. Six 25M (No. 8) bars in a circular arrangement and a 13M (No. 4) spiral with a pitch of 64 mm (2½ in.) made up the column reinforcement. The longitudinal and volumetric transverse reinforcement ratios were 1.3% and 1.9%, respectively. The footing was designed as a 1.83-m long x 0.91-m wide x 0.61-m deep (6 x 3 x 2 ft) precast concrete element and consisted of 25M (No. 8) longitudinal bars enclosed by 13M (No. 4) double hoops. The footing was designed to remain elastic and not undergo plastic deformations. The design inhibits shear failure from occurring in the column by using a shear span-to-depth ratio of more than 5.0 (corresponding to slender columns) along with closely spaced shear reinforcement. The desirable column failure mode was either

flexural or splice failure.

The GSS connectors were embedded in the footing of specimen Precast-1, with dowel bars projecting 178 mm (7 in.) from the precast column. A pregrout operation was conducted for this specimen using proprietary high-strength grout. To carry out a pregrout operation, both inlet and outlet ports of the six connectors were sealed during construction of the footing reinforcing bar cage. During erection of specimen Precast-1 and before lowering and positioning the precast concrete column, grout was pumped into the wide end opening of the embedded connectors. For precast concrete specimen Precast-2, the GSS connectors were located in the column plastic hinge region. A postgrout technique was implemented in which grout was pumped into the bottom port of the connectors and traveled up against gravity to fill the inside space of the connector.

Test Setup and Instrumentation

The lateral cyclic displacement and axial load were simultaneously applied to the column top using a servo-controlled actuator as shown in the test configuration of Fig. 4.3(a). An axial load of 520 kN (117 kip), 414 kN (93 kip), and 605 kN (136 kip) was applied to CIP, Precast-1, and Precast-2, respectively. This corresponds to an axial load index (ALI) of 0.06 that was used to simulate vertical loads tributary to the columns of a multicolumn bridge bent. ALI is defined as the ratio of axial load divided by the product of nominal concrete compressive strength and column gross cross-sectional area. An actuator placed on top of the column applied a compression force to a steel spreader beam which was connected to two high strength threaded rods. The lateral drift history consisted of increasing amplitudes of the predicted column yield drift ratio; two cycles

were employed for each drift ratio step to the east and west (ACI Committee 374 2013). Fig. 4.3(b) shows the drift ratio history versus number of cycles. The drift ratio is defined as the lateral displacement of the column top, where the actuator applies the lateral displacement, divided by the distance from top of the footing to center of the lateral displacement application, which was 2.44 m (8 ft), as shown in Fig. 4.3(a).

String potentiometers were used to measure the true displacement of the column top. Linear variable differential transformers (LVDT) were used to study the curvature distribution along the column end. LVDTs were mounted to the column end, over an approximately 762-mm (30-in.) region, to measure the relative vertical displacement between column cross-sections and provide data for curvature analysis.

Summary of Test Results

Test-day Material Properties

Tension tests of reinforcing bars were conducted along with compression tests on concrete cylinders and grout cubes for each specimen. Reinforcement consisted of 25M (No. 8) ASTM A706 Grade 60 (ASTM 2009) steel bars with an average yield and ultimate strength of 469 MPa (68 ksi) and 641 MPa (93 ksi), respectively. Table 4.2 shows the compressive strength of the concrete and high-strength grout on the test day of the specific test.

Hysteretic Performance

The response of the three specimens shows wide and stable hysteresis loops that indicate a relatively high energy dissipation capacity, as shown in Fig. 4.4. The damage

states mark three major events during the cyclic tests: end of flexural crack formation and initiation of cover spalling, yield penetration, and fracture of column longitudinal reinforcing bars. The extent of the damaged zone after termination of each test is also shown in Fig. 4.4.

Control specimen CIP had stable hysteresis loops with slight strength degradation caused by spalling of the relatively large unconfined concrete cover. To keep the sectional configuration of column reinforcing bars identical among all specimens, specimen CIP had the thickest cover so that the location of column longitudinal bars remained unchanged. Specimen CIP had the longest performance life. The extreme west column reinforcing bar fractured at the end of the second cycle of the 8% drift ratio, at a section 38 mm (1 ½ in.) above the column-to-footing interface. Subsequently, the extreme east column reinforcing bar fractured during the first cycle of the 9% drift ratio, 51 mm (2 in.) above the interface due to low-cycle fatigue; the specimen achieved a displacement ductility of 8.9; this quantity was calculated using the average cyclic envelope of the force-displacement response based on the concept of equal energy of an idealized elasto-plastic system (Park 1989). Major cracks and spalling of concrete were observed in the plastic hinge region, in addition to the fractured column bar and exposed spiral, as shown in Fig. 4.4(a).

Specimen Precast-1 had a stable performance up to the first cycle of the 7% drift ratio, during which the column east reinforcing bar fractured at a section 51 mm (2 in.) above the column-to-footing interface, due to low-cycle fatigue. There was no sign of excessive in-cycle or cyclic strength deterioration before fracture of the east reinforcing bar. The test was terminated after completion of the 7% drift ratio as a result of a 35%

strength reduction. The displacement ductility of this specimen was found to be equal to 6.1. A damage state similar to that of CIP was observed, with spalled concrete, flexural cracks, and exposed spiral, as shown in Fig. 4.4(b).

The overall hysteretic response of specimen Precast-2 indicated an entirely satisfactory and ductile performance. The hysteresis loops were wide and stable with minimal strength deterioration up to the first cycle of the 8% drift ratio, when the extreme east column reinforcing bar fractured 13 mm (½ in.) below the column-to-footing interface due to low-cycle fatigue. Debonding of dowel bars inside the footing resulted in an extended performance life, compared to Precast-1. The displacement ductility of this specimen was 6.8 implying that a more ductile response was achieved because of the debonded reinforcing bar region inside the footing. Compared to the other specimens, Precast-2 had a less severe damaged area near the column-footing interface. Fewer flexural cracks and concrete spalling with a smaller depth can be seen for this test subassembly in Fig. 4.4(c). The extreme east GSS connector and spiral reinforcement were visible in part at the end of the experiment. More detailed discussion of the experimental results can be found in Pantelides et al. 2014.

Computational Study

The application of prefabricated bridge elements and systems (PBES) as part of ABC is becoming a method of choice in many States in the US. In regions of high seismicity, the connections between such prefabricated elements may be critical for the structural integrity of the bridge, especially if the GSS connectors are used at moment-resisting joints. The results of the experiments discussed in the preceding sections, as

well as other experimental studies, suggest that there are significant performance differences between precast and conventional cast-in-place construction, under simulated seismic loads (Haber et al. 2014; Tazarv and Saiidi 2014; Pantelides et al. 2014). The performance differences include a distinct plastic hinging mechanism and a reduced displacement capacity for the precast subassemblies. Therefore, a reliable modeling strategy capable of predicting the seismic response of precast columns with GSS connectors is a valuable analysis and design tool for researchers and engineers.

Analysis Objective

The objective of the computational study was to develop a predictive modeling strategy for simulation of precast concrete bridge columns with GSS connections.

Nonlinear analysis of reinforced concrete components is complex. To develop an efficient computational model, it is helpful if simplified yet accurate models are incorporated. The proposed computational model is composed of a beam-column (stick-based) element with distributed plasticity. In the distributed plasticity models or fiber models, nonlinear material behavior can occur at any element cross-section. These cross-sections are discretized into a finite number of fibers and pertinent uniaxial material stress-strain relationships are assigned to each type of fiber. Numerical integration is evaluated along the element to obtain the global response.

Description of Proposed Computational Model

The proposed computational model was developed using the force-based beam-column element object in the OpenSees framework (McKenna et al. 2000; McKenna et

al. 2010). This includes incorporating a certain number of integration points, commonly between four and six, along the element; however, when dealing with strain-softening sections in structural members, the response of the element changes with a change in the number of integration points (Scott and Fenves 2006). This is because deformations are localized at one integration point only (located at the critical section along the beam-column element) leading to a loss of objectivity. Therefore, the response varies as the integration weight of that single integration point changes when changing the total number of integration points used in the element. Sideris (2012) investigated the response properties of force-based beam-column elements containing strain-softening sections, under quasi-static loading condition; lack of solution uniqueness was found to occur when such softening materials were used in force-based beam-column elements. The results of a preliminary pushover analysis of specimen CIP using one force-based beam-column element with four, five, or six Gauss-Lobatto integration points is presented in Fig. 4.5. As observed in this figure, the response is nonobjective as it varies considerably with the number of integration points. To address this issue, the plastic hinge integration scheme developed by Scott and Fenves (2006) was adopted in this study so that the proposed model could be used for a wide range of reinforced or precast concrete components. A modified version of this element found in the element library of OpenSees was used in this study. The modified element allows for spread of nonlinearity beyond the plastic hinge region unlike the original formulation that confines nonlinear behavior to the plastic hinge region, while the interior segment of the element remains linear elastic. One major advantage of using the force-based beam-column element with the plastic hinge integration scheme is that the user can specify a predefined plastic hinge

length using empirical equations available in the literature or based on direct observations from experiments.

The proposed computational model was developed using an iterative procedure to obtain the unique plastic hinge length that would result in an acceptable response under quasi-static cyclic load. Two criteria were incorporated to achieve a high level of accuracy: (1) Global response validation, which refers to the overall response of the model. In particular, the hysteretic performance of the proposed model is compared with that of the corresponding specimen to verify if strength and stiffness are in good agreement. A quantitative measure for this acceptance criterion is to compare the peak lateral force of the models and experiments. (2) Local or sectional response validation of the performance, which is implemented using a moment-curvature approach. A secondary local response criterion is fracture of reinforcing bars due to low-cycle fatigue which was the cause of failure for all specimens in this study based on experimental observations. Low-cycle fatigue is included in the proposed model as an indication of the ultimate displacement capacity.

The validation process is presented in the flowchart of Fig. 4.6. To initiate the process, sectional properties along with a trial value of plastic hinge length (L_p) were selected and the computational model was run. The iteration was continued until the difference between the response of the model and experiment was less than 12% for both the global and local response. Low-cycle fatigue was employed to determine the termination point in Fig. 4.6. This procedure is based upon transformation of the model for the precast specimens into an idealized equivalent cast-in-place model with a fictitious plastic hinge length capable of reproducing an acceptable global and local

performance.

The application of GSS connectors for connecting precast columns to precast footings altered the load transfer mechanism in the subassemblies. This load transfer is highly based upon the bond between reinforcing bars and surrounding high-strength grout; this signifies the importance of bond-slip in the response of such subassemblies. The bond-slip characteristics of all specimens were included in the proposed modeling strategy.

Bond-slip

Bond-slip of reinforcing bars is an important phenomenon that may influence the response of reinforced/precast concrete components during extreme seismic events. This is particularly significant at the interface of bridge piers and footings, cap beams, or pile caps due to the large inelastic demand adjacent to the joint region. Past research studies have shown that bond-slip affects both the local and global response of reinforced concrete members (Zhao and Sritharan 2007) and needs to be considered in the detailed analysis of reinforced/precast concrete components.

A nonlinear one-dimensional finite element model was used to investigate the bond-slip of reinforcing bars grouted inside the GSS connectors. This model was developed in OpenSees, based on the general schematic model described in past research studies (Viwathanatepa et al. 1979; Raynor et al. 2002; Steuck et al. 2009). The proposed model was composed of a series of discretized reinforcing bars (using nonlinear truss elements) connected to bond-slip springs (represented by zero-length elements) at each node. Both confined and unconfined regions were included in the model, as shown in Fig.

4.7(a), which presents the schematic of the bond-slip model. The unconfined region represents the grout cone that forms near the two ends of the GSS connector because of localized stresses around the unsupported ends; this would result in an inferior bond between the reinforcing bar and the surrounding grout. Acoustic emission (AE) monitoring was implemented in this research for a series of connector assembly experiments under monotonic tensile loads (Parks 2014). Fig. 4.7(b) shows a connector test assembly with AE sensors mounted near the factory and field ends (definition in Fig. 4.1), along with the grout cones which formed at the two ends. The AE event rate data revealed that formation of the grout cone started at the beginning of bar strain hardening, and was completed at approximately 1.2 times the bar actual yield strength. Bond constitutive laws for the unconfined and confined regions of grout were taken from the experimental results of bars grouted in corrugated steel ducts, as this was the closest condition to GSS connectors (Steuck et al. 2009); such experimental data is not yet available for GSS connectors. Fig. 4.8 shows the result of a tensile test of a GSS connector specimen connecting two 25M (No. 8) bars from Haber et al. (2013), along with the result of the proposed model developed in this study. A discretization study revealed that 50 bond-slip springs for each dowel bar are sufficient to obtain adequate performance; Fig. 4.8 shows that the overall response of the proposed model and the tension experiment are in good agreement.

For the case of reinforcing bars embedded in regular concrete, that is the CIP specimen, a similar model was created with different bond constitutive laws than the bar grouted in a GSS connector. The bond constitutive law for this model was taken from Eligehausen et al. (1983) for confined and unconfined concrete regions. Fig. 4.9 shows

the bond constitutive laws for confined and unconfined regions of the models for bars in the GSS connector assembly and bars embedded in regular concrete.

The depth of the unconfined region of the GSS connector was taken as 11.3 mm (0.445 in.) at the field end and 3.8 mm (0.15 in.) at the factory end of the connector (field and factory dowels are shown in Fig. 4.1); this corresponds to a cone angle of 45˚ and was comparable to observations made during tests on connector assemblies (Parks 2014). The depth of the unconfined region for a bar embedded in regular concrete as in the CIP specimen was assumed to be five times the bar diameter (Eligehausen et al. 1983), that is 127 mm (5.0 in.) for a 25M (No. 8) reinforcing bar.

To implement the results of the proposed one-dimensional bond-slip idealization in the computational model of the half-scale column specimens, a pseudo stress-strain relationship is derived for the reinforcing bar in the plastic hinge region, using the output results of the one-dimensional bond-slip idealization. The pseudo stress is defined as the output force in the outermost bar element divided by the reinforcing bar area, and the pseudo strain is defined as:

$$\varepsilon = \frac{u}{L_p} \tag{4.1}$$

where, u is the total end displacement of the bond-slip model that represents the displacement at the column-footing interface as shown in Fig. 4.10(a); L_p is the plastic hinge length of the half-scale computational model. However, for specimen CIP, u refers to the end displacement of the reinforcing bar embedded in conventional concrete. The fictitious elastic modulus of the resulting pseudo reinforcing bar is smaller than the elastic modulus of the original reinforcing bar without bond-slip. Fig. 4.10(b) shows a schematic stress-strain relationship for the pseudo and original reinforcing bars which

will be assigned to column longitudinal bars inside and outside the plastic hinge, respectively.

The precast subassemblies represent a bond-slip condition that is relatively concentrated at the column-footing interface where the GSS connectors are located. Therefore, the one-dimensional idealization was composed of reinforcing bars grouted inside the connector to obtain the pseudo stress-strain relationship for reinforcing bars within the plastic hinge zone of specimen Precast-1. For specimen Precast-2, the 203-mm (8-in.) debonded bar segment was also included in the one-dimensional idealization. The pseudo stress-strain relationship of specimen CIP was obtained using two separate parts representing a reinforcing bar embedded in the footing and column as described in D'Amoto et al. (2012) for a cast-in-place assembly. Consequently, the outcome of both parts was combined by adding strain values with an equal stress as observed for two systems in series. The resulting fictitious elastic modulus was found to be 119.2 GPa (17,291 ksi), 95.3 GPa (13,821 ksi), and 145.6 GPa (21,111 ksi) for Precast-1, Precast-2 and CIP specimens, respectively, implying that bond-slip was more pronounced for precast subassemblies compared to the CIP specimen; debonding of the footing bars for Precast-2 resulted in a lower fictitious elastic modulus. The resulting fictitious elastic modulus was employed for the reinforcement in the plastic hinge region of the half-scale specimen models. A conventional elastic modulus equal to 200 GPa (29,000 ksi) was used for the reinforcement outside the plastic hinge area.

Low-cycle Fatigue

From the experimental results, two extreme column bars of specimen CIP fractured due to low-cycle fatigue as a result of successive bending and restraightening. A premature reinforcing bar fracture occurred for Precast-1, while debonding of bars in the footing of Precast-2 resulted in a delayed fracture. To account for low-cycle fatigue in the proposed model, the ReinforcingSteel material in OpenSees was assigned to reinforcing bars. This material is capable of predicting low-cycle fatigue life of reinforcing bars, by using the Coffin-Manson (Manson 1965) expression along with a cumulative linear damage rule, as shown in Eq. (4.2) and Eq. (4.3), respectively (Kunnath et al. 2009).

$$\varepsilon^p = C_f(2N_f)^{-\alpha} \tag{4.2}$$

$$D_f = \frac{1}{\sum_{i=1}^{n}(2N_f)_i} \tag{4.3}$$

where, ε^p is plastic strain amplitude, C_f and α are material constants, and $2N_f$ is the number of half-cycles to failure. In this study, C_f and α values of 0.26 and 0.506 were used, respectively, based on the experimental investigation carried out by the ReinforcingSteel material developers (Mazzoni et al. 2007).

Model Layout

The proposed model consists of two nodes joined by one force-based beam-column element with the plastic hinge integration scheme. The schematic layout of the proposed model is shown in Fig. 4.11 for the three specimens. The lateral cyclic displacement, Δ, and axial monotonic load, P, are applied to the top node, as shown. A unique plastic hinge length was obtained for each specimen following the iterative process described previously in Fig. 4.6. For the case of specimen CIP, a plastic hinge

length of 305 mm (12.0 in.) was found to be adequate. This value correlates well with empirical expressions such as those provided by Priestley and Park (1987), or alternatively by Panagiotakos and Fardis (2001) for cyclic loading when reinforcing bar pullout is not present. The proposed model estimated fictitious plastic hinge lengths equal to 203 mm (8.0 in.) and 254 mm (10.0 in.) for Precast-1 and Precast-2, respectively; thus the fictitious plastic hinge length obtained for Precast-1 and Precast-2 was 67% and 83% of the plastic hinge length obtained for CIP, respectively. In this modeling strategy, the performance life of the subassemblies depends on the low-cycle fatigue life of longitudinal steel bars. By reducing the plastic hinge length of precast subassemblies, the plastic strain amplitude was increased and as a result, the number of half-cycles to failure was decreased; hence, premature bar fracture which was observed in the tests was determined for the Precast-1 and Precast-2 computational models.

The octagonal column was approximated by a circular section of equal cross-sectional area, to simplify the sectional discretization process. There were 40 circumferential and 20 radial subdivisions for the confined core concrete, and 40 circumferential and 5 radial subdivisions for the unconfined cover concrete as shown in Fig. 4.11. Fig. 4.12 presents the uniaxial material properties used for the model of specimen Precast-2. Concrete04 material was used for both confined and unconfined concrete with appropriate stress-strain properties, as shown in Fig. 4.12(a). ReinforcingSteel was used to define the uniaxial pseudo stress-strain relationship of the reinforcing bars in the plastic hinge region, and the original uniaxial stress-strain relationship outside the plastic hinge region (Fig. 4.12(b)).

Analysis Results and Comparison

Global Response

The global response of the proposed computational model is investigated using the hysteretic performance of each model developed for the corresponding specimen, namely the lateral force-drift response and energy dissipation capacity. Fig. 4.13 shows the lateral force-drift response for the proposed model along with experimental results up to one drift ratio before termination of the experiments. This corresponds to the drift ratio prior to bar fracture for the precast subassemblies as bar fracture happened during the first cycle of the subsequent drift ratio. For specimen CIP, however, one reinforcing bar fractured at the peak of the second cycle during the 8% drift ratio and another bar fractured during the first cycle of the 9% drift ratio; hence, the global response is presented up to the end of the 8% drift ratio. The proposed model correctly identified the cycle and drift ratio within which bar fracture occurred. For specimen CIP, the model identified the first cycle of the 9% drift ratio for bar fracture, and the first cycle of the 7% and 8% drift ratio for Precast-1 and Precast-2, respectively. The overall lateral force-drift results from the proposed model are in close agreement with the experiments, and the strength and stiffness parameters are satisfactory. The absolute difference between the peak lateral force of the experiment and the model was 6%, 1%, and 5% for CIP, Precast-1, and Precast-2, respectively.

Fig. 4.14 shows the hysteretic energy predicted by the proposed model in addition to that of the corresponding experiment, for each drift ratio. The hysteretic energy of the proposed model is slightly larger than the hysteretic energy from the experiments but within an acceptable range. There is only a 12.6%, 3.9%, 7.9% difference between the

experimental energy dissipation capacity and that of the computational model at 6% drift ratio, for CIP, Precast-1, and Precast-2, respectively. This difference may be attributed to inaccuracy of the proposed modeling strategy in simulating the reloading stiffness degradation.

Local Response

To investigate the accuracy of the proposed model for local response, curvature was selected as the acceptance criterion. The lowermost pair of LVDTs extending from the top of the footing to an elevation of 152 mm (6 in.) above the column-footing interface was used to obtain the end curvature from the experiments. The end curvature includes both the column base curvature and the effect of column end rotation due to bond-slip. This was found to be the most consistent experimental quantity to be compared with the curvature values obtained from the lowermost section of the proposed model as it represents the strain demand on the reinforcing bars near the column-footing interface.

The moment-end curvature envelope for the push direction of each specimen is presented in Fig. 4.15, up to the end of the 6% drift ratio, when LVDTs were removed from the specimens due to the limited stroke length. The end curvature values are normalized by multiplying the average curvature values by the column dimension of 533 mm (21 in.) The corresponding computational results suggest that the proposed model is capable of replicating local as well as global response. At 6% drift ratio, there is an 11.1%, 4.1%, and 10.8% difference between the peak curvature capacity obtained from the experiments and that of the proposed models for CIP, Precast-1, and Precast-2, respectively. The softening effect of the bond-slip which was incorporated by using a

pseudo stress-strain relationship in the plastic hinge region of the model, is included in Fig. 4.15 by presenting the moment-end curvature envelopes when bond-slip was not present in the analysis. The effective flexural stiffness (EI_{eff}) of the response including bond-slip was reduced by 20.0%, 31.6%, and 40.3% for CIP, Precast-1, and Precast-2, respectively, indicating a closer performance compared to the pertinent experimental results. The bond-slip effects were more pronounced for the precast subassemblies, especially Precast-2 with the elongation due to debonded reinforcing bars. Fig. 4.15 also shows photos of the specimens when the column top was at peak displacement during the 6% drift ratio corresponding to the curvature capacity of the critical sections for each specimen.

Conclusions

Experimental evaluation of column-to-footing tests conducted in this research provided qualitative and quantitative measures to evaluate precast and cast-in-place specimens under quasi-static cyclic loads. Key experimental findings and observations include the following:

(1) The control specimen, CIP, had a good hysteretic response with ductile performance. Extreme column bars fractured during the 8% and 9% drift ratio for specimen CIP because of low-cycle fatigue.

(2) Both precast concrete specimens had ductile performance comparable to the performance of specimen CIP, up to the failure point that was caused by premature reinforcing bar fracture because of strain concentration in the dowel bars near the column-footing interface.

(3) Specimen Precast-1, with grouted splice sleeve connectors inside the footing, had a stable performance up to a 7% drift ratio, when a reinforcing bar fractured.

(4) Specimen Precast-2, with grouted splice sleeve connectors in the plastic hinge region of the column and debonded bars in the footing, had a longer performance life up to an 8% drift ratio, when a reinforcing bar fractured.

A two-dimensional computational model was developed for seismic analysis of flexural bridge columns connected with grouted splice sleeve connectors. The modeling strategy is based on transformation of the model for the precast column with grouted splice sleeve connectors, to an idealized equivalent cast-in-place column with a fictitious plastic hinge length that is capable of simulating both the global and local response. A summary of findings for the computational study is offered:

(1) A force-based beam-column element type with plastic hinge integration scheme was used in an iterative procedure to determine the unique fictitious plastic hinge length of the equivalent cast-in-place columns and reproduce the experimental results. The plastic hinge integration scheme was implemented to avoid nonobjective response, and simulate premature reinforcing bar fracture, which had occurred in the tests of the precast subassemblies.

(2) The proposed model includes bond-slip of reinforcing bars in addition to low-cycle fatigue, and was successful in replicating both the global and local response.

(3) To account for bond-slip effects, a pseudo stress-strain relationship was obtained from the results of a one-dimensional model. The computed uniaxial pseudo stress-strain was subsequently incorporated into the column model over the plastic hinge region of each specimen and resulted in a closer agreement between the computational

model and the experiments.

(4) Low-cycle fatigue fracture of the reinforcing bars was determined for each model by incorporating a reinforcement material capable of tracking the cumulative plastic strain for the reinforcing bars.

(5) The plastic hinge length of the validated computational model for specimen CIP was in good agreement with available empirical relationships, while a fictitious plastic hinge length equal to 4/6 and 5/6 times the CIP specimen plastic hinge length was obtained for the idealized equivalent model of specimens Precast-1 and Precast-2, respectively.

(6) The implementation of a plastic hinge modeling strategy offers a simplified approach to seismic design and analysis of flexural precast concrete columns with grouted splice sleeve connectors.

Acknowledgements

The authors would like to acknowledge the financial support of the Utah, New York State, and Texas Departments of Transportation, the Mountain-Plains Consortium, and the Graduate School of the University of Utah. The authors wish to thank Dr. Lawrence D. Reaveley, Professor Emeritus at the University of Utah, for his invaluable input throughout the project. Special thanks are extended to Joel Parks, Dylan Brown, and Mark Bryant for their untiring efforts and support during the experiments. The authors are also grateful for the donation of materials by Splice Sleeve North America, and the assistance of Hanson Structural Precast (Forterra).

Notation

The following symbols are used in this paper:

$2N_f$ = number of half-cycles to failure

C_f = low-cycle fatigue material constant

D_f = fatigue damage

EI_{eff} = effective flexural stiffness

f'_c = compressive strength of concrete

f'_g = compressive strength of high-strength grout

L_p = length of plastic hinge

N_p = number of integration points

P = axial monotonic load

u = end displacement of one-dimensional connector model

α = low-cycle fatigue material constant

Δ = lateral cyclic displacement

ε = pseudo strain

ε^p = plastic strain amplitude

τ = bond stress

References

AASHTO. (2012). AASHTO LRFD *bridge design specification*, Washington, DC.

AASHTO. (2011). AASHTO *guide specifications for LRFD seismic bridge design*, Washington, DC.

American Concrete Institute (ACI). (2013). "Guide for testing reinforced concrete structural elements under slowly applied simulated seismic loads." *ACI 374*, Farmington Hills, MI.

ASTM. (2009a). "Standard specification for low-alloy steel deformed and plain bars for concrete reinforcement." *A706/A706M – 09*, West Conshohocken, PA.

Caltrans. (2010). *Seismic design criteria (SDC), version 1.6*, Sacramento, CA.

D'Amato, M., Braga, F., Gigliotti, R., Kunnath, S., and Laterza, M. (2012). "Validation of a modified steel bar model incorporating bond-slip for seismic assessment of concrete structures." *J. Struct. Eng.*, 10.1061/(ASCE)ST.1943-541X.0000588, 1351–1360.

Eligehausen, R., Popov, E. P., and Bertero, V. V. (1983). "Local bond stress-slip relationships of deformed bars under generalized excitations." *Report No. UCB/EERC-83/23*, Earthquake Engineering Research Center, Univ. of California, Berkeley, CA.

Haber, Z. B., Saiidi, M. S., and Sanders, D. H. (2014). "Seismic performance of precast columns with mechanically spliced column-footing connections." *ACI Struct. J.*, 111(3), 639–650.

Haber, Z. B., Saiidi, M. S., and Sanders, D. H. (2015). "Behavior and simplified modeling of mechanical reinforcing bar splices." *ACI Struct. J.*, 112(2), 179–188.

Haber, Z. B., Saiidi, M. S., and Sanders, D. H. (2013). "Precast column-footing connections for accelerated bridge construction in seismic zones." *Rep. No. CCEER 13-08*, Center for Civil Engineering Earthquake Research, Dept. of Civil and Environmental Engineering, Univ. of Nevada, Reno, NV.

Khaleghi, B., Schultz, E., Seguirant, S., Marsh, M. L., Haraldsson, O. S., Eberhard, M. O., and Stanton, J. F. (2012). "Accelerated bridge construction in Washington State: From research to practice." *PCI J.*, 57(4), 34–49.

Kunnath, S., Heo, Y., and Mohle, J. (2009). "Nonlinear uniaxial material model for reinforcing steel bars." *J. Struct. Eng.*, 10.1061/(ASCE)0733-9445(2009)135:4(335), 335–343.

Manson, S. S. (1965). "Fatigue: a complex subject—some simple approximations." *Exp. Mech.*, 5(7), 193–226.

Mazzoni, S., McKenna, F., Scott, M. H., Fenves, G. L., et al. (2007). "OpenSees command language manual." Printed on 1 July, 2007.

McKenna, F., Fenves, G., and Scott, M. (2000) "Open system for earthquake engineering simulation (OpenSees)." *Univ. of California, Berkeley, CA. (http://opensees.berkeley.edu).*

McKenna, F., Scott, M., and Fenves, G. (2010). "Nonlinear finite-element analysis software architecture using object composition." *J. Comput. Civ. Eng.*, 10.1061/(ASCE)CP.1943-5487.0000002, 95–107.

Panagiotakos, T. B., and Fardis, M. N. (2001). "Deformations of reinforced concrete members at yielding and ultimate." *ACI Struct. J.*, 98(2), 135–148.

Pantelides, C.P., Ameli, M. J., Parks, J.E., and Brown, D.N. (2014). "Seismic evaluation of grouted splice sleeve connections for precast RC bridge piers in ABC." *Rep. No. UT-14.09*, Utah Department of Transportation Research Division, SLC, UT.

Park, R. (1989). "Evaluation of ductility of structures and structural assemblages from laboratory testing" *Bulletin of the New Zealand National Society for Earthquake Engineering*, 22(3), 155–166.

Parks, J. E. (2014). "Seismic rehabilitation of column to pier cap accelerated bridge construction connections and acoustic emission monitoring assessment." MS Thesis, Univ. of Utah, Salt Lake City, UT.

Priestley, M. J. N., and Park, R. (1987). "Strength and ductility of concrete bridge columns under seismic loading." *ACI Struct. J.*, 84(1), 61–76.

Raynor, D. J., Lehman, D. E., and Stanton, J. F. (2002). "Bond-slip response of reinforcing bars grouted in ducts." *ACI Struct. J.*, 99(5), 568–576.

Scott, M. and Fenves, G. (2006). "Plastic hinge integration methods for force-based beam–column elements." *J. Struct. Eng.*, 10.1061/(ASCE)0733-9445(2006)132:2(244), 244–252.

Sideris, P. (2012). "Seismic analysis and design of precast concrete segmental bridges." PhD Dissertation, Univ. at Buffalo, The State Univ. of New York, Buffalo, NY.

Steuck, K. P., Eberhard, M. O., and Stanton, J. F. (2009). "Anchorage of large-diameter reinforcing bars in ducts." *ACI Struct. J.*, 106(4), 506–513.

Tazarv, M., and Saiidi, M. S. (2014). "Next generation of bridge columns for accelerated bridge construction in high seismic zones." *Rep. No. CCEER 14-06*, Center for Civil Engineering Earthquake Research, Dept. of Civil and Environmental Engineering, Univ. of Nevada, Reno, NV.

Viwathanatepa, S., Popov, E. P., and Bertero, V. V. (1979). "Effects of generalized loadings on bond of reinforcing bars embedded in confined concrete blocks." *Rep. No. UCB/EERC-79/22*, Univ. of California, Berkeley, CA.

Zhao, J., and Sritharan, S. (2007). "Modeling of strain penetration effects in fiber-based analysis of reinforced concrete structures." *ACI Struct. J.*, 104(2), 133–141.

Table 4.1. Test matrix.

No.	Specimen	Connector Location	Details
1	CIP	--	Cast-in-place
2	Precast-1	Footing	Precast
3	Precast-2	Column	Precast with debonding of bars in footing

Table 4.2. Test-day compressive strength of concrete and high-strength grout

Specimen	Concrete		High-Strength Grout	
	(ksi)	(MPa)	(ksi)	(MPa)
CIP	6.7	46	NA	NA
Precast-1	5.5	38	13.5	93
Precast-2	8.4	58	14.6	101

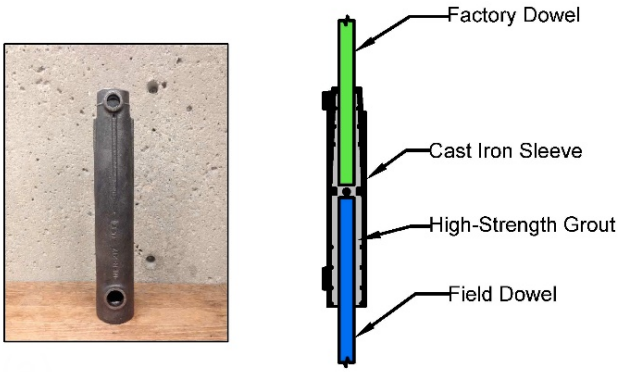

Fig. 4.1. Grouted splice sleeve (GSS) connector.

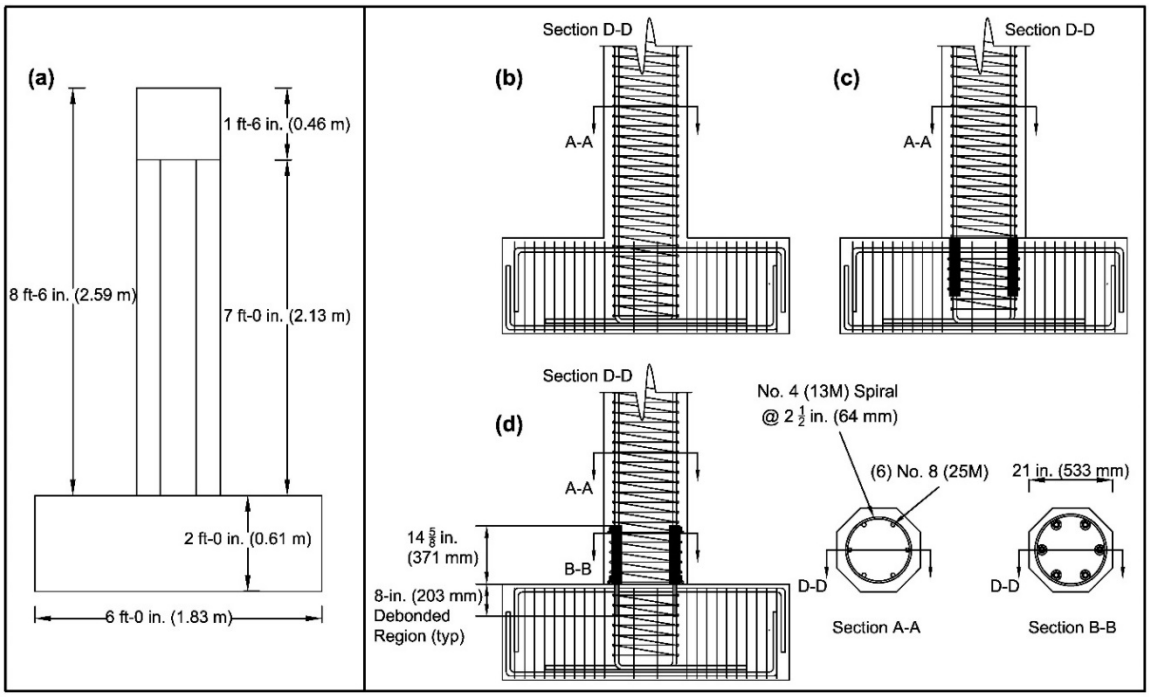

Fig. 4.2. Details of specimens: (a) Subassembly dimensions, (b) CIP, (c) Precast-1, and (d) Precast-2.

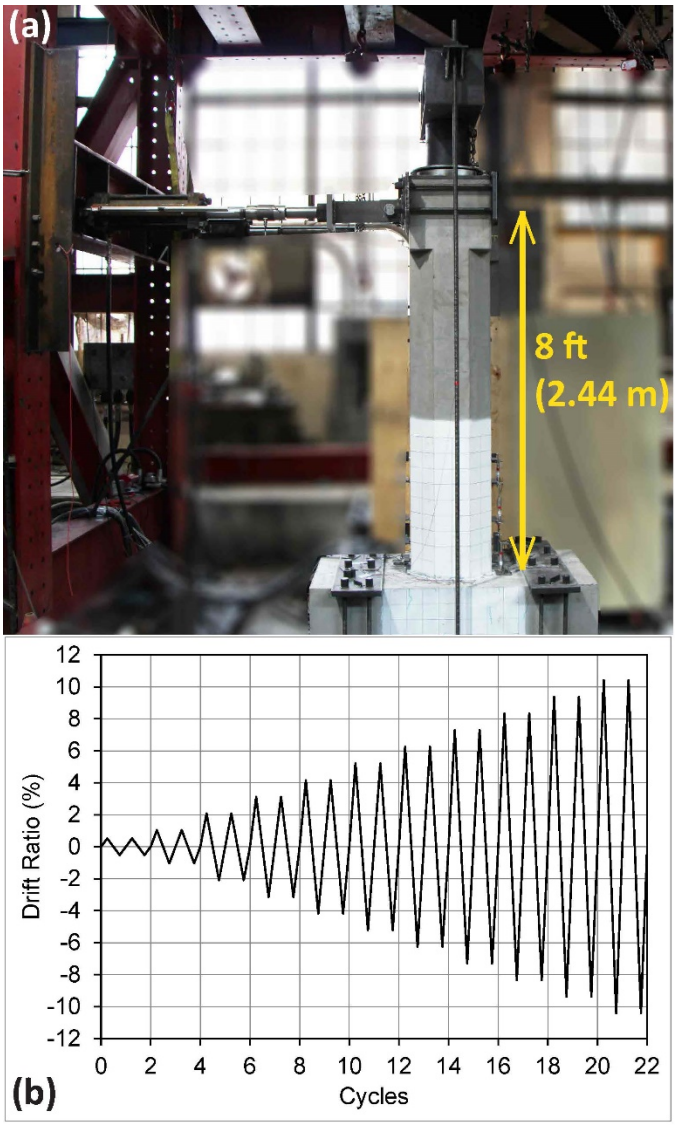

Fig. 4.3. Experimental setup: (a) Test configuration, and (b) Drift ratio history.

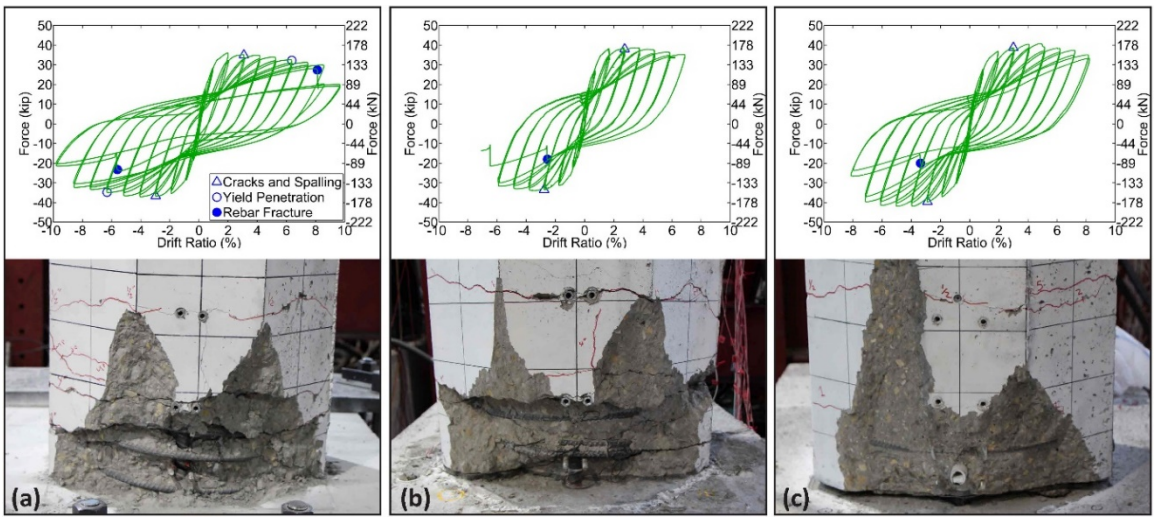

Fig. 4.4. Hysteretic response and damaged zone of specimens: (a) CIP, (b) Precast-1, and (c) Precast-2.

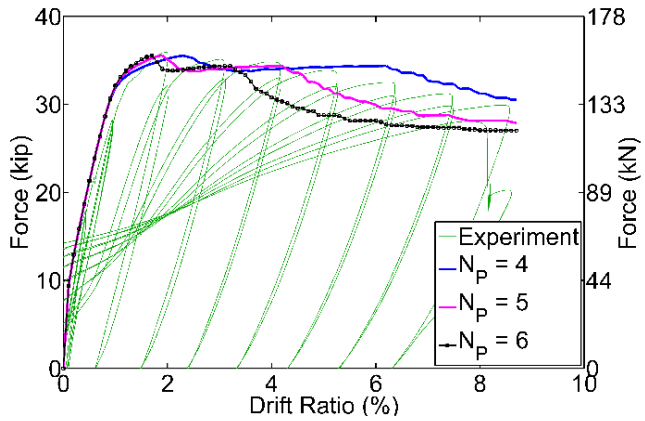

Fig. 4.5. Nonobjective pushover response (N_p: number of integration points).

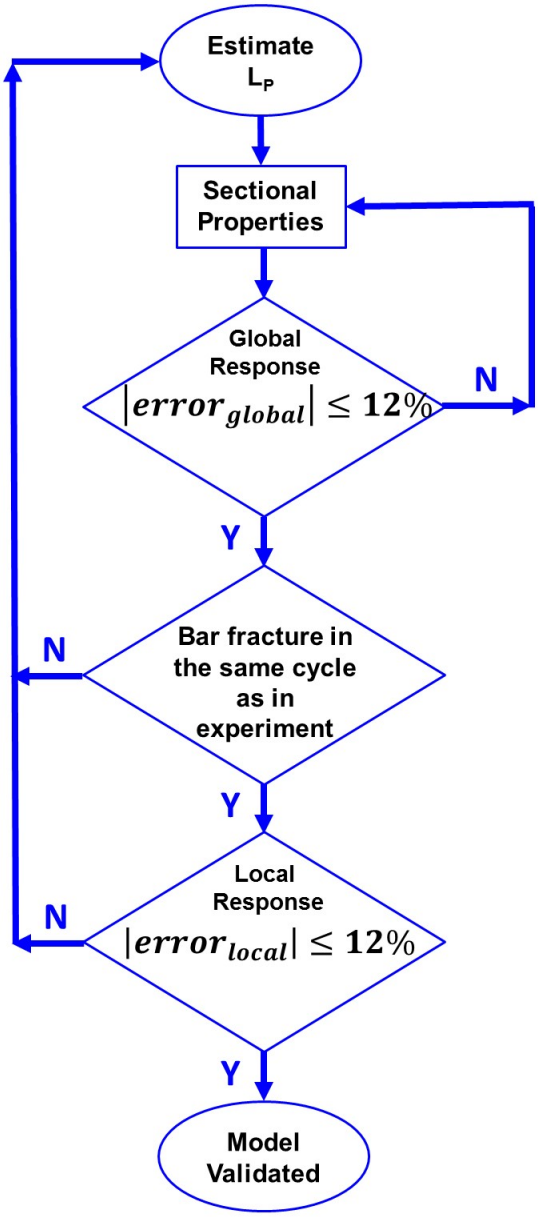

Fig. 4.6. Validation process.

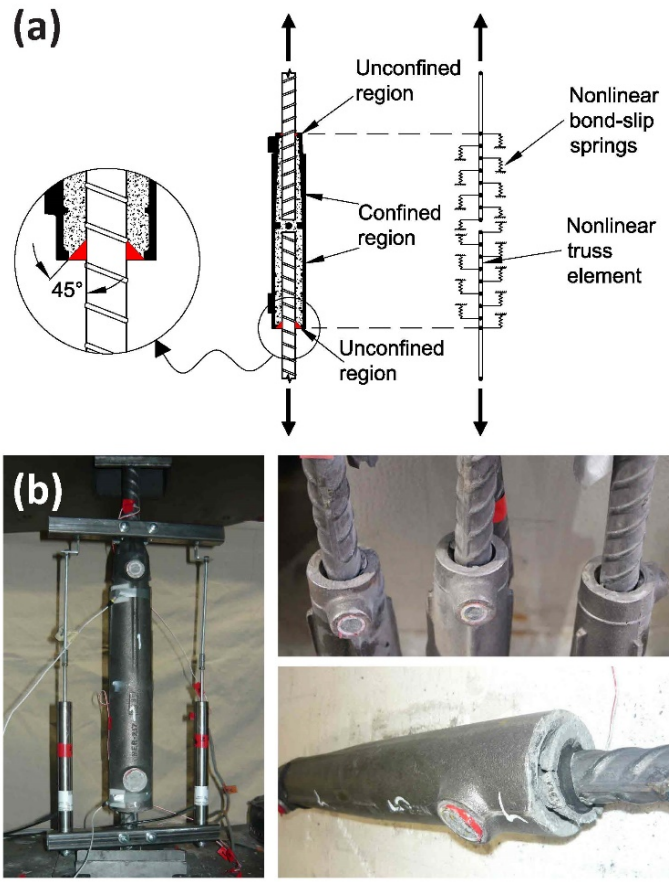

Fig. 4.7. Nonlinear bond-slip idealization: (a) Schematic of proposed bond-slip model, and (b) Connector test assembly with AE sensors and grout cone formation.

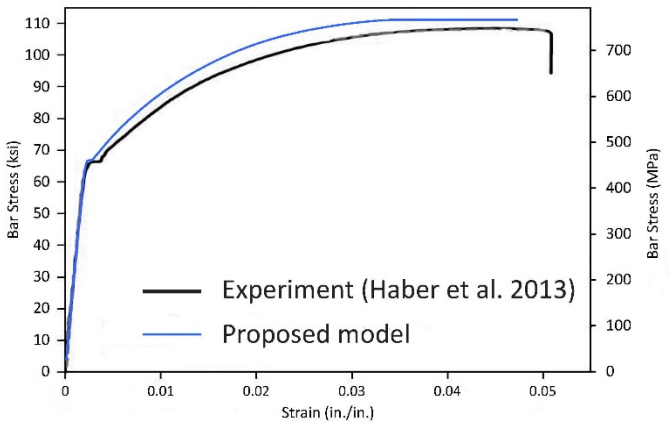

Fig. 4.8. Validation of proposed model for GSS connector in tension (experimental data from Haber et al. 2013).

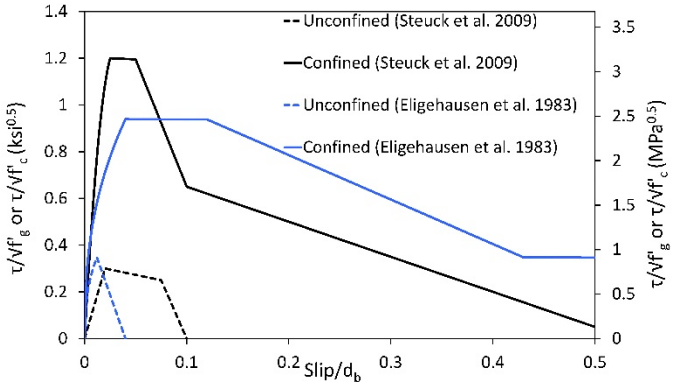

Fig. 4.9. Bond constitutive laws used for bars embedded in GSS connectors and regular concrete.

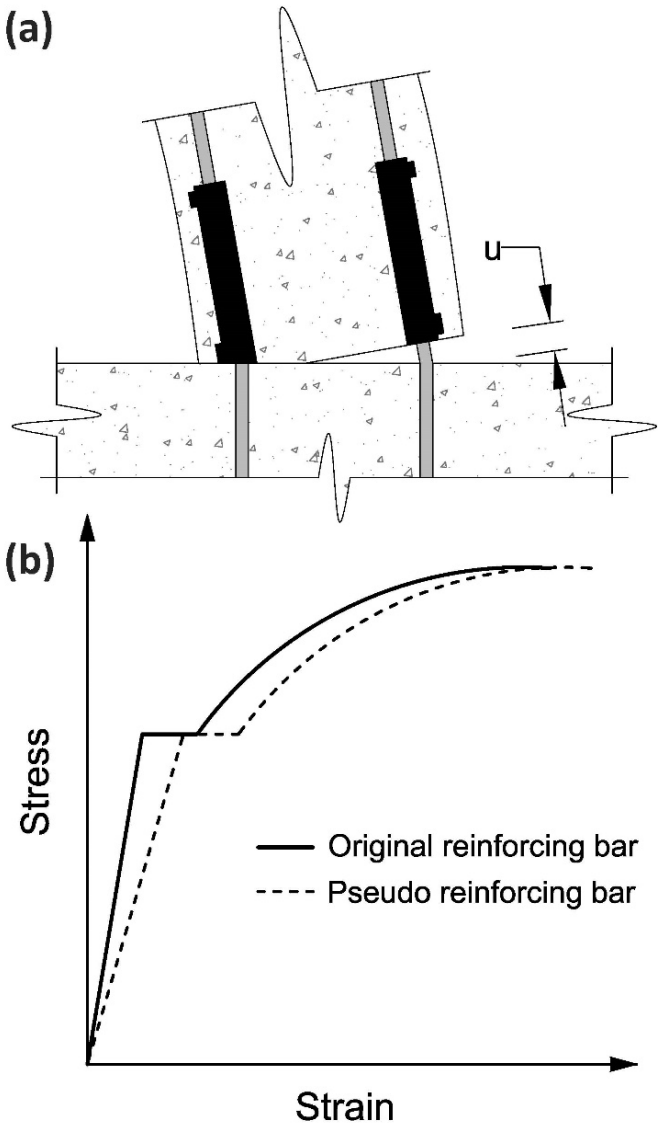

Fig. 4.10. End displacement representation: (a) GSS connector end displacement, and (b) Schematic of pseudo stress-strain relationship.

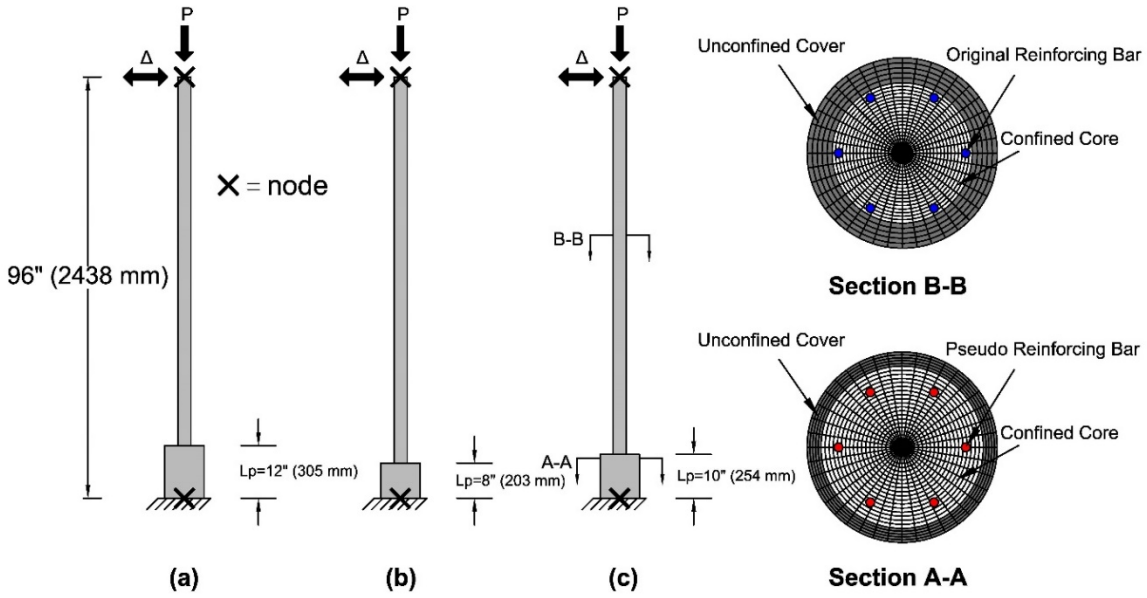

Fig. 4.11. Schematic layout of proposed model: (a) CIP, (b) Precast-1, and (c) Precast-2.

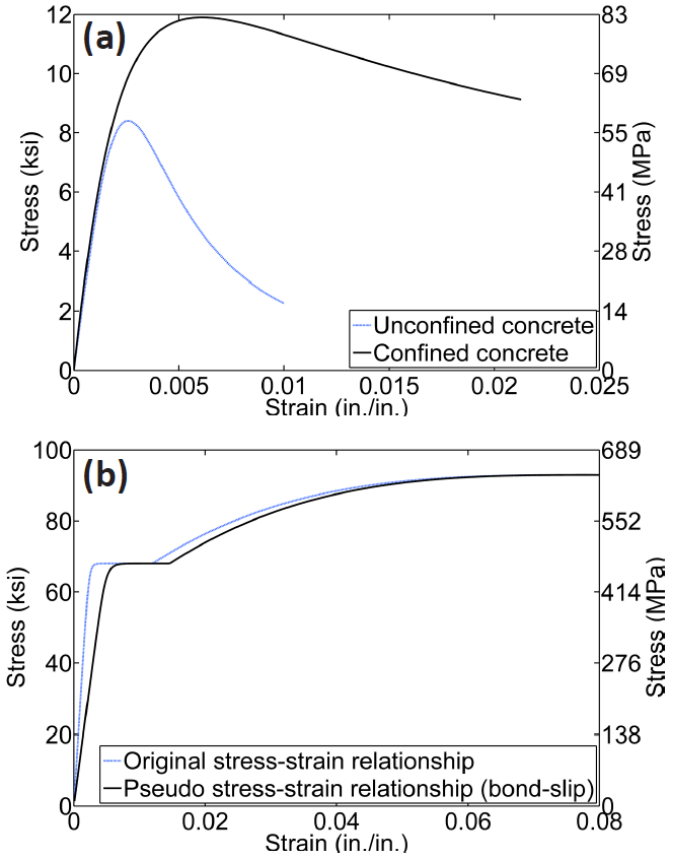

Fig. 4.12. Uniaxial material properties for Precast-2: (a) Concrete, and (b) Reinforcing. Bar.

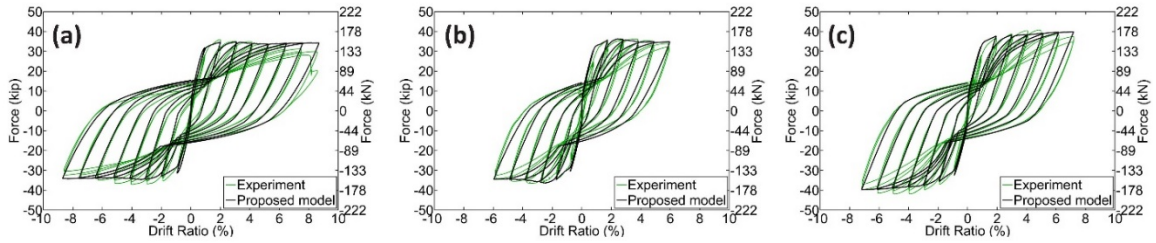

Fig. 4.13. Comparison of global response, in terms of hysteretic performance: (a) CIP, (b) Precast-1, (b) Precast-2.

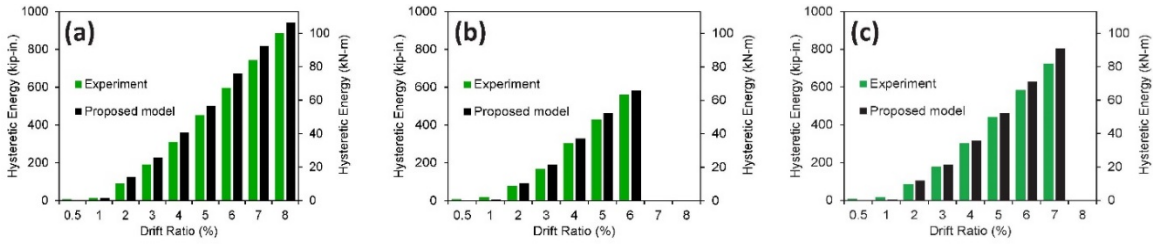

Fig. 4.14. Comparison of global response, in terms of energy dissipation: (a) CIP, (b) Precast-1, (b) Precast-2.

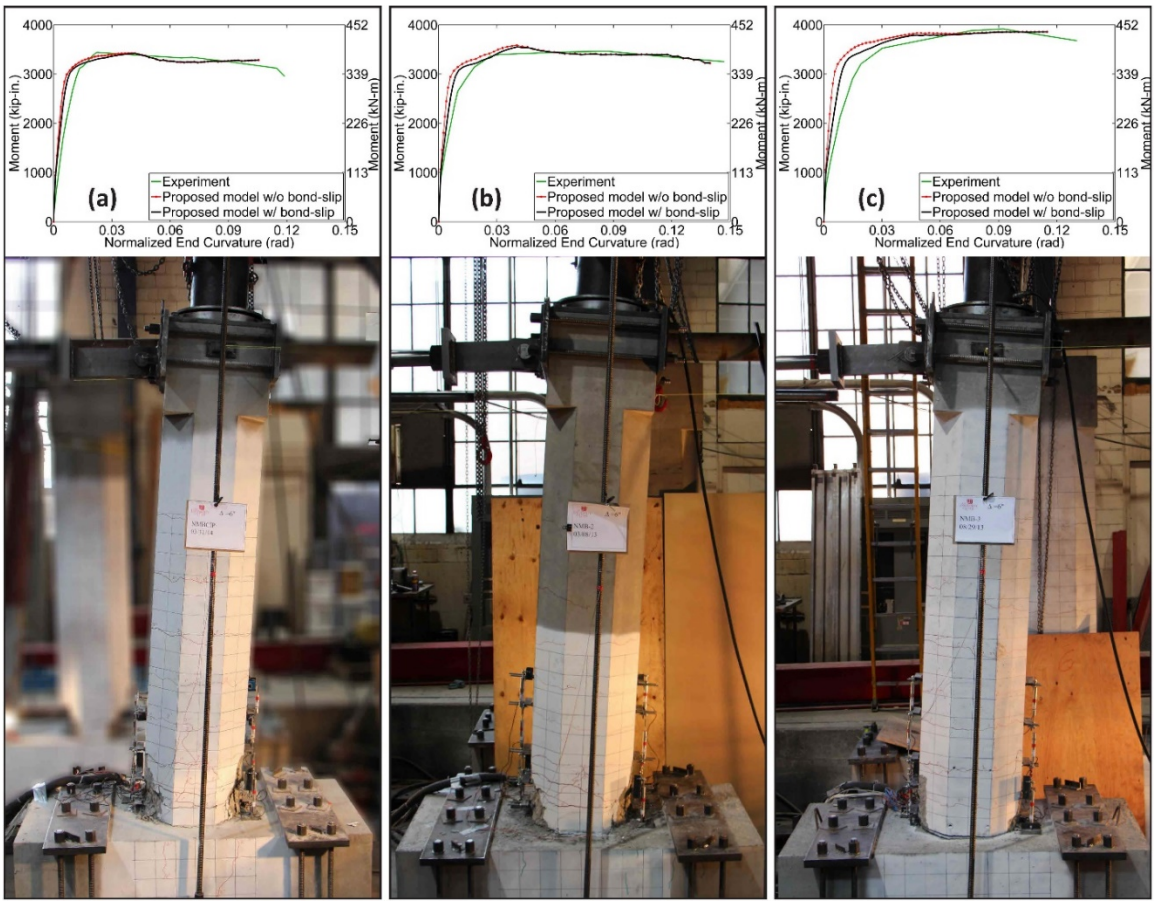

Fig. 4.15. Comparison of local response, in terms of moment-end curvature up to 6% drift ratio: (a) CIP, (b) Precast-1, (b) Precast-2.

CHAPTER 5

PARAMETRIC STUDY

Introduction

The proposed modeling strategy, which was validated in Chapter 4 using a series of half-scale experiments, may be applied to actual-size columns with similar configurations and under comparable loading conditions. This application requires a comprehensive study on the response sensitivity of the model to potential changes in pertinent modeling parameters. For a conventional medium-size bridge bent system with modern seismic detailing, the most important column parameters include longitudinal reinforcing bar ratio, column aspect ratio, axial load, and design displacement ductility. Therefore, a parametric study was developed by considering two different values associated with each of the aforementioned four parameters, using a 3-ft circular column reinforced with No. 9 longitudinal bars. Two levels of longitudinal reinforcing bar ratio were selected considering practical aspects of the design, that is, 1.38% and 1.96% corresponding to 14 No. 9 and 20 No. 9 bars, respectively. Two column aspect ratios equal to 4.0 and 5.0 were included indicating a column height of 12 ft and 15 ft, respectively. Two axial load levels were employed with an axial load index (ALI) equal to 5% and 10%; and lastly, design displacement ductility values equal to 7.0 and 11.0 were considered to study different transverse reinforcement alternatives.

The parametric study was carried out for columns with details similar to CIP, i.e., monolithic construction with no grouted splice sleeve (GSS) connectors, and alternatively for columns with details similar to Precast-2 which had GSS connectors in the column and debonding of footing bars for a length of 8.0 times the bar the diameter.

Design and Details of the Column Models

Sixteen CIP column models in addition to sixteen Precast-2 column models were studied to investigate the response of the proposed modeling strategy to varying parameters. The columns were assumed to represent bridge piers from a single-column bent implying a cantilever configuration. Fig. 5.1 shows a schematic of the two alternatives. The footing is assumed to be a 7-ft long x 7-ft wide x 3-ft deep capacity protected member with adequate reinforcement to resist the load effects transferred from the column.

Design Procedure

Table 5.1 shows the 32 modeling cases considered for this study and highlights the major differences between each alternative. The alternatives were grouped in pairs with exactly identical details for the models representing CIP and Precast-2 type columns as discussed in Chapter 4. The transverse reinforcement which was composed of closed circular single or double hoops was designed for a required level of confinement. This is the critical variable for the design displacement ductility values equal to 7.0 and 11.0; shear reinforcement would not govern the design for such slender and ductile columns.

A series of sectional analyses were carried out to determine the size and number

of hoops required to achieve a certain level of displacement ductility. Eq. (5.1) relates displacement ductility capacity (μ_D) of a cantilever column to curvature ductility (μ_φ) of the corresponding section, length of the plastic hinge (L_p), and height of the column (H) (Priestley et al. 1996).

$$\mu_D = 1 + 3(\mu_\varphi - 1)\frac{L_p}{H}(1 - 0.5\frac{L_p}{H}) \tag{5.1}$$

By rearranging Eq. (5.1) we can define the curvature ductility as a function of the given displacement ductility, as shown in Eq. (5.2):

$$\mu_\varphi = \frac{\mu_D - 1 + 3\frac{L_p}{H}(1 - 0.5\frac{L_p}{H})}{3\frac{L_p}{H}(1 - 0.5\frac{L_p}{H})} \tag{5.2}$$

According to AASHTO Guide Specifications (2011) and Caltrans Seismic Design Criteria (2010), the plastic hinge length is to be obtained from Priestley et al. (1996); however, it was noted in the previous chapter that the plastic hinge length relationship by Panagiotakos and Fardis (2001) has a better agreement with the experiments conducted in this research. The reason lies in the fact that actual displacement capacity of the tested CIP column was smaller than the predicted value using the plastic hinge length relationship of Priestley et al. (1996), because a different failure mode of low-cycle fatigue bar fracture occurred before the more typical hoop fracture (or core concrete crushing). From Panagiotakos and Fardis (2001), the plastic hinge length is given as:

$$L_p = 0.12H + 0.095a_{sl}d_b f_y \tag{5.3}$$

where, a_{sl} is equal to 0.0 if bar pullout is not present and is equal to 1.0 if pullout is present, d_b is the diameter of the column longitudinal bar (in.), and f_y is the bar yield strength in ksi.

Parameter a_{sl} was assumed to be zero for validation of the modeling strategy in

the previous chapter as pullout of column bar with GGSS connectors was not present during the column-to-footing experiments; hence, it was assumed that a_{sl} was zero for the models used in this chapter as well, knowing that modern seismic design procedures would prevent anchorage issues and pullout failure. As a result, Eq. (2) can be simplified further and be presented as a function of the required displacement ductility capacity, as shown in Eq. (4).

$$\mu_{\varphi} = 2.96\mu_D - 1.96 \tag{4}$$

When the required curvature ductility is known, a moment-curvature analysis is carried out using a trial transverse reinforcement scheme. Subsequently, an idealized moment-curvature curve is constructed to obtain the curvature ductility for the assumed column section. The idealized moment-curvature curve consists of: (1) an initial sloped line that intersects the actual curve at a point where the extreme reinforcing bar yields; (2) a horizontal line connecting the effective yield point and the ultimate point of the section. The ultimate point on the curve corresponds to onset of confined core crushing; the effective yield point is found by balancing the areas under the actual and idealized curves.

If the obtained curvature ductility is equal to or larger than the required value the design is accepted, otherwise more trials are needed.

Material Properties

An expected concrete compressive strength (f'_{ce}) equal to 6.0 ksi was used for the unconfined concrete along with an ultimate unconfined strain (ε_{cu}) of 0.005 in./in. The properties for confined concrete were found using Mander's model (Mander et al.

1988) for each case. Concrete04 from the OpenSees material library was used for both unconfined concrete cover and confined concrete core.

ReinforcingSteel from the OpenSees material library was assigned to the column reinforcing bars. Table 5.2 includes the stress properties for the Grade 60 ASTM A706 No. 9 reinforcing bars used in this study. These properties conform to the AASHTO Guide Specifications (2011).

Plastic Hinge Length for Models with Precast-2 Detailing

Based on the findings of Chapter 4, the reduced displacement capacity of precast specimens was simulated by incorporating a reduced plastic hinge length. In the absence of empirical relationships for precast columns with GSS connectors the reduction factor previously found for specimen Precast-2 was applied to the precast alternatives for the parametric study, as shown in Eq. (5.5).

$$L_{p,GSS} = \gamma_{GSS} L_P \tag{5.5}$$

where, $L_{p,GSS}$ is the reduced plastic hinge length of a precast column with GSS connectors in the column end and debonding of footing dowels for a length 8.0 times the bar diameter, and γ_{GSS} is a reduction factor for columns with such details; this was found to be equal to 5/6 according to the results from the computational study in Chapter 4.

Pseudo Stress-strain Relationship for Reinforcing Bars

The one-dimensional bond-slip idealization developed in Chapter 4 was used to obtain the pseudo stress-strain relationship for reinforcing bars inside the plastic hinge region, and includes softening effects from bond-slip, as shown in Fig. 5.2. For this, the

end displacement of a No. 9 bar embedded in conventional concrete was obtained for each modeling alternative with a different column height, then divided by the corresponding plastic hinge length to find the pseudo strains.

The bond-slip idealization for the models of precast columns was composed of a No. 9 factory dowel and a No. 9 field dowel grouted inside a No. 9 GSS, in addition to the debonded bar segment which was an extension of the field dowel, as shown in Fig. 5.3. The grout strength was assumed as 14.6 ksi. Confined and unconfined bond constitutive laws were used as described in Chapter 4; the unconfined properties were employed over unconfined areas near the two openings, referred to as the cone depth. The cone depth was obtained assuming a cone angle of 45° which resulted in 0.441 in. and 0.146 in. for the field and factory dowel, respectively. The total embedded length was taken as 7.88 in. and 7. 56 in. for the field and factory dowel, respectively. The resulting pseudo elastic modulus obtained for each model is presented in the following sections.

Details of Model Alternatives

Fig. 5.4 shows the moment-curvature plots for the final design of CIP columns including the idealized bilinear curves to obtain the curvature ductility capacity of the sections. The design details of the precast alternatives remained identical to the associated CIP to assess their performance comparatively. The final details for the column model alternatives that share the same height and number of main bars are presented in the same figure. Fig. 5.5 includes details for column models with a height equal to 12 ft and reinforced with 14 No. 9 longitudinal bars. The plastic hinge length for CIP and precast models was found to be 17.28 in. and 14.40 in. according to Eqs. (5.3)

and (5.5), respectively. The pseudo elastic modulus, which was obtained using the results of the bond-slip idealization, was found to be 24,159 ksi and 17,596 ksi for the CIP and precast models, respectively. The pseudo elastic moduli were used for the reinforcing bars in the plastic hinge region of the column models, whereas a nominal elastic modulus of 29,000 ksi was assigned to the reinforcing bars outside the plastic hinge region.

Fig. 5.6 shows the details for the 15-ft high column models reinforced with 14 No. 9 longitudinal bars. The plastic hinge length for these CIP and precast models was found to be 21.60 in. and 18.00 in., respectively. The pseudo elastic modulus for reinforcing bars inside the plastic hinge was found to be 27,483 ksi and 21,980 ksi, respectively.

The details for the 12-ft high column models reinforced with 20 No. 9 longitudinal bars are shown in Fig. 5.7. The plastic hinge lengths and therefore the pseudo elastic moduli are identical to the 12-ft high columns with 14 No. 9 bars.

Fig. 5.8 shows the details for column models with a height equal to 15 ft and reinforced with 20 No. 9 longitudinal bars. The plastic hinge lengths and therefore the pseudo elastic moduli are identical to the 15-ft high columns with 14 No. 9 bars. Table 5.3 summarizes the design details for all column models including the required and provided curvature ductility capacity along with the provided transverse hoops. It is noted that double hoops were essential to achieve a target displacement ductility demand of 11.0. The provided curvature ductility was slightly smaller than the required value for four column models as shown in Table 5.3; this slight difference was found to have insignificant effect on the response of the columns. The spacing of the closed hoops conformed to the AASHTO Guide Specifications (2011), which require the maximum

allowable spacing to be the smallest of: (a) 20% of the column diameter, i. e., 7.20 in., (b) six times the longitudinal bar diameter or 6.77 in., and (c) 6.00 in., which controls the spacing for the specific columns used in this chapter.

Model Layout

The layout for the cantilever column models is composed of two end nodes connected by a nonlinear beam-column element with a plastic hinge integration scheme. Fig. 5.9 shows the overall layout for the proposed model. The axial load was applied to the top node before the static cyclic displacement was applied using a similar displacement history to the experiments composed of two cycles per drift ratio with an increasing amplitude. The orientation of the model indicates that the analysis is carried out in the transverse direction of the bridge with columns in a single-curvature configuration. A shorter plastic hinge length was used for the precast model compared to the CIP model, as discussed in previous sections. The column sectional arrangements are shown in Fig. 5.9; the details are different for regions inside and outside the plastic hinge length. Fig. 5.10 shows cyclic envelopes for the uniaxial materials assigned to each fiber. Mander's model (Mander et al. 1988) was used to obtain the properties for the confined core. Concrete04 material was used for both confined and unconfined concrete. ReinforcingSteel material was assigned to steel fibers inside and outside the plastic hinge region; however, as discussed, a pseudo stress-strain behavior was used inside the plastic hinge region to account for the softening effects of bond-slip. ReinforcingSteel with conventional steel properties (Table 5.2) was incorporated for the column longitudinal bars outside the plastic hinge region.

Analysis Results

Analysis Termination Criteria and Mode of Failure

The analysis termination criteria, which represent the failure point for each column model, were set to be either the crushing of the extreme core concrete fiber or fracture of column longitudinal bars as a result of low-cycle fatigue. In the case of low-cycle fatigue, ultimate displacement was taken as the peak displacement of the cycle prior to low-cycle fatigue fracture of column bars. For example, considering column model 1 and column model 2, Fig. 5.11 shows the hysteresis response of the two alternatives; bar fracture due to low-cycle fatigue is also identified for both models. Fig. 5.11(a) indicates that for column model 1, two column bars fractured during the first cycle of the 7% drift ratio while four column bars fractured during the second cycle of the 7% drift ratio. On the other hand, Fig. 5.11 (b) shows that two column bars fractured during the second cycle of the 6% drift ratio, for column model 2. This implies that the precast model had a premature bar fracture due to the simulated localized demand which was introduced by shortening the plastic hinge length; furthermore, the failure mode was found to be low-cycle fatigue fracture of column bars, as the strain history for the core concrete suggests that crushing strain was not exceeded prior to bar fracture. Therefore, the ultimate drift was equal to 6% or 8.64 in. of displacement for both columns.

Considering column models 5 and 6 with identical details to column models 1 and 2 except a larger axial load equal to 610.7 kip (compared to the original value of 305.4 kip), crushing of the core occurred before reinforcing bar fractured for column model 6. Fig. 5.12(a) shows that the core concrete crushed barely after the fracture of the east column reinforcing bar for column model 5. Hence the failure mode was bar fracture due

to low-cycle fatigue. Column model 6 failed due to crushing of the core concrete near the peak displacement of the first cycle during the 6% drift ratio. The ultimate displacement for column model 6 was found to be equal to 7.65 in., corresponding to 5.3% drift ratio, while it was 8.64 in. (or 6.0% drift ratio) for column model 5.

Comparison of CIP and Precast-2 Alternatives

The major difference between CIP and Precast-2 alternatives is the length of the plastic hinge. In fact, the integration weight associated with each integration point along the column will change by specifying a new plastic hinge length for the precast model. This will mainly affect the integration point at the column end which, for the particular case of a cantilever column, is the most effective integration point.

A comparison of the model responses is provided in terms of both global and local response. The cyclic envelope of the hysteresis response is presented for models in respective groups along with the variation of strains in an extreme column longitudinal bar. The displacement ductility capacity (μ_C) is then obtained using a similar approach implemented to determine the curvature ductility. The failure mode for each column is discussed in addition to the peak compressive strain in the extreme fiber of the core concrete.

Column Model 1 and 2

The two columns were 12-ft high and were reinforced with 14 No. 9 main bars; under an axial load equal to 305.4 kip, the transverse reinforcement was composed of No. 6 closed circular hoops spaced at 3 in. on center. Fig. 5.13 shows both the global and

local response. The global response represented by the cyclic envelope indicates that there was a minimal difference between the two alternatives; a slightly lower initial elastic slope was achieved for the precast model due to a more pronounced bond-slip. On the other hand, the strain variation in the extreme longitudinal bar implies that a larger demand was introduced to the column end of the precast alternative which resulted in a premature fracture of column bars. As discussed earlier in this section, column bar fracture occurred during the first and second cycle of the 7% drift ratio for CIP, whereas bar fracture occurred during the second cycle of the 6% drift ratio for Precast-2. At the peak displacement during the 7% drift ratio, the compressive strain in the extreme fiber of the core concrete was 0.0171 in./in. and 0.0190 in./in. for CIP and Precast-2, respectively. Compared to the strain at onset of core crushing for these two models (core concrete ultimate strain), $\varepsilon_{cu} = 0.0190$ in./in., it is observed that there was a margin of 9.8% before the core crushed for CIP, while the core compressive strain was equal to the ultimate strain for Precast-2 implying that the compressive strains were 10.8% larger than that of the CIP.

The failure mode of both column models was found to be bar fracture due to low-cycle fatigue. Therefore, the ultimate displacement was associated with the peak displacement of the cycle prior to occurrence of bar fracture. This was found to be 8.64 in. or 6% in terms of drift ratio. The displacement ductility capacity was equal to 6.82 and 6.13 for CIP, and Precast-2, respectively. Fig. 5.14 shows the cyclic envelope along with the idealized curve constructed to obtain the displacement ductility values. Table 5.4 includes the summary of performance for both column models.

Column Model 3 and 4

The columns in this category were 12-ft high, reinforced with 14 No. 9 main bars, and 2 No. 6 closed hoops spaced at 3 in. on center to achieve a large displacement ductility of 11.0. An axial load equal to 305.4 kip was applied to the column top. Fig. 5.15 shows the global and local response comparison between the two columns. Similar to column model 1 and 2, there was no major difference between the global responses, but the local response, represented by strain variations in an extreme column bar, was different; the precast model had a larger local demand which resulted in early fracture of the column bars for column model 4. The failure mode was found to be column bar fracture due to low-cycle fatigue for both columns, similar to column model 1 and 2 in terms of drift ratio and cycle number. At peak displacement during the 7% drift ratio, compressive strain in the extreme fiber of the core concrete was found to be 0.0153 in./in. and 0.0189 in./in. for CIP and Precast-2, respectively. Compared to the strain at onset of core crushing for these two models (core concrete ultimate strain), $\varepsilon_{cu} = 0.0280$ in./in., it is observed that there was a margin of 45.4% (measured at 7% drift ratio) and 32.6% (measured at 6% drift ratio) before the core crushes for CIP and Precast-2, respectively. Comparing the peak strain values for the two columns, there was a 23.3% increase in compressive strain in the extreme fiber of the core concrete for the precast column.

The displacement ductility capacity was equal to 7.11 and 6.09 for CIP, and Precast-2, respectively. Fig. 5.16 shows the cyclic envelope along with the idealized curve constructed to obtain the displacement ductility values. Table 5.5 includes the summary of performance for both column models.

Column Model 5 and 6

Column models 5 and 6 were 12-ft high, reinforced with 14 No. 9 bars longitudinally, and a No. 6 closed hoop with a spacing equal to 2 ¾ in. on center. The axial load for these two columns was increased to 610.7 kip to investigate the axial load effects on the model. Fig. 5.17(a) shows that the precast column failed at a displacement of 7.65 in. unlike CIP which failed at an ultimate displacement equal to 8.64 in. Early failure of the precast alternative is attributed to crushing of the confined concrete core before column bars fractured due to low-cycle fatigue. This was caused by the increased axial load compared to the previous precast column models. On the other hand, the local response of the critical section, represented by the column bar strain variation shown in Fig. 5.17(b), indicates that the bar strain was larger for the precast column model. Considering the compressive strains in the extreme fiber of the concrete core at peak displacement of the column top during the 5% drift ratio, the strain value was 18.6% larger than that of the CIP—0.0189 in./in. versus 0.0159 in./in. for Precast-2 and CIP, respectively.

Displacement ductility capacity equal to 7.27 and 5.62 was obtained using the standard procedure for CIP and Precast-2, respectively. Fig. 5.18 shows the cyclic envelope for the two column models in addition to the respective idealized curves to find the displacement ductility capacity. A summary of performance characteristics is provided in Table 5.6.

Column Model 7 and 8

These columns were 12-ft high with 14 No. 9 longitudinal bars and 2 No. 7 closed hoops spaced at 3 ¼ in. on center. A 10% ALI equal to 610.7 kip axial load was applied to the columns. Fig. 5.19 shows the global and local responses obtained for the two columns. The global performance represented by the cyclic envelope was comparable while the local response differed considerably, as shown for the strain variation in the column bar. During the 7% drift ratio, the peak compressive strain in the extreme fiber of the concrete core was 0.0189 in./in. and 0.0235 in./in. for CIP and Precast-2, respectively, corresponding to a 24.3% increase in strains for the precast column. Compared to the strain at onset of core crushing for these two models (core concrete ultimate strain), $\varepsilon_{cu} = 0.0318$ in./in., it is observed that there was a margin of 40.5% (measured at 7% drift ratio) and 39.1% (measure at 6% drift ratio) before the core crushed for CIP and Precast-2, respectively. Fig. 5.20 presents the cyclic envelope and idealized curve for CIP and Precast-2. The displacement ductility capacity was found to be 7.28 and 6.27 for CIP and Precast-2, respectively. Table 5.7 includes the summary of performance for both column models.

Column Model 9 and 10

The height of column models 9 and 10 was 15 ft; they were reinforced with 14 No. 9 longitudinally and No. 6 closed hoops spaced at 3 in. on center transversely. An axial load equal to 305.4 kip was applied to the column top node. Fig. 5.21(a) shows that global response of the columns was similar; on the other hand, the local response, shown in Fig. 5.21 (b), was found to be different, as anticipated from the performance trend

observed for previous cases. The compressive strain in the extreme fiber of the core concrete was 0.0151 in./in. and 0.0190 in./in. for CIP and Precast-2, respectively, at the peak displacement of the 8% drift ratio—a 25.5% increase in compressive strains for Precast-2 with GSS connectors. Compared to core concrete ultimate strain, $\varepsilon_{cu} = 0.0190$ in./in., it is observed that there was 20.3% (measured at an 8% drift ratio) remaining compressive strain capacity for CIP. At the peak of the 7% drift ratio for Precast-2 (occurrence of bar fracture for this model), the remaining compressive strain capacity was 13.2%.

The displacement ductility capacity was found to be 6.45 and 5.95 for CIP and Precast-2, respectively. Fig. 5.22 includes the cyclic envelopes used to obtain the displacement ductility capacity of the two column models. A summary of performance characteristics is presented in Table 5.8.

Column Model 11 and 12

Similar to the previous two columns, column models 11 and 12 were 15-ft high reinforced with 14 No.9 main bars. The axial load was also identical to column 9 and 10, equal to 305.4 kip. To achieve a target displacement ductility of 11.0, the transverse reinforcement consisted of 2 No. 6 closed hoops at 3 in. on center. Fig. 5.23 presents the global and sectional response of the two columns. A similar trend in the sectional response comparison was observed for these two columns, compared to the previous models, as a result of an increased sectional demand at the interface of the precast column. The compressive strain was 0.0140 in./in. for the extreme core fiber, implying a 50.2% remaining compressive strain capacity for CIP at 8% drift ratio, when compared to

the ultimate compressive strain equal to $\varepsilon_{cu} = 0.0280$ in./in. For Precast-2, the peak compressive strain was 0.0171 in./in. during the 8% drift ratio. This corresponds to 22.7% increase in compressive strains evaluated at the same global displacement, compared to CIP. When bar fracture occurred for Precast-2, at peak of the 7% drift ratio, the compressive strain in the extreme core concrete fiber was equal to 0.0146 in./in. indicating a remaining compressive strain capacity of 47.8%.

Table 5.9 includes a performance summary for column models 11 and 12. The displacement ductility capacity was found to be 6.47 and 5.90 for CIP and Precast-2, respectively. Fig. 5.24 shows the cyclic envelopes and respective idealized curves.

Column Model 13 and 14

These columns were 15-ft high, reinforced with 14 No. 9 longitudinal bars, and No. 6 closed hoops at 2 ¾ in. on center. An axial load equal to 610.7 kip was applied to the columns. Fig. 5.25(a) shows that the ultimate displacement of Precast-2 was smaller than that of CIP. This is attributed to crushing of the core concrete which occurred at a drift of 6.66% slightly before bar fracture due to low-cycle fatigue; hence, the failure mode of Precast-2 was crushing of the concrete core. CIP failed due to low-cycle fatigue bar fracture during the first cycle of the 8% drift ratio. Comparing the compressive strains during the 5% drift ratio, the compressive strain in the extreme core fiber was 0.0152 in./in. and 0.0179 in./in. for CIP and Precast-2, respectively. This indicates a 17.5% increase for the precast column which can be seen in Fig. 5.25(b) for strains in the column bars.

Table 5.10 contains the performance summary for column model 13s and 14. The

displacement ductility capacity was 6.75 and 5.86 for CIP and Precast-2, respectively. This was obtained using the cyclic envelopes along with the idealized curves presented in Fig. 5.26.

Column Model 15 and 16

The columns in this category had a height equal to 15 ft, and reinforcement composed of 14 No. 9 longitudinal and 2 No. 7 closed hoops spaced at 3 ¼ in. on center. An axial load of 610.7 kip was applied to the column corresponding to a 10% ALI. Fig. 5.27 shows a comparable global response for the two columns which failed as a result of low-cycle fatigue bar fracture. The sectional response was found to be different due to larger strain demands in the bars for the precast column, although this did not change the ultimate displacement value compared to CIP, since low-cycle fatigue occurred during the second cycle of the last drift ratio. Compared to $\varepsilon_{cu} = 0.0318$ in./in., there was a 46.0% remaining compressive strain capacity at the peak displacement of the 8% ratio for CIP with a compressive strain equal to 0.0172 in./in.; for Preacst-2, a 43.8% margin was found at peak displacement of the 7% drift ratio during which column bars fractured. Fig. 5.28 shows the cyclic envelopes and idealized curves used to obtain the displacement ductility capacity for both columns. A displacement ductility capacity equal to 6.67 and 6.12 was found for CIP and Precast-2, respectively. Table 5.11 includes a summary of performance characteristics for the two columns.

Column Model 17 and 18

The columns in this category were 12-ft high, reinforced with 20 No. 14 longitudinal bars, and No. 6 closed hoops at 2 ½ in. on center transverse reinforcement. An axial load equal to 305.4 kip was maintained on both columns throughout the simulation. Fig. 5.29 shows the envelope of the force-displacement relationship for both columns, in addition to the strain variation in one extreme column bar. Both columns failed due to bar fracture as a result of low-cycle fatigue. The compressive strain in the extreme fiber of concrete core of Precast-2 was 0.0187 in./in. at the peak displacement during the 6% drift ratio. The compressive strain in the extreme fiber of CIP was also 0.0187 in./in. at the peak displacement of the 7% drift ratio. This implies that there was an 11.0% remaining compressive strain capacity at failure due to bar fracture, for both columns. At 7% drift, the compressive strain in the extreme fiber of Precast-2 was 0.021 in./in. which indicates a 12.7% increase with respect to that of CIP.

Fig. 5.30 shows the cyclic envelopes and the idealized curves constructed to obtain the displacement ductility capacity of column model 17 and 18, which was found to be 6.35 and 5.66, respectively. Table 5.12 includes a summary of performance characteristics for the two columns.

Column Model 19 and 20

A column height of 12 ft and main bar arrangement composed of 20 No. 9 were incorporated for the columns in this category. Under an axial load equal to 305.4 kip, transverse reinforcement consisted of 2 No. 7 closed hoops at 3 in. on center to achieve a target displacement ductility of 11.0. However, column bars fractured due to low-cycle

fatigue before the provided level of confinement resulted in a large displacement capacity. Fig. 5.31 shows the global and local response of both columns. A slightly more softened force-displacement was achieved for Precast-2 as a result of more pronounced bond-slip at the interface. The local demand was considerably larger at the interface of Precast-2 by incorporating a shorter plastic hinge length, imposing a premature bar fracture one cycle prior to CIP bar fracture. Due to the high confinement level, there was a large remaining compressive strain capacity at bar fracture for both columns, that is, 52.1% and 51.0% for CIP and Precast-2, respectively, when compared to $\varepsilon_{cu} = 0.0333$ in./in.. At 7% drift ratio, the compressive strain in the extreme fiber of the core concrete was 0.0159 in./in. and 0.0189 in./in. for CIP and Precast-2, respectively, indicating an 18.9% increase for the precast alternative.

The displacement ductility capacity of CIP and Precast-2 was found to be 6.37 and 5.61, respectively, as presented in Fig. 5.32. Table 5.13 contains a performance summary for column model 19 and 20.

Column Model 21 and 22

No. 7 closed hoops at 3 in. on center were used for these two 12-ft columns which were reinforced with 20 No. 9 longitudinal bars. The axial load was increased to 610.7 kip to study the effect of a larger axial load level. Fig. 5.33(a) shows that the cyclic envelopes were similar, whereas the sectional response, presented in Fig. 5.33(b), was different between the two alternatives; the precast column experienced a larger sectional demand as represented by the column bar strain variation. The ultimate compressive strain, $\varepsilon_{cu} = 0.0226$ in./in., was exceeded after extreme column bars fractured for CIP,

hence the failure mode was bar fracture due to low-cycle fatigue. Precast-2 failed because of core concrete crushing which occurred slightly before fracture of extreme bars, at 5.77% drift ratio, during the first cycle of the 6% drift ratio. Comparing the peak compressive strains at 5% drift ratio, the compressive strain was 0.0163 in./in. and 0.0195 in./in. for CIP and Precast-2, respectively, indicating a 19.4% increase for the precast column.

Table 5.14 includes a summary of performance characteristics for both columns. The displacement ductility was found to be 6.46 and 5.57 for CIP and Precast-2, respectively. Fig. 5.34 shows the cyclic envelopes along with the idealized curves which were used to obtain displacement ductility capacity.

Column Model 23 and 24

These two columns had a height equal to 12 ft, 20 No. 9 longitudinal bars, and 2 No. 7 at 2 ¾ in. on center. The design objective for displacement ductility was 11.0; an axial load equal to 610.7 kip was applied to both column models. The global and local response are shown in Fig. 5.35 for both column models. An increased sectional demand for Precast-2 is observed in Fig. 5.35(b). Both columns failed because of bar fracture due to low-cycle fatigue. CIP had a peak compressive strain of 0.0202 in./in. during the 7% drift ratio, whereas Precast-2 had a peak compressive strain equal to 0.0228 in./in. This corresponds to a 13.0% increase in sectional demand for Precast-2. Compared to the $\varepsilon_{cu} = 0.0349$ in./in., there was a 42.1% remaining compressive strain capacity for CIP. On the other hand, at bar fracture of Precast-2, which happened during the 6% drift ratio, Precast-2 had a 43.0% remaining compressive strain capacity.

Fig. 5.36 shows the cyclic envelopes in addition to the idealized curves constructed to obtain displacement ductility capacity. Table 5.15 includes the performance characteristics for both columns. The displacement ductility capacity was found to be 6.54 and 5.73 for CIP and Precast-2, respectively.

Column Model 25 and 26

Columns 25 and 26 were 15-ft high and reinforced with 20 No. 9 longitudinal bars, and No. 6 hoops at 2.5 in. spacing on center. An axial load equal to 305.4 kip was applied to the columns which were designed to achieve a displacement ductility of 7.0. The global and section responses are presented in Fig. 5.37 which shows a very similar global but different sectional performance. Both columns failed due to low-cycle fatigue bar fracture, during the 1st cycle of the 8% drift ratio and the 2nd cycle of the 7% drift ratio for CIP and Precast-2, respectively. The ultimate compressive strain capacity of the core concrete was 0.021 in./in. which was not exceeded before fracture of bars. CIP had a peak compressive strain of 0.0165 in./in. during the 8% drift ratio indicating a reserve compressive strain capacity equal to 21.5%. The remaining compressive strain capacity for Precast-2 was 18.8% during the 7% drift ratio when bar fracture occurred for this column. Precast-2 had a peak compressive strain of 0.0200 in./in. during the 8% drift ratio which implies a 21.1% increase in strain demand.

The displacement ductility capacity was found to be equal to 6.00 and 5.62 for CIP and Precast-2, using the cyclic envelopes shown in Fig. 5.38. Table 5.16 contains a summary of key performance characteristics for both columns.

Column Model 27 and 28

Columns 27 and 28 were 15-ft high under a 305.4-kip axial load, and reinforced with 20 No. 9 longitudinal bars and 2 No. 7 hoops at 3 in. spacing on center. The columns were detailed in such a way to achieve a displacement ductility capacity of 11.0. Fig. 5.39 shows the cyclic envelopes and column bar strain variation during the response. Both columns failed due to low-cycle fatigue bar fracture, during the first cycle of 8% drift ratio and second cycle of the 7% drift ratio, for CIP and Precast-2, respectively. CIP had a reserve compressive strain capacity of 56.7% while Precast-2 had a reserve compressive strain capacity equal to 55.3%, when bar fracture occurred. The peak compressive strain was 0.0144 in./in. and 0.0179 in./in. for CIP and Precast-2, respectively, during the 8% drift ratio, corresponding to a 23.9% increase in section strains.

Table 5.17 includes a summary of response parameters for both columns. The displacement ductility capacity obtained using the cyclic envelopes and pertinent idealized curves of Fig. 5.40, was found to be 5.94 and 5.60 for CIP and Precast-2, respectively.

Column Model 29 and 30

These two columns were 15-ft high, reinforced with 20 No. 9 longitudinal bars, and No. 7 hoops at 3 in. spacing on center. An axial load equal to 610.7 kip was applied to both columns which were detailed to achieve a displacement ductility of 7.0. Fig. 5.41 shows the global and sectional response of the columns. The force-drift envelopes were comparable but the column bar strain was larger for Precast-2. Both columns failed due

to low-cycle fatigue bar fracture, even though the compressive strain in the core concrete was very close to the ultimate strain $\varepsilon_{cu} = 0.0226$ in./in., because of a relatively large axial load. At fracture of the column bars, there was only a 4.0% and 5.0% remaining compressive strain capacity for CIP and Precast-2, respectively. During the 6% drift ratio, the compressive strain of the extreme core concrete fiber was 0.0155 in./in. and 0.0182 in./in. for CIP and Precast-2, respectively. This strain comparison was carried out during the 6% drift ratio because there was a convergence error for Precast-2 after bar fracture occurred during the 7% drift ratio.

Fig. 5.42 shows the cyclic envelopes in addition to the idealized curves to obtain the displacement ductility capacity which was found to be 6.16 and 5.80 for CIP and Precast-2, respectively. Table 5.18 includes the key analysis results for both column models.

Column Model 31 and 32

The last two column models were similar to columns 29 and 30 with the exception of a design target displacement ductility which was increased to 11.0; therefore, 2 No. 7 hoops spaced at 2 ¾ in. were used uniformly along the 15-ft high columns which had 20 No. 9 longitudinal bars. Fig. 5.43(a) shows that both columns had a similar strength and displacement capacity while Fig. 5.43(b) indicates a difference in strain demands for the critical section. Both columns failed because of low-cycle fatigue bar fracture. Compared to $\varepsilon_{cu} = 0.0349$ in./in., there was a 47.2% and 47.7% reserve compressive strain capacity for CIP and Precast-2, respectively, when bar fracture occurred. During the 8% drift ratio, CIP and Precast-2 had a peak core concrete strain

equal to 0.0184 in./in. and 0.0207 in./in. (a 12.1% increase), respectively, implying that a more localized demand was present for the precast column.

Table 5.19 includes the key response parameters for both columns such as displacement ductility capacity values which were obtained using Fig. 5.44. A displacement ductility capacity equal to 6.10 and 5.65 was found for CIP and Precast-2, respectively.

Effect of Parameters on Response of Column Models

This section includes a discussion on the influence of each parameter on the overall performance of the column models. The four aforementioned parameters were design displacement ductility, axial load on column, column height, and number of column longitudinal bars. Fig. 5.45 shows the cyclic envelopes for all CIP models reinforced with 14 No. 9 longitudinal bars. The overall response of the columns follows a logical trend which is expected to occur for reinforced concrete members under simultaneous lateral and axial loading. For instance, the strength capacity of the columns increased with an increase in axial load, whereas the strength decreased with an increase in column height. Similarly, columns with 20 No.9 longitudinal bars had an expected performance under varied parameters. Fig. 5.46 shows the cyclic envelopes for all eight CIP alternatives with 20 No. 9 longitudinal bars. It is important to note that the effects of parameter variation are only discussed using CIP columns for brevity. It was observed in the previous section that the precast alternatives had a similar global response to the corresponding CIP columns, while an increased sectional deformation was achieved representing a more localized demand. Nevertheless, for the precast columns, the

response trend was the same as in CIP alternatives under changing parameters.

Table 5.20 includes the displacement ductility capacity values obtained for all 32 column models. As discussed previously, all precast columns had a smaller displacement ductility capacity compared to their respective CIP columns. Also, it is noted that the obtained displacement ductility capacity values were always smaller than the required values except for the case of column model 7 which is very close to the required quantity. The difference between required and obtained values was more pronounced for the columns with a design displacement capacity equal to 11.0. The reason lies in the fact that the termination criterion used in the design displacement ductility procedure was based on the onset of core concrete crushing; analysis results showed that low-cycle fatigue bar fracture occurred prior to core concrete crushing for 29 column models out of the total 32 columns. It is noted that low-cycle fatigue bar fracture is highly sensitive to characteristics of the loading history and therefore the strain history for individual main column bars. The findings of this chapter apply to the specific loading history which was developed based on extensive research on reinforced concrete components (ACI Committee 374 2013).

Precast column model 22 had the lowest displacement ductility capacity, $\mu_C = 5.57$, among the columns under study. This was attributed to a relatively large axial load applied to this column which had a shorter analytical plastic hinge compared to its CIP alternative. As a result core concrete crushing occurred before bar fracture.

The results suggest that there is an upper bound displacement ductility capacity due to low-cycle fatigue bar fracture which is likely to happen under the ground motions with many large-amplitude cycles. For instance, displacement ductility capacity of 11.0 is

not achievable for bridge columns with details similar to the columns studied herein. The following sections provide a more detailed discussion on the effect of each parameter on the response of the columns.

Design Displacement Ductility

Two different design displacement ductility values equal to 7.0 and 11.0 were studied. As discussed earlier in this chapter, the conventional design procedure outlined in bridge specifications takes into account core crushing, or hoop fracture, when obtaining the design displacement ductility. However, it was noted that for the specific column configurations considered herein, a different failure mode was achieved for all CIP columns, which is low-cycle fatigue bar fracture. Therefore, regardless of the design objective, most of the columns only performed up to a 7% and 8% drift ratio for the 12-ft and 15-ft high columns, respectively.

Fig. 5.47(a) shows the cyclic envelopes of column models 1 and 3 with a design displacement ductility equal to 7.0 and 11.0, respectively. It is observed that both columns had a similar initial and postcracking stiffness. The postyield strength of column model 3 was slightly larger than that of column model 1 which is due to a stronger core concrete as a result of larger confinement. The ultimate displacement capacity was identical as both columns failed during the same cycle and drift ratio because of low-cycle fatigue bar fracture.

Fig. 5.47(b) shows the strain variation for an extreme column bar of both columns which indicates that the difference between the columns was insignificant. It was noted that tensile strains were slightly larger while compressive strains were slightly smaller for

column model 3. This is attributed to a stronger core concrete which resulted in a reduction of the depth of the section neutral axis.

Axial Load

Axial load values of 305.4 kip and 610.7 kip which corresponds to a 5% and 10% ALI, respectively, were employed to study the global and local response of the column models. In general, for columns with relatively low axial load such as bridge columns, the lateral force capacity increases with an increase in axial load as long as the sectional demand remains below the balanced point of the sectional capacity. This behavior is observed in Fig. 5.48(a) which shows the cyclic envelopes for column model 1 and column model 5 under 5% and 10% axial load, respectively. There was a 14.2% increase in the peak strength when axial load was increased from 305.4 kip to 610.7 kip. This resulted in a larger stiffness for column model 5. However, the displacement capacity is usually expected to decrease under larger axial loads as concrete crushing happens earlier in the response. This phenomenon was not observed for column model 5 because low-cycle fatigue bar fracture occurred before crushing of concrete; Fig. 5.48(b) illustrates why low-cycle fatigue bar fracture for this particular column was rather insensitive to this level of change in axial load. It is noted that the increased axial load did affect the displacement capacity of three other column models. In particular, column models 6, 14, and 22, all of which were precast and under 10% axial load, failed due to core concrete crushing, thus achieving a reduced ultimate displacement.

Fig. 5.48(b) shows the strain variation in extreme longitudinal bars of column models 1 and 5. Under larger axial load, there was an increase in compressive strains and

a decrease in tensile strains for column model 5, caused by a deeper neutral axis due to a higher axial load. Comparing the two curves, it appears that a strain shift occurred for column model 5 under a larger axial load implying that the strain range, which is the main parameter in determining the low-cycle fatigue life of a reinforcing bar, remained similar to the strain range for column model 1. This explains why column model 5 did not fail before column model 1.

Column Height

The simulated columns had two distinct heights of 12 ft and 15 ft corresponding to an aspect ratio equal to 4 and 5, respectively. It is known that an increase in the column height (with identical sectional configurations) would result in a reduction in lateral force capacity of the column as the moment arm becomes larger. This can be seen in Fig. 5.49(a) which shows the cyclic envelopes for column model 1 and column model 9. Consequently, stiffness decreased resulting in a softer response for column model 9. However, the displacement capacity of column model 9 was found to be 45.8% larger than that of column model 1 which is attributed to delayed bar fracture because of a lower demand on the critical section. This is shown in Fig. 5.49(b) which compares the variation of strains for the extreme column bar of the two column models. It is noted that even though the displacement capacity of column model 9 increased because of a larger height, the displacement ductility capacity decreased from 6.82 to 6.45, as discussed in the previous section. The reduction is due to the fact that the yield displacement also increases with an increase in the column height, as shown Fig. 5.49(a).

Column Longitudinal Reinforcing Bars

Two reinforcing bar ratios equal to 1.38% and 1.96%, which correspond to 14 No. 9 and 20 No. 9 longitudinal bars, were considered. It is evident that a column reinforced with more longitudinal bars has a larger strength than an identical column reinforced with fewer bars. This is verified in Fig. 5.50(a) that shows the cyclic envelopes for column model 1 and column model 17; there was a 32.1% increase in the lateral force capacity when 20 No. 9 bars were used instead of 14 No. 9 bras. The postcracking stiffness also increased by incorporating more longitudinal bars, as anticipated. The ultimate displacement, however, remained the same since both columns failed due to low-cycle fatigue bar fracture and the strain range in column bars did not change significantly as shown in Fig. 5.50(b). The strain variation presented in Fig. 5.50(b) indicates a small reduction in tensile strains followed by a slight increase in compressive strains implying an insignificantly deeper neutral axis which did not change the bar fracture drift ratio and cycle. The displacement ductility capacity was reduced from 6.82 for column model 1 to 6.35 for column model 17 because of a small increase in the effective yield displacement for column model 17.

Effects of P-Δ

P-Δ effects can cause loss of lateral resistance, ratchetting, and dynamic instability (Deierlein et al 2010). Hence they need to be included in nonlinear static or dynamic analyses of bridges in seismic zones, unless the effect of gravity load is found to be negligible. P-Δ was not included in the validation process of the modeling strategy due to the experimental setup preventing P-Δ effects, nor was it studied for the 32 column

models discussed herein so far. Chapter 6 will focus on a prototype bridge bent under static and dynamic loads, which will require P-Δ to be considered. Therefore, one CIP and one Precast-2 are examined, when a P-Δ transformation is activated in the computational model.

P-Δ Effects on Half-Scale Column Experiments

Fig. 5.51 shows the test setup that was used for the experiments reported in Chapter 3. It is observed that the axial load was transferred to the column using a follower force system. That is, it can be assumed that the direction of the axial load always followed the longitudinal axis of the column. A spherical plate which was mounted on top of the column along with a pinned rod connection at the bottom helped direct the axial load to follow the longitudinal axis of the column at every instant during the test. A schematic approximation of the load transfer mechanism and P-Δ effects is shown in Fig. 5.52. Assuming a rigid body rotation of the axial load transfer system, which consisted of two high-strength threaded rods in addition to a hydraulic actuator and the top and bottom pinned fixtures, the axial load is decomposed into a vertical and a horizontal load component. This results in clockwise (M_v) and counterclockwise (M_h) P-Δ moment components at the base of the column. The axial load components, bending moment components, and the rotation angle (θ) are defined as follows.

$$P_v = P\cos\theta \tag{5.6}$$

$$P_h = P\sin\theta \tag{5.7}$$

$$M_v = P_v\Delta \tag{5.8}$$

$$M_h = P_h H\cos\theta \tag{5.9}$$

$$\theta = \tan^{-1}\frac{\Delta}{H} \tag{5.10}$$

where, P_v and P_h are the vertical and horizontal components of the axial load, Δ is the horizontal displacement at the column top, and H is the distance from the column base to the elevation of the lateral load.

Assuming small angles as a result of small horizontal displacements, compared to the overall column height, an approximation using Taylor Series up to the 2nd order reveals that the P-Δ moments can be defined as shown in Eq. (11) and Eq. (12).

$$M_v = P\Delta\left(1 - \frac{\Delta^2}{2H^2}\right) \approx P\Delta \tag{5.11}$$

$$M_h = P\frac{\Delta}{H}H\left(1 - \frac{\Delta^2}{2H^2}\right) \approx P\Delta \tag{5.12}$$

Hence, the P-Δ moments are counterbalanced and consequently P-Δ effects were not included in the experimental data analysis, nor was it considered for the computational model validation process.

P-Δ Effects on Column Model 29 and 30

Column model 29 and 30 were 15-ft high, and reinforced with 20 No. 9 longitudinal bars and No. 7 hoops at 3 in. spacing on center. An axial load equal to 610.7 kip (10% ALI) was applied to these two columns, which were detailed to achieve a displacement ductility of 7.0. As anticipated, inclusion of P-Δ resulted in a different global response for both columns while the sectional response remained identical to the sectional response of the columns without P-Δ. The hardening postyield performance of both columns changed to a softening performance with a small negative slope as shown in Fig. 5.53(a) and Fig. 5.54(a) for CIP and Precast-2, respectively. The softening force-displacement relationship resulted in a smaller effective yield displacement, and a larger

displacement ductility capacity, as presented in Fig. 5.53(b) and 5.54(b) for CIP and Precast-2, respectively. There was a 13.1% and 13.3% increase in the displacement ductility capacity of CIP and Precast-2, respectively, when P-Δ was present. Since this increase is only attributed to the softening response and is not a realistic property of the column, it is more prudent to obtain the displacement ductility capacity without P-Δ effects to achieve a higher level of conservatism. On the other hand, there was a 17.4% and 18.0% reduction in the peak strength for CIP and Precast-2, respectively.

Effects of Plastic Hinge Length Variation

The local response of columns is a function of the analytical plastic hinge length incorporated in the proposed model. The design procedure which was discussed previously included recommendations about applying a fictitious plastic hinge length for precast columns with GSS connectors. This section investigates the sensitivity in both the global and local response of a Precast-2 column model when the plastic hinge length is varied using 0.5-in. length increments. The objective is to ascertain the response sensitivity due to a change in the assumed plastic hinge length. The precast column model 30 was selected which had 20 No. 9 longitudinal bars, a column height equal to 15 ft, an ALI of 10%, and a design displacement ductility equal to 7.0. It was previously shown that the fictitious plastic hinge length was found to be 18.0 in. for this column model. An upper-bound and a lower-bound plastic hinge length equal to 20.0 in. and 16.0 in. was used, respectively. Table 5-21 includes the response variation as a result of a change in the plastic hinge length. The failure mode was found to be either low-cycle fatigue bar fracture or crushing of concrete core. Table 5-21 shows that the yield

displacement of the column was unaffected while the sectional ultimate curvature, ultimate displacement, displacement ductility capacity, and mode of failure changed with a variation in the assumed plastic hinge length.

Fig. 5. 55(a) shows how the ultimate curvature at 6% drift ratio changes as a result of a varying plastic hinge length. As anticipated, sectional curvature increased with a decrease in the plastic hinge length. The largest absolute curvature difference was found to be 10% for an 11% (2.0-in.) change in the plastic hinge length. Fig. 5. 55(b) shows the displacement ductility capacity values obtained for the plastic hinge length variation incorporated in the column model. The displacement ductility capacity decreased with a decrease in the plastic hinge length because of a larger sectional demand. However, the displacement ductility capacity remained relatively unchanged with an increase in the plastic hinge length up to 20.0 in. because low-cycle fatigue bar fracture occurred during the 2nd cycle of the 7% drift ratio or 1st cycle of the 8% drift ratio for plastic hinge lengths equal or larger than 18.0 in. This resulted in an ultimate drift ratio equal to 7% (12.6 in.) for a plastic hinge length equal to or greater than 17.5 in. and smaller than 20.0 in.

Conclusions

A parametric study was conducted on actual size bridge columns to assess the accuracy of the proposed modeling strategy which was introduced Chapter 4. The objective was to ascertain the applicability of the proposed model to both cast-in-place monolithic columns and precast bridge columns with grouted splice sleeve connectors. In addition, the effect of varying the parameters on column response was investigated. Two

alternatives were considered: a cast-in-place column with monolithic details representing CIP in the previous chapter and a precast column with grouted splice sleeves in the column end and debonding of dowel bars in the footing (Precast-2). Sixteen CIP and sixteen Precast-2 columns were studied with varying parameters. The findings of this parametric study can be summarized as follows. It is noted that the findings apply to ductile slender columns investigated in this chapter in addition to similar cases. Extension of this modeling strategy to a more general group of columns with considerable design differences requires further investigation.

- The results from the analysis were in good agreement with anticipated performance for cast-in-place monolithic and precast column models with grouted splice sleeve connectors.
- An empirical relationship was used to determine the length of the plastic hinge for cast-in-place column models. To include a more localized damage for the precast column models, the computational model was constructed with a shorter plastic hinge. In the absence of an empirical plastic hinge length relationship, the reduction factor, which was obtained in Chapter 4, was incorporated. This resulted in a low-cycle fatigue bar fracture in fewer cycles, for all precast column models compared to CIP models.
- All cast-in-place column models failed due to low-cycle fatigue bar facture, while precast column models failed due to low-cycle fatigue bar fracture and crushing of core concrete. The amount of axial load played an important role in the failure mode of precast column models.
- The global strength of cast-in-place and precast column models was similar for all

column models. Even though bar fracture occurred in fewer cycles for the precast alternatives, the ultimate displacement was found to be identical to the cast-in-place models; this is because bar fracture occurred during the second cycle of the last drift ratio for the precast column models. That is, the displacement capacity of Precast-2 column models was close to that of CIP column models as observed in the experiments.

- The displacement ductility of precast column models was found to be smaller than that of cast-in-place column models mainly due to a larger effective yield displacement, as a result of a larger bond-slip for the precast alternatives.
- A very large displacement ductility capacity is unachievable for bridge columns with modern seismic detailing under several displacement reversals due to the presence of low-cycle fatigue fracture of longitudinal bars. Even though a design displacement ductility of 11.0 was aimed for half of the column models, the maximum displacement ductility capacity reached in the simulations was found to be 7.28.
- An increase in the design displacement ductility resulted in increased confined concrete properties in terms of both stress and strain. Consequently, there was a small increase in the lateral force capacity of the column model; however, the displacement capacity was unaffected because bar fracture occurred before crushing of the core concrete. Higher confinement was found to have a small effect on the low-cycle fatigue life of the column bars.
- Column lateral strength increased with an increase in the column axial load as anticipated for column models with design capacities below the balanced point.

The displacement capacity of three column models was reduced because of the increased compressive demand which resulted in crushing of the core concrete. The displacement capacity of the other 29 column models was not affected by the axial load increase because there was a considerable remaining compressive strain capacity when low-cycle fatigue bar fracture occurred.

- An increase in the column model height resulted in a decrease in lateral strength of the column as expected. On the other hand, the displacement capacity increased with an increase in column model height because of a lower strain demand at the column end. However, the displacement ductility capacity did not increase because the effective yield displacement of the higher column model was larger than that of the shorter column model.
- Column models reinforced with more longitudinal bars had a larger lateral strength than column models with fewer bars. The displacement capacity was not affected by this change because the sectional strain demand did not change drastically due to incorporating more longitudinal bars; thus the low-cycle fatigue life of the longitudinal bars was similar to that of the column models with fewer bars.
- Inclusion of P-Δ effects changed the hardening post-yield global response to a softening post-yield global response, but did not make any modifications in the sectional response. The lateral strength was reduced by 18% due to P-Δ effects, but the displacement capacity was unaffected. The displacement ductility capacity was increased by 13% because the negative slope of the force-displacement response imposed a smaller effective yield displacement.

- For the Precast-2 column model, sectional curvature was magnified when reduced plastic hinge lengths compared to the assumed plastic hinge length were incorporated. There was a 10% change in the value of the ultimate curvature as a result of an 11% change in the assumed plastic hinge length.
- The displacement ductility capacity of the Precast-2 column model remained relatively unchanged for values of the assumed plastic hinge length above the value established based on the half-scale experiments. This is the case since failure of the column was due to low-cycle fatigue bar fracture.

References

AASHTO. (2012). AASHTO LRFD *bridge design specification*, Washington, DC.

AASHTO. (2011). AASHTO guide specifications for LRFD s*eismic bridge design*, Washington, DC.

American Concrete Institute (ACI). (2013). "Guide for testing reinforced concrete structural elements under slowly applied simulated seismic loads." *ACI 374*, Farmington Hills, MI.

ASTM. (2009a). "Standard specification for low-alloy steel deformed and plain bars for concrete reinforcement." *A706/A706M – 09*, West Conshohocken, PA.
Caltrans. (2010). *Seismic design criteria (SDC), version 1.6*, Sacramento, CA.

Deierlein, G. G., Reinhorn, A., M., Willford, M. R. (2010). "Nonlinear structural analysis for seismic design, a guide for practicing engineers." *NIST GCR 10-917-5*, National Institute of Standards and Technology, Gaithersburg, MD.

Mander, J. B., Priestley, M. J. N., and Park, R. (1988). "Theoretical stress-strain model for confined concrete." *J. Struct. Eng.*, 10.1061/(ASCE)0733-9445(1988)114:8(1804), 1804-1826.

Panagiotakos, T. B., and Fardis, M. N. (2001). "Deformations of reinforced concrete members at yielding and ultimate." *ACI Struct. J.*, 98(2), 135–148.

Priestley, M. J. N., Seible, F., and Calvi, G. M. (1996). *Seismic design and retrofit of bridges*. John Wiley & Sons, Inc., New York, NY.

Table 5.1. Modeling alternatives for parametric study.

Model No.	Details	Bar Ratio (%)	Column Aspect Ratio	ALI (%)	Displacement Ductility
1	CIP	1.38	4	5	7.0
2	Precast-2	1.38	4	5	NA
3	CIP	1.38	4	5	11.0
4	Precast-2	1.38	4	5	NA
5	CIP	1.38	4	10	7.0
6	Precast-2	1.38	4	10	NA
7	CIP	1.38	4	10	11.0
8	Precast-2	1.38	4	10	NA
9	CIP	1.38	5	5	7.0
10	Precast-2	1.38	5	5	NA
11	CIP	1.38	5	5	11.0
12	Precast-2	1.38	5	5	NA
13	CIP	1.38	5	10	7.0
14	Precast-2	1.38	5	10	NA
15	CIP	1.38	5	10	11.0
16	Precast-2	1.38	5	10	NA
17	CIP	1.96	4	5	7.0
18	Precast-2	1.96	4	5	NA
19	CIP	1.96	4	5	11.0
20	Precast-2	1.96	4	5	NA
21	CIP	1.96	4	10	7.0
22	Precast-2	1.96	4	10	NA
23	CIP	1.96	4	10	11.0
24	Precast-2	1.96	4	10	NA
25	CIP	1.96	5	5	7.0
26	Precast-2	1.96	5	5	NA
27	CIP	1.96	5	5	11.0
28	Precast-2	1.96	5	5	NA
29	CIP	1.96	5	10	7.0
30	Precast-2	1.96	5	10	NA
31	CIP	1.96	5	10	11.0
32	Precast-2	1.96	5	10	NA

Table 5.2. Reinforcing bar material properties

Specified Yield Stress, f_y (ksi)	60
Expected Yield Stress, f_{ye} (ksi)	68
Expected Tensile Stress, f_{ue} (ksi)	95
Strain at Onset of Strain Hardening, ε_{sh}, (in./in.)	0.0125
Reduced Ultimate Tensile Strain, ε^R_{su}, (in./in.)	0.09
Ultimate Tensile Strain, ε_{su}, (in./in.)	0.12

Table 5.3. Design details of column models.

Model No.	Details	Axial Load (kip)	H (ft)	Lp (in.)	Main Bar	μ_D Required	μ_ϕ Required	Transverse Bar	μ_ϕ Provided
1	CIP	305.4	12	17.28	14 No. 9	7.0	18.73	No. 6 @ 3"	19.04
2	Precast-2	305.4	12	14.40	14 No. 9	NA	NA	No. 6 @ 3"	NA
3	CIP	305.4	12	17.28	14 No. 9	11.0	30.55	2 No. 6 @ 3"	31.10
4	Precast-2	305.4	12	14.40	14 No. 9	NA	NA	2 No. 6 @ 3"	NA
5	CIP	610.7	12	17.28	14 No. 9	7.0	18.73	No. 6 @ 2 ¾"	18.80
6	Precast-2	610.7	12	14.40	14 No. 9	NA	NA	No. 6 @ 2 ¾"	NA
7	CIP	610.7	12	17.28	14 No. 9	11.0	30.55	2 No. 7 @ 3 ¼"	31.23
8	Precast-2	610.7	12	14.40	14 No. 9	NA	NA	2 No. 7 @ 3 ¼"	NA
9	CIP	305.4	15	21.60	14 No. 9	7.0	18.73	No. 6 @ 3"	19.04
10	Precast-2	305.4	15	18.00	14 No. 9	NA	NA	No. 6 @ 3"	NA
11	CIP	305.4	15	21.60	14 No. 9	11.0	30.55	2 No. 6 @ 3"	31.10
12	Precast-2	305.4	15	18.00	14 No. 9	NA	NA	2 No. 6 @ 3"	NA
13	CIP	610.7	15	21.60	14 No. 9	7.0	18.73	No. 6 @ 2 ¾"	18.80
14	Precast-2	610.7	15	18.00	14 No. 9	NA	NA	No. 6 @ 2 ¾"	NA
15	CIP	610.7	15	21.60	14 No. 9	11.0	30.55	2 No. 7 @ 3 ¼"	31.23
16	Precast-2	610.7	15	18.00	14 No. 9	NA	NA	2 No. 7 @ 3 ¼"	NA
17	CIP	305.4	12	17.28	20 No. 9	7.0	18.73	No. 6 @ 2 ½"	18.29*
18	Precast-2	305.4	12	14.40	20 No. 9	NA	NA	No. 6 @ 2 ½"	NA
19	CIP	305.4	12	17.28	20 No. 9	11.0	30.55	2 No. 7 @ 3"	30.85
20	Precast-2	305.4	12	14.40	20 No. 9	NA	NA	2 No. 7 @ 3"	NA
21	CIP	610.7	12	17.28	20 No. 9	7.0	18.73	No. 7 @ 3"	18.75
22	Precast-2	610.7	12	14.40	20 No. 9	NA	NA	No. 7 @ 3"	NA
23	CIP	610.7	12	17.28	20 No. 9	11.0	30.55	2 No. 7 @ 2 ¾"	30.22*
24	Precast-2	610.7	12	14.40	20 No. 9	NA	NA	2 No. 7 @ 2 ¾"	NA
25	CIP	305.4	15	21.60	20 No. 9	7.0	18.73	No. 6 @ 2 ½"	18.29*
26	Precast-2	305.4	15	18.00	20 No. 9	NA	NA	No. 6 @ 2 ½"	NA
27	CIP	305.4	15	21.60	20 No. 9	11.0	30.55	2 No. 7 @ 3"	30.85
28	Precast-2	305.4	15	18.00	20 No. 9	NA	NA	2 No. 7 @ 3"	NA
29	CIP	610.7	15	21.60	20 No. 9	7.0	18.73	No. 7 @ 3"	18.75
30	Precast-2	610.7	15	18.00	20 No. 9	NA	NA	No. 7 @ 3"	NA
31	CIP	610.7	15	21.60	20 No. 9	11.0	30.55	2 No. 7 @ 2 ¾"	30.22*
32	Precast-2	610.7	15	18.00	20 No. 9	NA	NA	2 No. 7 @ 2 ¾"	NA

Table 5.4. Summary of performance for column models 1 and 2.

Performance Characteristic	Column Model 1	Column Model 2
Column type	CIP	Precast-2
Plastic hinge length (in.)	17.28	14.40
Failure mode	Bar fracture	Bar fracture
Bar fracture drift (%)	7	6
Bar fracture cycle	1	2
Ultimate drift (%)	6	6
Ultimate displacement (in.)	8.64	8.64
Effective yield displacement (in.)	1.27	1.41
Effective yield force (kip)	140.3	136.2
Displacement ductility capacity	6.82	6.13
Peak compressive strain @ 7% drift (in./in.)	0.0171	0.0190

Table 5.5. Summary of performance for column models 3 and 4.

Performance Characteristic	**Column Model 3**	**Column Model 4**
Column type	CIP	Precast-2
Plastic hinge length (in.)	17.28	14.40
Failure mode	Bar fracture	Bar fracture
Bar fracture drift (%)	7	6
Bar fracture cycle	1	2
Ultimate drift (%)	6	6
Ultimate displacement (in.)	8.64	8.64
Effective yield displacement (in.)	1.22	1.42
Effective yield force (kip)	136.9	139.2
Displacement ductility capacity	7.11	6.09
Peak compressive strain @ 7% drift (in./in.)	0.0153	0.0189

Table 5.6. Summary of performance for column models 5 and 6.

Performance Characteristic	**Column Model 5**	**Column Model 6**
Column type	CIP	Precast-2
Plastic hinge length (in.)	17.28	14.40
Failure mode	Bar fracture	Crushing of core concrete
Bar fracture drift (%)	7	6
Bar fracture cycle	1	2
Ultimate drift (%)	6	5.31
Ultimate displacement (in.)	8.64	7.65
Effective yield displacement (in.)	1.19	1.36
Effective yield force (kip)	155.5	157.2
Displacement ductility capacity	7.27	5.62
Peak compressive strain @ 5% drift (in./in.)	0.0159	0.0189

Table 5.7. Summary of performance for column models 7 and 8.

Performance Characteristic	Column Model 7	Column Model 8
Column type	CIP	Precast-2
Plastic hinge length (in.)	17.28	14.40
Failure mode	Bar fracture	Bar fracture
Bar fracture drift (%)	7	6
Bar fracture cycle	1	2
Ultimate drift (%)	6	6
Ultimate displacement (in.)	8.64	8.64
Effective yield displacement (in.)	1.19	1.38
Effective yield force (kip)	160.5	162.9
Displacement ductility capacity	7.28	6.27
Peak compressive strain @ 7% drift (in./in.)	0.0189	0.0235

Table 5.8. Summary of performance for column models 9 and 10.

Performance Characteristic	Column Model 9	Column Model 10
Column type	CIP	Precast-2
Plastic hinge length (in.)	21.60	18.00
Failure mode	Bar fracture	Bar fracture
Bar fracture drift (%)	8	7
Bar fracture cycle	1	2
Ultimate drift (%)	7	7
Ultimate displacement (in.)	12.60	12.60
Effective yield displacement (in.)	1.95	2.11
Effective yield force (kip)	107.5	108.8
Displacement ductility capacity	6.45	5.95
Peak compressive strain @ 8% drift (in./in.)	0.0151	0.0190

Table 5.9. Summary of performance for column models 11 and 12.

Performance Characteristic	Column Model 11	Column Model 12
Column type	CIP	Precast-2
Plastic hinge length (in.)	21.60	18.00
Failure mode	Bar fracture	Bar fracture
Bar fracture drift (%)	8	7
Bar fracture cycle	1	2
Ultimate drift (%)	7	7
Ultimate displacement (in.)	12.60	12.60
Effective yield displacement (in.)	1.95	2.14
Effective yield force (kip)	109.6	111.2
Displacement ductility capacity	6.47	5.90
Peak compressive strain @ 8% drift (in./in.)	0.0140	0.0171

Table 5.10. Summary of performance for column models 13 and 14.

Performance Characteristic	Column Model 13	Column Model 14
Column type	CIP	Precast-2
Plastic hinge length (in.)	21.60	18.00
Failure mode	Bar fracture	Crushing of core concrete
Bar fracture drift (%)	8	7
Bar fracture cycle	1	2
Ultimate drift (%)	7	6.66
Ultimate displacement (in.)	12.60	12.00
Effective yield displacement (in.)	1.87	2.05
Effective yield force (kip)	124.5	125.9
Displacement ductility capacity	6.75	5.86
Peak compressive strain @ 5% drift (in./in.)	0.0152	0.0179

Table 5.11. Summary of performance for column models 15 and 16.

Performance Characteristic	Column Model 15	Column Model 16
Column type	CIP	Precast-2
Plastic hinge length (in.)	21.60	18.00
Failure mode	Bar fracture	Bar fracture
Bar fracture drift (%)	8	7
Bar fracture cycle	1	2
Ultimate drift (%)	7	7
Ultimate displacement (in.)	12.60	12.60
Effective yield displacement (in.)	1.89	2.06
Effective yield force (kip)	128.5	130.3
Displacement ductility capacity	6.67	6.12
Peak compressive strain @ 8% drift (in./in.)	0.0172	0.0213

Table 5.12. Summary of performance for column models 17 and 18.

Performance Characteristic	**Column Model 17**	**Column Model 18**
Column type	CIP	Precast-2
Plastic hinge length (in.)	17.28	14.40
Failure mode	Bar fracture	Bar fracture
Bar fracture drift (%)	7	6
Bar fracture cycle	1	2
Ultimate drift (%)	6	6
Ultimate displacement (in.)	8.64	8.64
Effective yield displacement (in.)	1.36	1.53
Effective yield force (kip)	175.7	178.0
Displacement ductility capacity	6.35	5.66
Peak compressive strain @ 7% drift (in./in.)	0.0186	0.0210

Table 5.13. Summary of performance for column models 19 and 20.

Performance Characteristic	**Column Model 19**	**Column Model 20**
Column type	CIP	Precast-2
Plastic hinge length (in.)	17.28	14.40
Failure mode	Bar fracture	Bar fracture
Bar fracture drift (%)	7	6
Bar fracture cycle	1	2
Ultimate drift (%)	6	6
Ultimate displacement (in.)	8.64	8.64
Effective yield displacement (in.)	1.36	1.53
Effective yield force (kip)	180.2	183.1
Displacement ductility capacity	6.37	5.61
Peak compressive strain @ 7% drift (in./in.)	0.0159	0.0189

Table 5.14. Summary of performance for column models 21 and 22.

Performance Characteristic	Column Model 21	Column Model 22
Column type	CIP	Precast-2
Plastic hinge length (in.)	17.28	14.40
Failure mode	Bar fracture	Crushing of core concrete
Bar fracture drift (%)	7	6
Bar fracture cycle	1	2
Ultimate drift (%)	6	5.77
Ultimate displacement (in.)	8.64	8.31
Effective yield displacement (in.)	1.34	1.50
Effective yield force (kip)	196.7	198.3
Displacement ductility capacity	6.46	5.57
Peak compressive strain @ 5% drift (in./in.)	0.0164	0.0195

Table 5.15. Summary of performance for column models 23 and 24.

Performance Characteristic	Column Model 23	Column Model 24
Column type	CIP	Precast-2
Plastic hinge length (in.)	17.28	14.40
Failure mode	Bar fracture	Bar fracture
Bar fracture drift (%)	7	6
Bar fracture cycle	1	2
Ultimate drift (%)	6	6
Ultimate displacement (in.)	8.64	8.64
Effective yield displacement (in.)	1.32	1.51
Effective yield force (kip)	202.3	205.7
Displacement ductility capacity	6.54	5.73
Peak compressive strain @ 7% drift (in./in.)	0.0202	0.0228

Table 5.16. Summary of performance for column models 25 and 26.

Performance Characteristic	Column Model 25	Column Model 26
Column type	CIP	Precast-2
Plastic hinge length (in.)	21.60	18.00
Failure mode	Bar fracture	Bar fracture
Bar fracture drift (%)	8	7
Bar fracture cycle	1	2
Ultimate drift (%)	7	7
Ultimate displacement (in.)	12.60	12.60
Effective yield displacement (in.)	2.10	2.24
Effective yield force (kip)	140.3	142.0
Displacement ductility capacity	6.00	5.62
Peak compressive strain @ 8% drift (in./in.)	0.0165	0.0200

Table 5.17. Summary of performance for column models 27 and 28.

Performance Characteristic	Column Model 27	Column Model 28
Column type	CIP	Precast-2
Plastic hinge length (in.)	21.60	18.00
Failure mode	Bar fracture	Bar fracture
Bar fracture drift (%)	8	7
Bar fracture cycle	1	2
Ultimate drift (%)	7	7
Ultimate displacement (in.)	12.60	12.60
Effective yield displacement (in.)	2.12	2.25
Effective yield force (kip)	143.9	145.7
Displacement ductility capacity	5.94	5.60
Peak compressive strain @ 8% drift (in./in.)	0.0144	0.0179

Table 5.18. Summary of performance for column models 29 and 30.

Performance Characteristic	Column Model 29	Column Model 30
Column type	CIP	Precast-2
Plastic hinge length (in.)	21.60	18.00
Failure mode	Bar fracture	Bar fracture
Bar fracture drift (%)	8	7
Bar fracture cycle	1	2
Ultimate drift (%)	7	7
Ultimate displacement (in.)	12.60	12.60
Effective yield displacement (in.)	2.05	2.17
Effective yield force (kip)	157.0	158.7
Displacement ductility capacity	6.16	5.80
Peak compressive strain @ 6% drift (in./in.)	0.0155	0.0182

Table 5.19. Summary of performance for column models 31 and 32.

Performance Characteristic	Column Model 31	Column Model 32
Column type	CIP	Precast-2
Plastic hinge length (in.)	21.60	18.00
Failure mode	Bar fracture	Bar fracture
Bar fracture drift (%)	8	7
Bar fracture cycle	1	2
Ultimate drift (%)	7	7
Ultimate displacement (in.)	12.60	12.60
Effective yield displacement (in.)	2.08	2.23
Effective yield force (kip)	161.6	163.9
Displacement ductility capacity	6.10	5.65
Peak compressive strain @ 8% drift (in./in.)	0.0184	0.0207

Table 5.20. Comparison of the obtained displacement ductility capacity values.

Model No.	Column Details	Axial Load (kip)	H (ft)	Main Bar	Transverse Bar	μ_D Required	μ_D Obtained	Failure Mode
1	CIP	305.4	12	14 No. 9	No. 6 @ 3.00"	7.0	6.82	BF*
2	Precast-2	305.4	12	14 No. 9	No. 6 @ 3.00"	NA	6.13	BF
3	CIP	305.4	12	14 No. 9	2 No. 6 @ 3.00"	11.0	7.11	BF
4	Precast-2	305.4	12	14 No. 9	2 No. 6 @ 3.00"	NA	6.09	BF
5	CIP	610.7	12	14 No. 9	No. 6 @ 2.75"	7.0	7.27	BF
6	Precast-2	610.7	12	14 No. 9	No. 6 @ 2.75"	NA	5.62	CC**
7	CIP	610.7	12	14 No. 9	2 No. 7 @ 3.25"	11.0	7.28	BF
8	Precast-2	610.7	12	14 No. 9	2 No. 7 @ 3.25"	NA	6.27	BF
9	CIP	305.4	15	14 No. 9	No. 6 @ 3.00"	7.0	6.45	BF
10	Precast-2	305.4	15	14 No. 9	No. 6 @ 3.00"	NA	5.95	BF
11	CIP	305.4	15	14 No. 9	2 No. 6 @ 3.00"	11.0	6.47	BF
12	Precast-2	305.4	15	14 No. 9	2 No. 6 @ 3.00"	NA	5.90	BF
13	CIP	610.7	15	14 No. 9	No. 6 @ 2.75"	7.0	6.75	BF
14	Precast-2	610.7	15	14 No. 9	No. 6 @ 2.75"	NA	5.86	CC
15	CIP	610.7	15	14 No. 9	2 No. 7 @ 3.25"	11.0	6.67	BF
16	Precast-2	610.7	15	14 No. 9	2 No. 7 @ 3.25"	NA	6.12	BF
17	CIP	305.4	12	20 No. 9	No. 6 @ 2.50"	7.0	6.35	BF
18	Precast-2	305.4	12	20 No. 9	No. 6 @ 2.50"	NA	5.66	BF
19	CIP	305.4	12	20 No. 9	2 No. 7 @ 3.00"	11.0	6.37	BF
20	Precast-2	305.4	12	20 No. 9	2 No. 7 @ 3.00"	NA	5.61	BF
21	CIP	610.7	12	20 No. 9	No. 7 @ 3.00"	7.0	6.46	BF
22	Precast-2	610.7	12	20 No. 9	No. 7 @ 3.00"	NA	5.57	CC
23	CIP	610.7	12	20 No. 9	2 No. 7 @ 2.75"	11.0	6.54	BF
24	Precast-2	610.7	12	20 No. 9	2 No. 7 @ 2.75"	NA	5.73	BF
25	CIP	305.4	15	20 No. 9	No. 6 @ 2.50"	7.0	6.00	BF
26	Precast-2	305.4	15	20 No. 9	No. 6 @ 2.50"	NA	5.62	BF
27	CIP	305.4	15	20 No. 9	2 No. 7 @ 3.00"	11.0	5.94	BF
28	Precast-2	305.4	15	20 No. 9	2 No. 7 @ 3.00"	NA	5.60	BF
29	CIP	610.7	15	20 No. 9	No. 7 @ 3.00"	7.0	6.16	BF
30	Precast-2	610.7	15	20 No. 9	No. 7 @ 3.00"	NA	5.80	BF
31	CIP	610.7	15	20 No. 9	2 No. 7 @ 2.75"	11.0	6.10	BF
32	Precast-2	610.7	15	20 No. 9	2 No. 7 @ 2.75"	NA	5.65	BF

*Bar Fracture
**Core Crushing

Table 5.21. Effect of plastic hinge length variation on sectional and global response of column model Precast-2.

L_p (in.)	Failure Mode	φ_u @ 6% (1/in.)	Δ_y (in.)	Δ_u (in.)	μ_Δ
16.0	BF*	0.00318	2.19	10.80	4.92
16.5	BF	0.00309	2.19	10.80	4.93
17.0	CC**	0.00302	2.20	12.31	5.61
17.5	BF	0.00295	2.19	12.60	5.75
18.0***	BF	0.00288	2.17	12.60	5.80
18.5	BF	0.00282	2.18	12.60	5.77
19.0	BF	0.00275	2.18	12.60	5.78
19.5	BF	0.00269	2.18	12.60	5.79
20.0	BF	0.00264	2.17	12.60	5.80

*Bar Fracture
**Core Crushing
***Plastic hinge length was equal to 18.0 in. based on proposed modeling strategy.

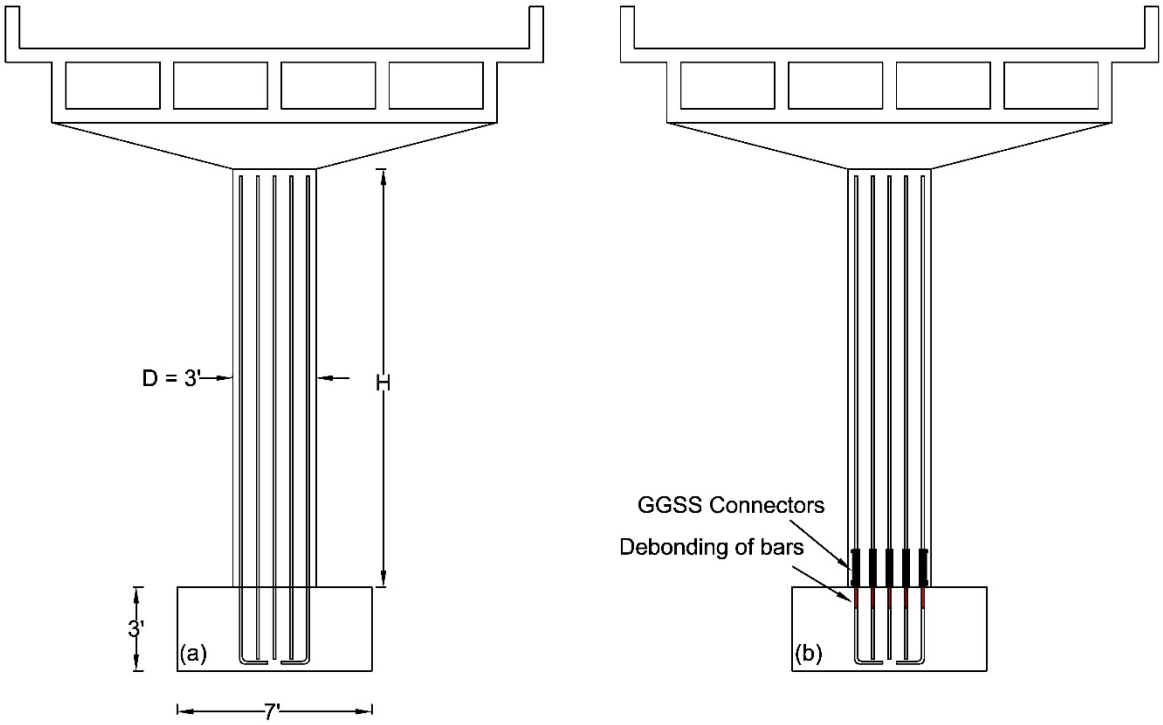

Fig. 5.1. Schematic of the two model types: (a) CIP; (b) Precast-2.

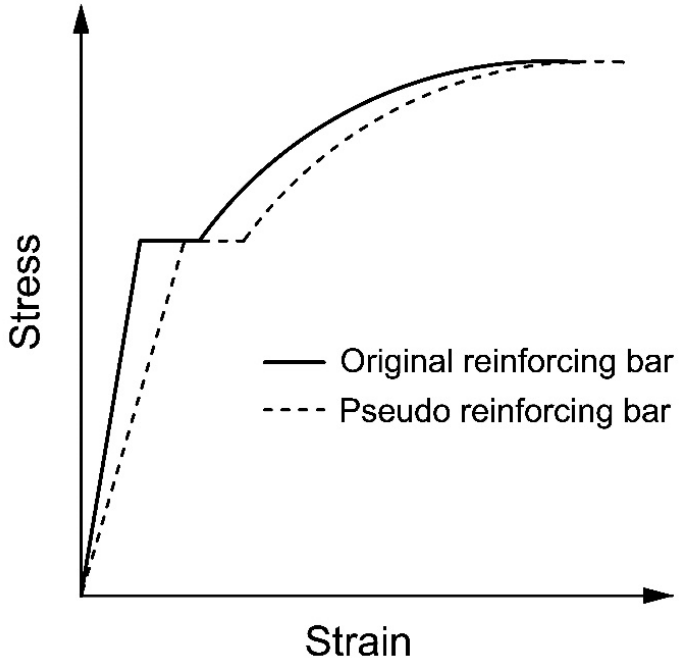

Fig. 5.2. Schematic of a pseudo stress-strain relationship.

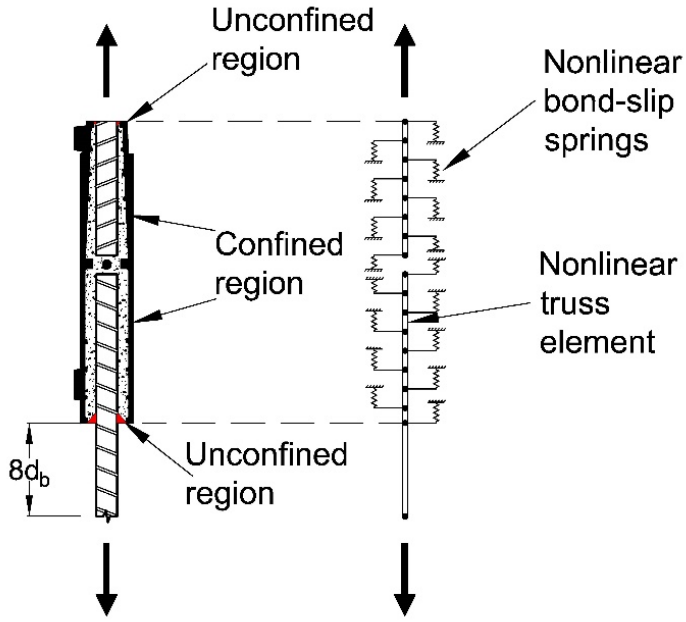

Fig. 5.3. Schematic of bond-slip idealization for precast column models.

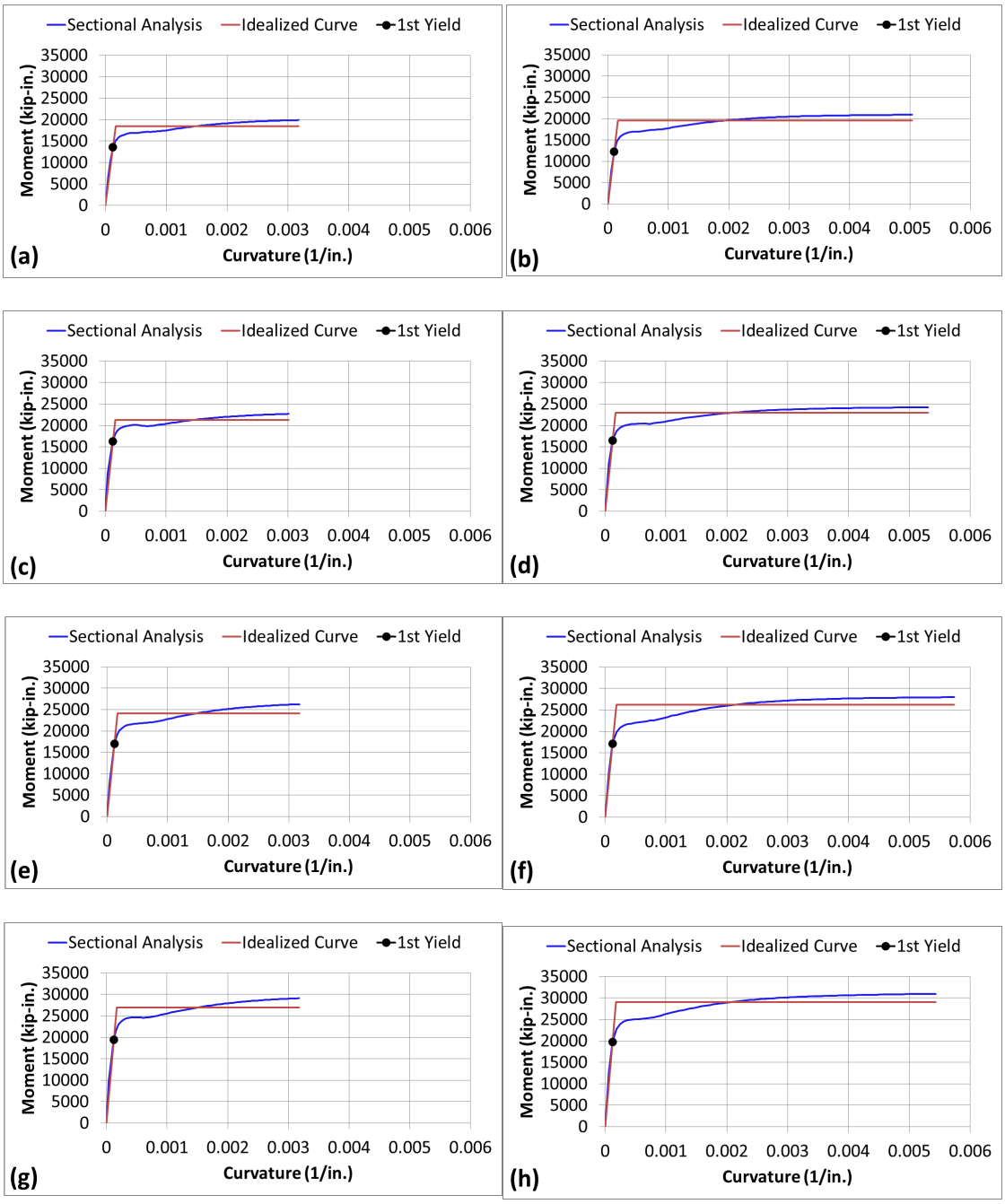

Fig. 5.4. Moment-curvature response for CIP models: (a) model 1 and 9, $\mu_\varphi = 19.04$; (b) model 3 and 11, $\mu_\varphi = 31.10$; (c) model 5 and 13, $\mu_\varphi = 18.80$; (d) model 7 and 15, $\mu_\varphi = 31.23$; (e) model 17 and 25, $\mu_\varphi = 18.29$; (f) model 19 and 27, $\mu_\varphi = 30.85$; (g) model 21 and 29, $\mu_\varphi = 18.75$; (h) model 23 and 31, $\mu_\varphi = 30.22$.

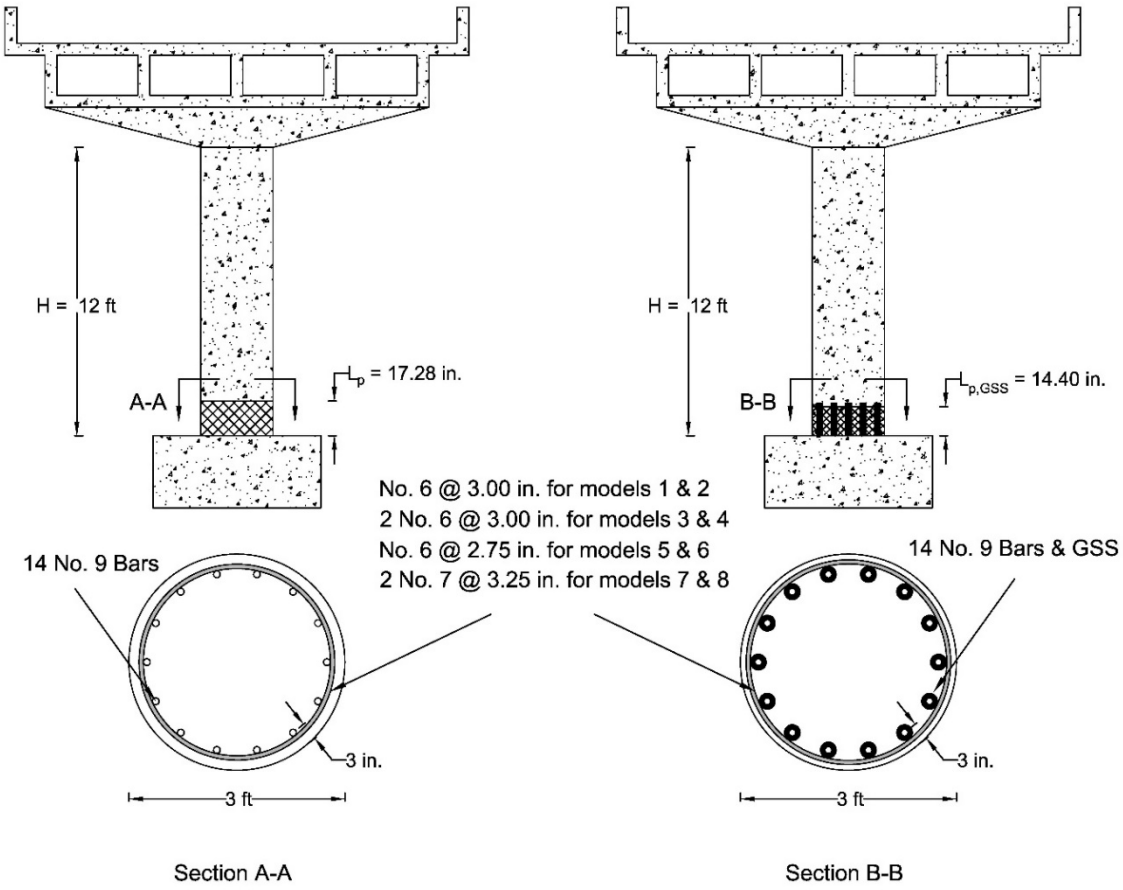

Fig. 5.5. Details of column models with H = 12 ft and 14 No. 9 bars.

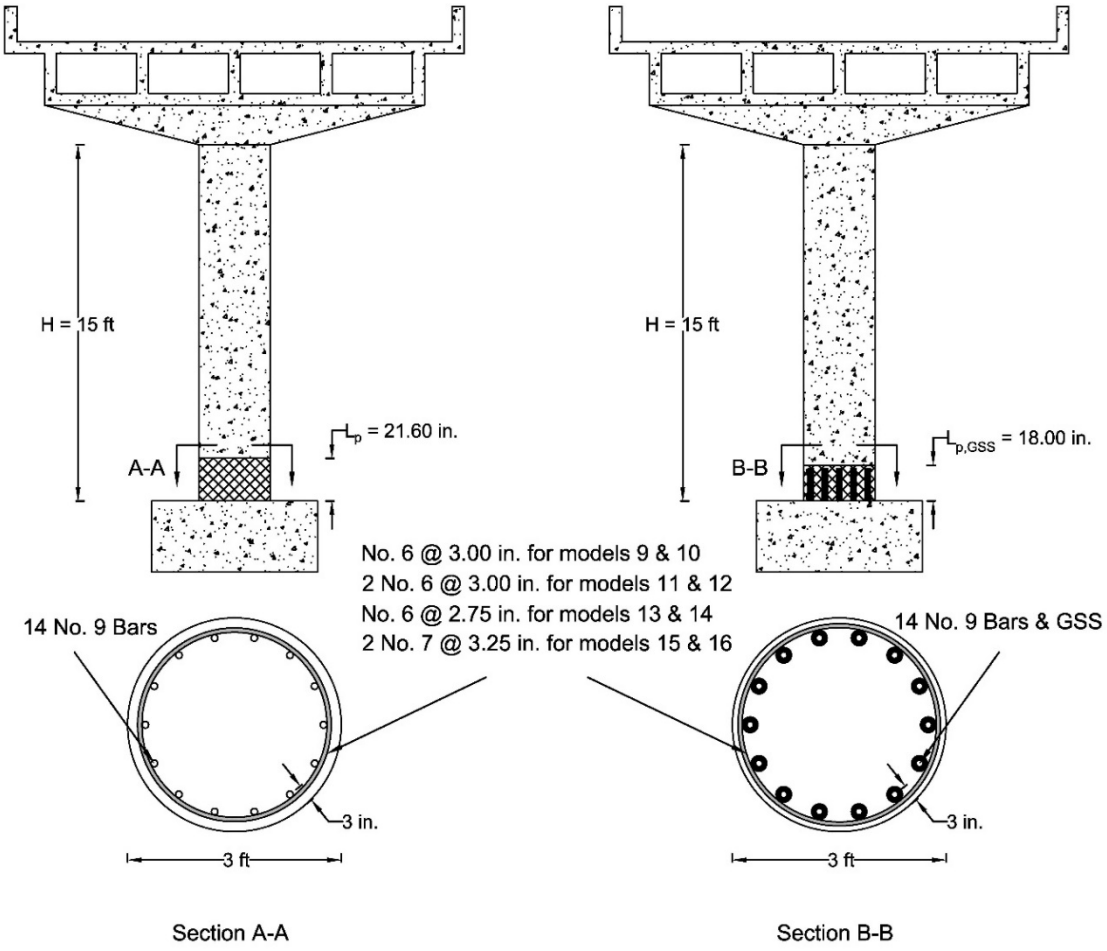

Fig. 5.6. Details of column models with H = 15 ft and 14 No. 9 bars.

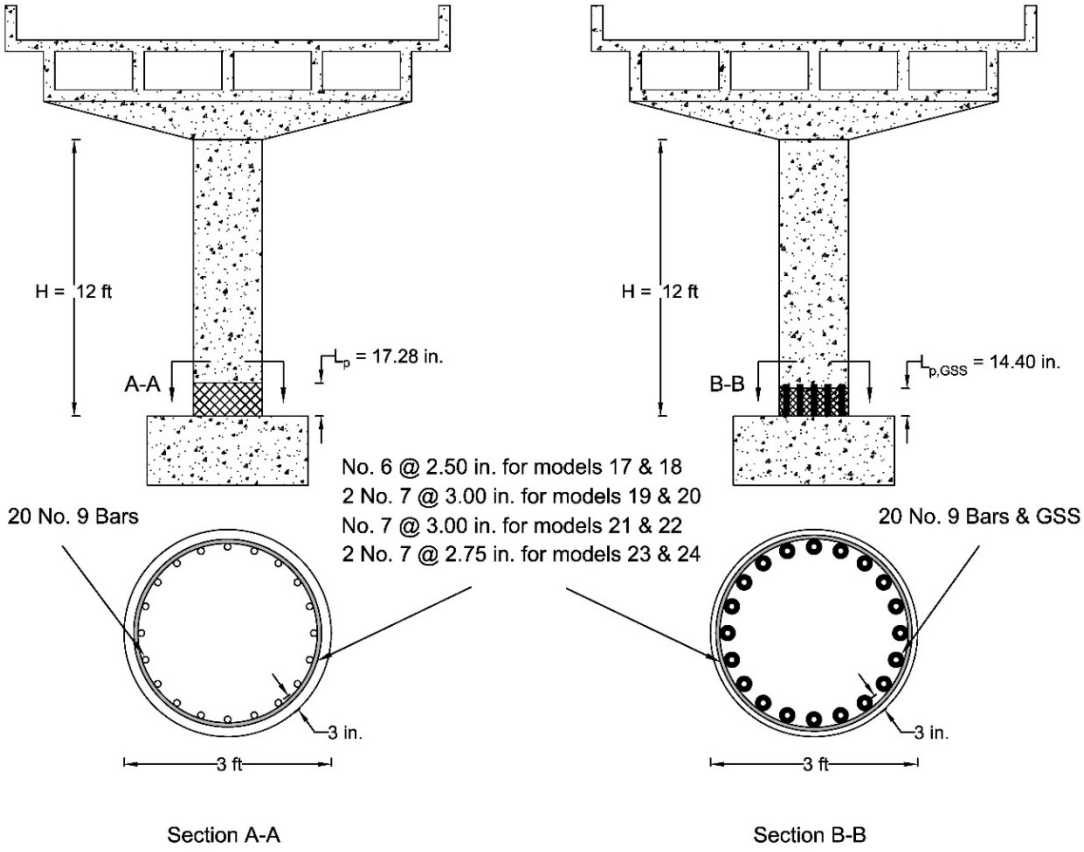

Fig. 5.7. Details of column models with H = 12 ft and 20 No. 9 bars.

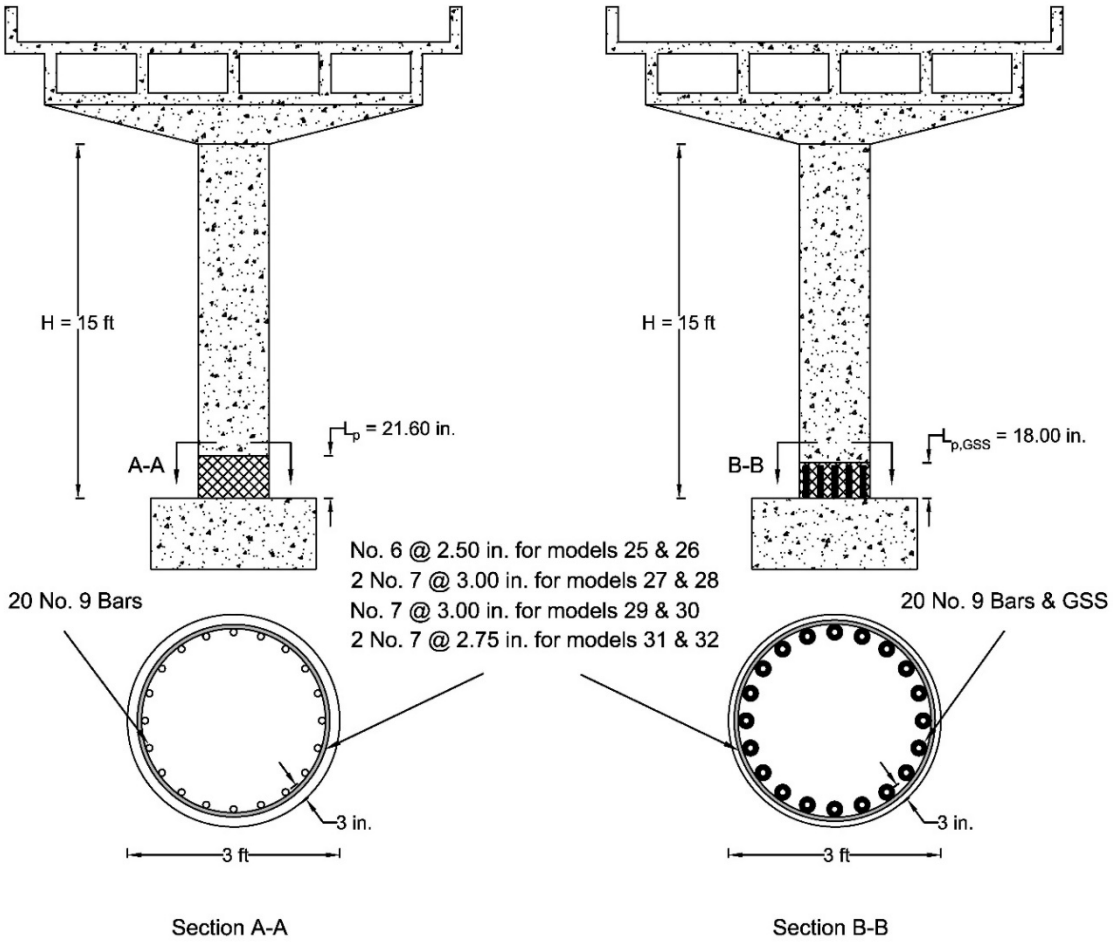

Fig. 5.8. Details of column models with H = 15 ft and 20 No. 9 bars.

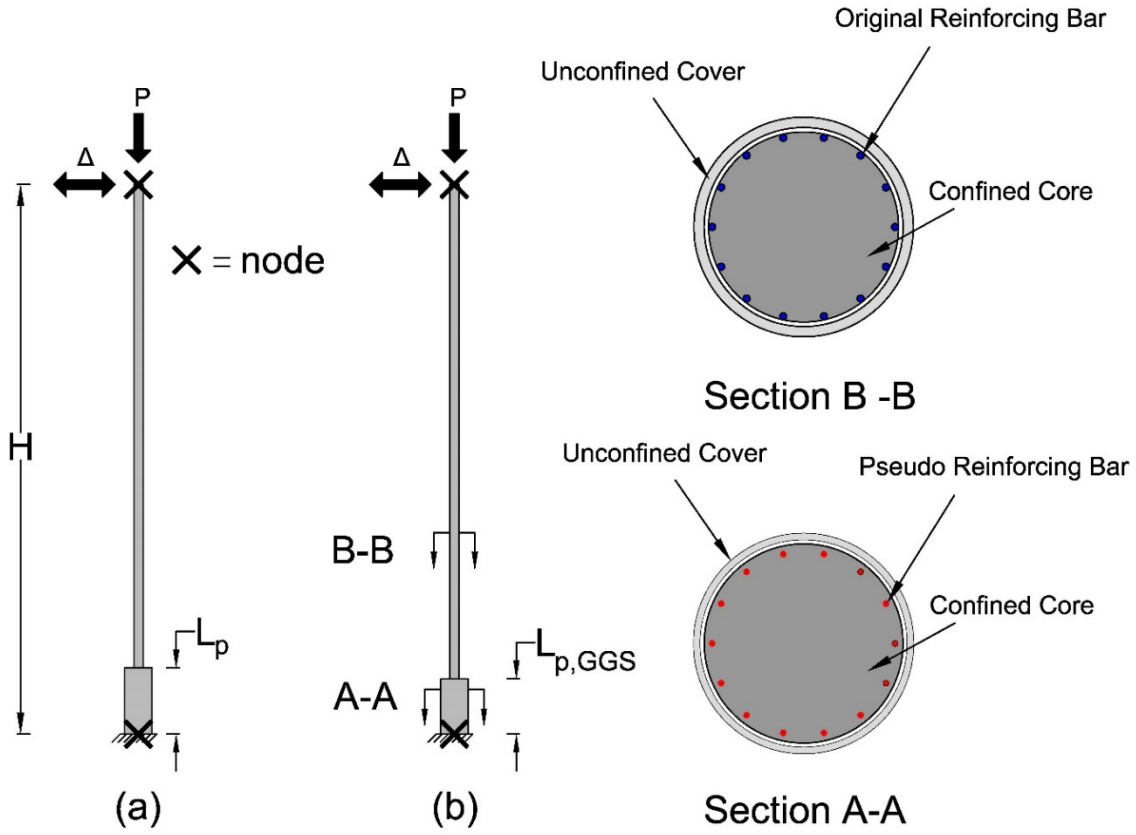

Fig. 5.9. Example of column model layout: (a) column model 9 (CIP); (b) column model 10 (Precast-2).

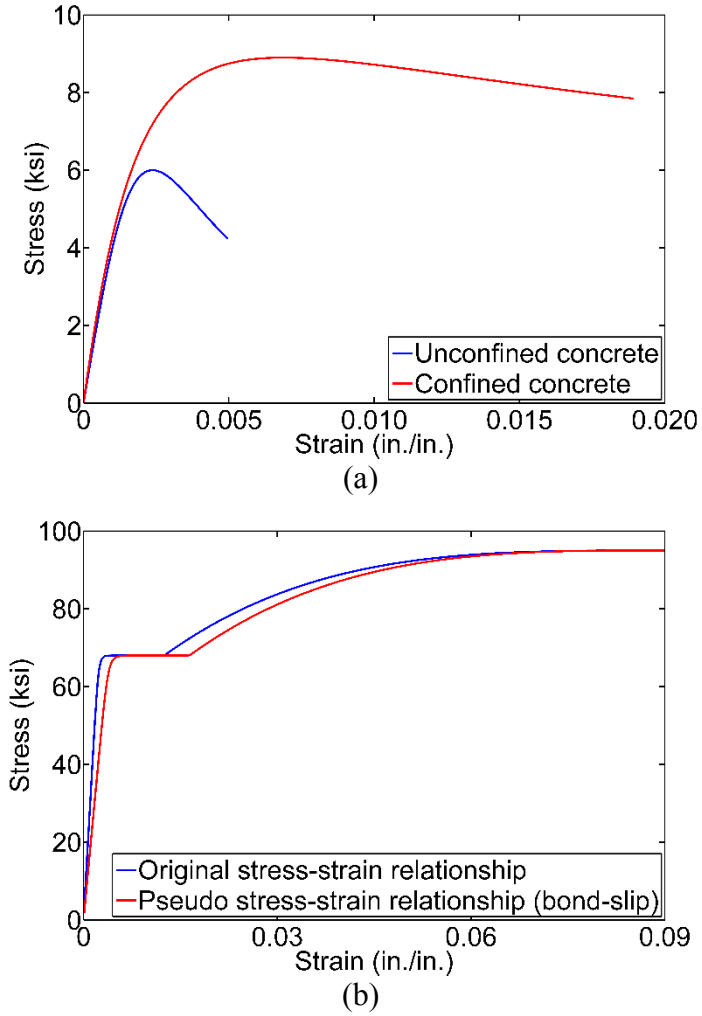

Fig. 5.10. Uniaxial material properties for column model 10: (a) concrete (CIP); (b) reinforcing bar.

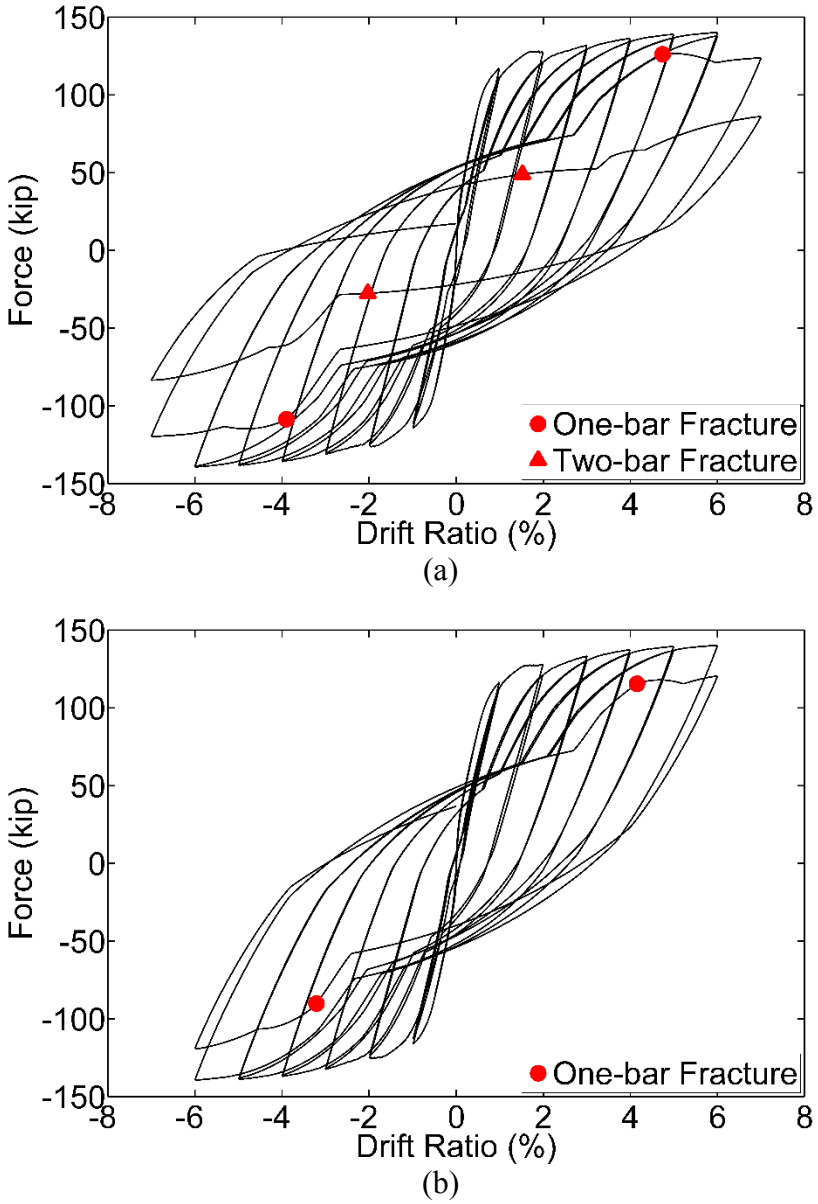

Fig. 5.11. Example of hysteresis response: (a) column model 1 (with CIP details), ultimate drift = 6.0%; (b) column model 2 (with Precast-2 details), ultimate drift = 6.0%.

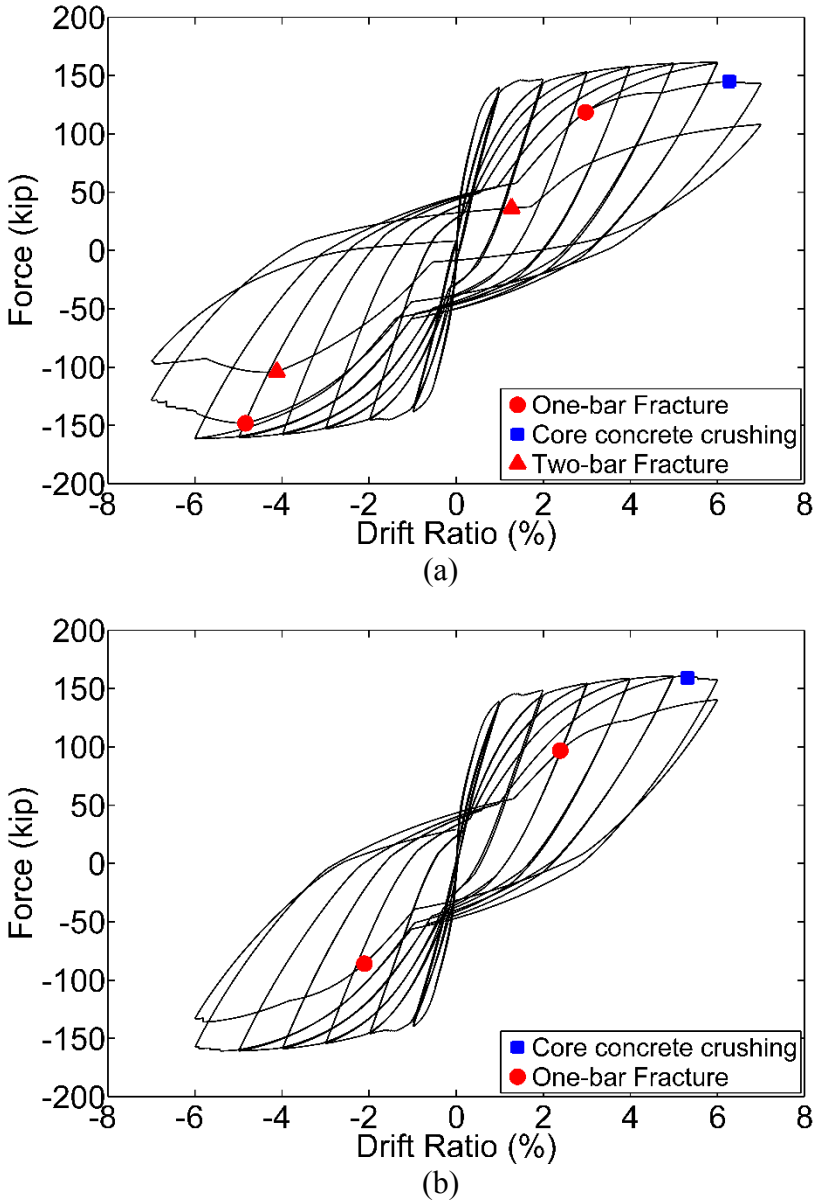

Fig. 5.12. Example of hysteresis response: (a) column model 5 (with CIP details), ultimate drift = 6.0%; (b) column model 6 (with Precast-2 details), ultimate drift = 5.3%.

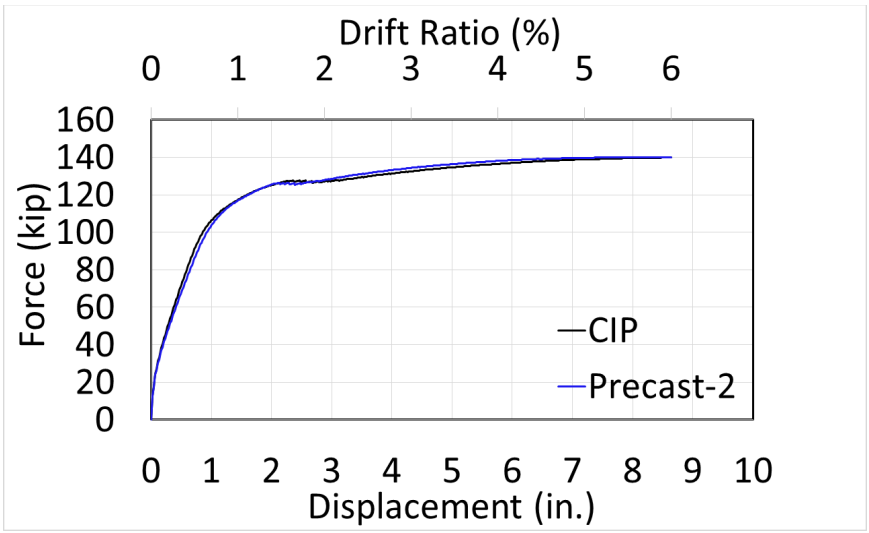

(a)

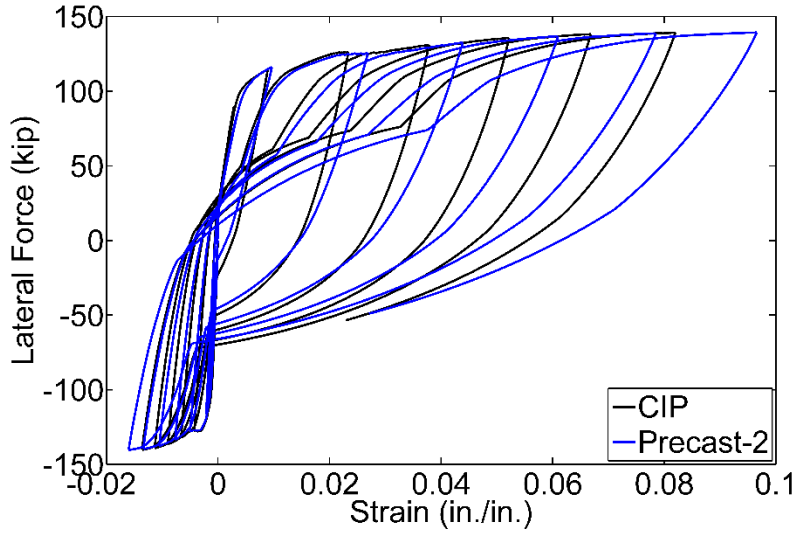

(b)

Fig. 5.13. Comparison of column model 1 (CIP) and 2 (Precast-2): (a) cyclic envelope; (b) strains in the column extreme bar.

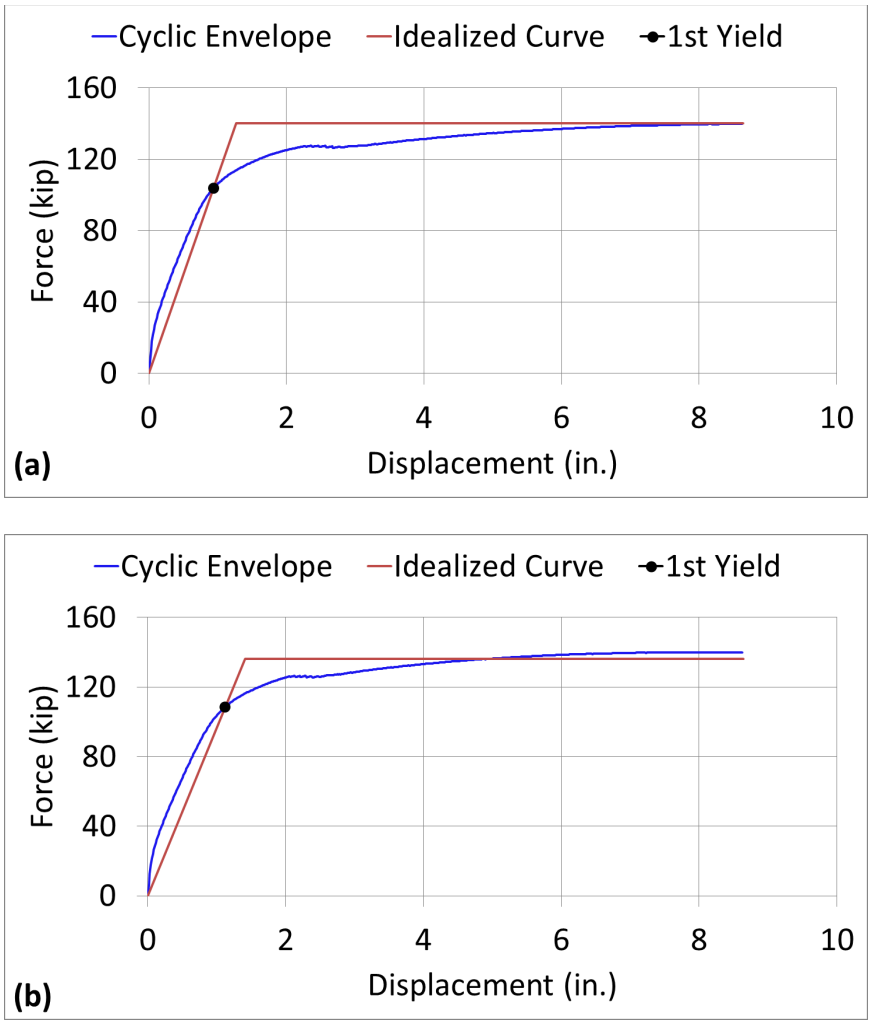

Fig. 5.14. Displacement ductility capacity: (a) column model 1 (CIP), $\mu_C = 6.82$; (b) column model 2 (Precast-2), $\mu_C = 6.13$.

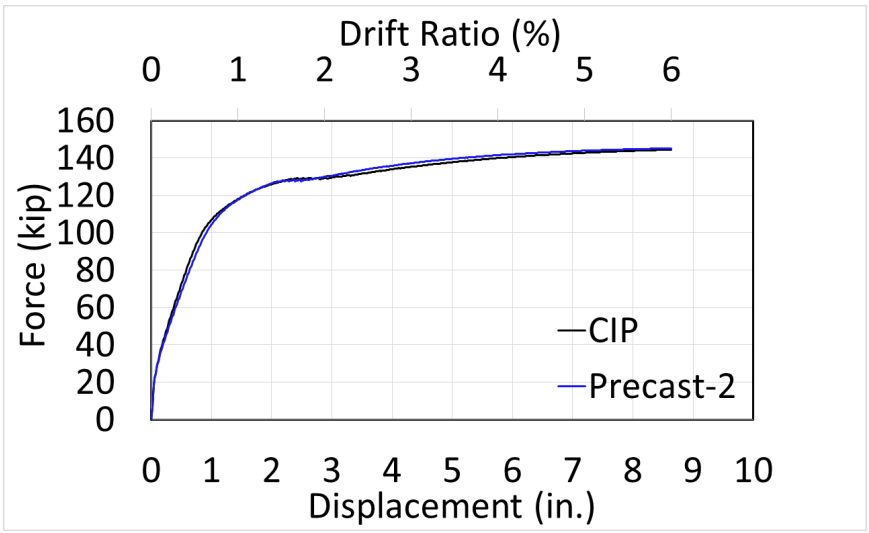

(a)

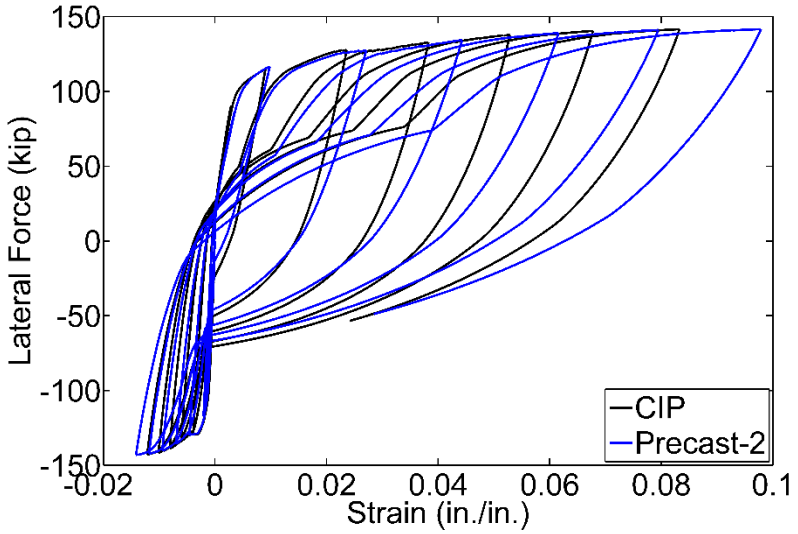

(b)

Fig. 5.15. Comparison of column model 3 (CIP) and 4 (Precast-2): (a) cyclic envelope; (b) strains in the column extreme bar.

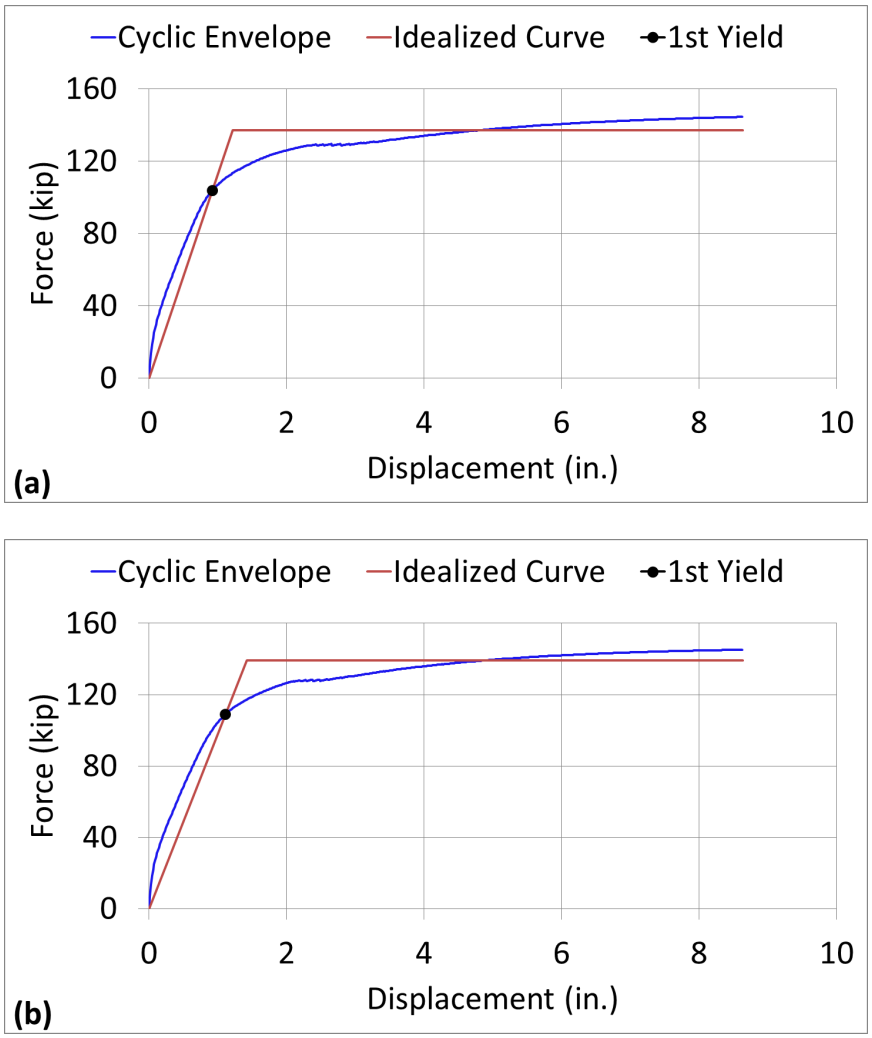

Fig. 5.16. Displacement ductility capacity: (a) column model 3 (CIP), $\mu_C = 7.11$; (b) column model 4 (Precast-2), $\mu_C = 6.09$.

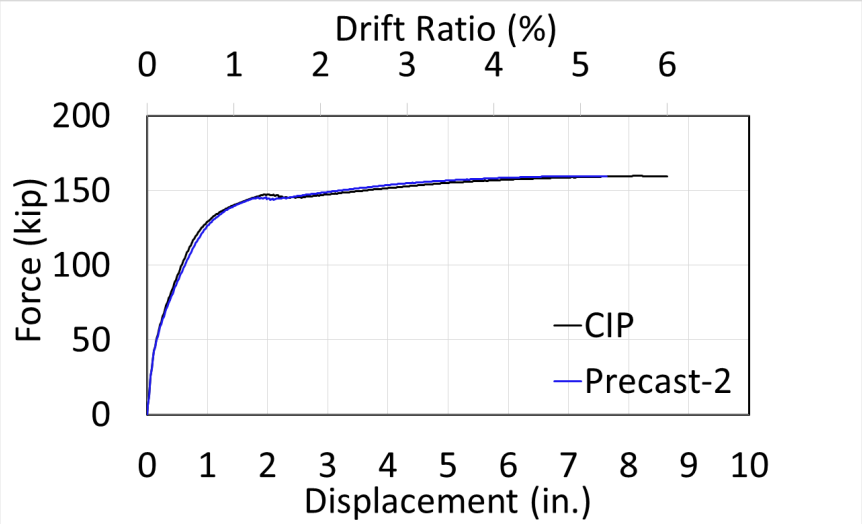

(a)

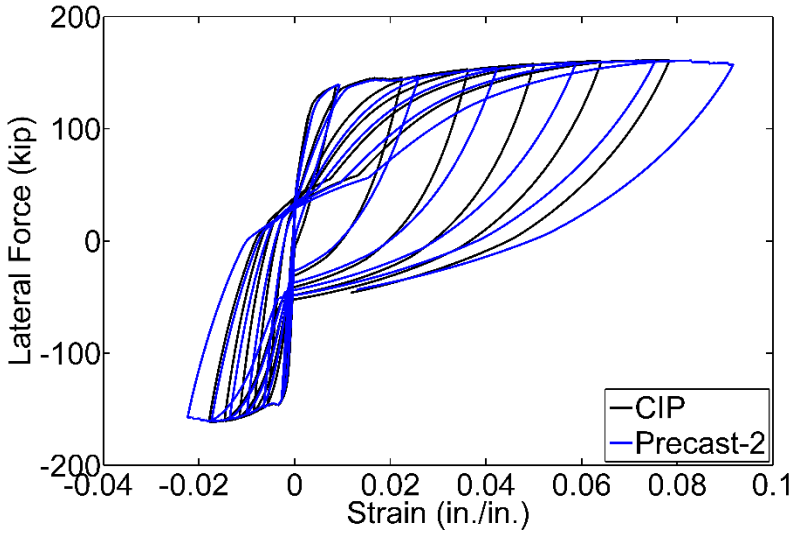

(b)

Fig. 5.17. Comparison of column model 5 (CIP) and 6 (Precast-2): (a) cyclic envelope; (b) strains in the column extreme bar.

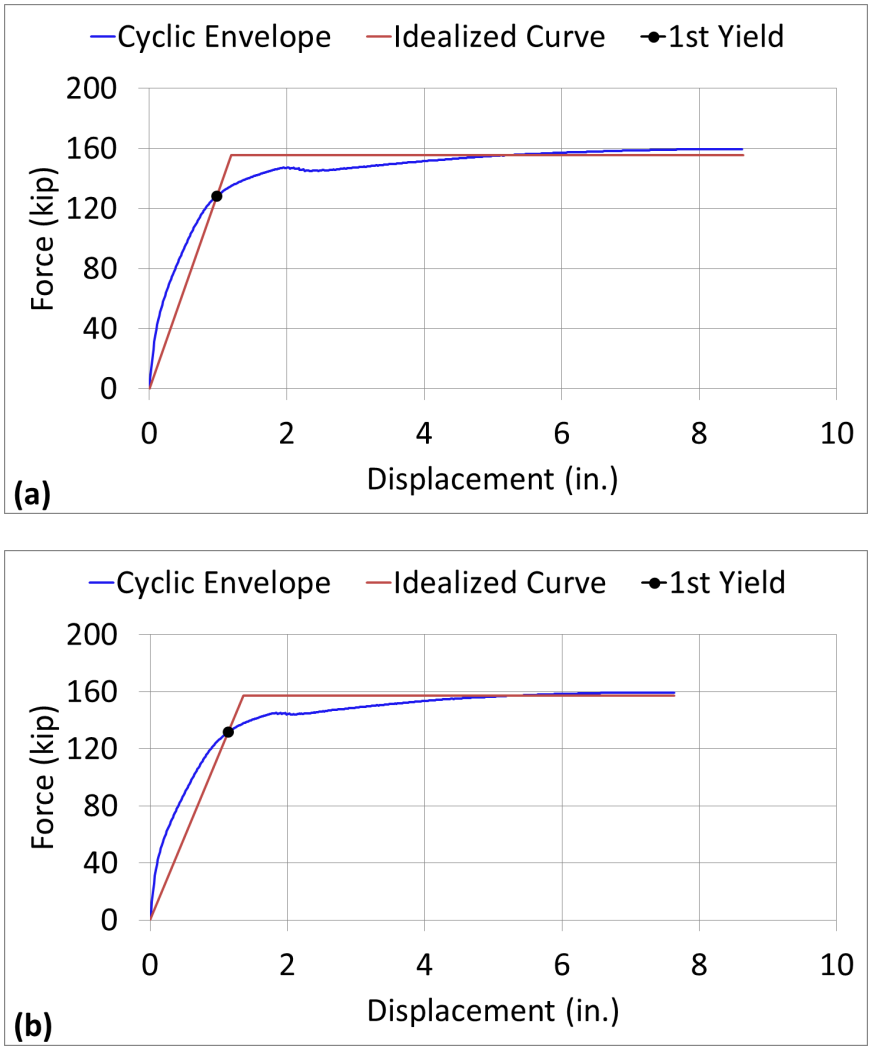

Fig. 5.18. Displacement ductility capacity: (a) column model 5 (CIP), $\mu_C = 7.27$; (b) column model 6 (Precast-2), $\mu_C = 5.62$.

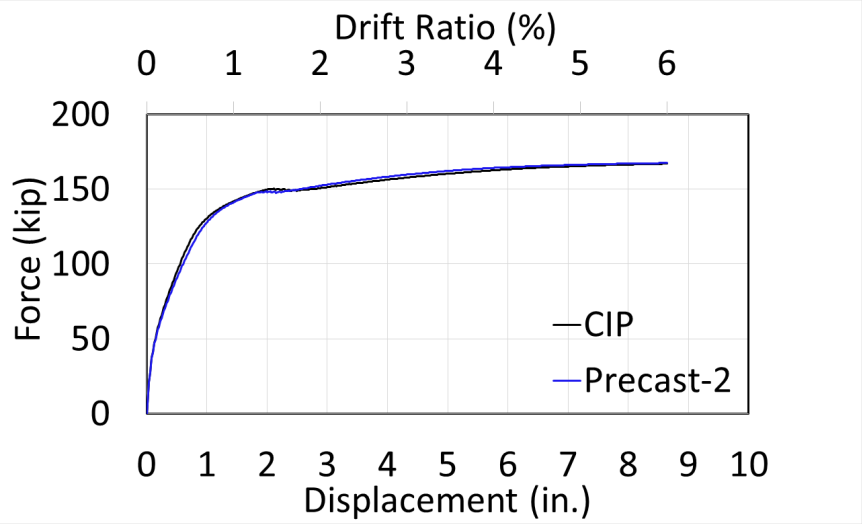

(a)

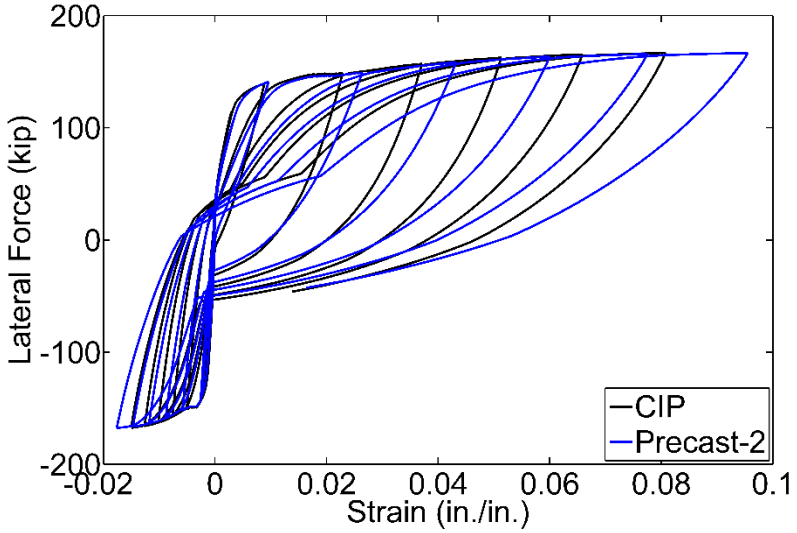

(b)

Fig. 5.19. Comparison of column model 7 (CIP) and 8 (Precast-2): (a) cyclic envelope; (b) strains in the column extreme bar.

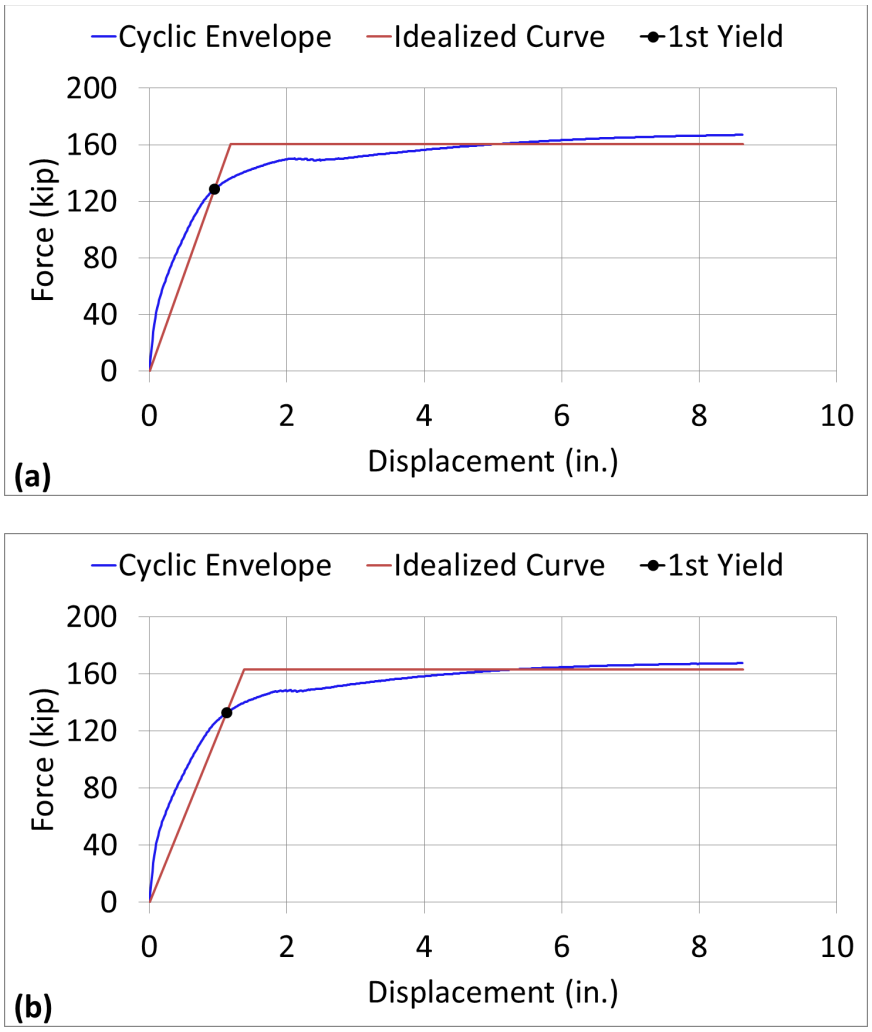

Fig. 5.20. Displacement ductility capacity: (a) column model 7 (CIP), $\mu_C = 7.28$; (b) column model 8 (Precast-2), $\mu_C = 6.27$.

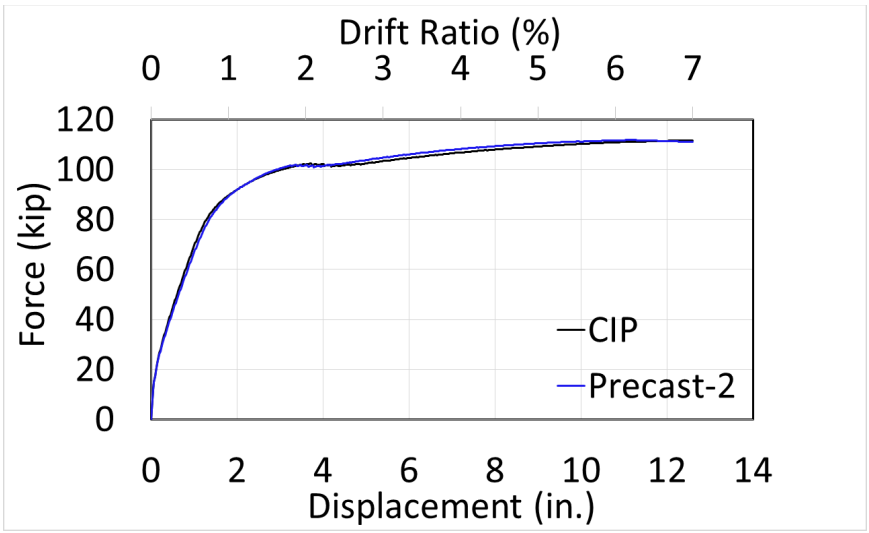

(a)

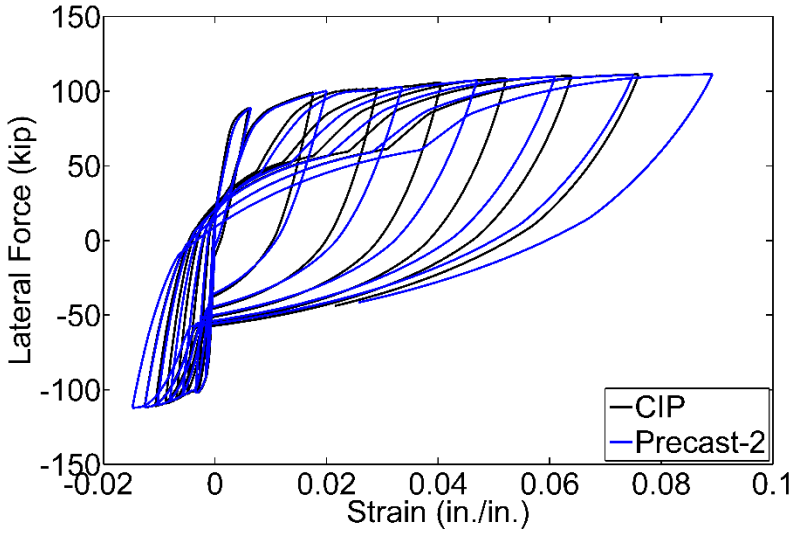

(b)

Fig. 5.21. Comparison of column model 9 (CIP) and 10 (Precast-2): (a) cyclic envelope; (b) strains in the column extreme bar.

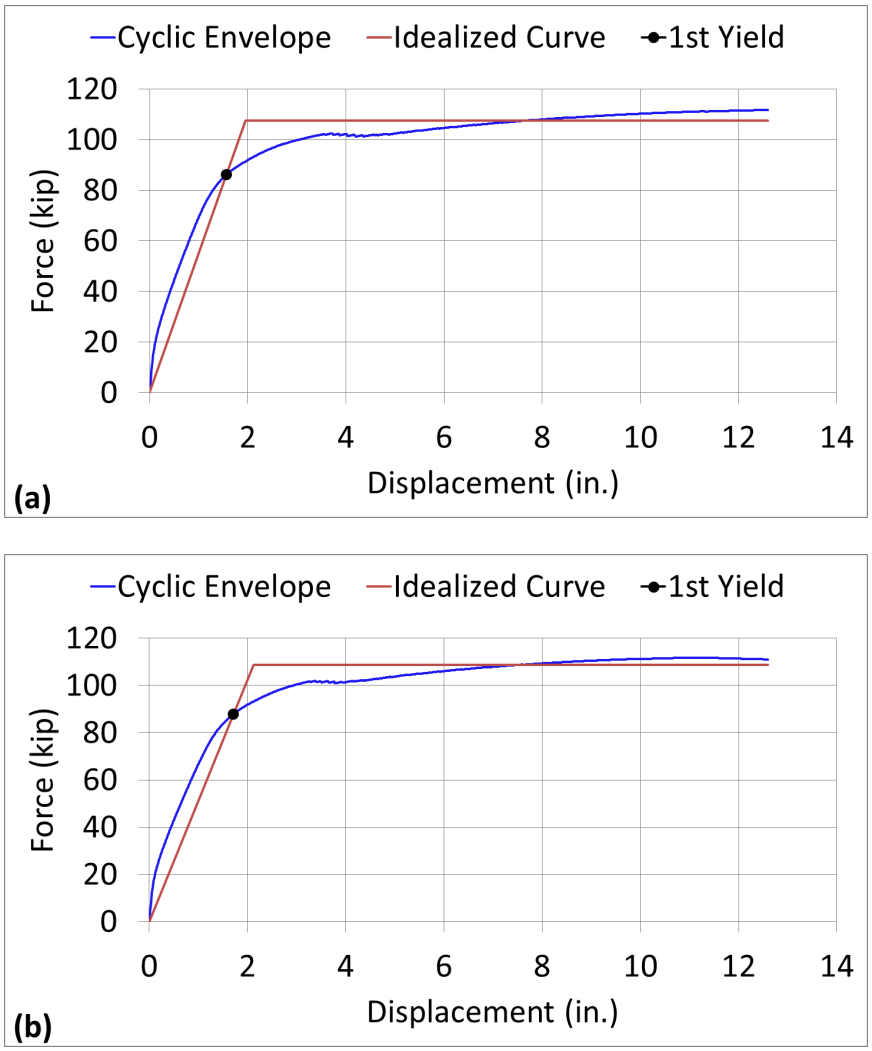

Fig. 5.22. Displacement ductility capacity: (a) column model 9 (CIP), $\mu_C = 6.45$; (b) column model 10 (Precast-2), $\mu_C = 5.95$.

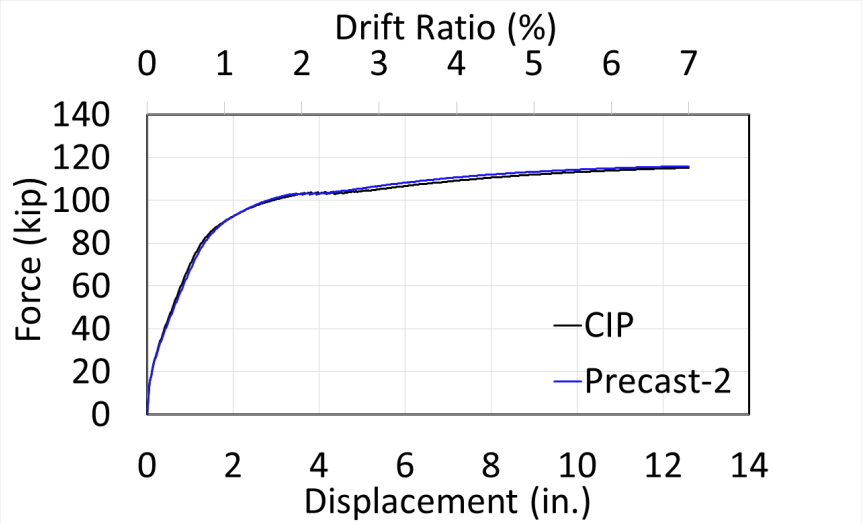

(a)

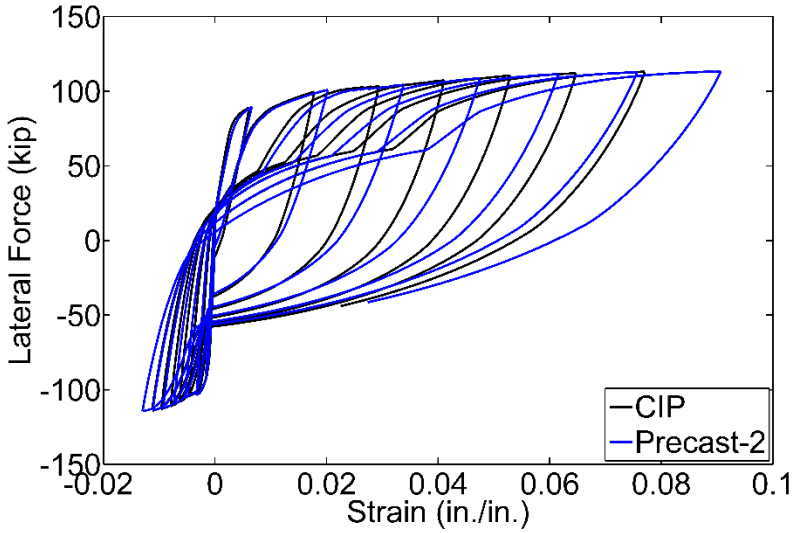

(b)

Fig. 5.23. Comparison of column model 11 (CIP) and 12 (Precast-2): (a) cyclic envelope; (b) strains in the column extreme bar.

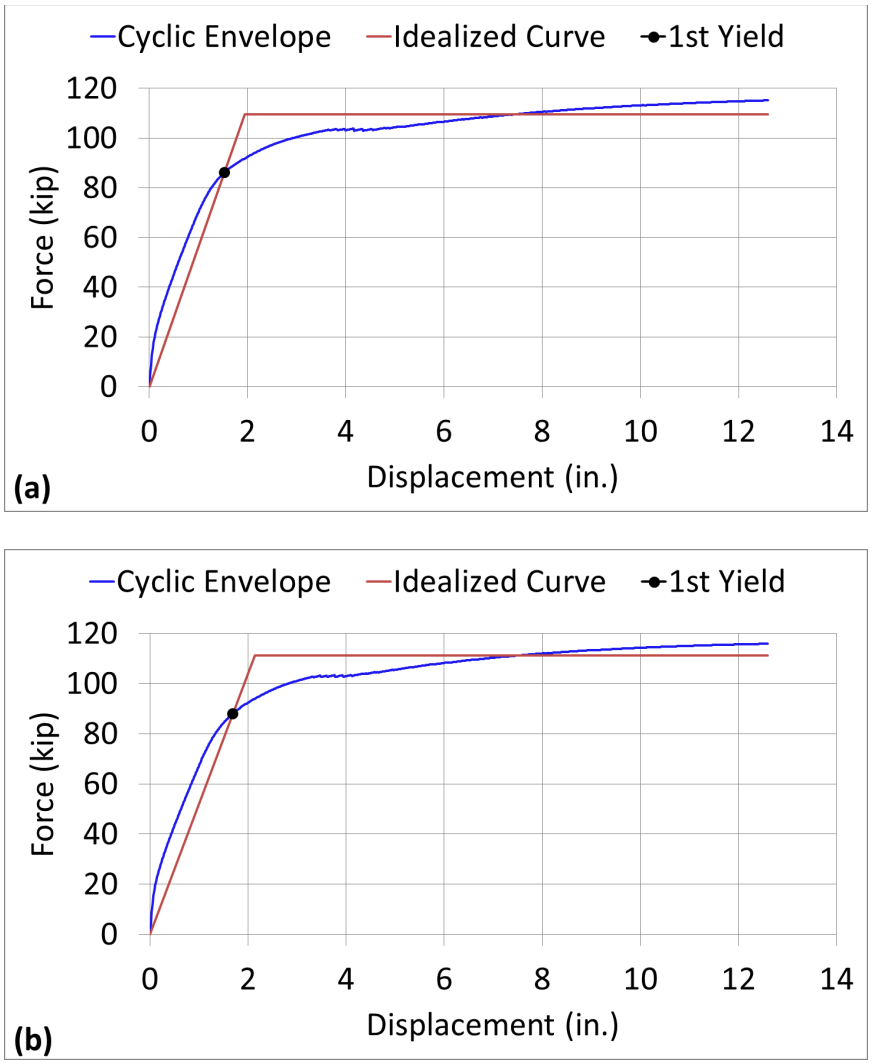

Fig. 5.24. Displacement ductility capacity: (a) column model 11 (CIP), $\mu_C = 6.47$; (b) column model 12 (Precast-2), $\mu_C = 5.90$.

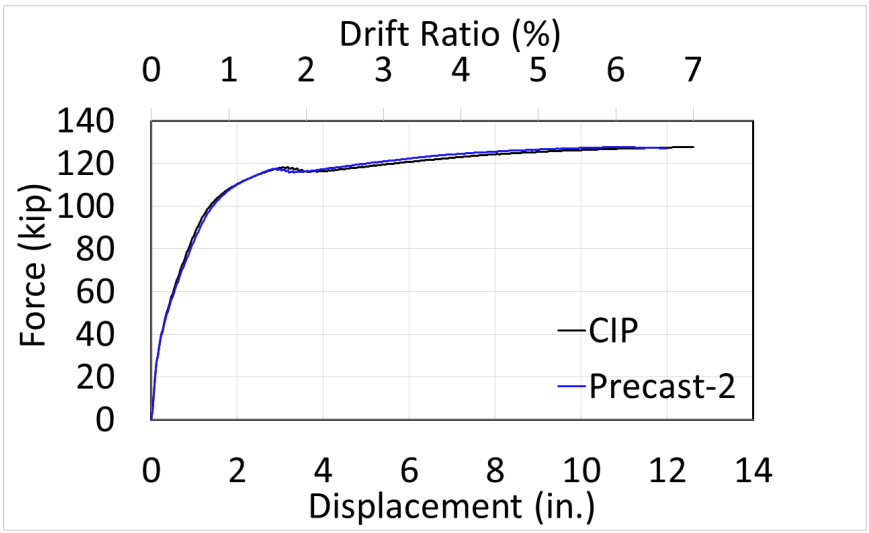

(a)

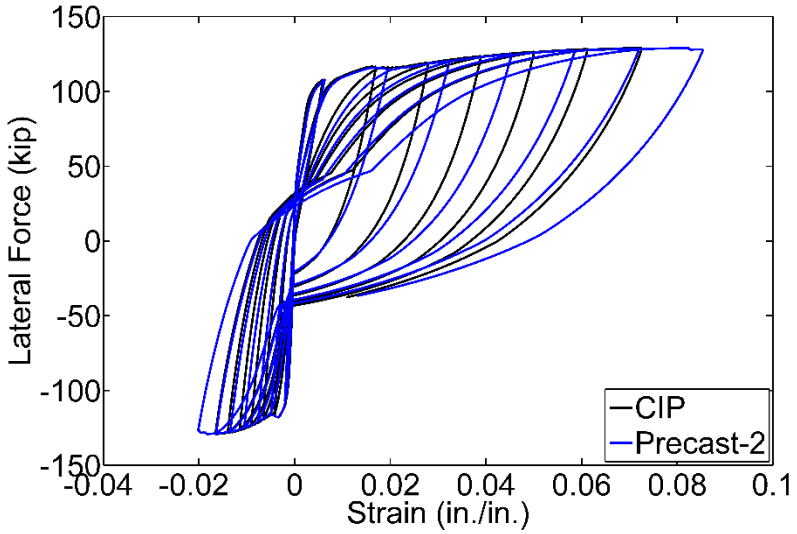

(b)

Fig. 5.25. Comparison of column model 13 (CIP) and 14 (Precast-2): (a) cyclic envelope; (b) strains in the column extreme bar.

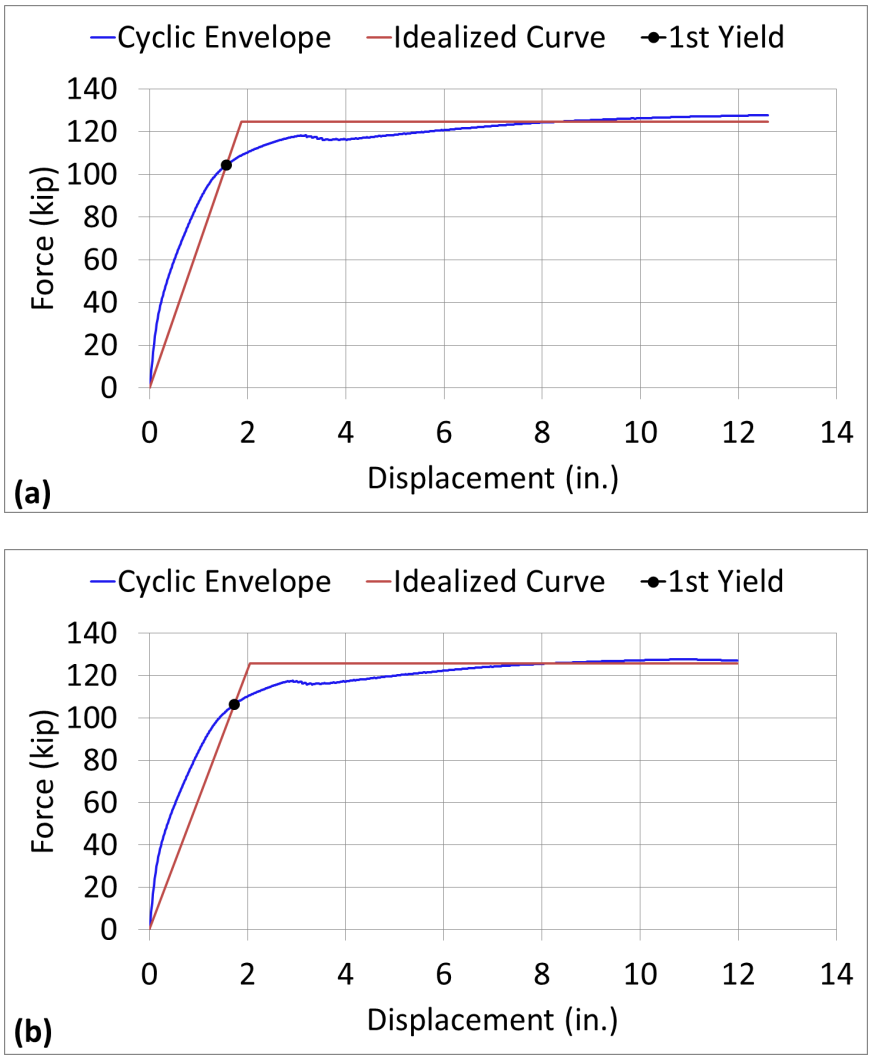

Fig. 5.26. Displacement ductility capacity: (a) column model 13 (CIP), $\mu_C = 6.75$; (b) column model 14 (Precast-2), $\mu_C = 5.86$.

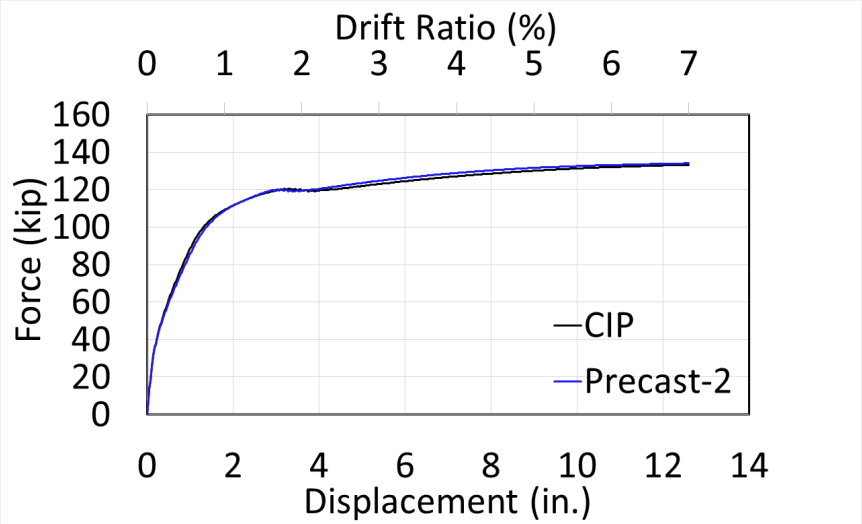

(a)

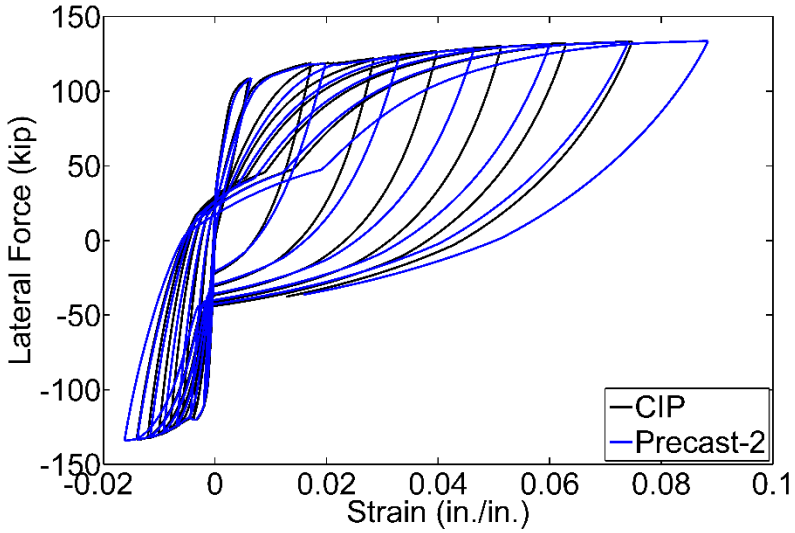

(b)

Fig. 5.27. Comparison of column model 15 (CIP) and 16 (Precast-2): (a) cyclic envelope; (b) strains in the column extreme bar.

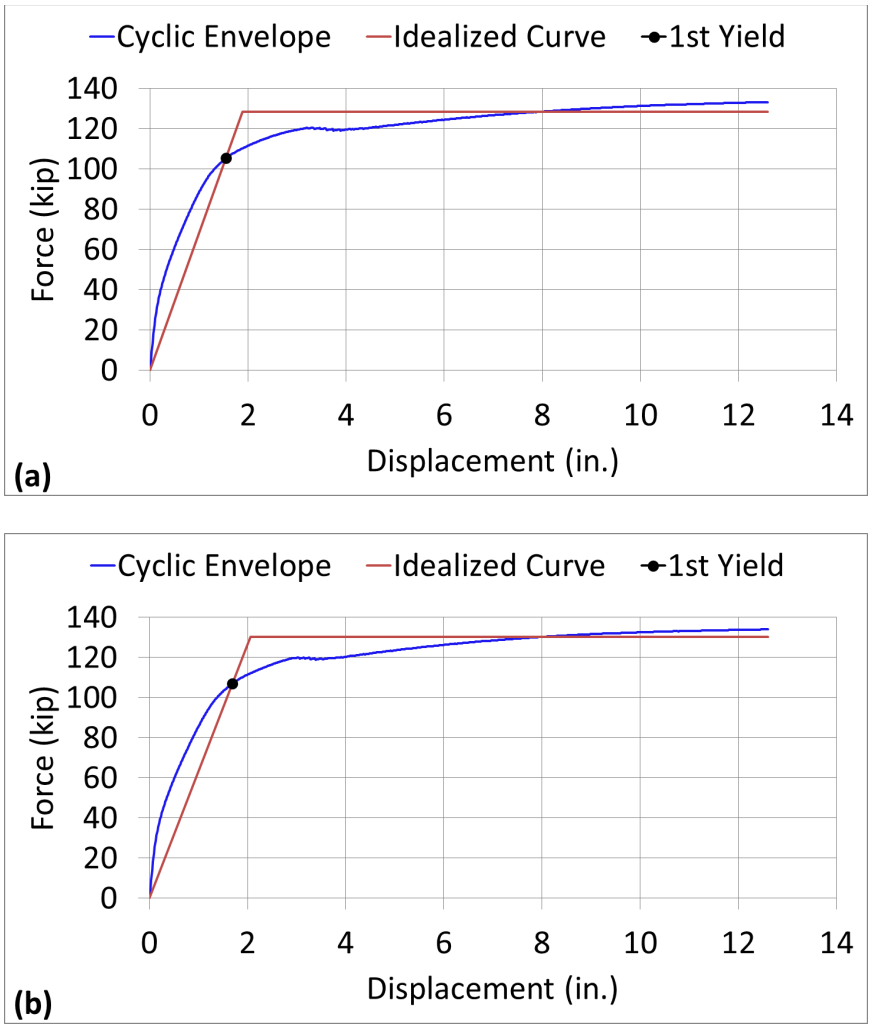

Fig. 5.28. Displacement ductility capacity: (a) column model 15 (CIP), $\mu_C = 6.67$; (b) column model 16 (Precast-2), $\mu_C = 6.12$.

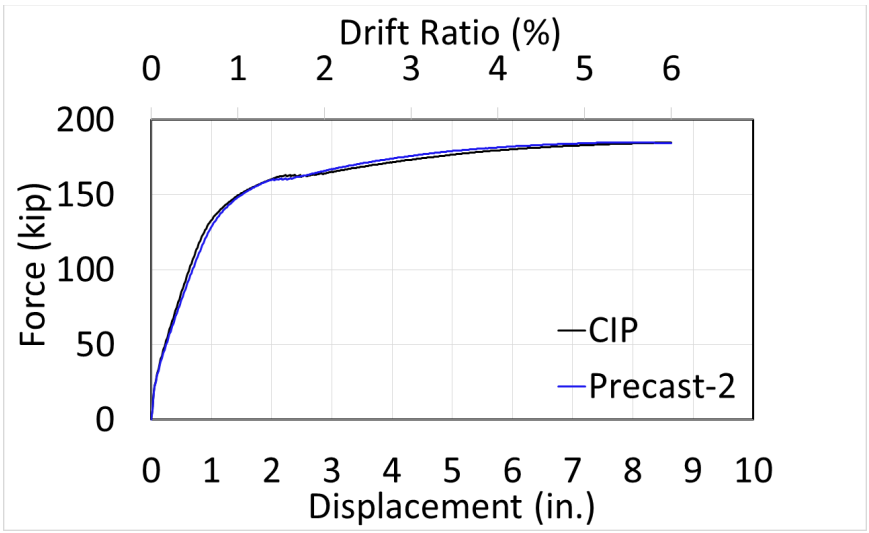

(a)

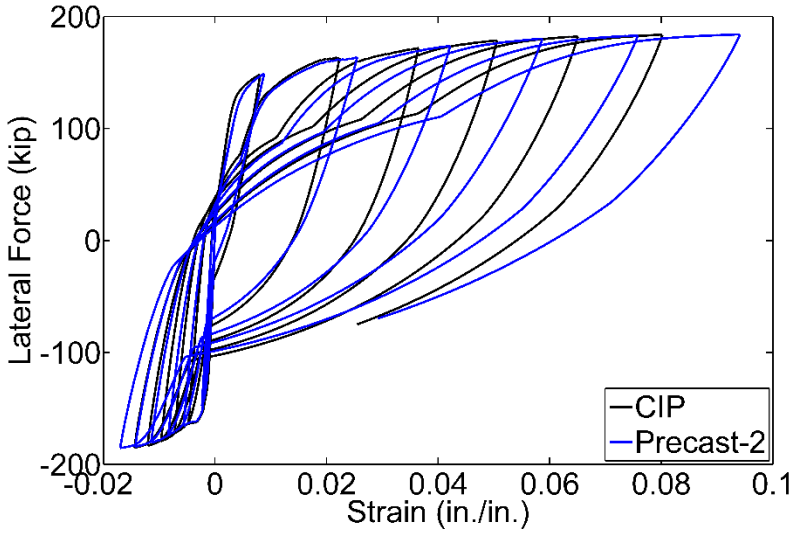

(b)

Fig. 5.29. Comparison of column model 17 (CIP) and 18 (Precast-2): (a) cyclic envelope; (b) strains in the column extreme bar.

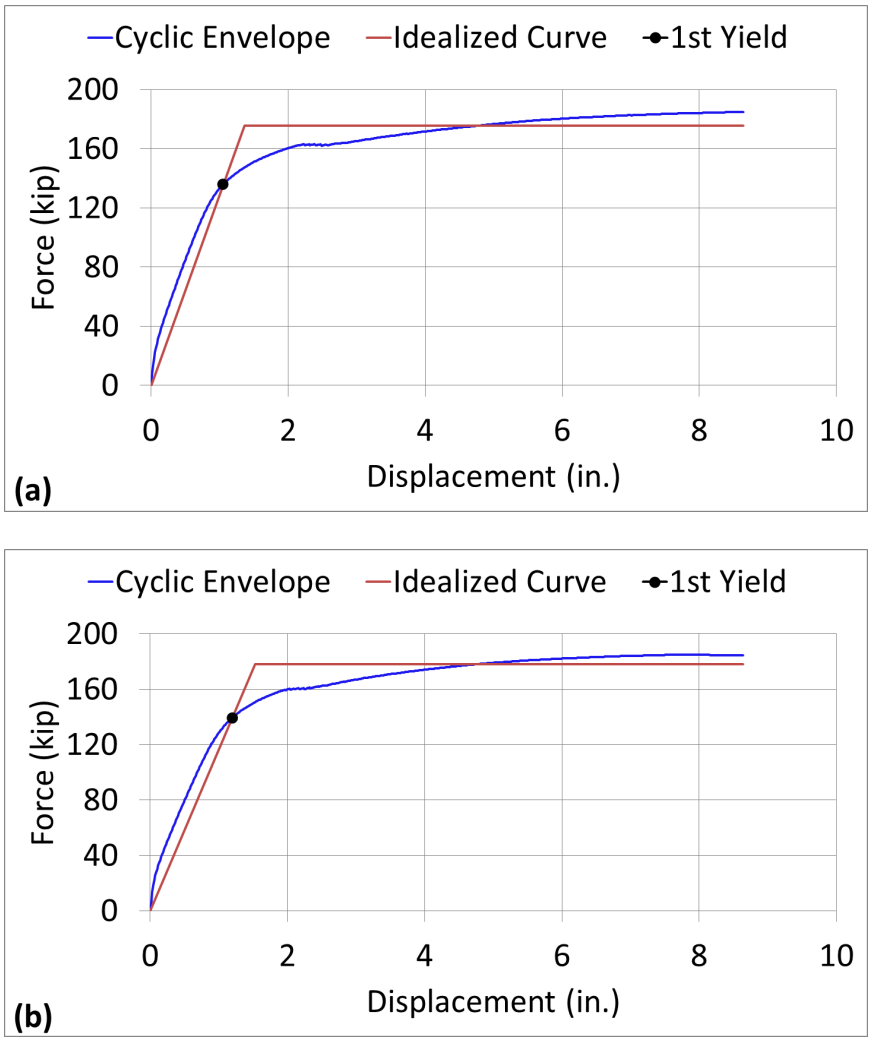

Fig. 5.30. Displacement ductility capacity: (a) column model 17 (CIP), $\mu_c = 6.35$; (b) column model 18 (Precast-2), $\mu_c = 5.66$.

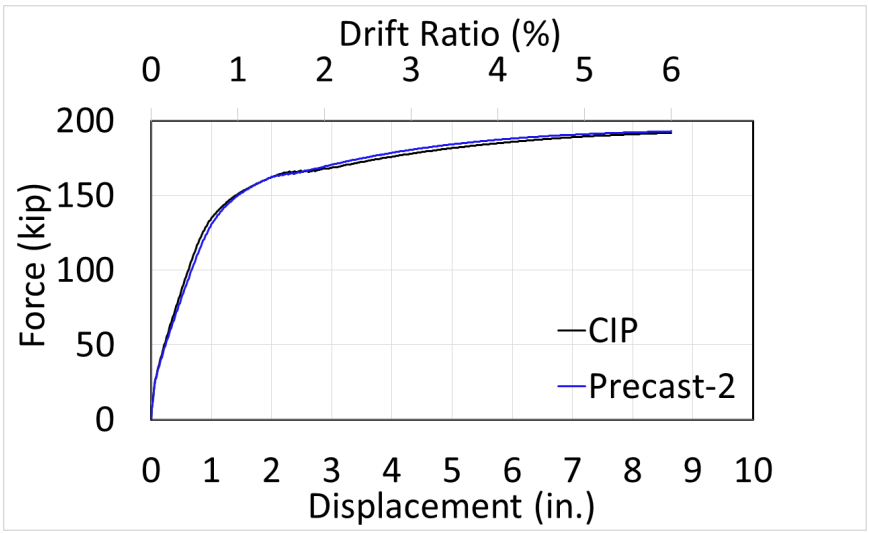

(a)

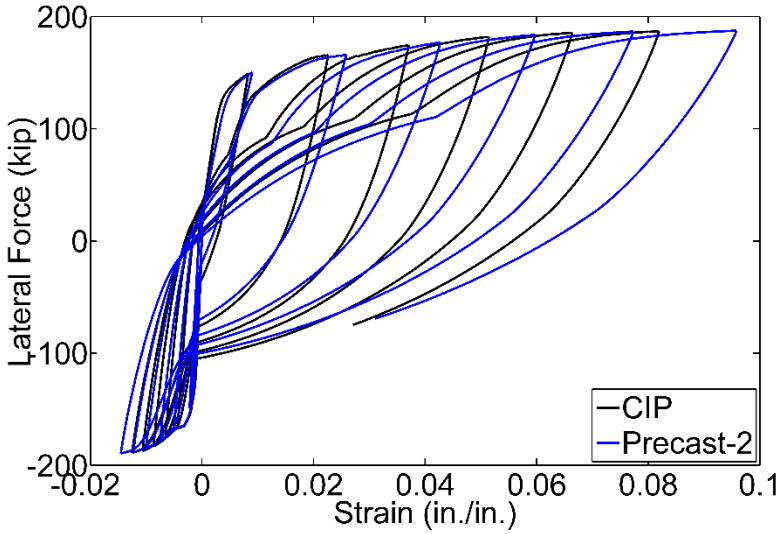

(b)

Fig. 5.31. Comparison of column model 19 (CIP) and 20 (Precast-2): (a) cyclic envelope; (b) strains in the column extreme bar.

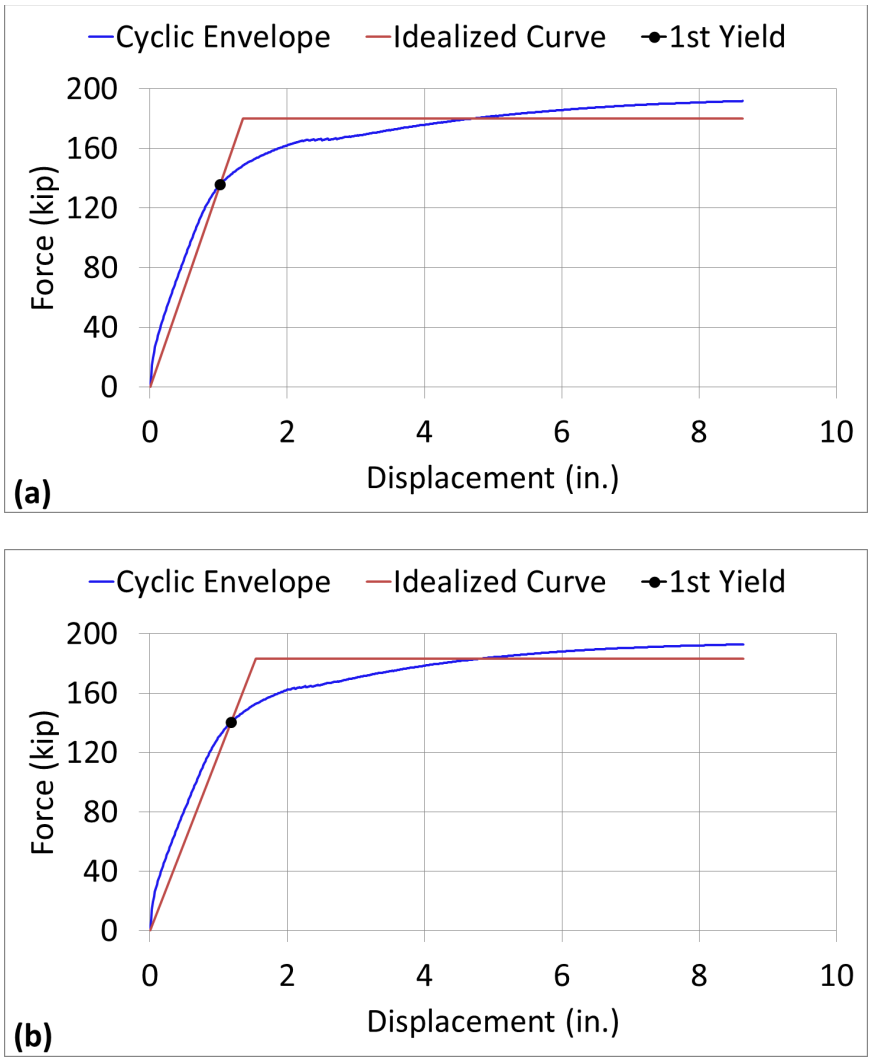

Fig. 5.32. Displacement ductility capacity: (a) column model 19 (CIP), $\mu_C = 6.37$; (b) column model 20 (Precast-2), $\mu_C = 5.61$.

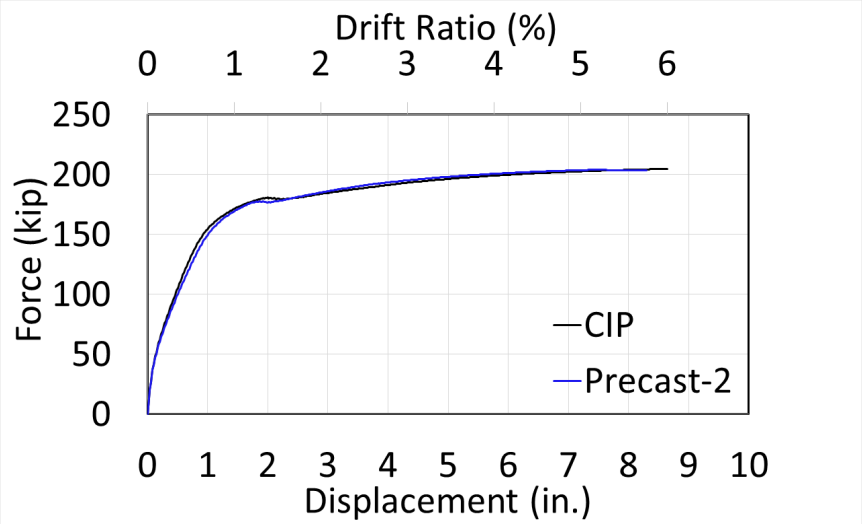

(a)

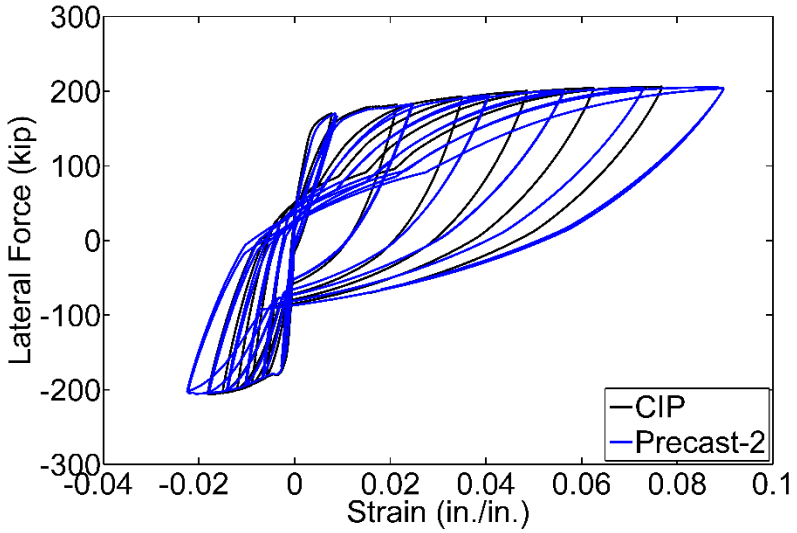

(b)

Fig. 5.33. Comparison of column model 21 (CIP) and 22 (Precast-2): (a) cyclic envelope; (b) strains in the column extreme bar.

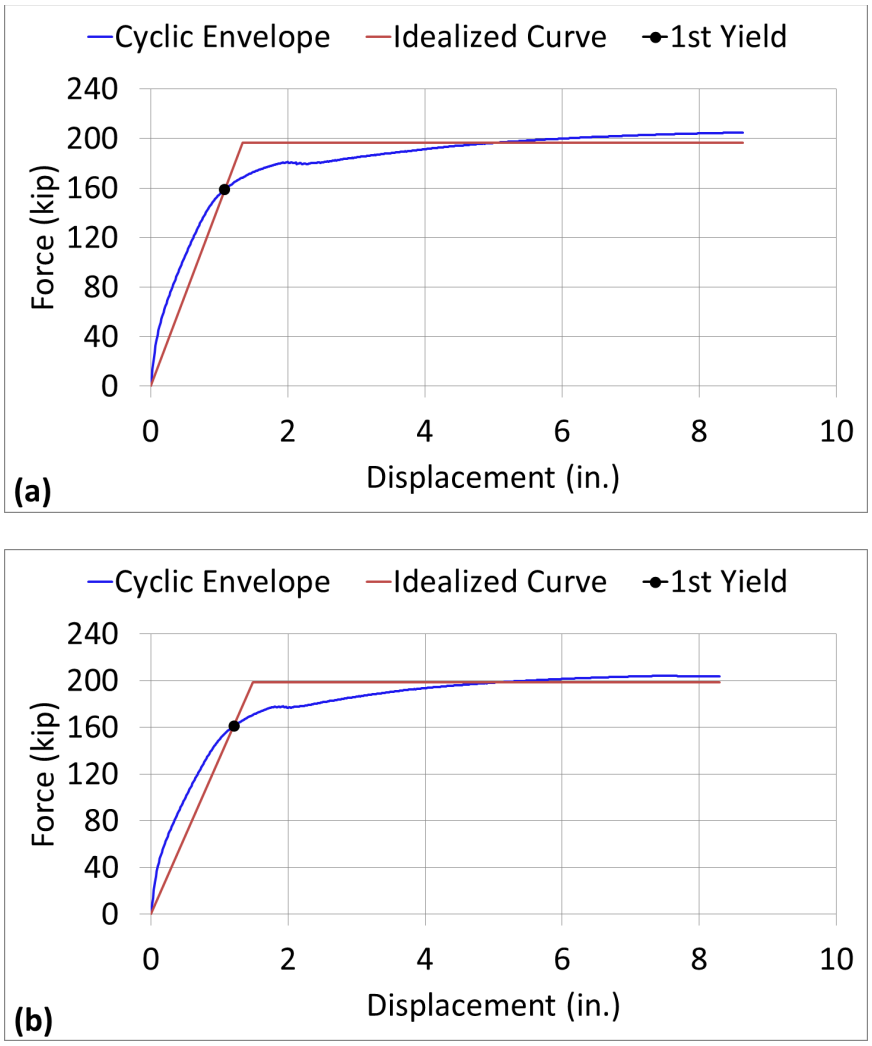

Fig. 5.34. Displacement ductility capacity: (a) column model 21 (CIP), $\mu_C = 6.46$; (b) column model 22 (Precast-2), $\mu_C = 5.57$.

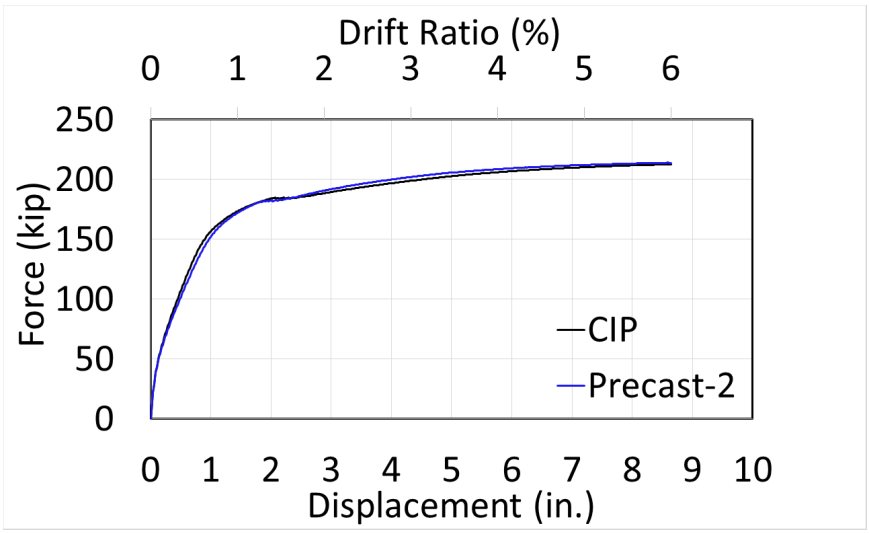

(a)

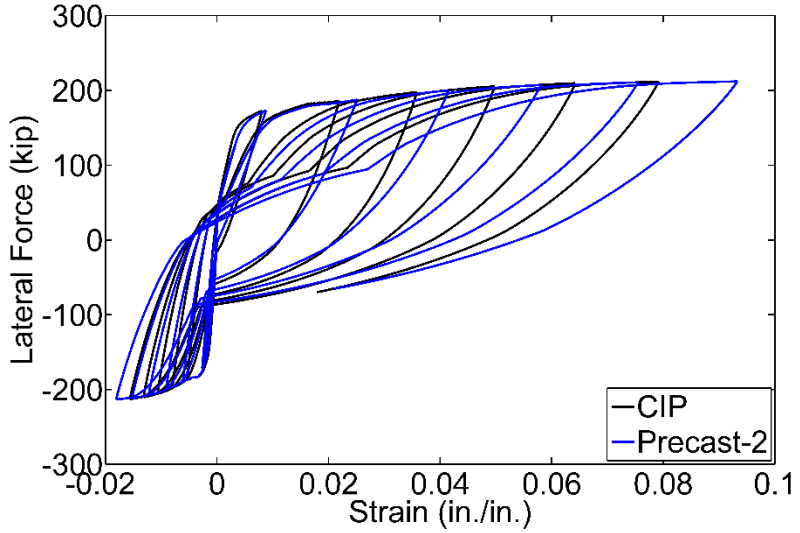

(b)

Fig. 5.35. Comparison of column model 23 (CIP) and 24 (Precast-2): (a) cyclic envelope; (b) strains in the column extreme bar.

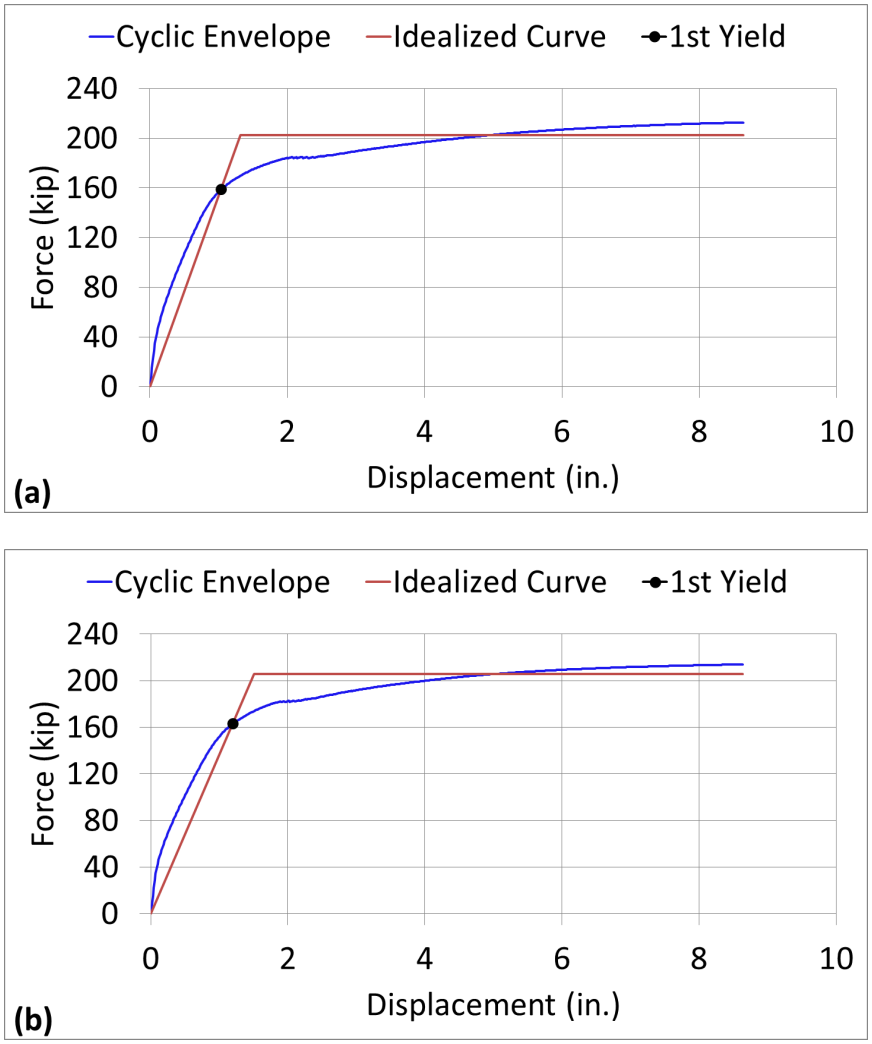

Fig. 5.36. Displacement ductility capacity: (a) column model 23 (CIP), $\mu_C = 6.54$; (b) column model 24 (Precast-2), $\mu_C = 5.73$.

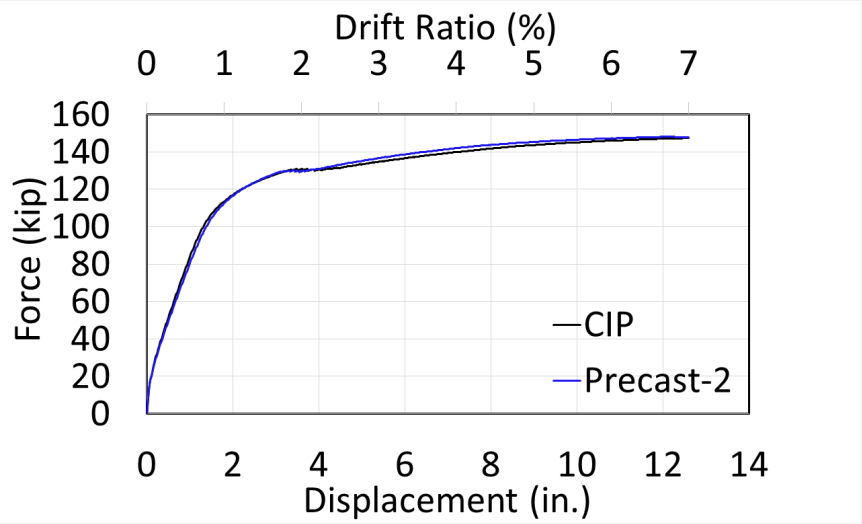

(a)

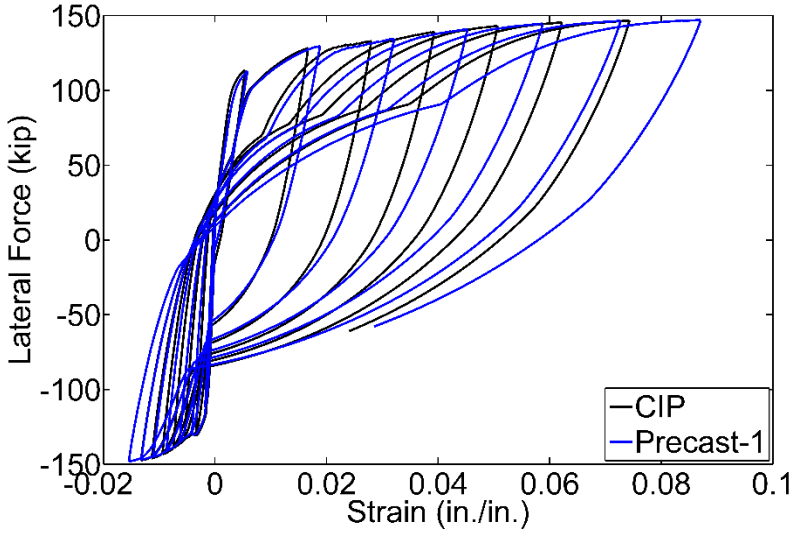

(b)

Fig. 5.37. Comparison of column model 25 (CIP) and 26 (Precast-2): (a) cyclic envelope; (b) strains in the column extreme bar.

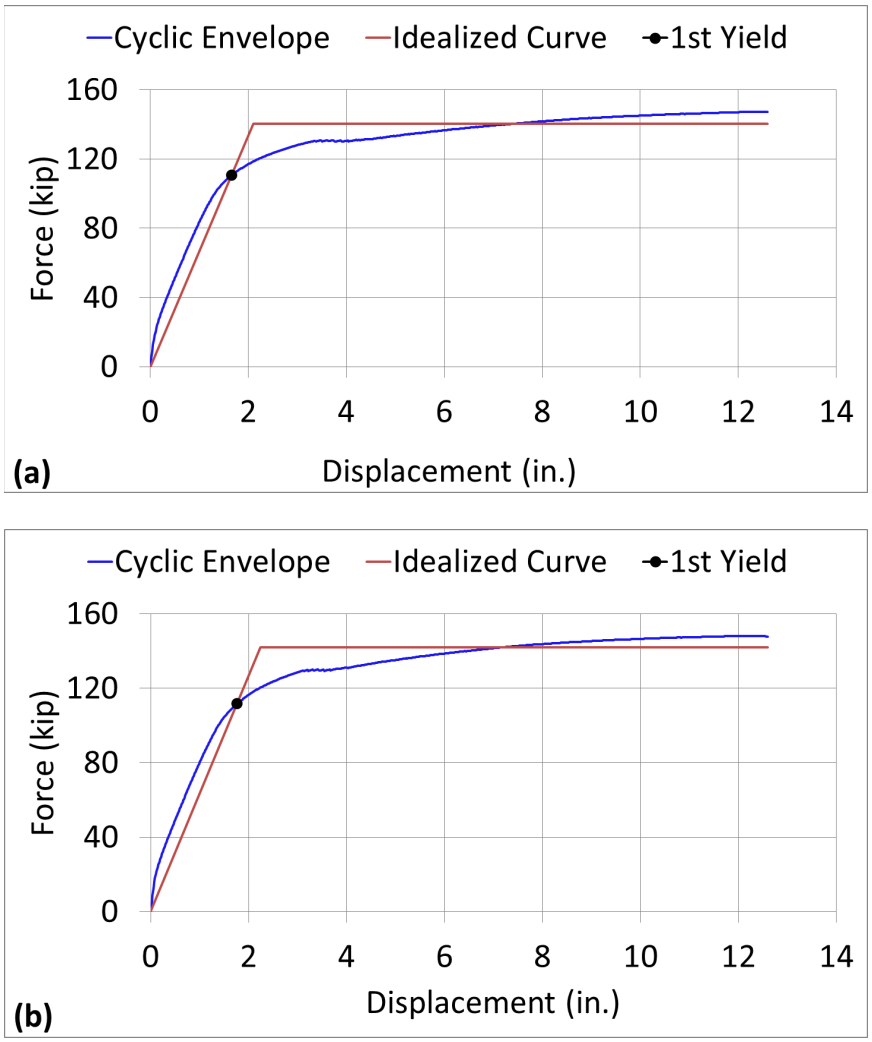

Fig. 5.38. Displacement ductility capacity: (a) column model 25 (CIP), $\mu_C = 6.00$; (b) column model 26 (Precast-2), $\mu_C = 5.62$.

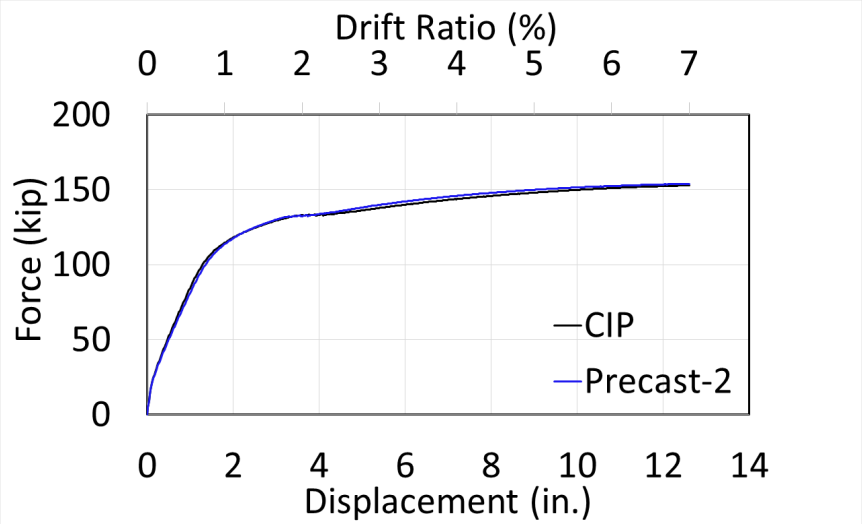

(a)

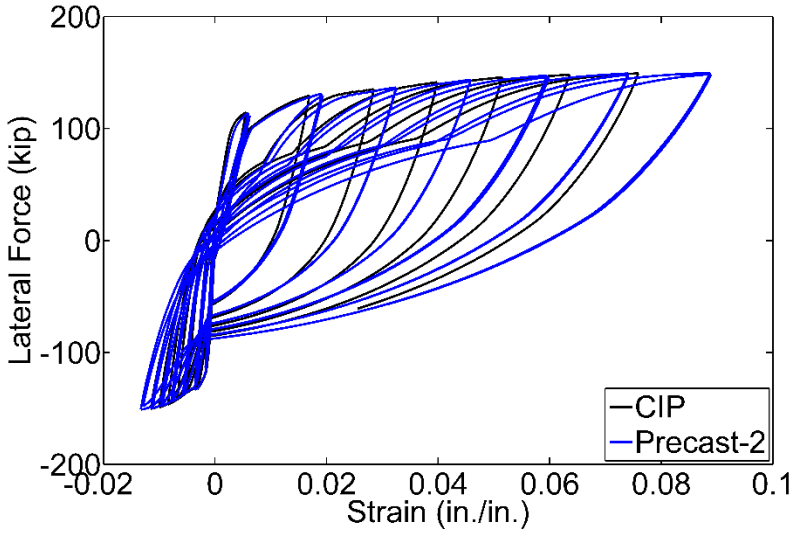

(b)

Fig. 5.39. Comparison of column model 27 (CIP) and 28 (Precast-2): (a) cyclic envelope; (b) strains in the column extreme bar.

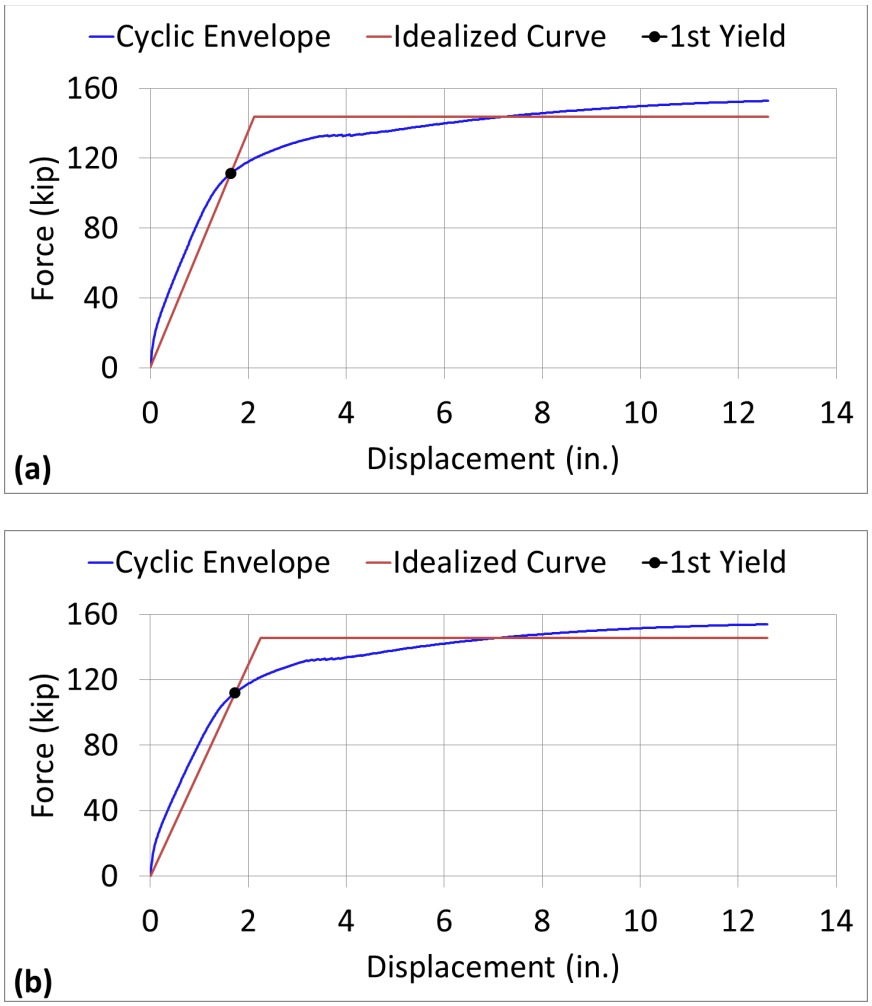

Fig. 5.40. Displacement ductility capacity: (a) column model 27 (CIP), $\mu_C = 5.94$; (b) column model 28 (Precast-2), $\mu_C = 5.60$.

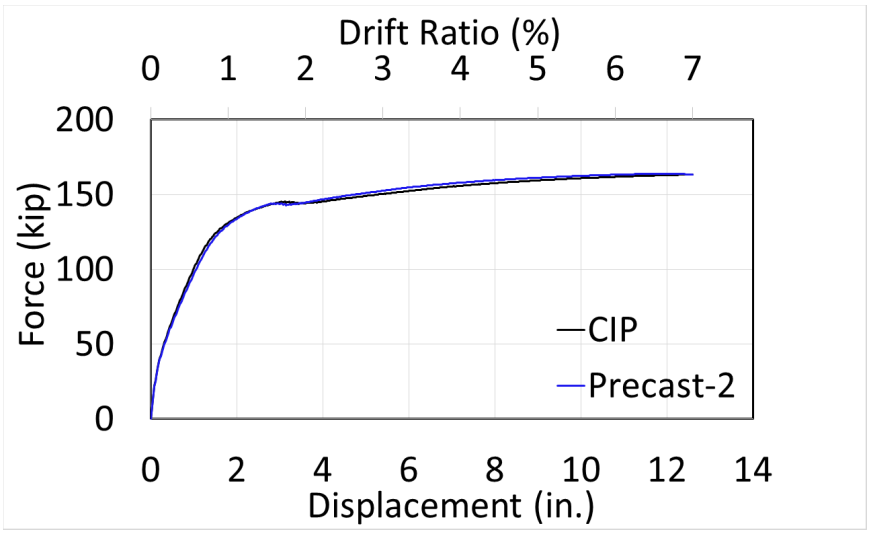

(a)

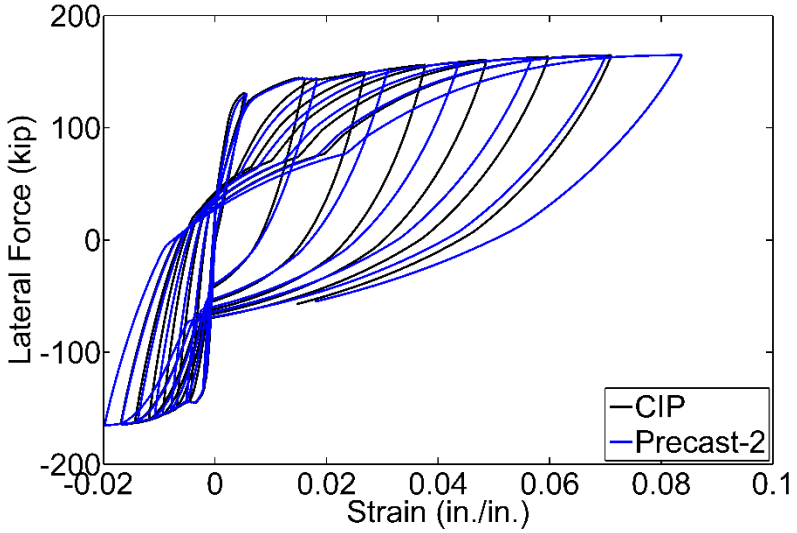

(b)

Fig. 5.41. Comparison of column model 29 (CIP) and 30 (Precast-2) (a) cyclic envelope; (b) strains in the column extreme bar.

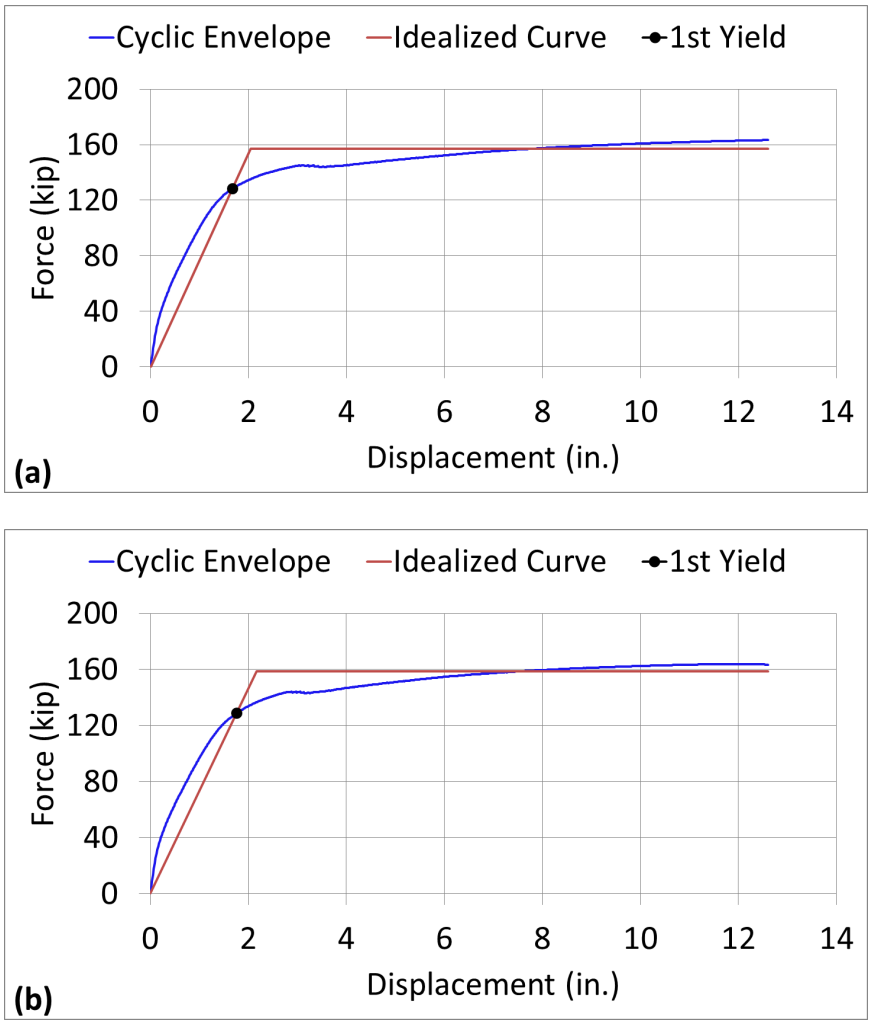

Fig. 5.42. Displacement ductility capacity: (a) column model 29 (CIP), $\mu_c = 6.16$; (b) column model 30 (Precast-2), $\mu_c = 5.80$.

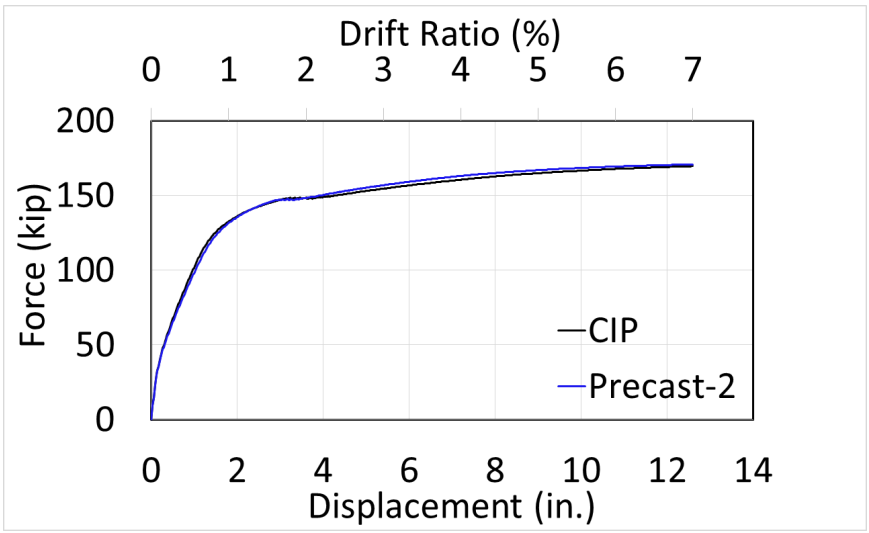

(a)

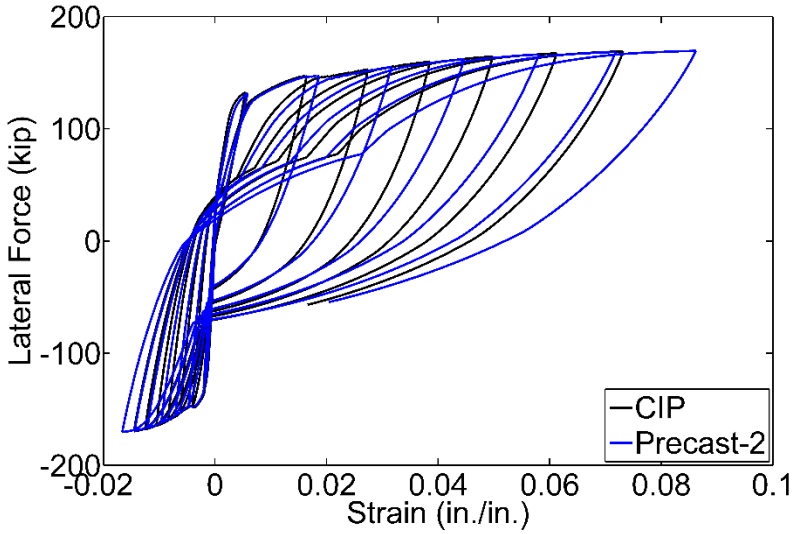

(b)

Fig. 5.43. Comparison of column model 31 (CIP) and 32 (Precast-2) (a) cyclic envelope; (b) strains in the column extreme bar.

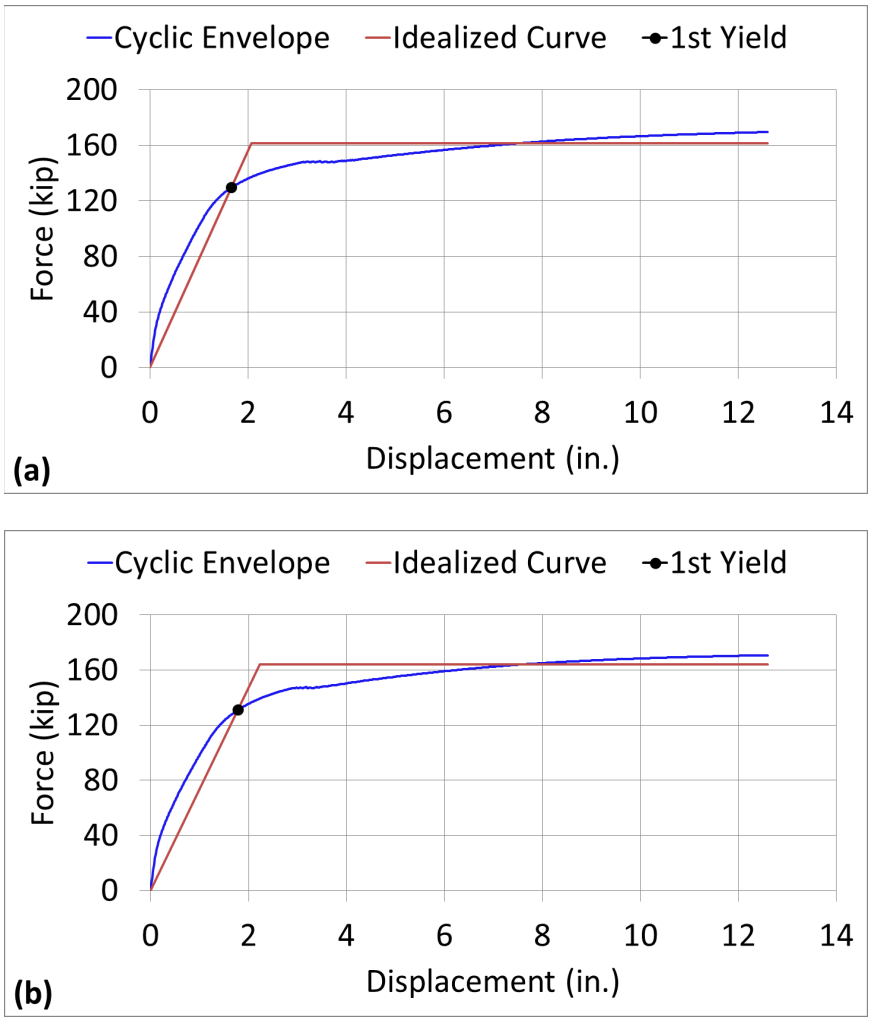

Fig. 5.44. Displacement ductility capacity: (a) column model 31 (CIP), $\mu_C = 6.10$; (b) column model 32 (Precast-2), $\mu_C = 5.65$.

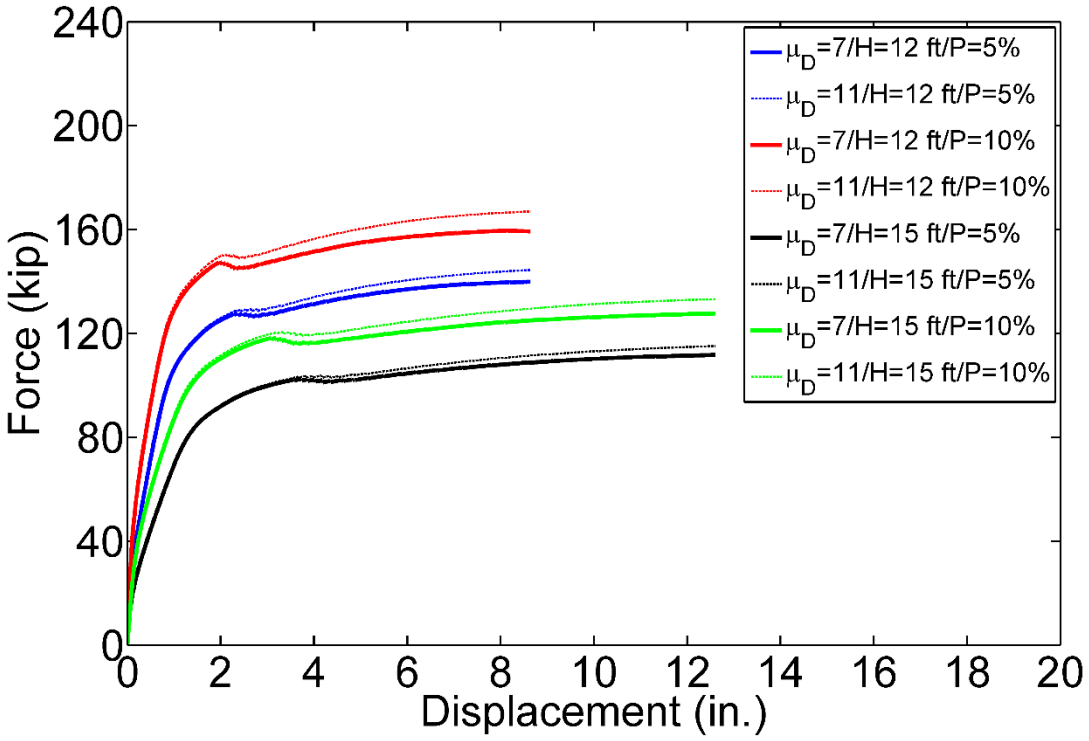

Fig. 5.45. Comparison of global response for CIP columns reinforced with 14 No. 9 bars.

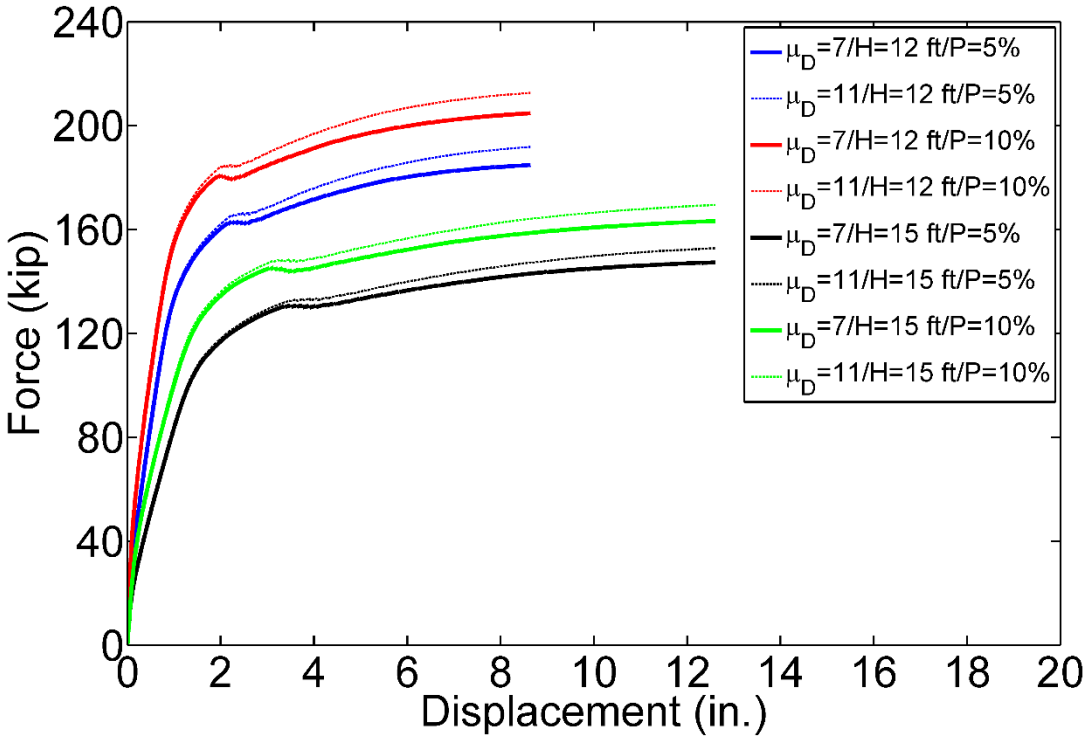

Fig. 5.46. Comparison of global response for CIP columns reinforced with 20 No. 9 bars.

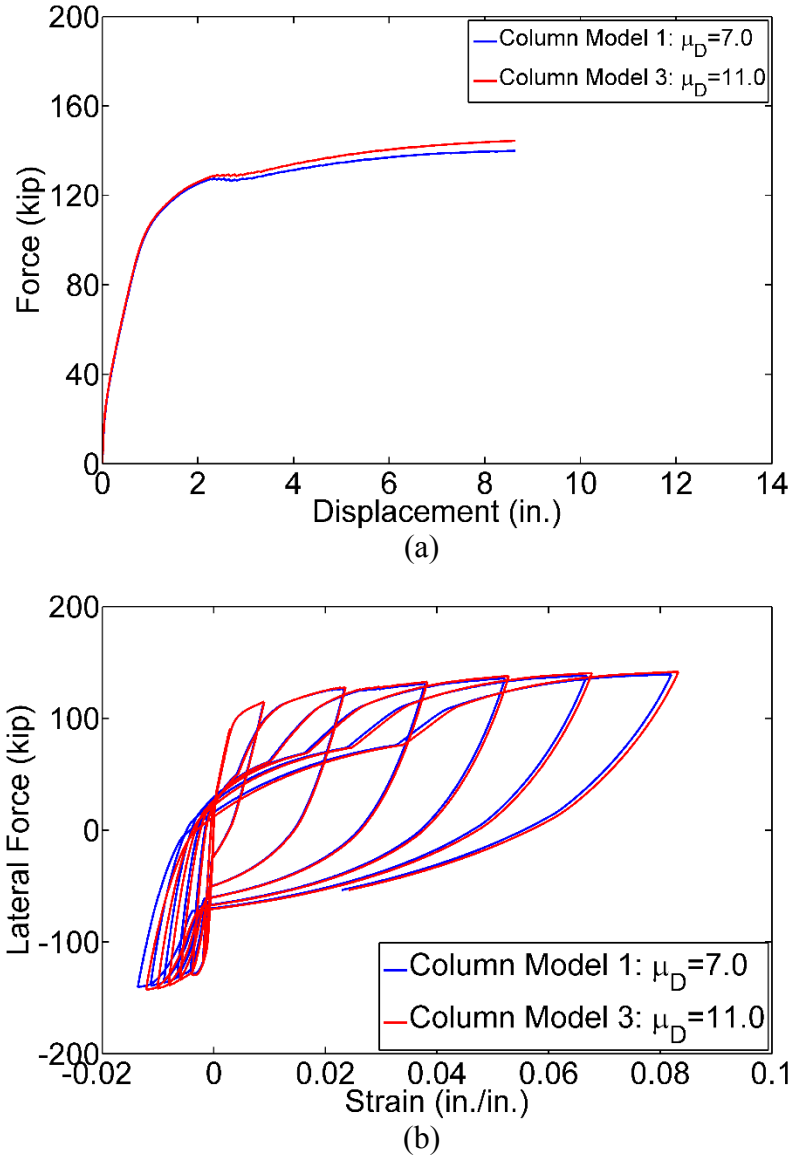

Fig. 5.47. Effect of change in design displacement ductility for CIP columns with 14 No.9 bars.

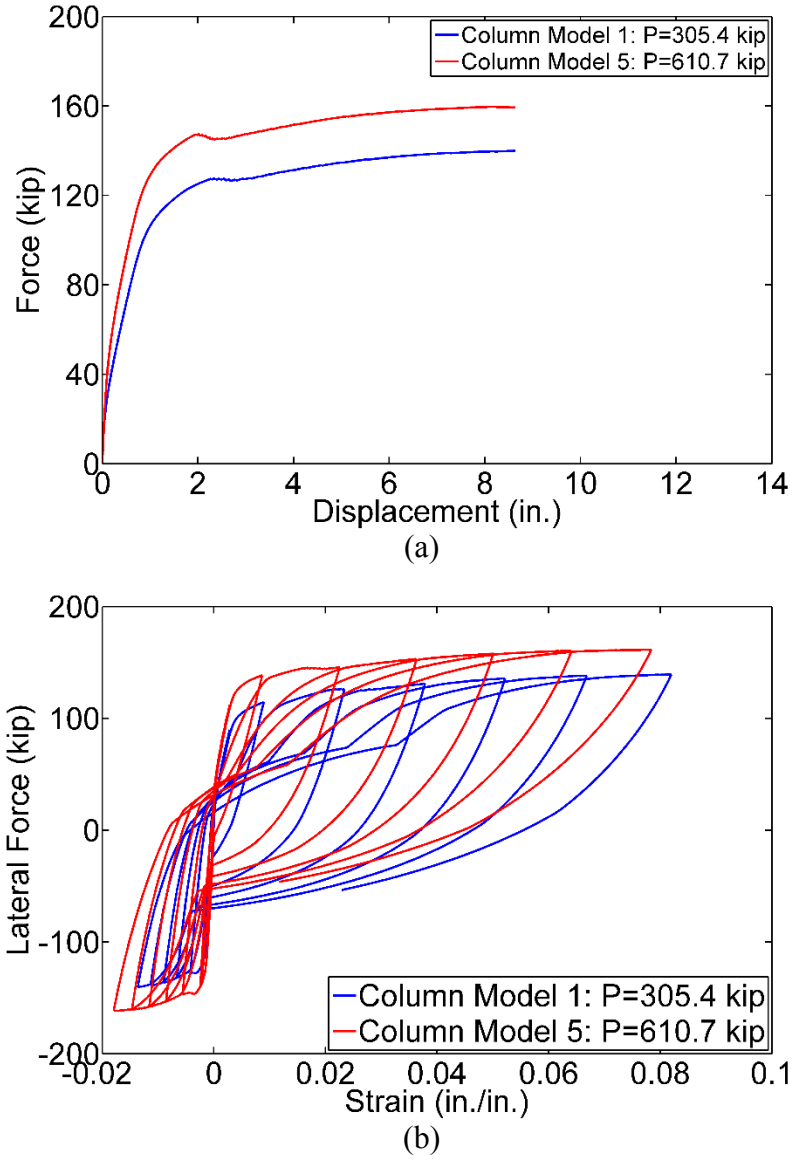

Fig. 5.48. Effect of change in axial load for CIP columns with 14 No.9 bars.

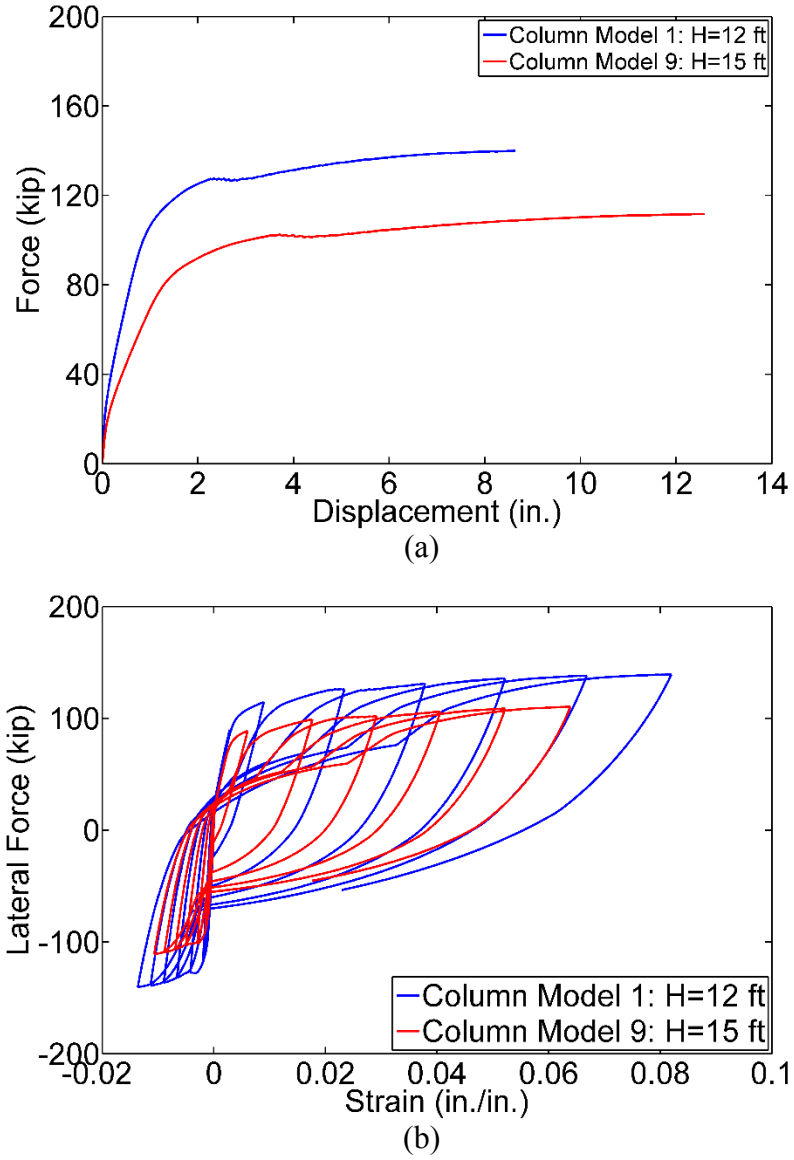

Fig. 5.49. Effect of change in height for CIP columns with 14 No.9 bars.

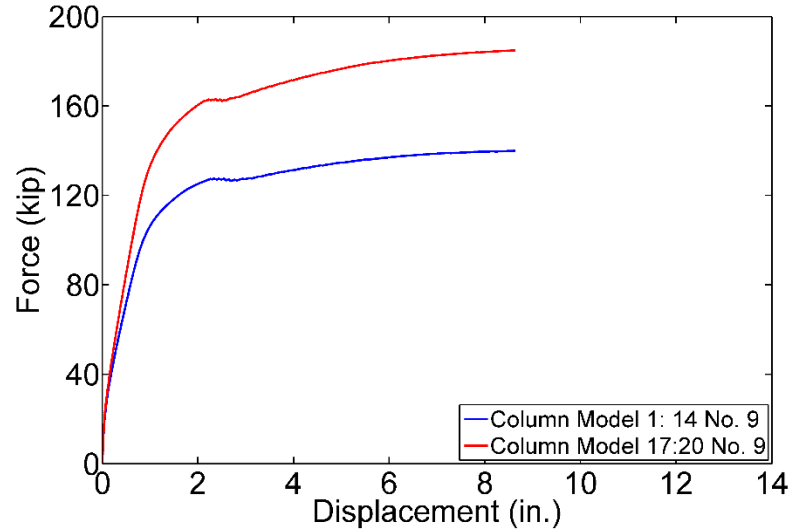

(a)

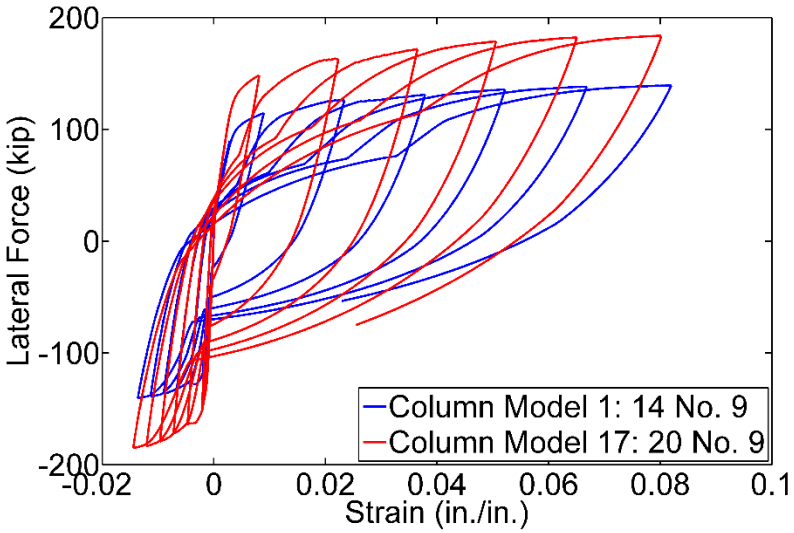

(b)

Fig. 5.50. Effect of change in number of longitudinal bars for 12-ft high CIP columns.

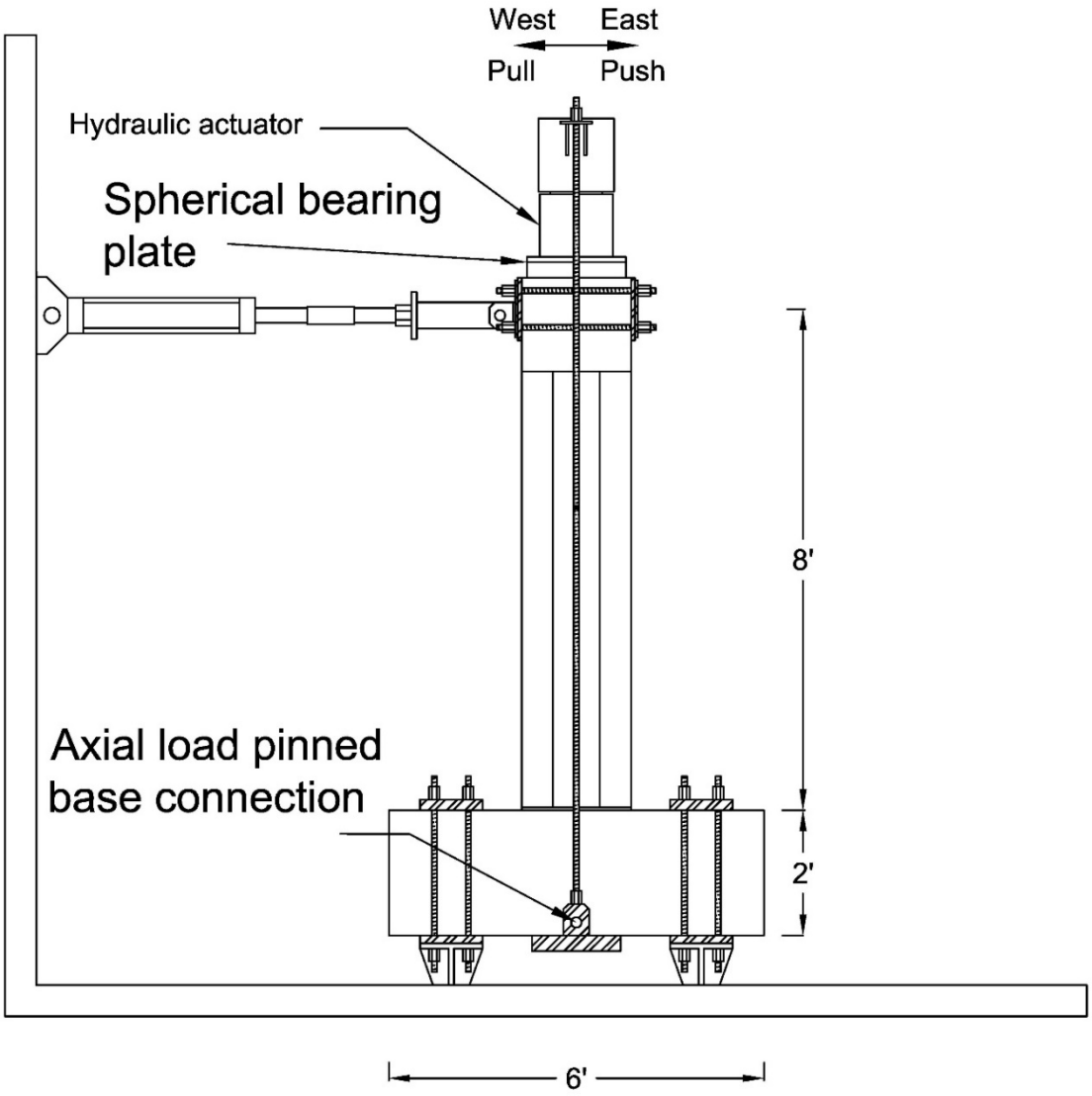

Fig. 5.51. Test setup for column-to-footing specimens.

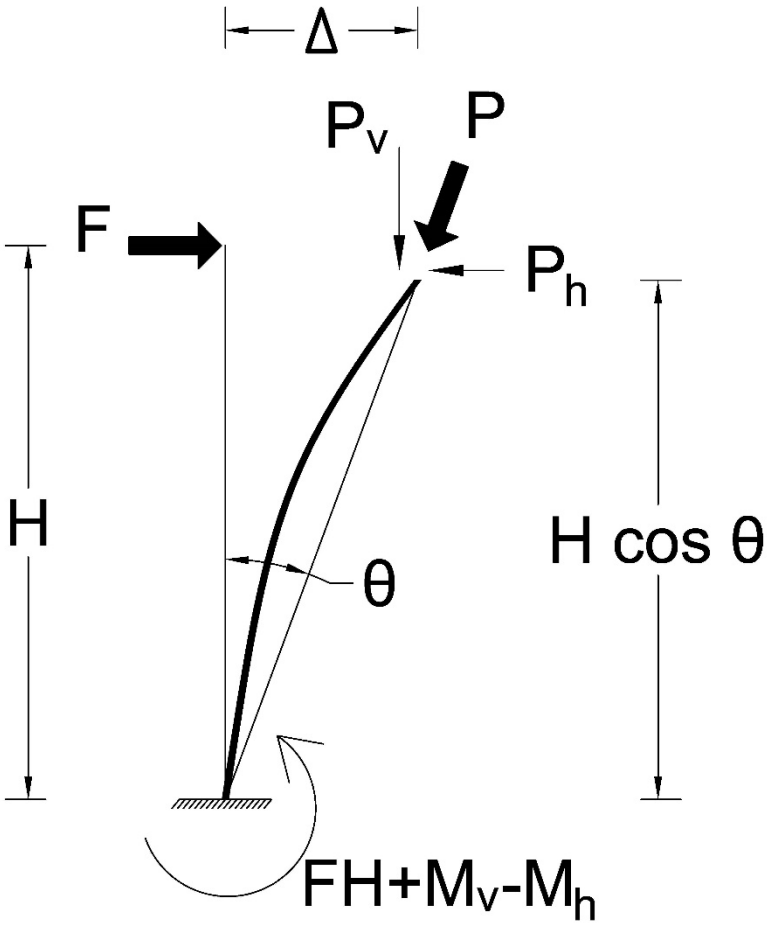

Fig. 5.52. Schematic approximation of P-Δ effects.

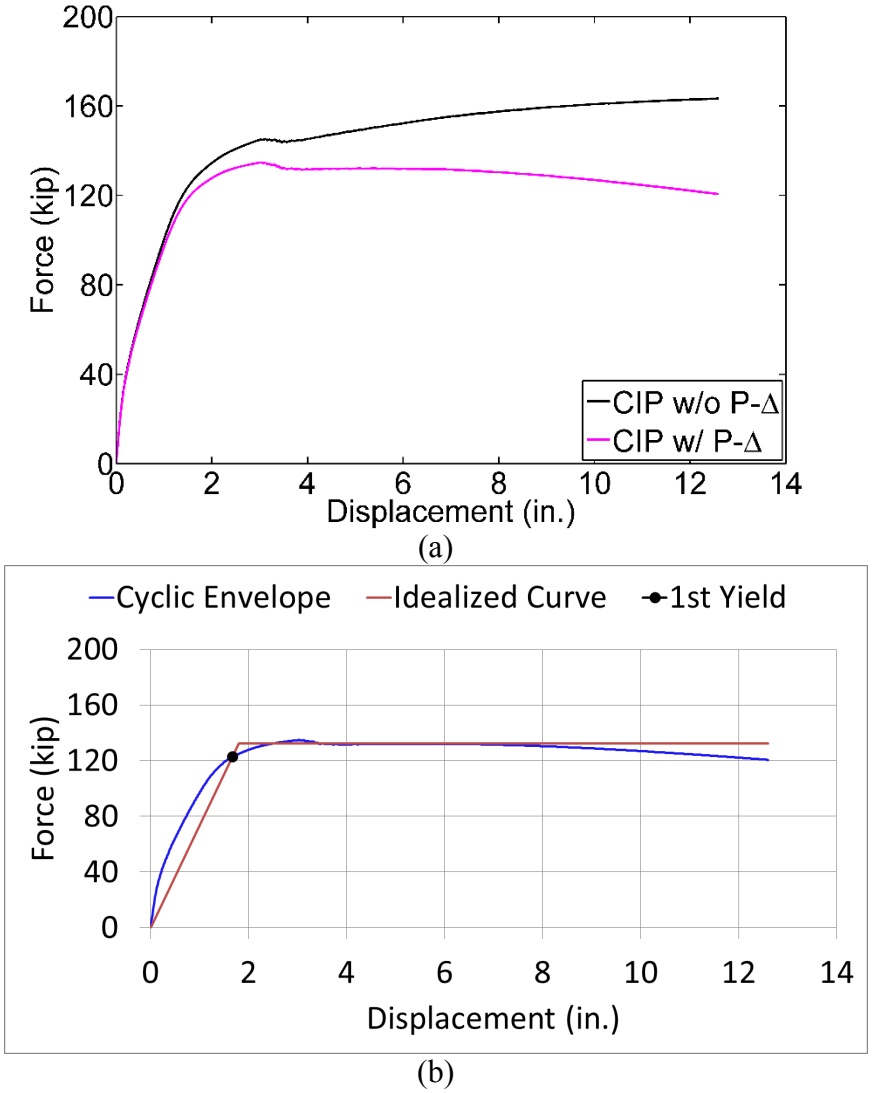

Fig. 5.53. P-Δ effects on column model 29 (CIP): (a) comparison of cyclic envelopes; (b) displacement ductility capacity, $\mu_C = 6.98$.

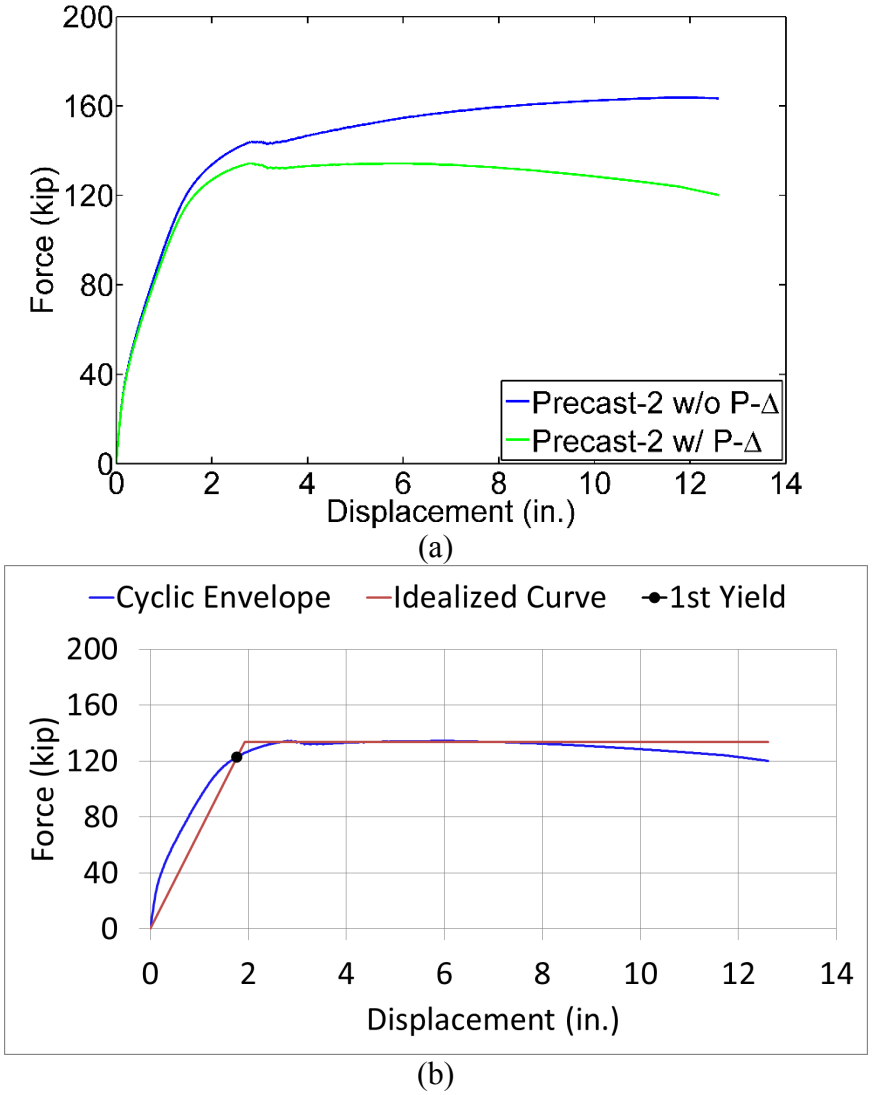

Fig. 5.54. P-Δ effects on column model 30 (Precast-2): (a) comparison of cyclic envelopes; (b) displacement ductility capacity, $\mu_c = 6.56$.

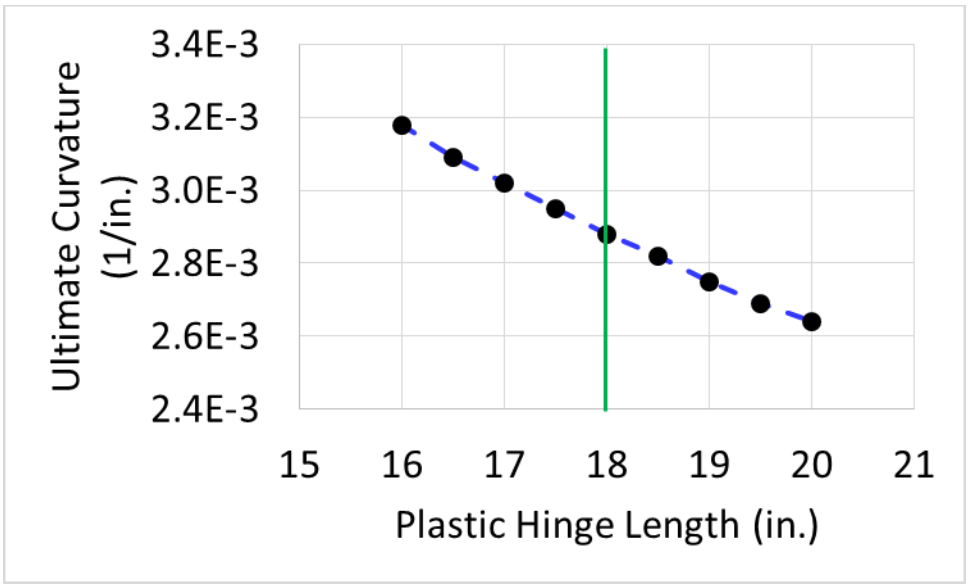

(a)

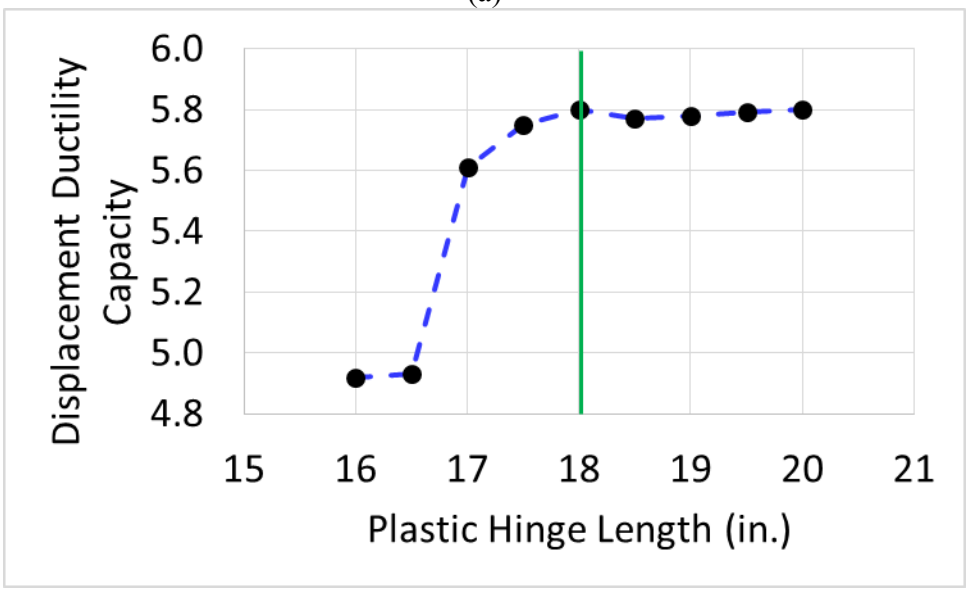

(b)

Fig. 5.55. Effects of plastic hinge length variation on the response of Precast-2: (a) change in ultimate curvature during 6% drift ratio; (b) change in displacement ductility capacity.

CHAPTER 6

NONLINEAR TIME-HISTORY ANALYSIS OF A BRIDGE BENT SYSTEM

Introduction

This chapter presents the design and analysis of a prototype multicolumn bridge bent system in accordance with AASHTO Guide Specifications. The analytical model which was validated with the experiments and later verified using a parametric study is used to model one monolithic and two precast bridge bents with similar details to Precast-1 and Precast-2 specimens, which were discussed in Chapter 4. The objective of this chapter is to study the application of grouted splice sleeve (GSS) connectors in multi-column bents and investigate the effect of GSS connections on the response of the bridge bents. Two types of analysis are performed: (1) static cyclic analysis to find the capacity of the system, and (2) nonlinear time-history analysis to find the level of demand on the bridge bent. This will provide information on capacity-demand relationships for the bridge bent alternatives considered in this study, and will reveal more insight into the overall behavior of the bents under various input ground motions. The following three main sections include the design and details of the models, results of the static cyclic analyses for the three bent systems, and results of the nonlinear time-history analyses for the three bent systems including a discussion on demand levels compared to capacity of

the bridge bents.

Design and Details of the Bridge Bents

Selection of a Baseline Bridge Bent

The bridge bent was designed based on the configurations of Bent #6 of the South Temple Bridge at Interstate 15 in Salt Lake City, Utah, which was tested to failure in-situ as part of a research study focused on seismic rehabilitation of seismically deficient bridges (Pantelides et al. 2001). The bridge was built in 1963 prior to the application of modern seismic detailing that is outlined in the current bridge seismic codes such as the AASHTO Guide Specifications and Caltrans Seismic Design Criteria; therefore, appropriate changes were made to include a modern scheme of seismic detailing for the purposes of this chapter.

The original bent was composed of three 36-in. square columns with 16 No. 10 bars which is equal to a reinforcement ratio of 1.57%. The cap beam had a 3 ft by 4 ft rectangular cross section. The compressive strength of the concrete was measured to be 4.64 ksi and the yield strength of the reinforcement was measured to be 48 ksi.
Bent #6 was retrofitted using carbon fiber reinforced polymer (CFRP) jackets for flexural improvement of the column plastic hinge regions, shear strengthening of columns, increased clamping pressure for lap splice regions, and shear strengthening of the joints. In addition, a CFRP U-strap concept was incorporated to prevent the column bars from pulling out of the joint area. Other rehabilitation techniques that were implemented on Bent #6 include improvement of the pile-to-pile cap connections using high-strength rods, and application of a reinforced concrete grade beam to minimize the lateral

movement of the pile caps.

Bent #6 which was tested under quasi-static cyclic loads with increasing amplitudes had a peak lateral force capacity of 495 kip and achieved a peak lateral displacement equal to 10.4 in., after application of the seismic rehabilitation techniques. A similar bent with no seismic enhancement (Bent #5) had only achieved 340 kip peak lateral force capacity and 5.9 in. peak lateral displacement.

To incorporate seismic detailing into the design and follow current design practice in Utah, several changes were made to Bent #6. The columns were changed to 3-ft diameter circular cross-sections. The columns were reinforced with 14 No. 9 longitudinal bars which is equivalent to a 1.38% steel ratio to adopt ABC recommendations for prefabricated bridge piers. Transverse reinforcement was made of No. 6 closed hoops spaced at 3 in. on center following the design procedure discussed in the parametric study in Chapter 5, to achieve a target displacement ductility of 7.0. A 2-in. cover was used for both the monolithic and precast bridge bents. The width of the cap beam was increased to 4 ft to account for current design recommendations; the footing depth was assumed to be 3 ft. An expected concrete compressive strength equal to 6 ksi was used in addition to Grade 60 ASTM A706 reinforcing bars as discussed in Chapter 5.

Three bridge bents were considered for this study as shown in Table 6.1. A bridge bent constructed monolithically was used as an ideal system without GSS connectors or lap splices (CIP); the second alternative was composed of precast columns with GSS connectors inside the footings and the cap beam (Precast-1); and the third bent consisted of precast columns with GSS connectors inside the columns and debonding of footing and cap beam bars over a length of 8.0 bar diameters (Precast-2). Fig. 6.1 to Fig. 6.3

show the details for bridge bents CIP, Precast-1, and Precast-2, respectively.

Layout of the Bridge Bent Model

The bridge bent was assumed to have a Type 1 earthquake resisting system (ERS), which is a ductile substructure along with an essentially elastic superstructure. Thus, the cap beam was modeled using an elastic element called elasticBeamColumn in the OpenSees element library. This implies that plastic hinging could only occur in the columns; therefore, the columns were modeled using forceBeamColumn elements with a plastic hinge integration scheme (Scott and Fenves 2006) which allows nonlinear behavior along the column. Elastic elements with rigid links (rigidLink) were incorporated at the upper end of the ductile columns inside the cap beam to constrain the rotational and translational degrees of freedom. Overall, the computational model was composed of 11 nodes and 10 elements as shown in Fig. 6.4. The length of the plastic hinges was obtained from the equations discussed in Chapter 5 for monolithic and precast conditions. The plastic hinge length for CIP was found to be 17.28 in. The plastic hinge reduction factor (γ_{GSS}) was found to be 2/3 and 5/6 for Precast-1 and Precast-2, respectively, resulting in a plastic hinge length equal to 11.52 in. and 14.40 in.

An axial load equal to 305.4 kip, corresponding to an axial load index (ALI) of 5%, was applied to the upper node of each column. Masses were assumed to be lumped at nodes 8, 9, and 10 for the dynamic analysis; a tributary nodal mass equal to 0.9478 k-s^2/in., 0.9669 k-s^2/in., and 0.9478 k-s^2/in. was applied to node 8, 9, and 10, respectively, in the horizontal direction of the bent parallel to the cap beam longitudinal axis. Confined and unconfined concrete were assigned to the concrete core and cover using

concrete04 material; ReinforcingSteel was incorporated for column bars inside and outside the plastic hinge region. A pseudo stress-strain relationship was derived for reinforcing bars inside the plastic hinge region based on the results of the one-dimensional bond-slip model for the three alternatives. The resulting pseudo modulus which was found using a linear regression with respect to the bond-slip model output was assigned to the reinforcing bars inside the plastic hinge region, to account for the softening effects of the bond-slip. The pseudo modulus was equal to 24,159 ksi, 20,631 ksi, and 17,596 ksi for CIP, Precast-1, and Precast-2, respectively. As can be observed, bond-slip was more pronounced for Precast-2 with the intentional debonding.

The columns were assumed to be fully fixed at the bottom and soil-foundation effects were not considered in this study.

Analysis of the Bridge Bents

Static Cyclic Analysis

Nonlinear Static cyclic analysis was performed to obtain the capacity of the bridge bents under a cyclic displacement loading history. According to the AASHTO Guide Specifications, a pushover analysis is required to find the reliable displacement capacity for bridges located in seismic design category (SDC) D which includes areas in Salt Lake City, Utah. The objective of performing a cyclic analysis, which can also be referred to as cyclic pushover analysis, was to investigate the low-cycle fatigue bar fracture. It was intended to first ascertain the potential failure mode of the bridge bents, and then find their ultimate displacement capacity. A cyclic displacement history similar to that of the experiments was used; it was composed of increasing displacement

amplitudes in terms of the bridge bent drift with two cycles per drift ratio. The displacement history was applied to Node 7 at an elevation equal to 312 in. above the footings as shown in Fig. 6.4.

Analysis Results for Bent CIP

Bridge bent CIP had a ductile response until five column reinforcing bars fractured due to low-cycle fatigue during the second cycle of the 6% drift ratio. Examination of the sectional response revealed that the core stayed intact until Node 7 reached a drift ratio of 6.59% which is equal to 20.56 in., indicating that low-cycle fatigue bar fracture was the failure mode for this bridge bent. Hence, the ultimate displacement was governed by bar fracture at 18.72 in. or 6% in terms of the lateral drift ratio. Fig. 6.5 shows the hysteresis response of CIP including the low-cycle fatigue fracture of the columns longitudinal bars. P-Δ effects were included in the cyclic analysis to consider the effects of geometric nonlinearity.

Bent CIP achieved a peak lateral force capacity equal to 370.0 kip which occurred at a displacement of 12.36 in. (3.96% drift ratio). The displacement ductility capacity of the right column was found to be 7.09 which is close to the assumed target displacement ductility of 7.00. On the other hand, a similar approach was taken to obtain the displacement ductility of the bridge bent using the base shear for the three columns. The cyclic envelope along with the idealized curve is shown in Fig. 6.6(a) and Fig. 6.6(b) for the single column and the bridge bent, respectively. The displacement ductility capacity of the bridge bent was found to be 7.04. It is noted that P-Δ transformation was not included for the results that were used to compute the displacement ductility capacity

values for the sake of conservatism and to be more consistent with the simplified procedure for the target displacement ductility.

A capacity envelope was constructed using the cyclic response of CIP (including P-Δ), with four significant performance points identified on the capacity curve. These four points indicate the occurrence of column bar yielding, onset of concrete cover crushing, onset of concrete core crushing, and low-cycle fatigue bar fracture. The low-cycle fatigue bar fracture marks the peak displacement of the last cycle without any bar fracture. For example, CIP column bars began to fracture during the second cycle of the 6% drift ratio. Therefore the low-cycle fatigue life of CIP would end one cycle earlier, which is the first cycle of the 6% drift ratio; thus, the ultimate drift can still be considered as 6%. Fig. 6.7 shows the capacity envelope for bent CIP. The capacity envelope will be used in the upcoming sections that discuss the results of the dynamic analyses.

Analysis Results for Bent Precast-1

Bridge bent Precast-1 had premature bar fractures during the second cycle of the 5% drift ratio, when eight column bars fractured due to low-cycle fatigue. The sectional response indicated that the onset of concrete core crushing was reached at a drift of 4.60% which happened prior to bar fracture. Therefore, the ultimate displacement was governed by onset of core concrete crushing at 14.35 in. or 4.6% drift ratio. Fig. 6.8 shows the hysteresis response of Precast-1 including the occurrence of the core concrete crushing and low-cycle fatigue bar fracture.

Bent Precast-1 had a peak lateral force capacity equal to 378.0 kip corresponding to a displacement of 11.86 in. (3.80% drift). The displacement ductility capacity of both

the right column and the bridge bent was found to be 5.82, as shown in Fig. 6.9. The capacity envelope for Precast-1 is presented in Fig. 6.10 including the four previously mentioned performance points. Compared to CIP, it is observed that Precast-1 had a smaller displacement capacity; in addition, core crushing occurred before bar fracture for bent Precast-1.

Analysis Results for Bent Precast-2

Precast-2 had a relatively good hysteresis response which was terminated during the first cycle of the 6% drift ratio due to crushing of the concrete core under compression; this occurred at a displacement equal to 17.16 in. which is equivalent to a 5.50% drift ratio. Subsequently, 10 column bars fractured because of low-cycle fatigue during the second cycle of the 6% drift ratio. Hence, crushing of the core governs the displacement capacity of the system at 5.5%drift ratio. Fig. 6.11 presents the hysteresis response of Bent Precast-2 in which core crushing occurs prior to bar fracture.

Precast-2 achieved a peak force capacity equal to 362.5 kip corresponding to a displacement of 12.39 in. (3.97% drift). The displacement ductility capacity of the right column was 6.48, whereas the displacement ductility capacity of the bridge bent was 6.47. This is shown in Fig. 6.12 for both cases, using the cyclic envelopes (without the P-Δ effect) and idealized curves.

The capacity envelope of Bent Precast-2 which was constructed using the cyclic response is shown in Fig. 6.13. It contains useful information on the performance of the bent by showing the points at which first bar yielding, crushing of the cover, crushing of the core, and bar fracture happened.

Comparison of the Three Bent Systems

Under the imposed cyclic displacement history, the three bridge bents had a similar response in terms of the lateral force capacity. This can be seen in Fig. 6.14 in which a pushover comparison is provided. Precast-2 had a slightly smaller force capacity which is due to the fact that the column bars were located ¾ in. closer to the centroid of the cross-section. This was carried out to keep the 2-in. cover consistent for all three bents—a scenario that would be implemented for actual construction. On the other hand, Bent Precast-1 had a slightly larger force capacity; this is attributed to the increased level of sectional demands as a result of the reduction in the assigned plastic hinge length. The application of the intentional debonding for the dowels of Precast-2 resulted in a reduced postcracking stiffness compared to the other two bents. In addition to debonding, the reduced stiffness was caused in part due to a smaller sectional moment arm for the column bars of this bent. As anticipated, the most important performance difference was found in displacement capacity of the three bent models. CIP which failed due to the low-cycle fatigue column bar fracture had a displacement capacity of 18.72 in., whereas, bents Precast-1 and Precast-2, both of which failed because of crushing of the concrete core, reached an ultimate displacement equal to 14.35 in. and 17.16 in., respectively. Therefore, the precast bents achieved a smaller displacement ductility capacity compared to CIP. Table 6.2 provides a comparison between the performance capacities of the three bents.

Nonlinear Time-History Analysis

Nonlinear dynamic analysis may be required by the bridge design codes for irregular bridges located in seismic regions. A series of nonlinear dynamic analyses were performed to study the demand levels of the three bridge bent alternatives under historic ground motions. The objective was to investigate the nonlinear dynamic response of the bridge bents and compare the displacement demand levels with the predicted capacity. Also, it was intended to compare the displacement demand levels among the three bent alternatives.

The computational model used for the nonlinear time-history analyses was identical to the model which was used for the cyclic analysis in the previous section (Fig. 6.4). A nodal mass equal to 0.9478 kip-s^2/in., 0.9669 kip-s^2/in., and 0.9478 kip-s^2/in. was applied to Node 8, Node 9, and Node 10, respectively, including the tributary dead weight of the structural components in addition to the 5% ALI for the columns. A stiffness-proportional damping was incorporated using a 5% damping ratio. An average acceleration method was adopted for the iterative solution process.

Selection of Ground Motions

AASHTO Guide Specifications requires at least three spectrally matched ground motion records for a time-history analysis. It was assumed that this bridge bent was located in downtown Salt Lake City, Utah, which is in close proximity to active normal faults capable of producing major ground shaking. Site Class D (stiff soil) was used to determine the design response spectrum that is based on the USGS ground motion maps with 7% chance of exceedance in 75 years (or a return period equal to 1035 years). Using

the USGS design maps tool, the design spectral coefficients were found to be 0.489 g for the effective peak ground acceleration (A_s), 1.167 g for the short-period spectral acceleration (S_{DS}), and 0.666 g for the long-period spectral acceleration (S_{D1}). Since the one-second period design spectral acceleration exceeds 0.50 g, this bridge is considered to be in seismic design category (SDC) D which implies that downtown Salt Lake City is among the regions of highest seismicity.

The PEER Ground Motion Database was used to find records that were representative of the seismic characteristics for the bridge location. Priority was given to earthquake magnitude, faulting mechanism, proximity to fault rupture, and finally site class condition. To study near-field effects, four pulse-like ground motions were selected with a Joyner-Boore distance of less than 10 km. Another suite of ground motions were also selected which included four independent records without a distinct pulse in the velocity time-history. Table 6.3 contains the eight selected events used in this study, while Fig. 6.15 shows the design acceleration response spectrum along with the acceleration response spectra for the selected records.

The principal components of the ground motions were found by obtaining the transformed acceleration records following the procedure outlined in Bartlett (2004). Subsequently, the events were spectrally matched using SeismoMatch, then baseline-corrected in SeismoSignal to remove the unwanted drift that was introduced into the records (SeismoSoft 2013). The response spectra for the processed records are shown in Fig. 6.16. The time-histories for two records, one pulse-like (Montenegro) and one not pulse-like (Iwate), are shown in Fig. 6.17 and Fig. 6.18, respectively, including both the unmatched (after transformation) and spectrally matched condition.

In addition to the eight selected ground motions, four more extreme conditions were considered for each bent by applying a uniform scale factor of 1.5 and 2.0 to the ground accelerations of Montenegro and Iwate records. This was carried out to investigate the response at a near-failure condition. Therefore, each of the three bridge bents was studied under 12 records overall.

Analysis Results for Bent CIP

The fundamental natural period for the bridge bent CIP was found to be 0.436 s. The force-drift response of CIP was constructed and plotted with the CIP capacity envelope for the selected ground motions as shown Fig. 6.19. The largest drift demand for bent CIP was achieved under Iwate with a 1.97% drift ratio corresponding to a 6.15-in. bent displacement. Compared to the capacity envelope, the demand was beyond crushing of the concrete cover which implies a relatively large spalling close to column-footing and column-cap beam interfaces. However, compared to the CIP drift capacity of 6%, the capacity-to-demand ratio for this particular record was equal to 3.05. Table 6.4 includes drift demands for all ground motions along with the corresponding capacity to demand ratio. The average peak drift demand was found to be 1.77% (5.52 in.) which results in a capacity-to-demand ratio equal to 3.40. The bent displacement response is presented in Fig. 6.20 for the eight ground motions.

The application of a uniform scale factor of 1.5 and 2 for the ground acceleration records resulted in a magnified bent displacement response as presented in Fig. 6.21 for Montenegro and Iwate ground motions. The increased demand was more pronounced under the scaled Montenegro with a peak drift demand equal to 2.90% (9.05 in.) and

5.57% (17.38 in.) resulting in a capacity-to-demand ratio of 2.07 and 1.08 for a scale factor of 1.5 and 2.0, respectively. For the scaled Iwate record, a peak drift demand equal to 2.43% (7.58 in.) and 2.88% (8.99 in.) was achieved which implies a capacity-to-demand ratio of 2.47 and 2.08 for a scale factor of 1.5 and 2.0, respectively. Compared to the capacity envelope, bent CIP did not fail under these scaled records even though the drift demand was considerably close to bar fracture and the onset of concrete core crushing under Montenegro with a scale factor equal to 2.0. Strain reversals for the column bars were not large enough to cause a low-cycle fatigue bar fracture for any of the ground motions. Fig. 6.22 shows the bent displacement response for the scaled ground motions, and Table 6.5 includes the capacity-to-demand ratios for bent CIP under the scaled Montenegro and Iwate.

Analysis Results for Bent Precast-1

The fundamental natural period of the bridge bent Precast-1 was 0.436 s. Fig. 6.23 shows the force-drift response of bent Precast-1 to the eight ground motions compared against the capacity envelope with the performance points of reinforcing bar yield, cover crushing, core crushing, and low-cycle fatigue bar fracture. The largest drift demand equal to 1.90% (5.93 in.), was achieved under the Iwate and Superstition Hills events, and corresponds to a capacity-to-drift ratio of 2.42 considering the Precast-1 drift capacity of 4.6% against core crushing. In terms of the damage state at the end of the response, most of the ground motions caused crushing of the 2-in. cover close to the two ends of all columns. The average peak drift demand was found to be 1.75% (5.46 in.) corresponding to a capacity-to-demand ratio of 2.62. Table 6.6 includes drift demands

and capacity-to-demand ratios for all ground motions. The bent displacement response is shown Fig. 6.24 for all records.

Bent Precast-1 had an increased response under the uniformly-scaled Montenegro and Iwate. Fig. 6.25 shows that the drift demand under Montenegro with a scale factor of 2.0 exceeded core crushing and bar fracture which implied a failure condition; however, plastic strain reversals were not severe enough to cause a low-cycle fatigue bar fracture. For the scaled Iwate with both 1.5 and 2.0 factors, the drift demand went well beyond the cover crushing condition which indicates a complete spalling in the plastic hinge regions for all columns. The peak drift demand was 2.61% (8.14 in.) and 5.58% (17.41 in.) corresponding to a capacity-to-demand ratio of 1.76 and 0.82, under Montenegro with a scale factor of 1.5 and 2.0, respectively. For the scaled Iwate record, a peak drift demand equal to 2.50% (7.80 in.) and 3.00% (9.36 in.) was achieved which implies a capacity-to-demand ratio of 1.84 and 1.53 for the scale factor of 1.5 and 2.0, respectively. Fig. 6.26 shows the bent displacement response for the two scaled records, and Table 6.7 contains the demand levels due to the scaled Montenegro and Iwate.

Analysis Results for Bent Precast-2

The fundamental natural period of Precast-2 was 0.439 s. The force-drift response of this bridge bent under the eight ground motions is shown in Fig. 6.27, with the capacity curve for Precast-2. The largest drift demand was found to be 2.08% (6.49 in.) due to Iwate; this corresponds to a capacity-to-demand ratio of 2.64 for Precast-2 with a drift capacity equal to 5.5% against core crushing. The demand resulted in crushing of the cover adjacent to the column-footing and column-cap beam interface for all three

columns. Table 6.8 includes the capacity-to-demand ratios for all ground motions. The average peak drift demand was 1.9% (5.93 in.) resulting in a capacity-to-demand ratio of 2.90. The bent displacement response is shown in Fig. 6.28 for all ground motions. An amplified response was achieved as a result of the uniformly-scaled records as shown in Fig. 6.29 for both Montenegro and Iwate. This was more critical for Montenegro with a scale factor of 2.0 as Precast-2 reached a peak drift equal to 5.79% (18.06 in.) which exceeded the threshold for the core crushing implying failure condition, but stayed below the onset of bar fracture. The capacity-to-demand ratio for Montenegro with scale factor of 2.0 was 0.95. Precast-2 had a peak drift equal to 3.61% (11.26 in.) under Montenegro with a scale factor of 1.5 which corresponds to a drift capacity-to-demand ratio of 1.52. The peak drift due to the scaled Iwate was found to be 2.42% (7.55 in.) and 2.72% (8.49 in.) for the scale factor equal to 1.5 and 2.0, respectively, exceeding the cover spalling capacity but still considered to be in a functional condition as the capacity-to-demand ratio was 2.27 and 2.02, respectively. Table 6.9 includes the demands under the uniformly-scaled Montenegro and Iwate, while Fig. 6.30 shows the displacement response of bridge bent Precast-2.

Comparison of the Three Bent Systems

Overall, the three bent alternatives had a comparable response to the ground motions. Table 6.10 and Table 6.11 include the peak drift ratios achieved for every bent system under each ground motion for the original eight records and the uniformly-scaled records, respectively. The tabulated drift ratios along with the resulting capacity-to-demand ratios suggest that the demand levels were of a similar order of magnitude,

particularly for bents CIP and Precast-1. On the other hand, bent Precast-2 drift demands were larger for six out of eight ground motions which is due mostly to the intentional debonding implemented for the footing and cap beam dowel bars. Moreover, the flexural stiffness of bent Precast-2 columns was slightly smaller as the column bars were ¾-in. closer to the column cross-sectional centroid to keep the minimum cover constant for all three bent systems. Fig. 6.31 presents the drift demands for all bridge bents under all ground motions considered in this study; it also includes the drift capacity of each bent using horizontal lines in respective colors. Drift demands were increased under Iwate with a scale factor of 1.5 and 2.0 and Montenegro with a scale factor of 1.5 for the three bents, but did not cause failure. However, Montenegro with a uniform scale of 2.0 resulted in a failure for the two precast bents as the drift demands exceeded the onset of concrete core crushing criteria. Low-cycle-fatigue bar fracture did not occur for any of the bridge bents as a result of the nonlinear time-history analyses.

Fig. 6.32 shows the drift capacity-to-demand ratios for the three bents under all 12 ground motions. Among the three bent alternatives and under the original eight ground motions, CIP and Precast-1 had the highest and lowest drift capacity-to-demand ratios, with Precast-2 always in between, except under Darfield for which Precast-2 achieved a smaller drift capacity-to-demand ratio than Precast-1. This ratio remained above 3.05, 2.42, and 2.62 for CIP, Precast-1, and Precast-2, respectively. For the scaled records, the three bent alternatives achieved a drift capacity-to-demand ratio above 1.0 under Iwate with a scale factor of 1.5 and 2.0, and Montenegro with a scale factor of 1.5. Bents Precast-1 and Precast-2 failed due to Montenegro with a scale factor of 2.0, as both reached the threshold of core crushing; for this scaled record, a capacity-to-drift ratio of

1.08, 0.82, and 0.95 was achieved for CIP, Precast-1, and Precast-2, respectively.

Two parameters were found to affect the dynamic response of the bridge bents simulated with the proposed modeling strategy: pseudo modulus of the steel reinforcing bars and the plastic hinge length. It was noted that a reduction in the pseudo modulus resulted in an increase in the natural period of the system because of the consequent reduction in stiffness. This was anticipated as it is perceived that slippage of reinforcing bars or application of intentional debonding, both of which were implicitly modeled herein by obtaining a reduced steel modulus, would elongate the vibration period of the structural system. The plastic hinge length was found to have a smaller effect on the response compared to the pseudo modulus. A reduction in the plastic hinge length caused a slight reduction in the natural period of the system. This was attributed to an increase in the stiffness as an unreduced nominal reinforcing bar modulus of 29000 ksi was used outside the plastic hinge area. Depending on the characteristics of the ground motion records, the period change may result in a different response.

Conclusions

In the absence of experiments on full-scale precast bridge substructures connected with grouted splice sleeves, this chapter was developed to ascertain the performance of such components. A typical multicolumn bridge bent was designed and detailed in accordance with the current recommendations of bridge seismic design codes to achieve a ductile performance. Three bent systems were considered, one cast-in-place bridge bent with monolithic details (CIP), one precast bent composed of precast columns with grouted splice sleeves in the footings and the cap beam (Precast-1), and one precast bent

made of precast columns with grouted splice sleeves in the column and debonded footing and cap beam dowel bars (Precast-2). The mathematical models used to simulate the structures were constructed based on the modeling strategy which was developed and validated in previous chapters. Static cyclic analysis was performed to find the capacity of the bridge bents, as if these bents were tested under a quasi-static cyclic displacement history, and nonlinear time-history analysis was performed using eight spectrally matched records to obtain the demand levels. The findings are summarized as follows:

- The static cyclic analysis revealed that strength of the three bents was similar, but displacement capacity of the precast bridge bents was smaller than that of bent CIP.
- Bent CIP had a displacement capacity of 18.72 in. (6.0% drift) and a displacement ductility capacity of 7.04. The displacement ductility capacity of a column in this bridge bent was 7.09 which was close to the design objective equal to 7.00. Bent CIP failed due to low-cycle fatigue fracture of the column bars at 6.0% drift ratio.
- Precast-1 had a reduced displacement capacity of 14.35 in. (4.6% drift); both the bridge bent and the column achieved a displacement ductility of 5.82. Precast-1 failed due to crushing of concrete core prior to the low-cycle fatigue bar fracture at 5.0% drift ratio.
- Bent Precast-2 had a reduced displacement capacity of 17.16 in. (5.5%) and a displacement ductility capacity of 6.47. The displacement ductility capacity of a column in this bridge bent was 6.48. Precast-2 failed due to crushing of the concrete core prior to the low-cycle fatigue bar fracture at 6% drift ratio.
- The nonlinear time-history analysis revealed that the displacement demands due

to the spectrally matched suite of ground motions are below the displacement capacity for both cast-in-place and precast bridge bents. A peak displacement demand equal to 6.15 in. (1.97% drift), 5.93 in. (1.90% drift), and 6.49 in. (2.08% drift) was achieved for bents CIP, Precast-1, and Precast-2, respectively.

- Compared to displacement capacity of the bridge bents under study, an acceptable level of remaining displacement capacity was available before failure occurs for the three bent systems. A drift capacity-to-demand ratio of 3.1, 2.4, and 2.6 was achieved for bents CIP, Precast-1, and Precast-2, respectively, using the peak drift demand.
- Compared to capacity envelopes and performance points, damage to the columns under the spectrally matched records consisted of yielding of main column bars and spalling of the cover.
- The precast bridge bents failed under a pulse-like ground motion with a uniform scale factor of 2.0 due to crushing of the concrete core. Low-cycle-fatigue bar fracture did not occur for any of the bridge bents as a result of the nonlinear time-history analyses.
- Debonding of the dowel bars increased the displacement capacity as well as displacement demands for Precast-2. Further investigation is needed to make a comprehensive assessment of debonding effects on the overall performance.

References

AASHTO. (2011). AASHTO *guide specifications for LRFD seismic bridge design*, Washington, DC.

Bartlett, S. F. (2004). “Ground response analysis and design spectra for UDOT bridges

on soft soil sites." *Draft Rep. No. 208*, Utah Department of Transportation Research Division, SLC, UT.

Caltrans. (2010). *Seismic design criteria (SDC), version 1.6*, Sacramento, CA.

Pantelides, C. P., Gergely, J., and Reaveley, L. D. (2001). "In-situ verification of rehabilitation and repair of reinforced concrete bridge bents under simulated seismic loads." *Earthquake Spectra*, 17(3), 507–530.

Pacific Earthquake Engineering Research Center (PEER). "PEER strong motion database." ⟨http://ngawest2.berkeley.edu/⟩ (Feb., 2016).

Scott, M. and Fenves, G. (2006). "Plastic hinge integration methods for force-based beam–column elements." *J. Struct. Eng.*, 10.1061/(ASCE)0733-9445(2006)132:2(244), 244–252.

Seismosoft, SeismoMatch v2.1.2, Pavia, Italy: Seismosoft Ltd, 2013.

Seismosoft, SeismoSignal v5.1.2, Pavia, Italy: Seismosoft Ltd, 2013.

United States Geological Survey (USGS). "USGS design maps and tools." ⟨http://earthquake.usgs.gov⟩ (Feb., 2016).

Table 6.1. Bridge bent models.

Bent No.	**Designation**	**Details**
1	CIP	Monolithic construction
2	Precast-1	GSS connectors inside footings and cap beam
3	Precast-2	GSS connectors in column, debonding in footings and cap beam

Table 6.2. Comparison between the three bent systems.

Bridge Bent	Failure Mode	Ultimate Drift (%)	Effective Yield Displacement (in.)	Ultimate Displacement (in.)	Displacement Ductility Capacity	Peak Force Capacity (kip)
CIP	LCF bar fracture	6.0	2.66	18.72	7.04	370.0
Precast-1	Crushing of core	4.6	2.47	14.35	5.82	378.0
Precast-2	Crushing of core	5.5	2.65	17.16	6.47	362.5

Table 6.3. Characteristics of time-histories used in this study.

No.	Event	Year	Mw	Station	Mechanism	Rjb*	Rrup**	Pulse	Site Class
						(km)	(km)		
1	Irpinia_ Italy-01	1980	6.90	Sturno	Normal	6.78	10.84	Yes	C
2	Montenegro_ Yugoslavia	1979	7.10	Ulcinj-Hotel Olimpic	Reverse	3.97	5.76	Yes	D
3	Darfield_ New Zealand	2010	7.00	DSLC	Strike Slip	5.28	8.46	Yes	D
4	El Mayor-Cucapah_ Mexico	2010	7.20	Westside Elementary	Strike Slip	10.31	11.44	Yes	D
5	Corinth_ Greece	1981	6.60	Corinth	Normal	10.27	10.27	No	D
6	Iwate_Japan	2008	6.90	IWTH24	Reverse	3.10	5.18	No	C
7	Kobe_ Japan	1995	6.90	Amagasaki	Strike Slip	11.34	11.34	No	D
8	Superstition Hills-02	1987	6.54	Westmorland Fire St.	Strike Slip	13.03	13.03	No	D

*Rjb is the Joyner-Boore distance (The shortest distance to the surface projection of the rupture plane).
**Rrup is the closest distance to the rupture plane.

Table 6.4. Drift demands and capacity-to-demand ratios for CIP.

No.	Ground Motion	Pos. Drift (%)	Neg. Drift (%)	Peak Drift (%)	C/D
1	Irpinia	1.25	1.76	1.76	3.41
2	Montenegro	1.33	1.76	1.76	3.41
3	Darfield	1.28	1.68	1.68	3.57
4	El Mayor	1.71	1.48	1.71	3.51
5	Corinth	0.94	1.65	1.65	3.64
6	Iwate	1.97	1.08	1.97	3.05
7	Kobe	1.72	1.25	1.72	3.49
8	Superstition Hills	1.87	1.49	1.87	3.21
			Average =	1.77	3.40

Table 6.5. CIP drift demands and capacity-to-demand ratios for uniformly scaled records.

No.	Ground Motion	Scale Factor	Pos. Drift (%)	Neg. Drift (%)	Peak Drift (%)	C/D
1	Montenegro-1.5	1.5	2.90	1.59	2.90	2.07
2	Montenegro-2	2.0	5.57	1.36	5.57	1.08
3	Iwate-1.5	1.5	2.22	2.43	2.43	2.47
4	Iwate-2	2.0	2.54	2.88	2.88	2.08

Table 6.6. Drift demands and capacity-to-demand ratios for Precast-1.

No.	Ground Motion	Pos. Drift (%)	Neg. Drift (%)	Peak Drift (%)	C/D
1	Irpinia	1.28	1.77	1.77	2.60
2	Montenegro	1.30	1.77	1.77	2.60
3	Darfield	1.29	1.57	1.57	2.93
4	El Mayor	1.72	1.44	1.72	2.67
5	Corinth	0.96	1.65	1.65	2.79
6	Iwate	1.90	1.05	1.90	2.42
7	Kobe	1.74	1.27	1.74	2.64
8	Superstition Hills	1.90	1.54	1.90	2.42
			Average =	1.75	2.62

Table 6.7. Precast-1 drift demands and capacity-to-demand ratios for uniformly scaled records.

No.	Ground Motion	Scale Factor	Pos. Drift (%)	Neg. Drift (%)	Peak Drift (%)	C/D
1	Montenegro-1.5	1.5	2.61	1.65	2.61	1.76
2	Montenegro-2	2.0	5.58	1.26	5.58	0.82
3	Iwate-1.5	1.5	2.22	2.50	2.50	1.84
4	Iwate-2	2.0	2.46	3.00	3.00	1.53

Table 6.8. Drift demands and capacity-to-demand ratios for Precast-2.

No.	Ground Motion	Pos. Drift (%)	Neg. Drift (%)	Peak Drift (%)	C/D
1	Irpinia	1.36	1.76	1.76	3.13
2	Montenegro	1.90	1.63	1.90	2.89
3	Darfield	1.53	1.90	1.90	2.89
4	El Mayor	1.59	2.04	2.04	2.70
5	Corinth	1.09	1.63	1.63	3.37
6	Iwate	2.08	1.16	2.08	2.64
7	Kobe	1.90	1.42	1.90	2.89
8	Superstition Hills	1.98	1.60	1.98	2.78
			Average =	1.90	2.90

Table 6.9. Precast-2 drift demands and capacity-to-demand ratios for uniformly scaled records.

No.	Ground Motion	Scale Factor	Pos. Drift (%)	Neg. Drift (%)	Peak Drift (%)	C/D
1	Montenegro-1.5	1.5	3.61	1.04	3.61	1.52
2	Montenegro-2	2.0	5.79	1.54	5.79	0.95
3	Iwate-1.5	1.5	2.16	2.42	2.42	2.27
4	Iwate-2	2.0	2.60	2.72	2.72	2.02

Table 6.10. Drift demands for the three bents.

		CIP		Precast-1		Precast-2	
No.	Ground Motion	Peak Drift (%)	C/D	Peak Drift (%)	C/D	Peak Drift (%)	C/D
1	Irpinia	1.76	3.41	1.77	2.60	1.76	3.13
2	Montenegro	1.76	3.41	1.77	2.60	1.90	2.89
3	Darfield	1.68	3.57	1.57	2.93	1.90	2.89
4	El Mayor	1.71	3.51	1.72	2.67	2.04	2.70
5	Corinth	1.65	3.64	1.65	2.79	1.63	3.37
6	Iwate	1.97	3.05	1.90	2.42	2.08	2.64
7	Kobe	1.72	3.49	1.74	2.64	1.90	2.89
8	Superstition Hills	1.87	3.21	1.90	2.42	1.98	2.78
	Peak =	1.97	3.05	1.90	2.42	2.08	2.64
	Average =	1.77	3.40	1.75	2.62	1.90	2.90

Table 6.11. Drift demands for the three bents under uniformly scaled ground motions.

			CIP		Precast-1		Precast-2	
No.	Ground Motion	Scale Factor	Peak Drift (%)	C/D	Peak Drift (%)	C/D	Peak Drift (%)	C/D
1	Montenegro-1.5	1.5	2.90	2.07	2.61	1.76	3.61	1.52
2	Montenegro-2	2.0	5.57	1.08	5.58	0.82	5.79	0.95
3	Iwate-1.5	1.5	2.43	2.47	2.50	1.84	2.47	2.23
4	Iwate-2	2.0	2.88	2.08	3.00	1.53	2.72	2.02

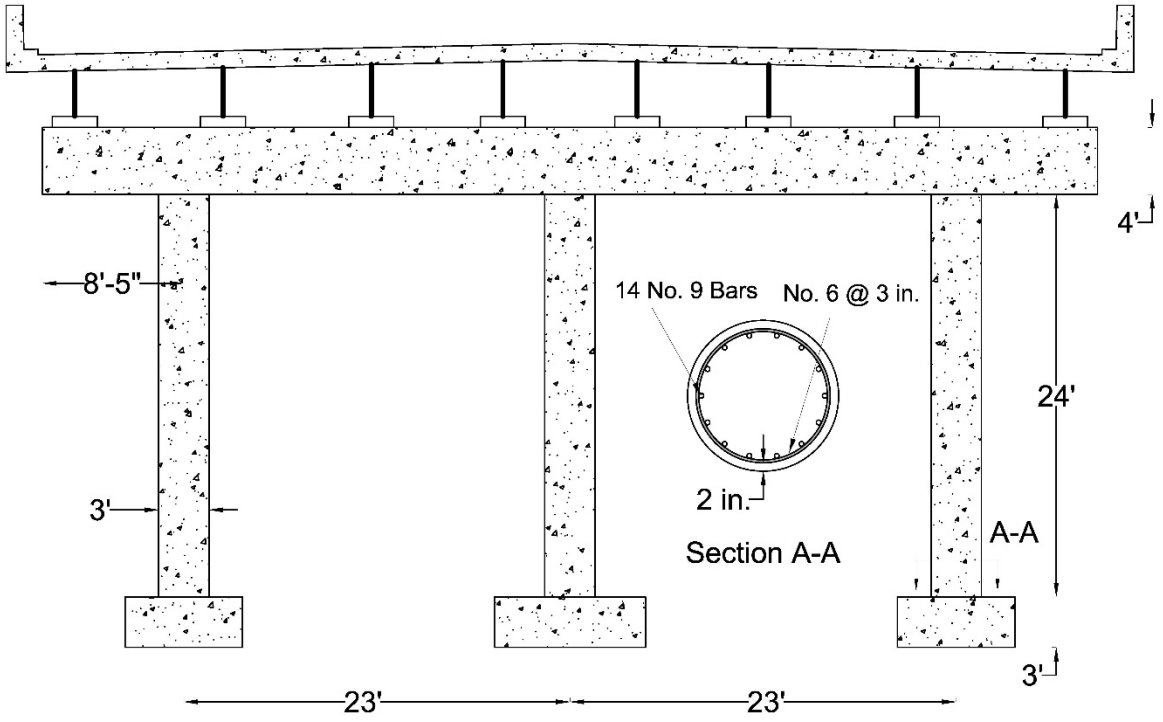

Fig. 6.1. Details of bridge bent CIP.

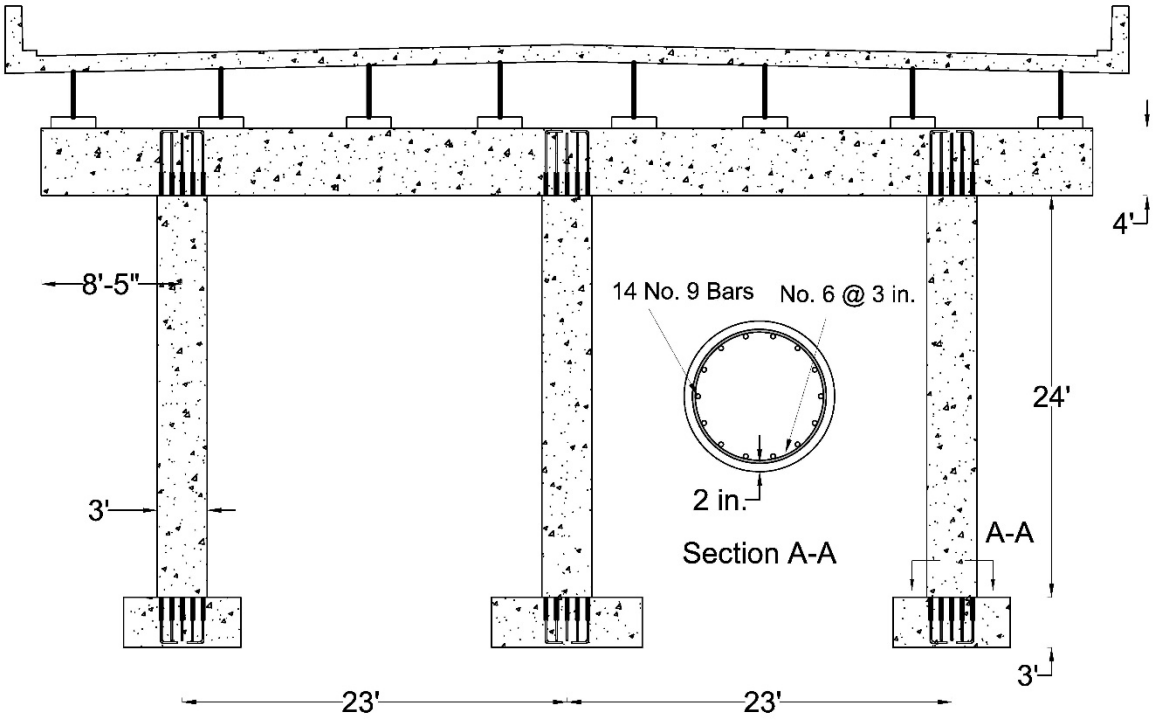

Fig. 6.2. Details of bridge bent Precast-1.

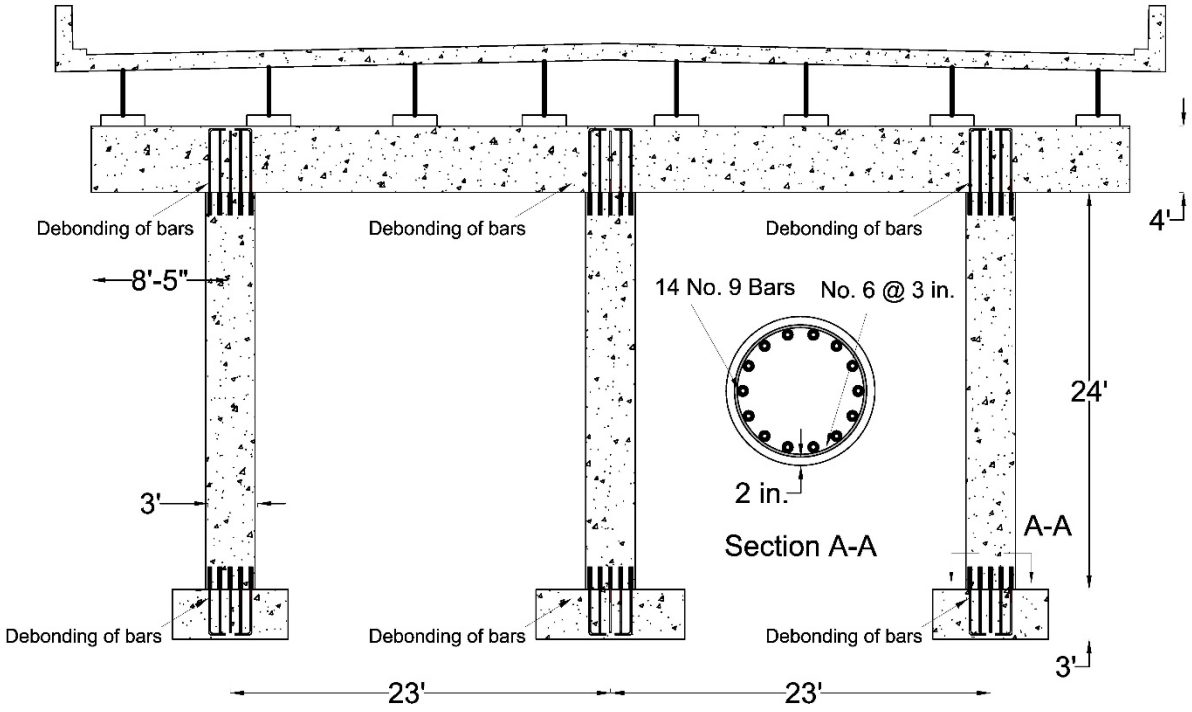

Fig. 6.3. Details of bridge bent Precast-2.

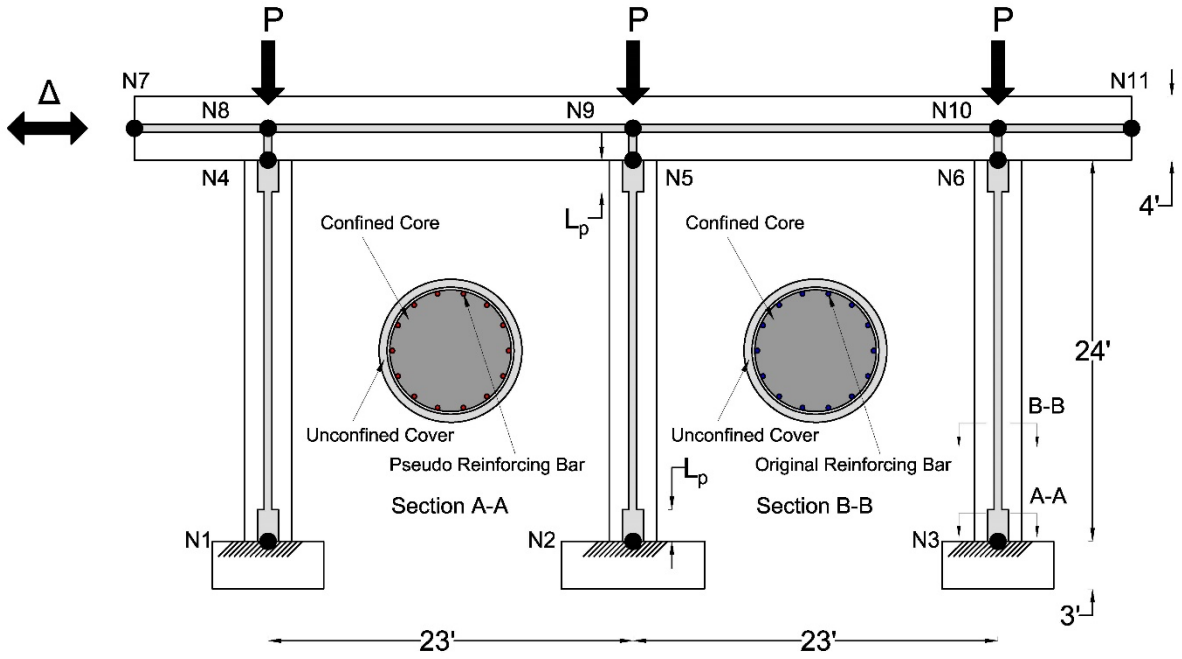

Fig. 6.4. Computational model schematic.

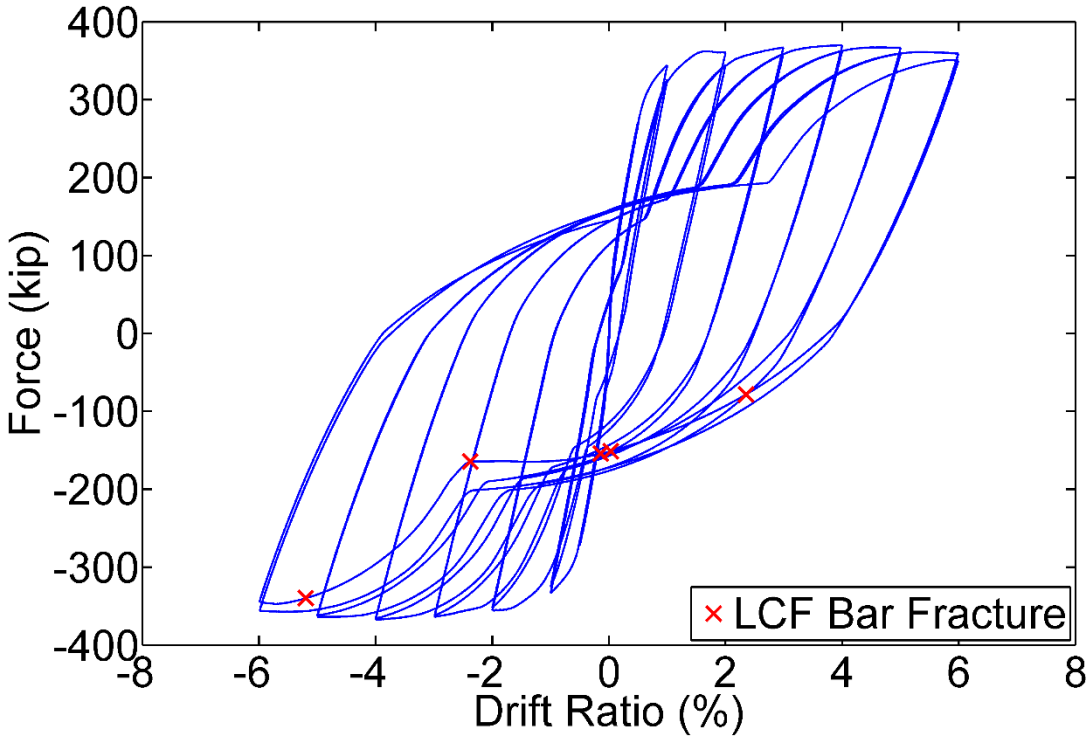

Fig. 6.5. Hysteresis response of CIP.

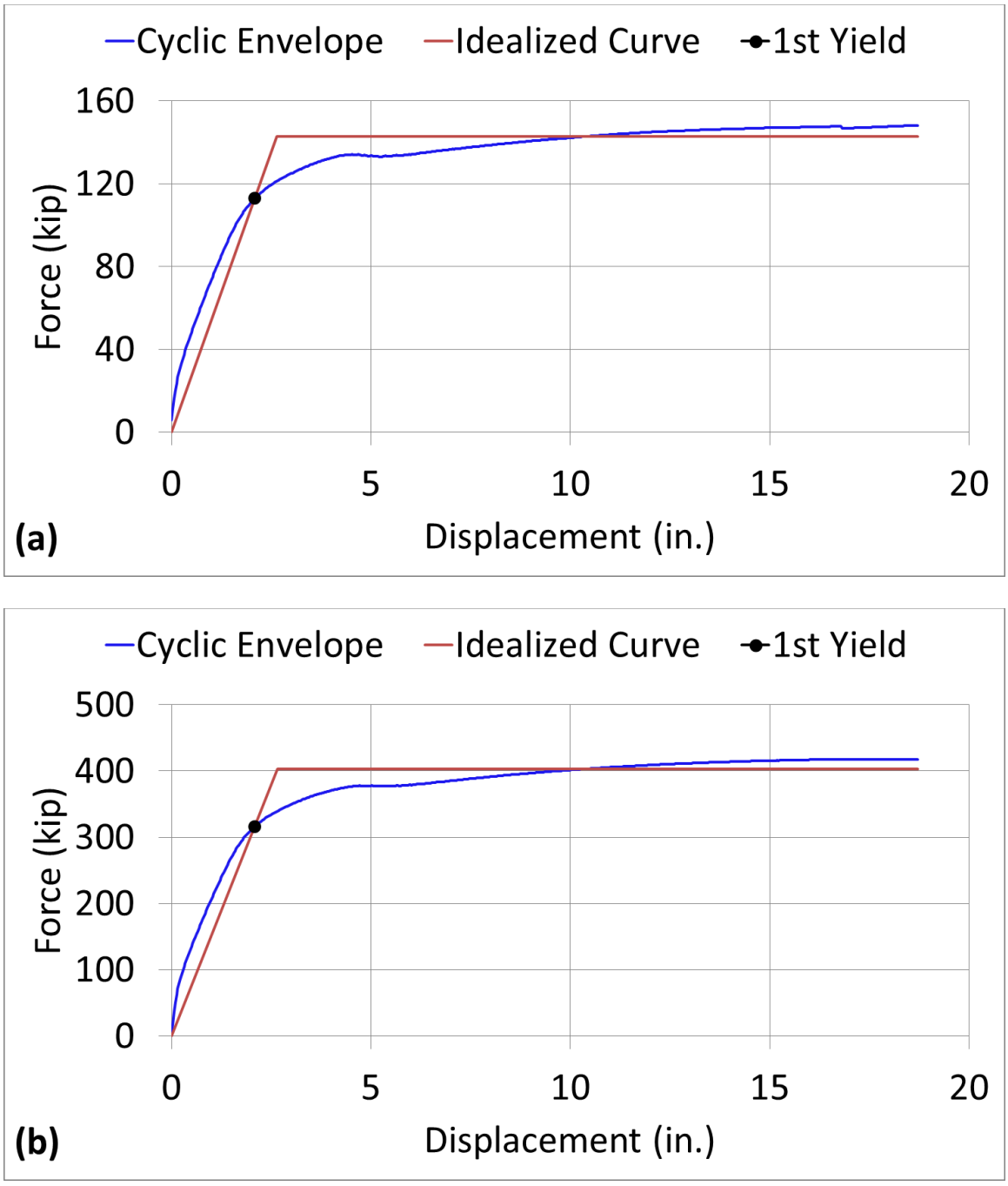

Fig. 6.6. Displacement ductility capacity for CIP: (a) right column, $\mu_C = 7.09$; (b) bridge bent, $\mu_C = 7.04$.

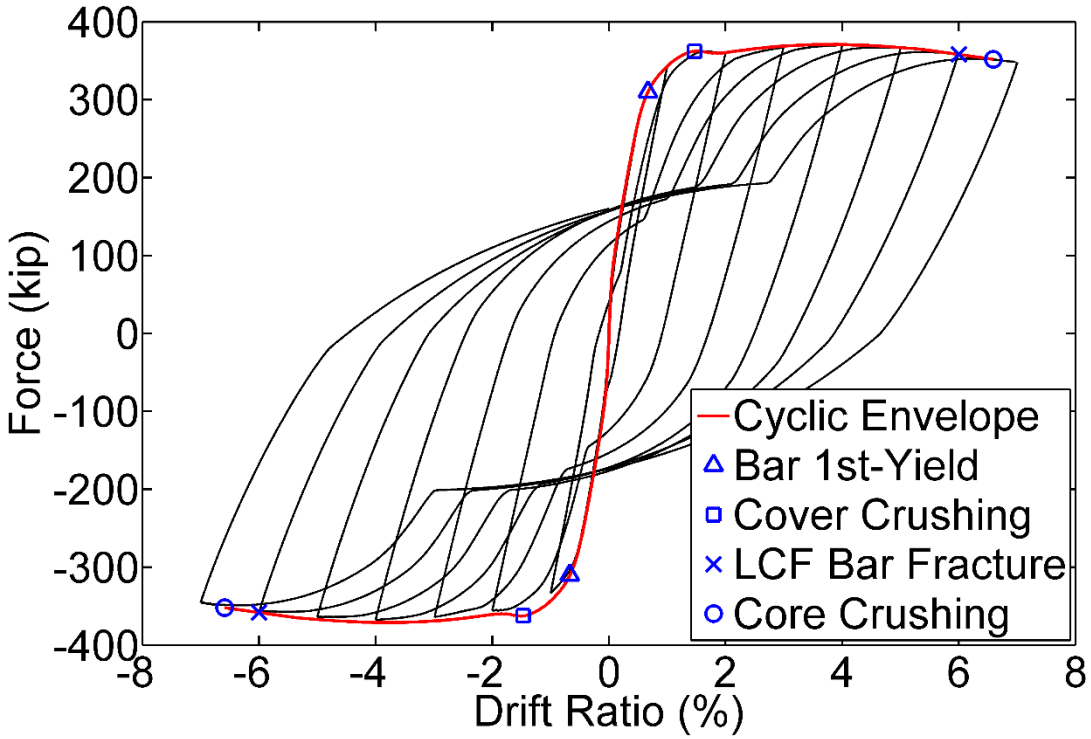

Fig. 6.7. Capacity envelope for CIP.

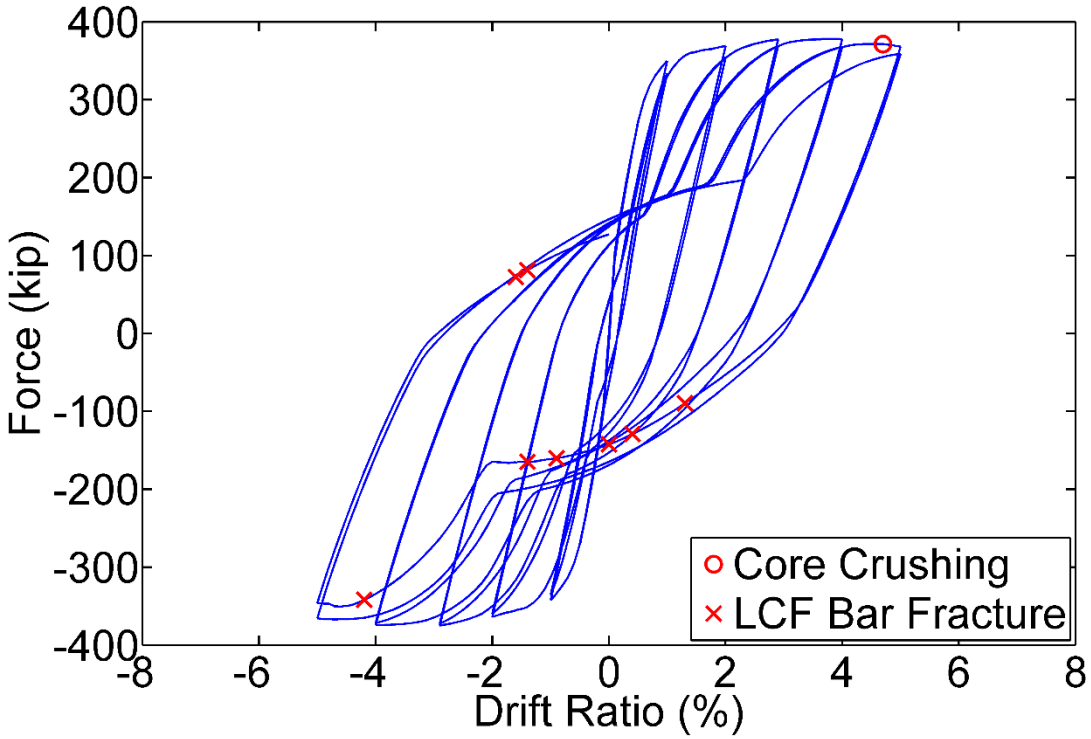

Fig. 6.8. Hysteresis response of Precast-1.

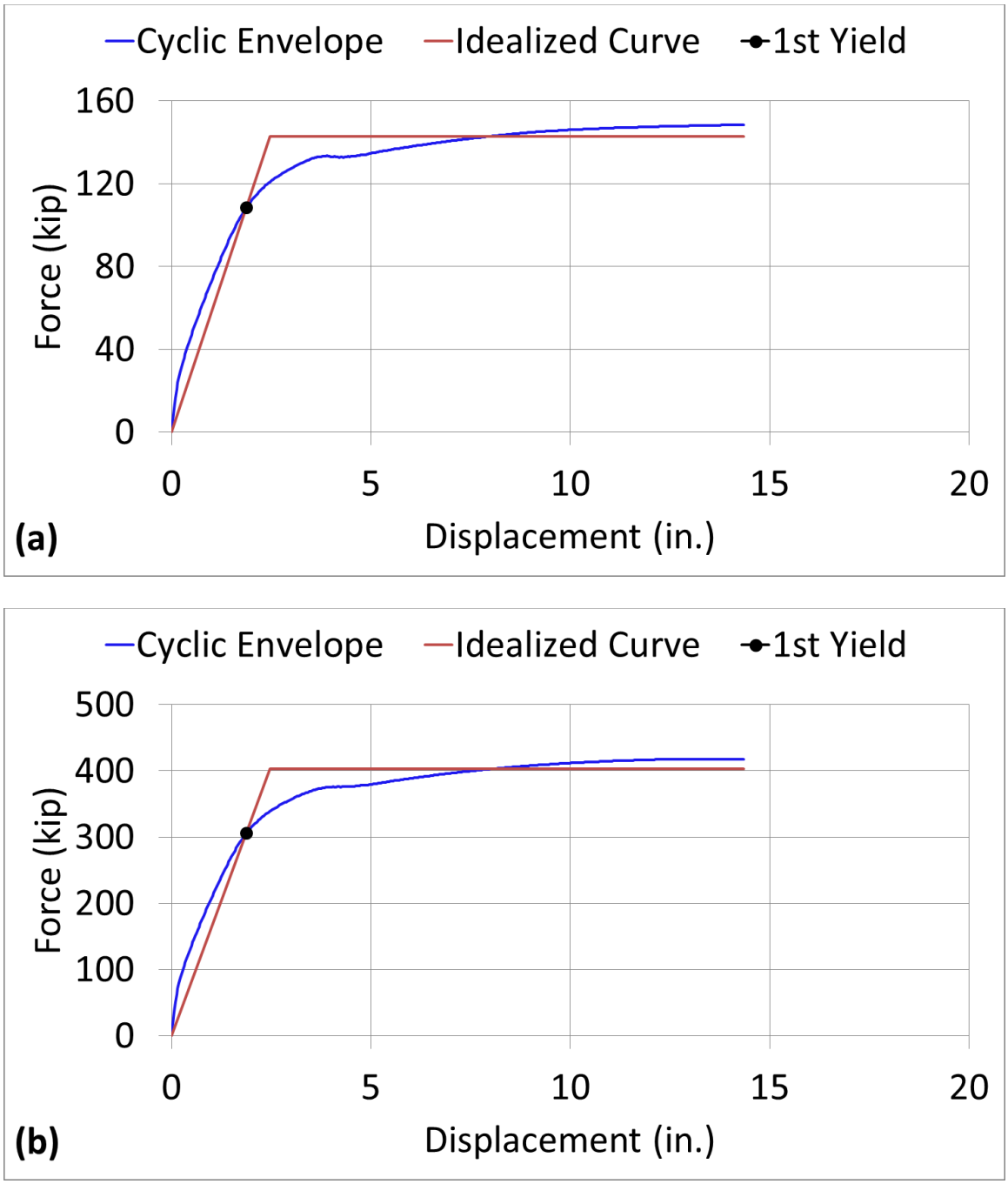

Fig. 6.9. Displacement ductility capacity for Precast-1: (a) right column, $\mu_C = 5.82$; (b) bridge bent, $\mu_C = 5.82$.

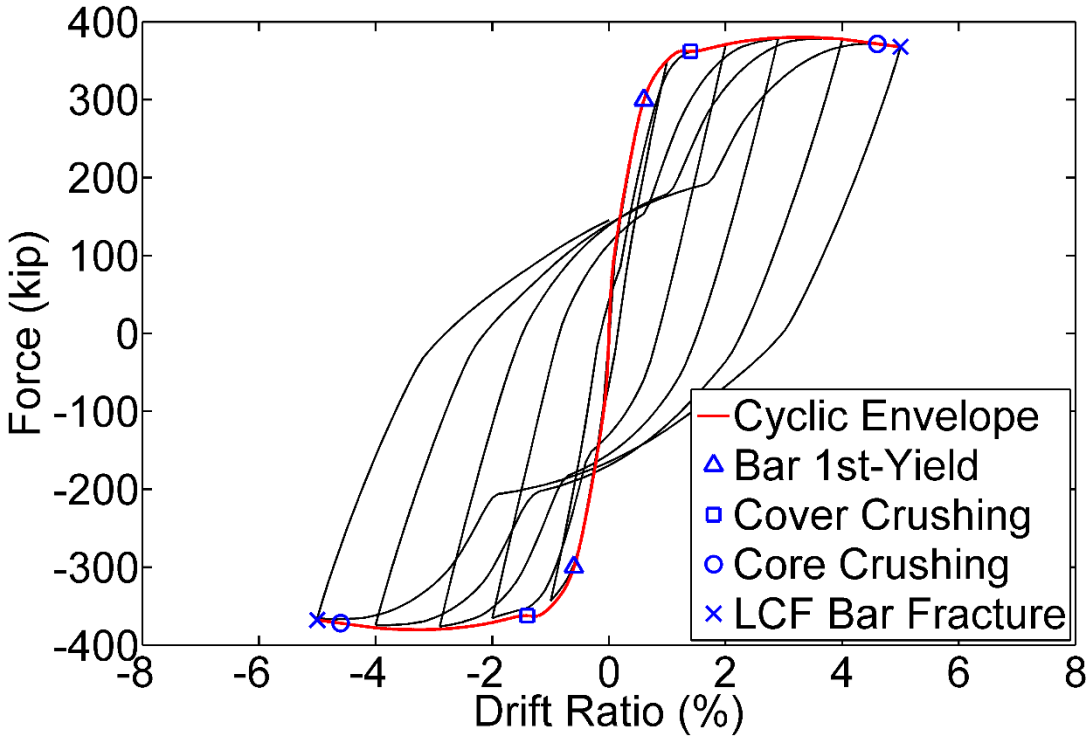

Fig. 6.10. Capacity envelope for Precast-1.

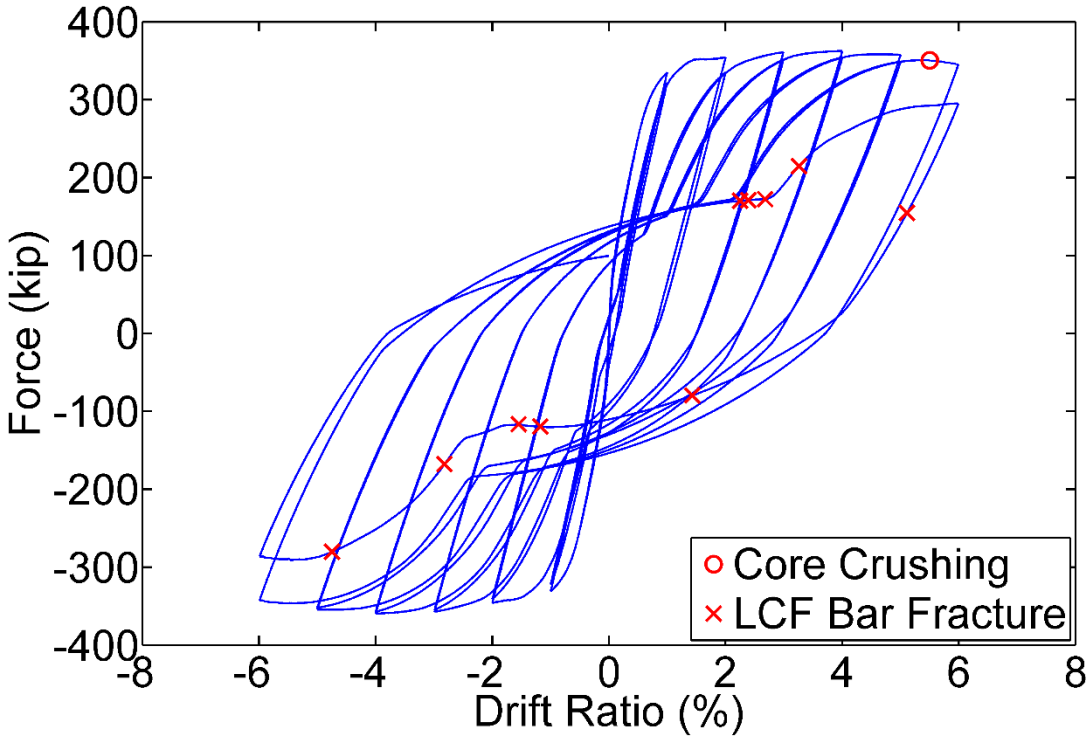

Fig. 6.11. Hysteresis response of Precast-2.

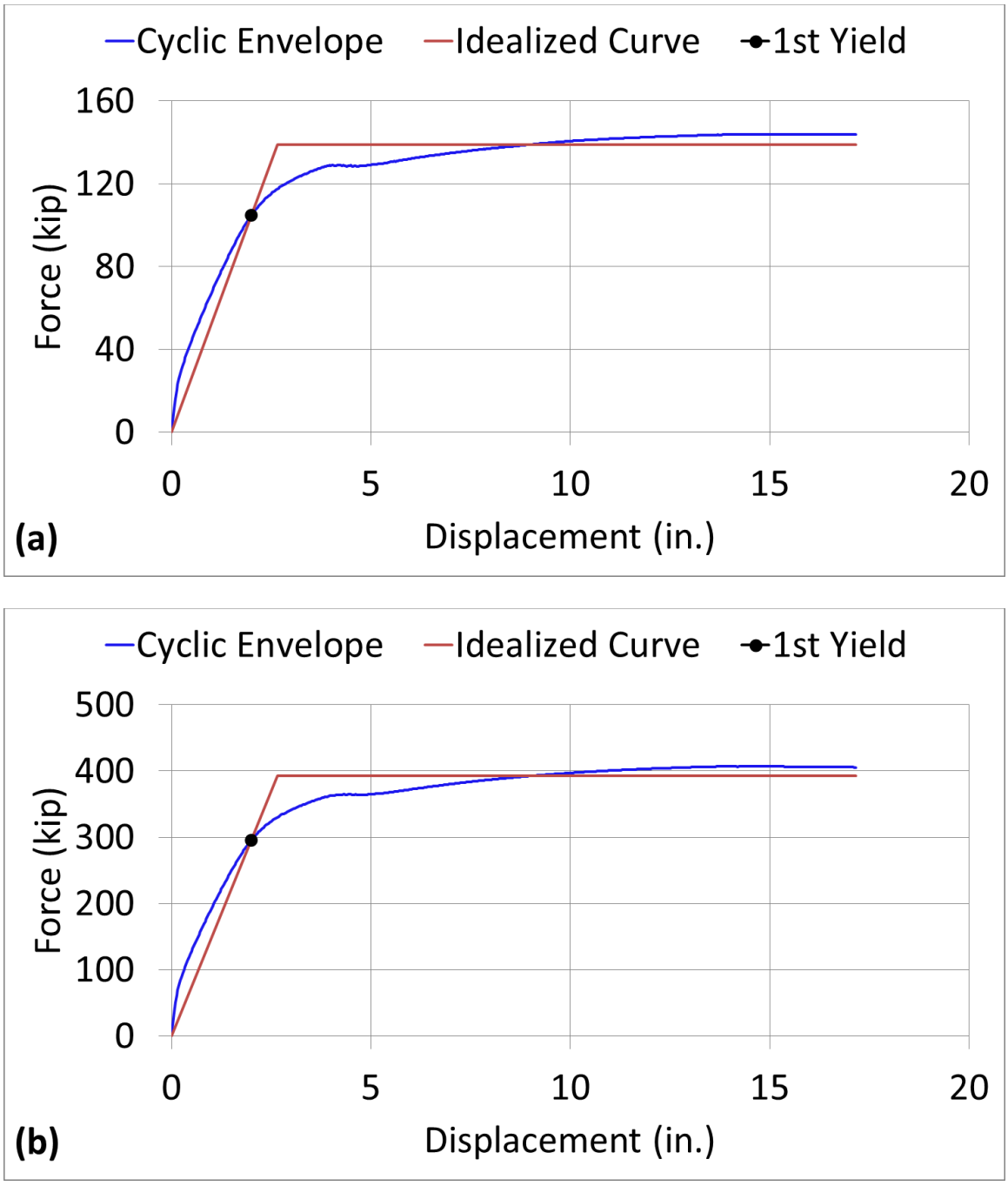

Fig. 6.12. Displacement ductility capacity for Precast-2: (a) right column, $\mu_C = 6.48$; (b) bridge bent, $\mu_C = 6.47$.

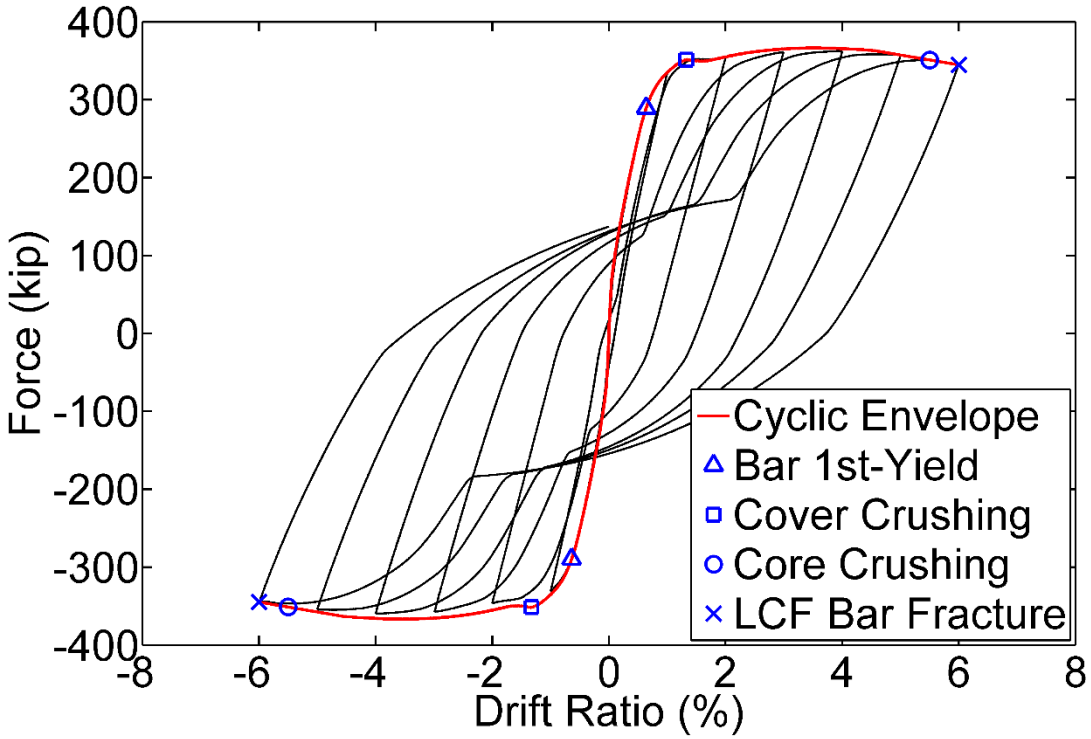

Fig. 6.13. Capacity envelope for Precast-2.

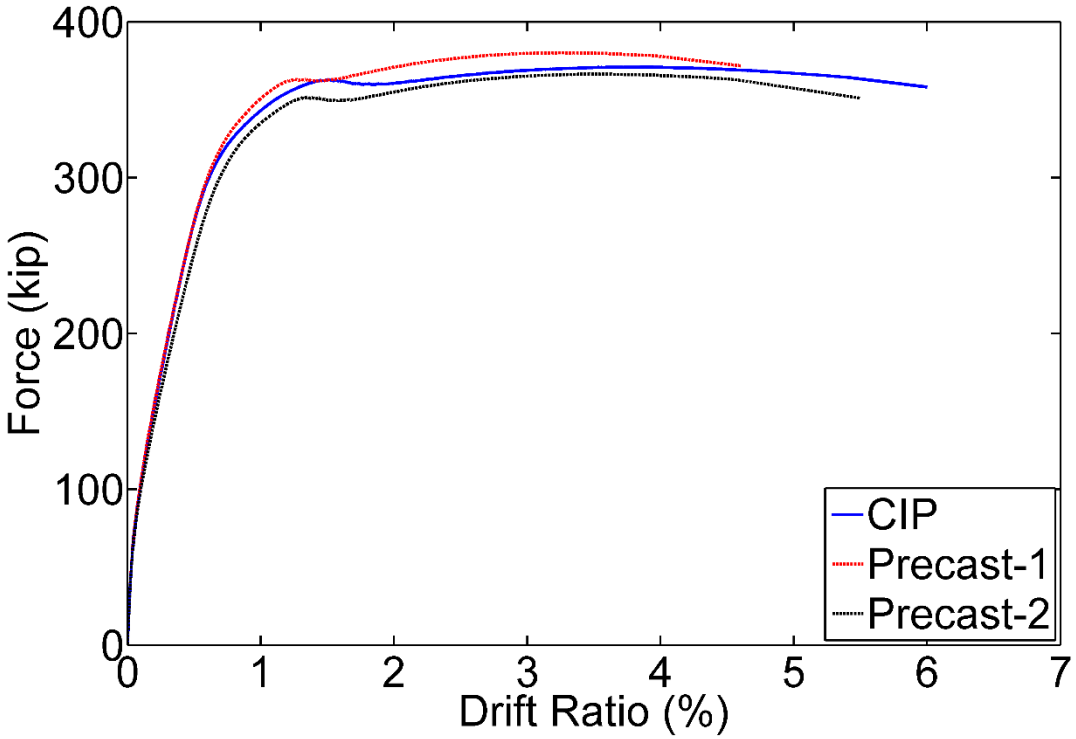

Fig. 6.14. Pushover comparison of the bridge bents.

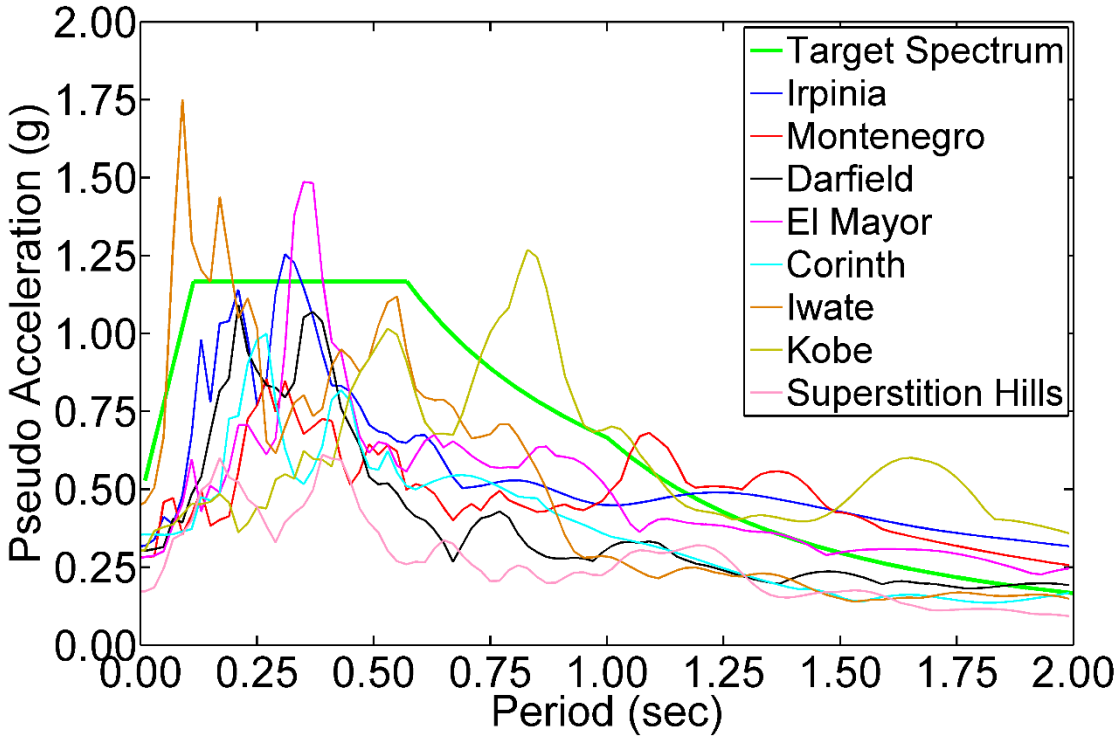

Fig. 6.15. Design acceleration response spectrum and unmatched response spectra.

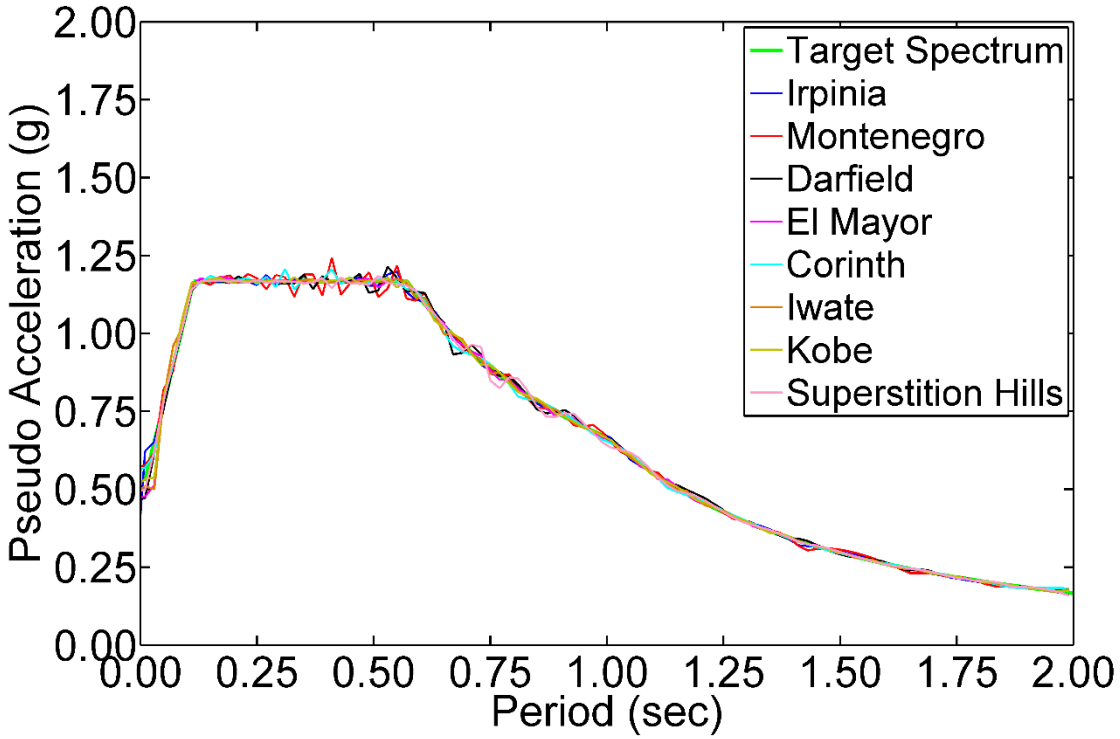

Fig. 6.16. Design acceleration response spectrum and matched response spectra.

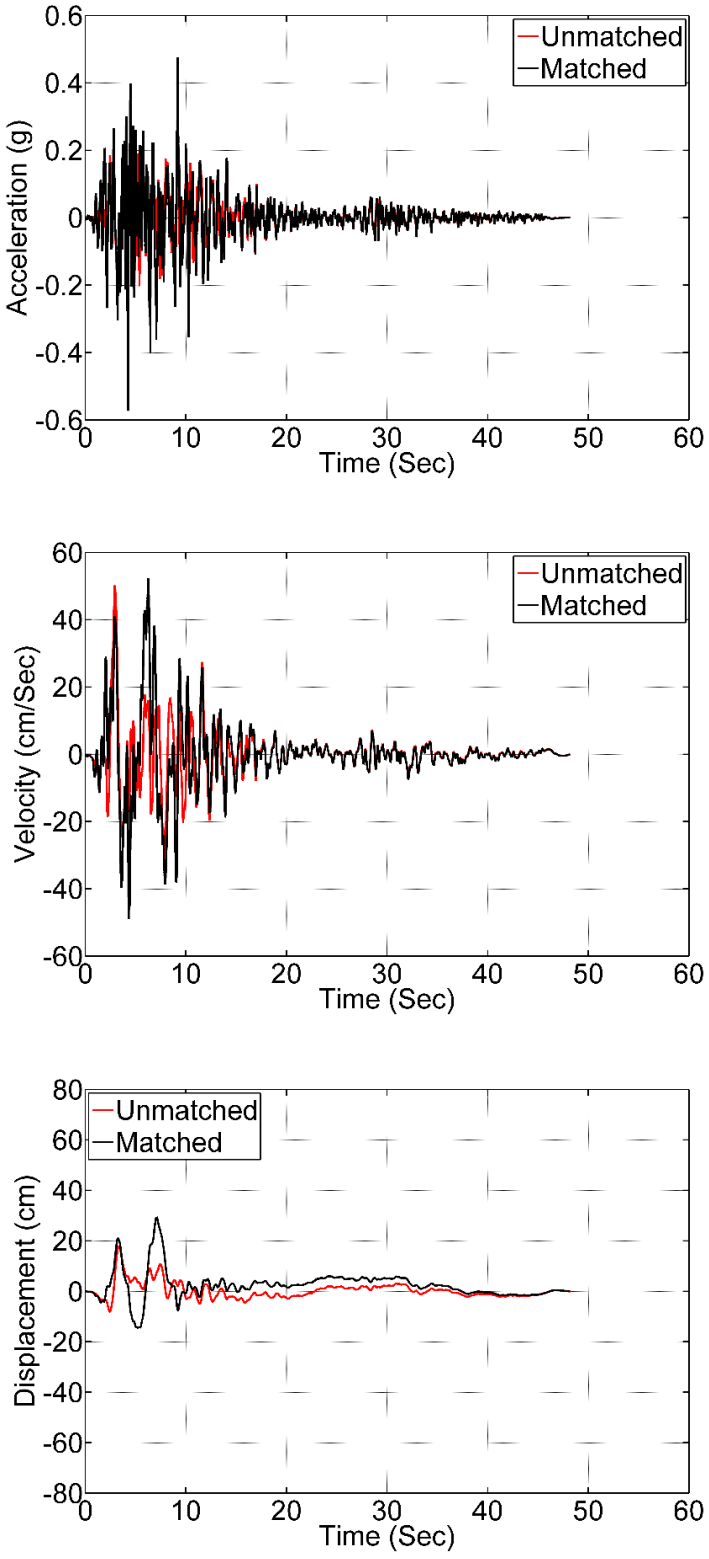

Fig. 6.17. Time-histories for Montenegro ground motion (pulse-like).

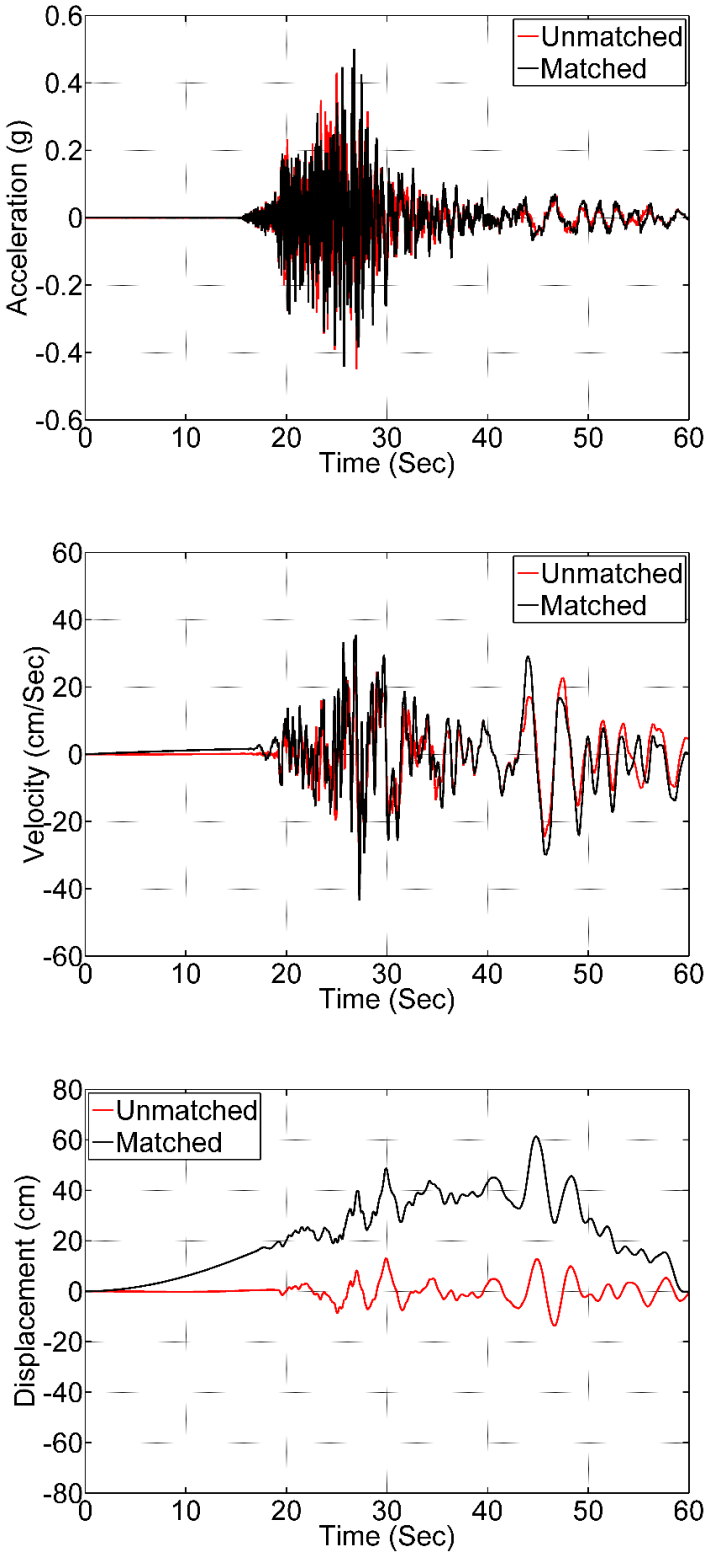

Fig. 6.18. Time-histories for Iwate ground motion (not pulse-like).

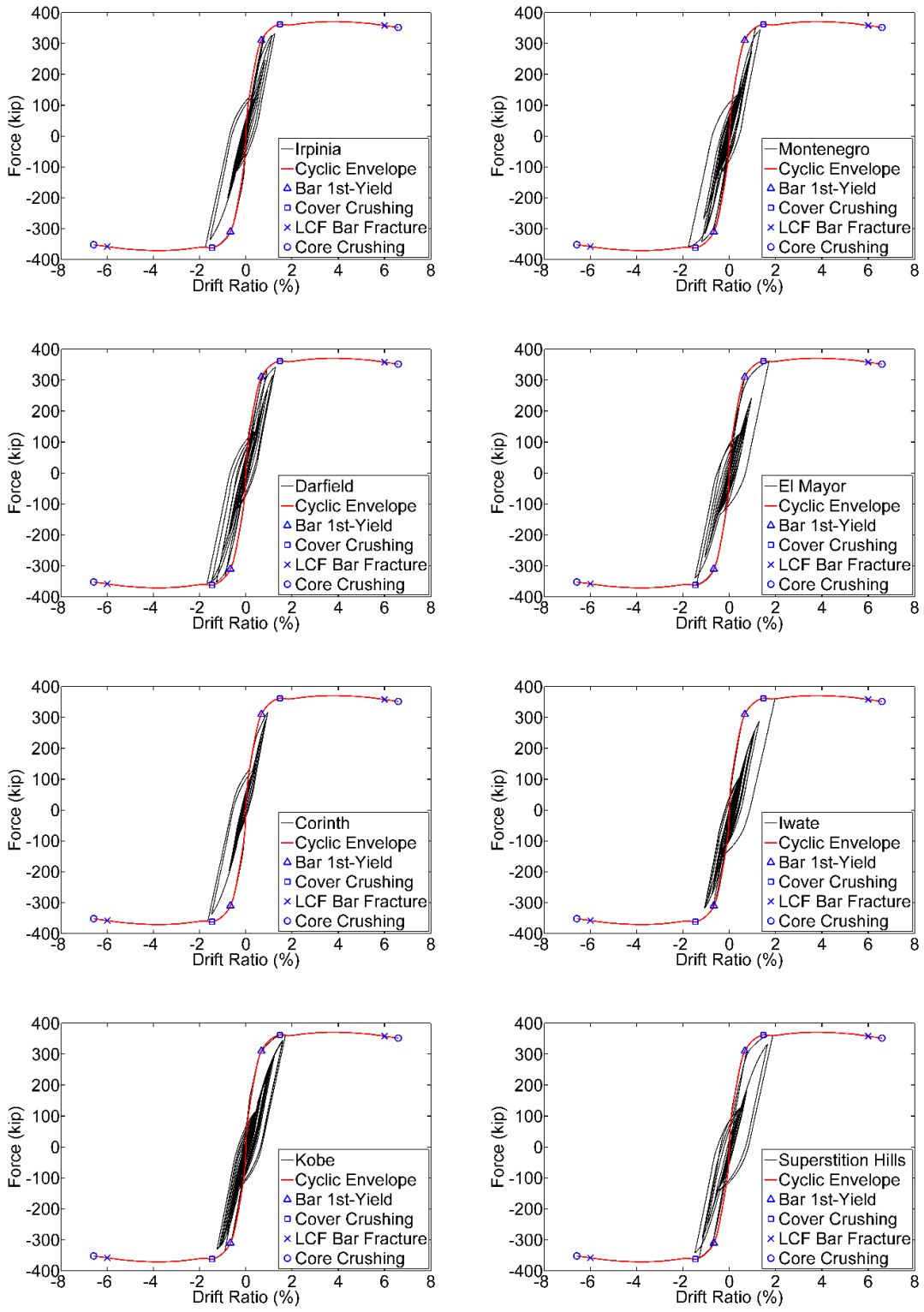

Fig. 6.19. Force-Drift response of CIP to ground motions.

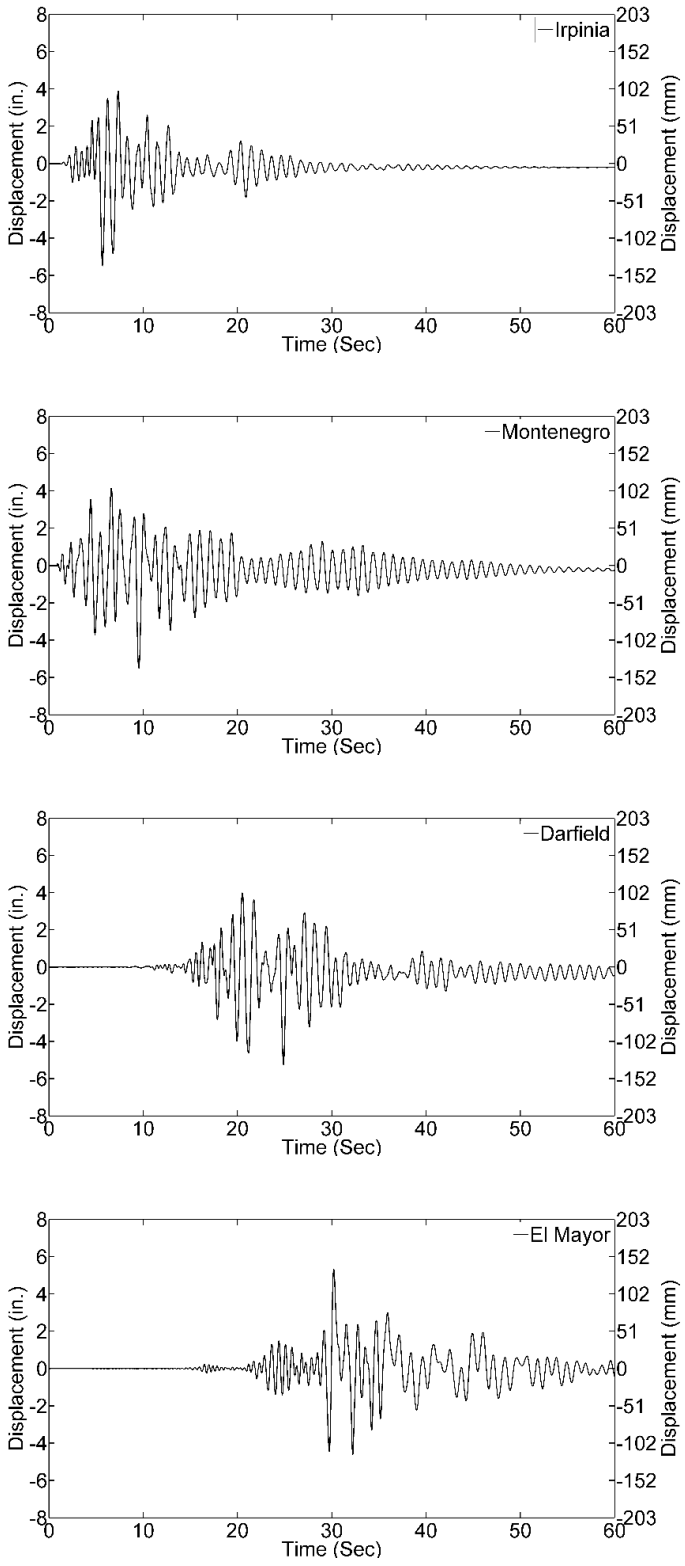

Fig. 6.20. CIP displacement response to ground motions.

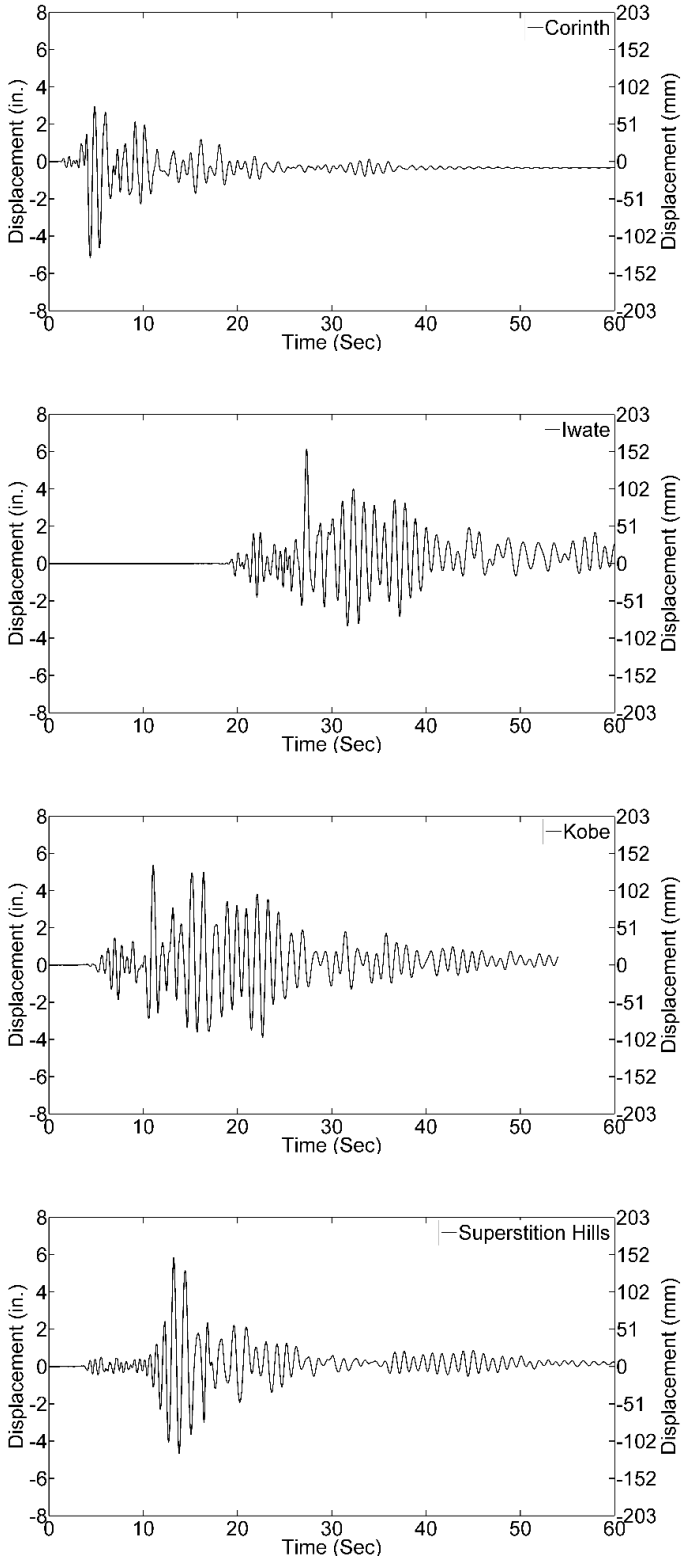

Fig. 6.20 (continued).

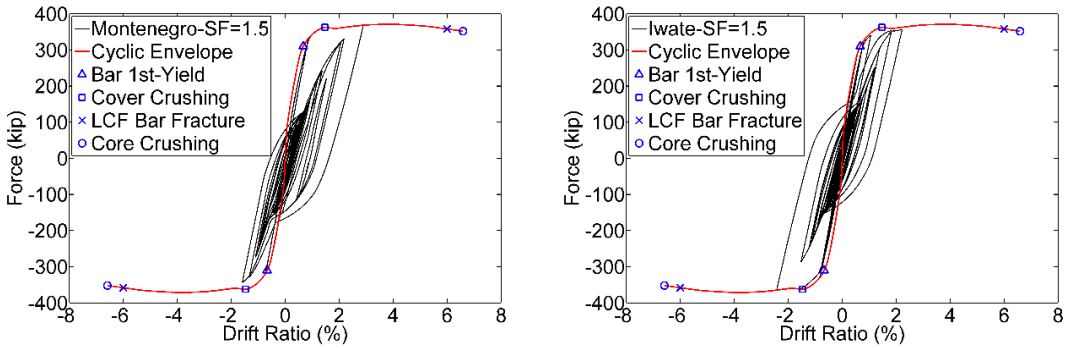

(a)

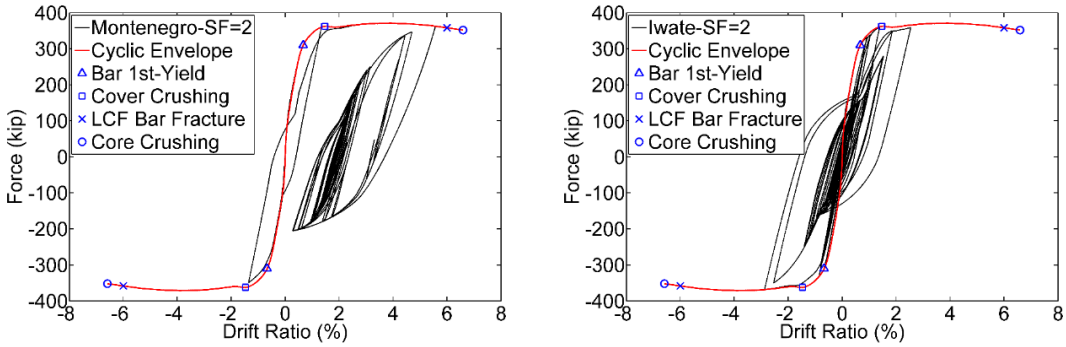

(b)

Fig. 6.21. Force-Drift response of CIP to uniformly scaled ground motions: (a) scale factor of 1.5; (b) scale factor of 2.0.

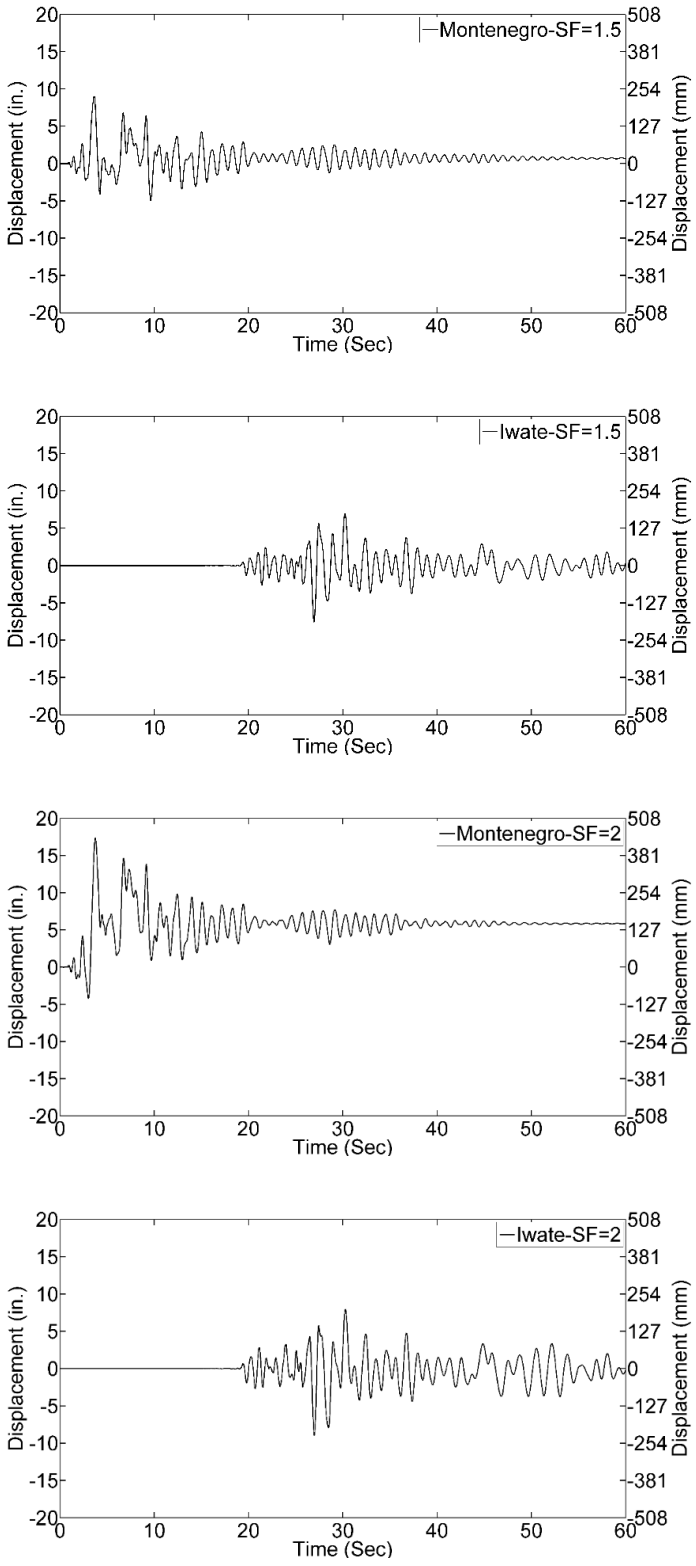

Fig. 6.22. CIP displacement response to uniformly scaled ground motions.

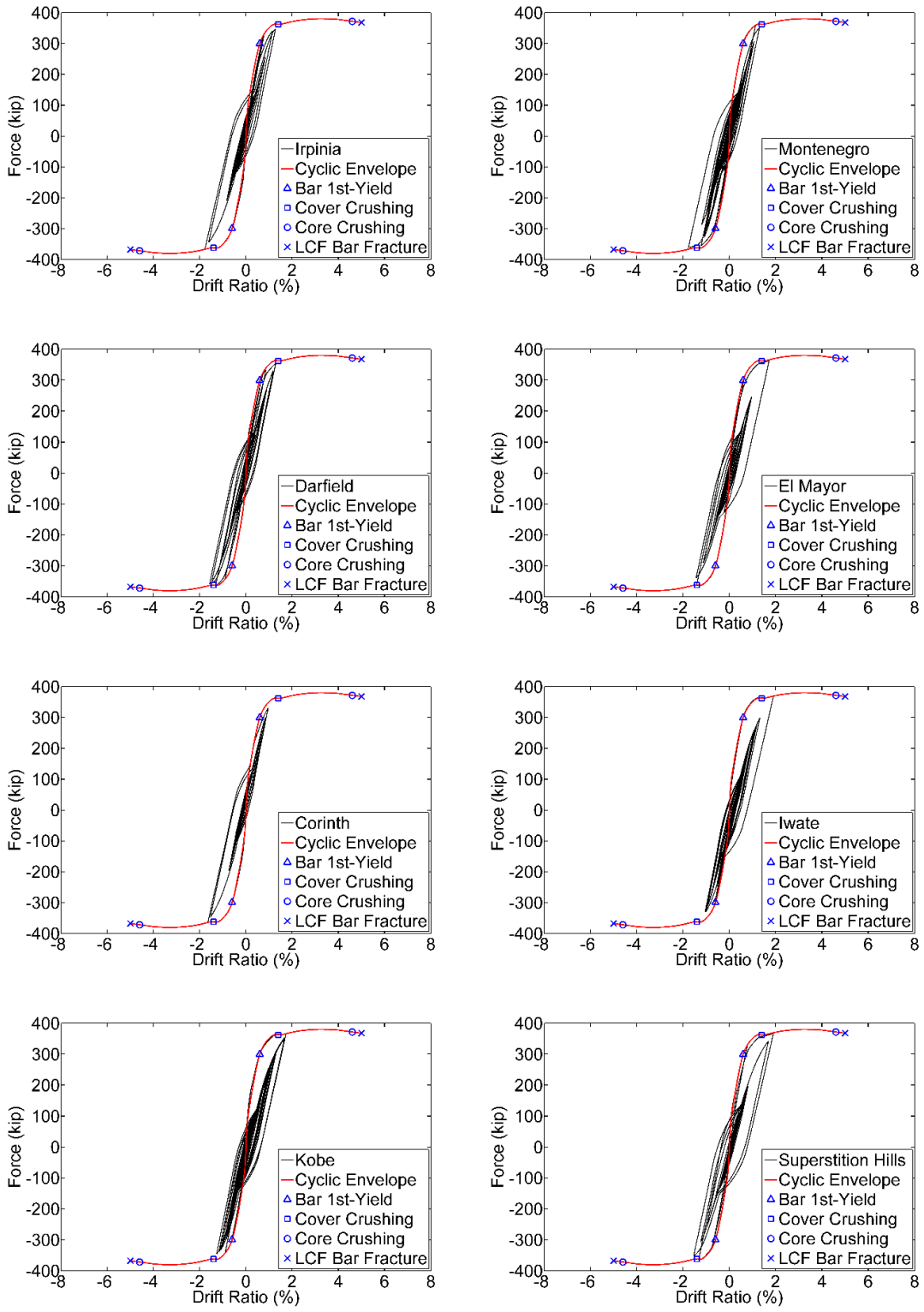

Fig. 6.23. Force-Drift response of Precast-1 to ground motions.

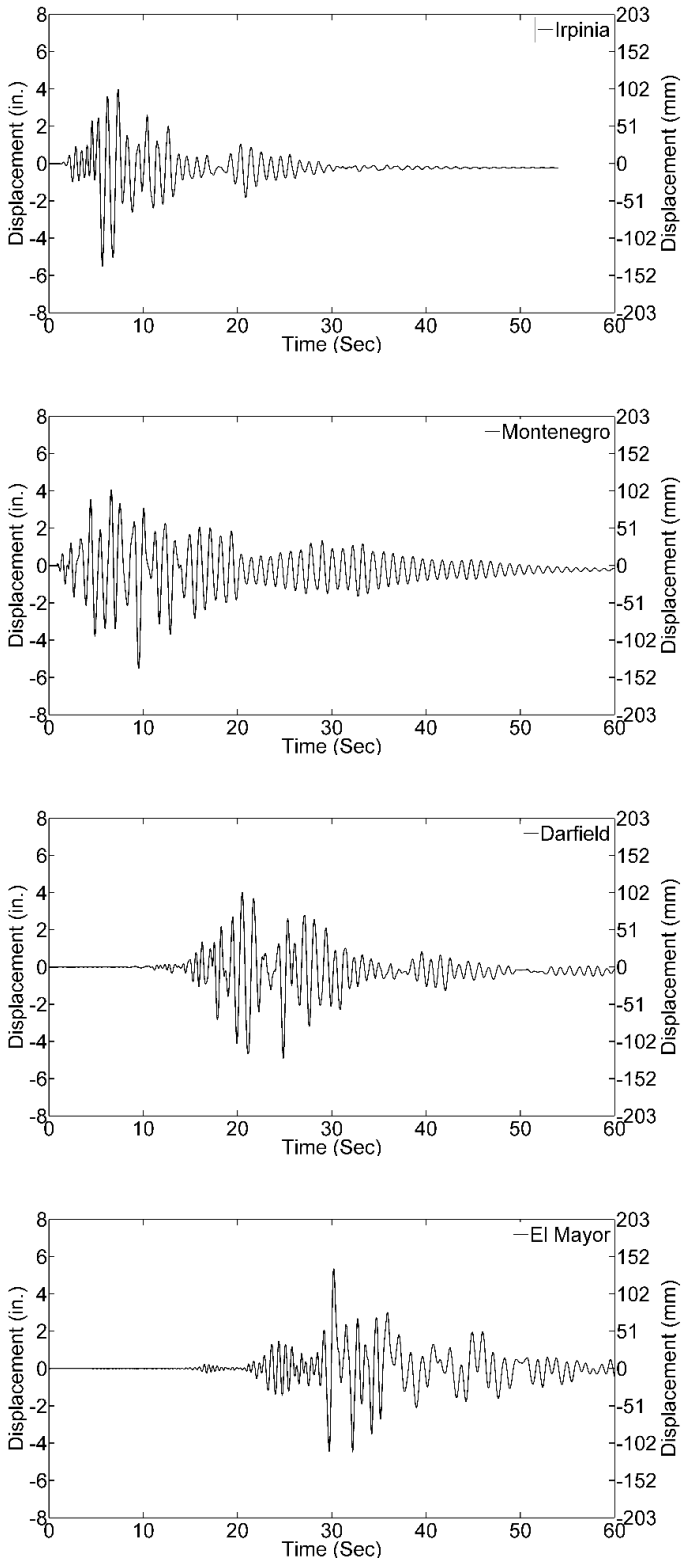

Fig. 6.24. Precast-1 displacement response to ground motions.

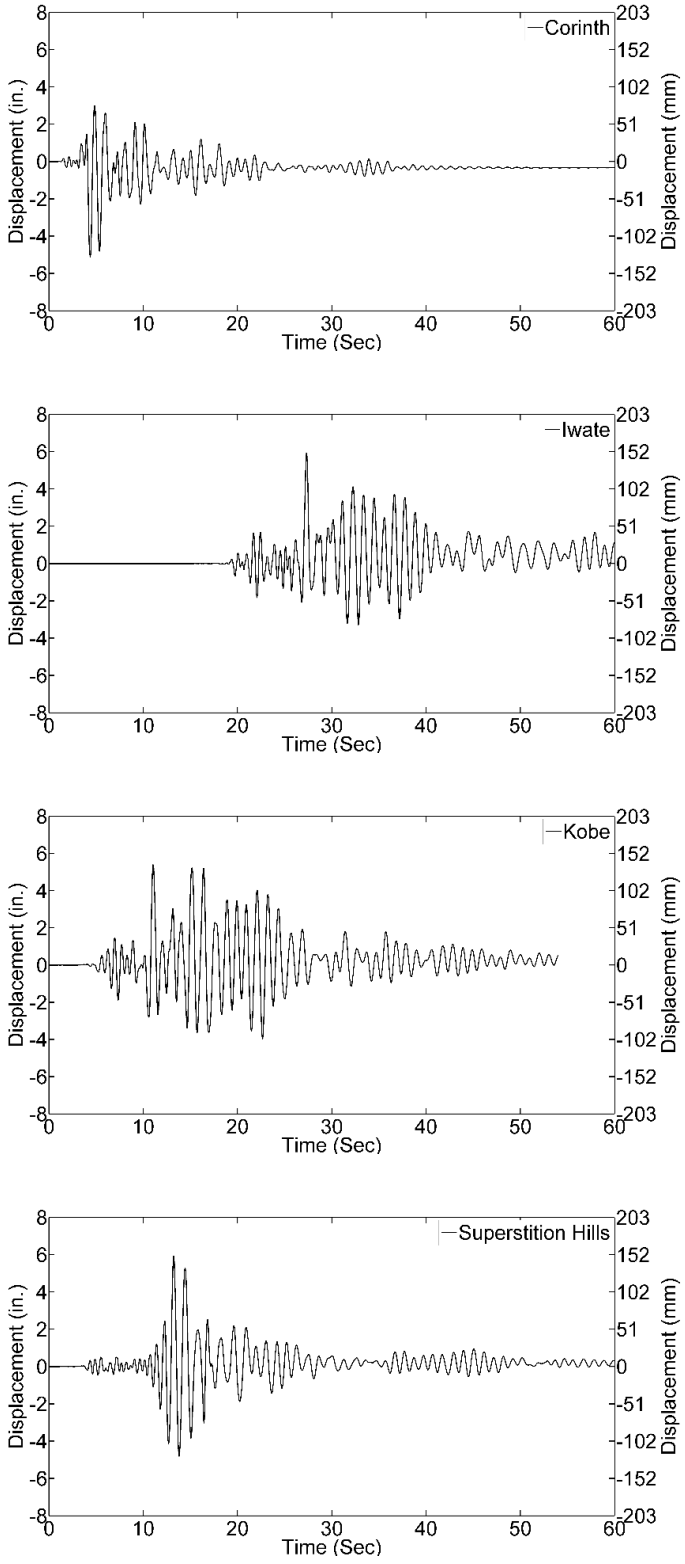

Fig. 6.24 (continued).

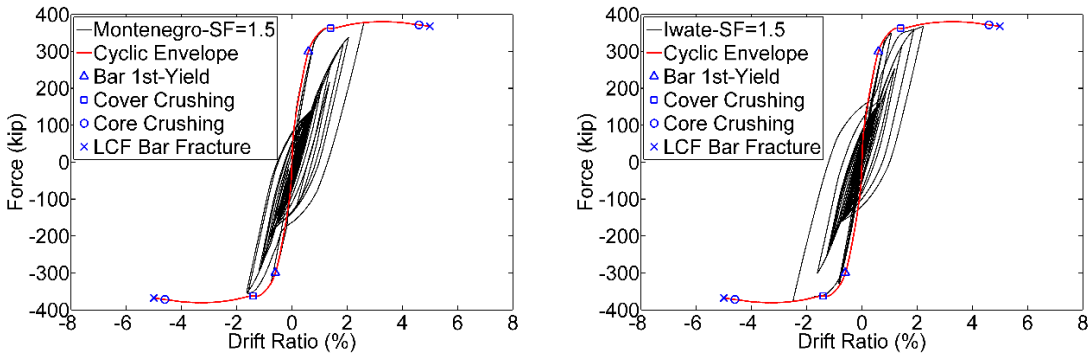

(a)

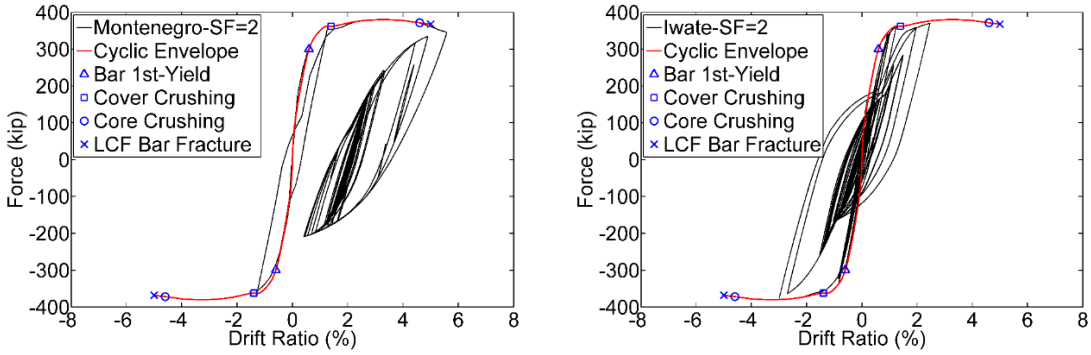

(b)

Fig. 6.25. Force-Drift response of Precast-1 to uniformly scaled ground motions: (a) scale factor of 1.5; (b) scale factor of 2.0.

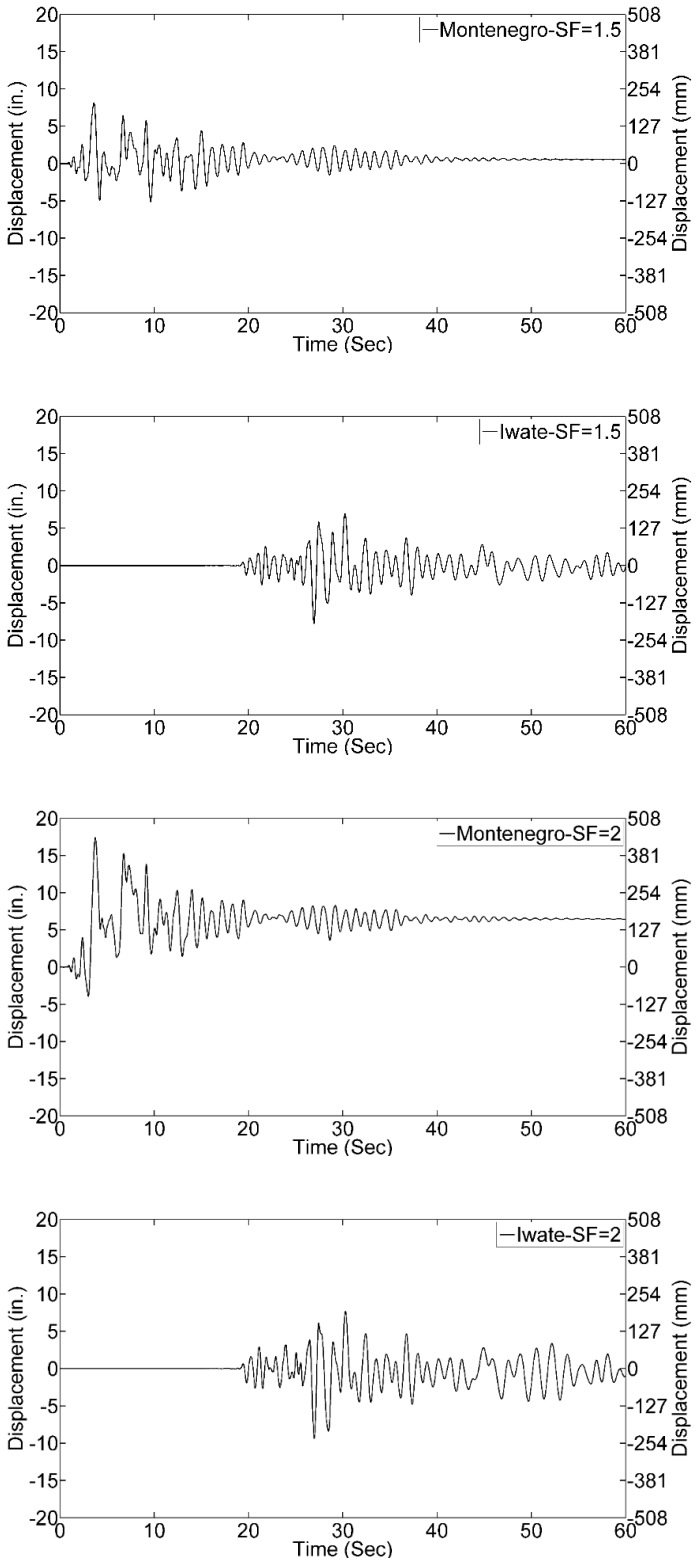

Fig. 6.26. Precast-1 displacement response to uniformly scaled ground motions.

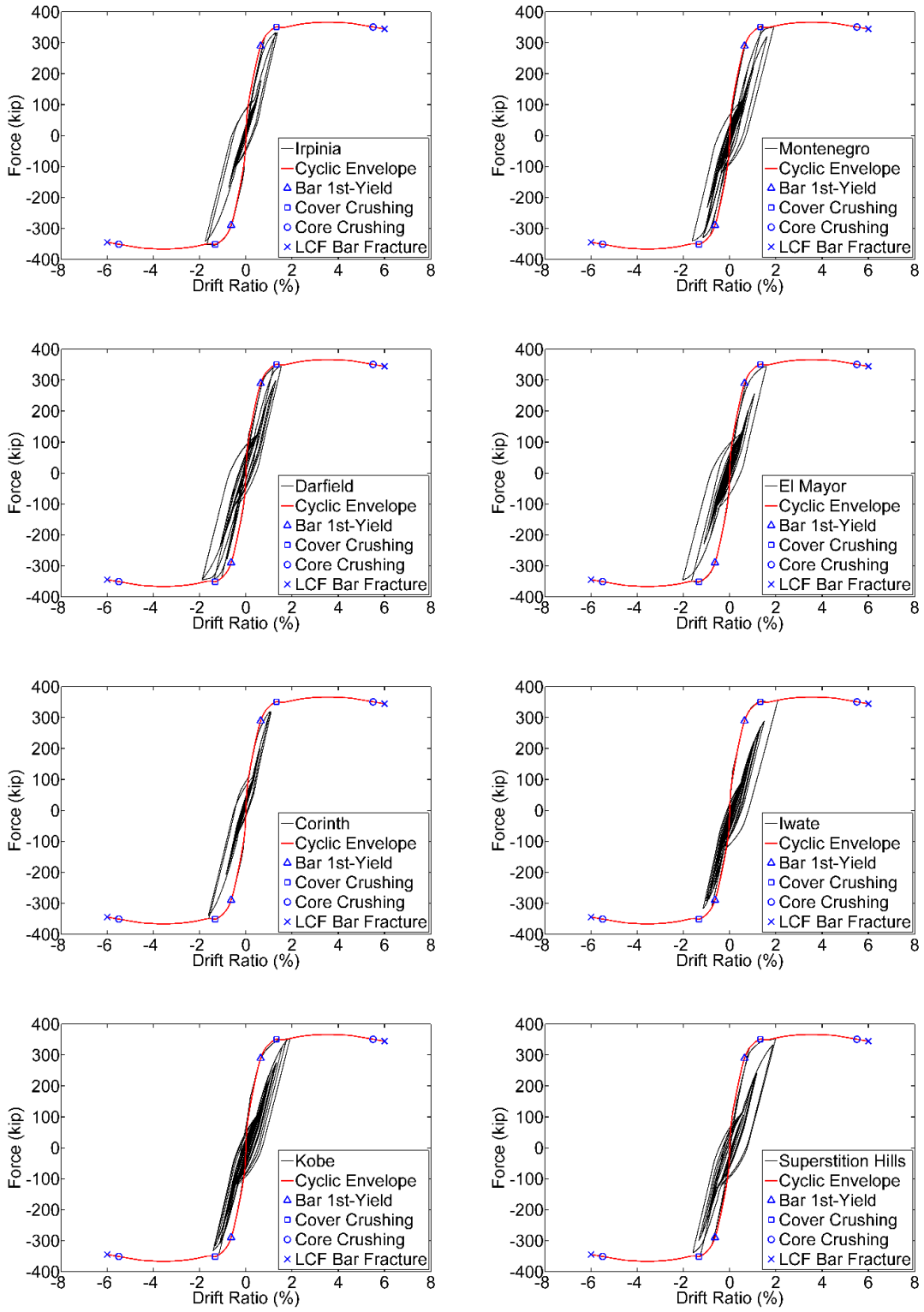

Fig. 6.27. Force-Drift response of Precast-2 to ground motions.

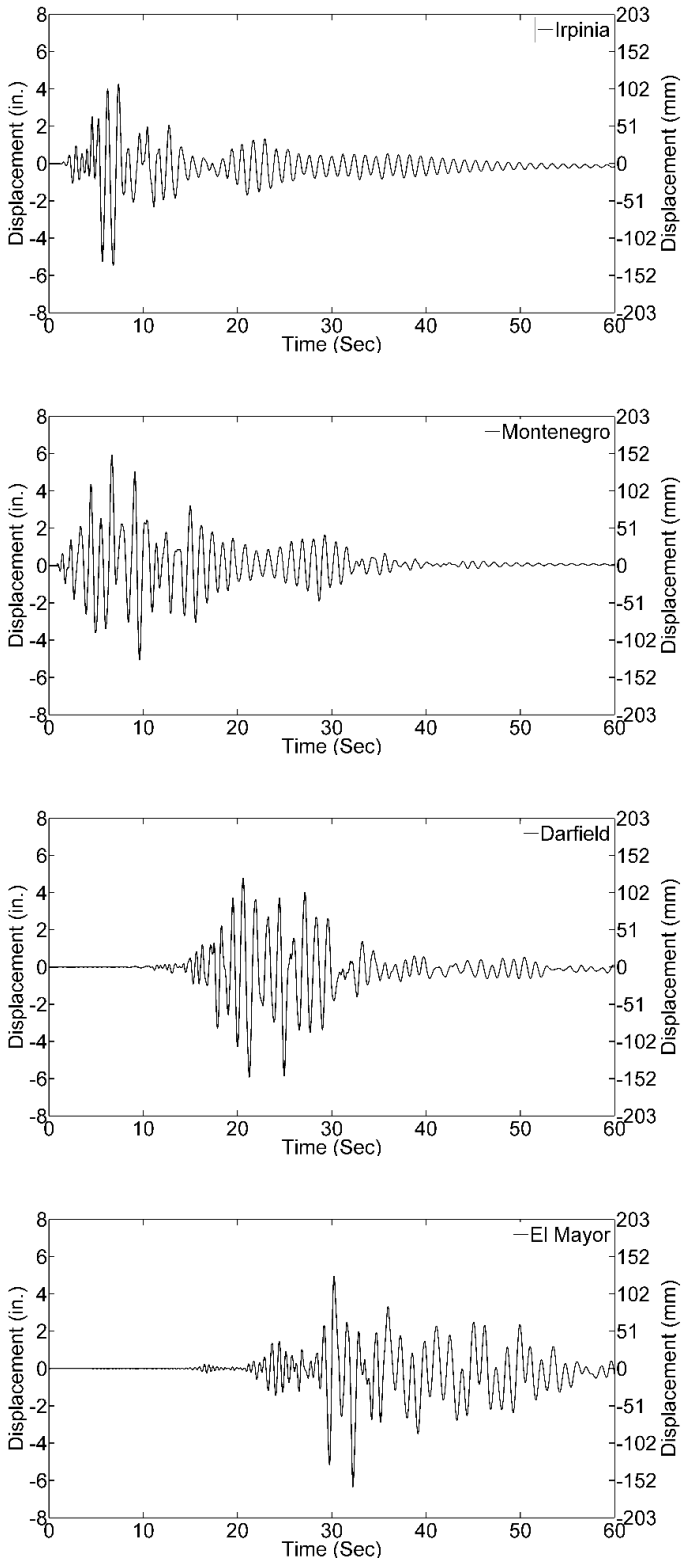

Fig. 6.28. Precast-2 displacement response to ground motions.

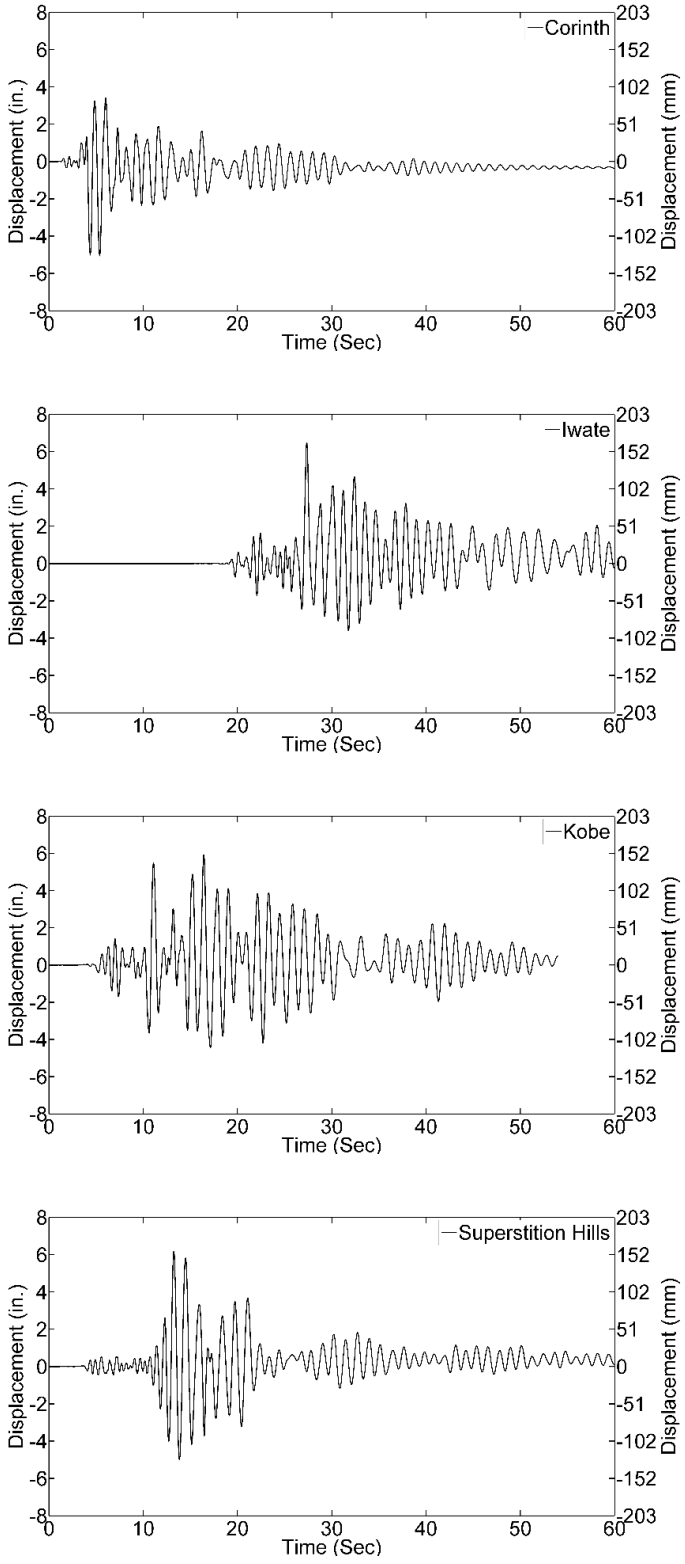

Fig. 6.28 (continued).

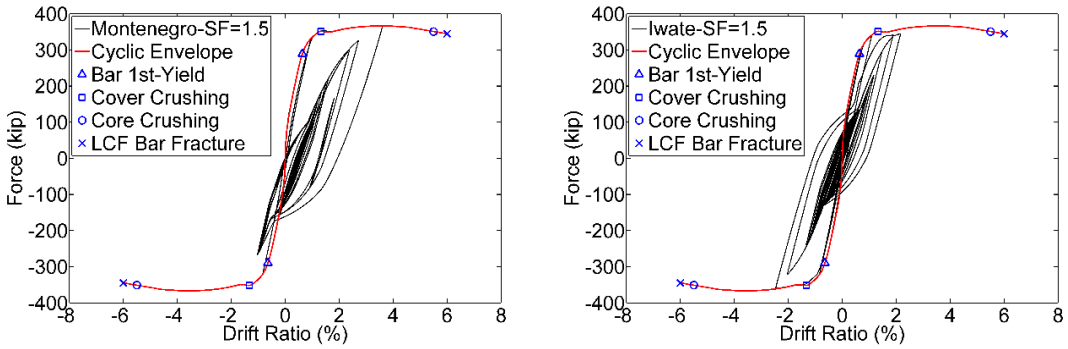

(a)

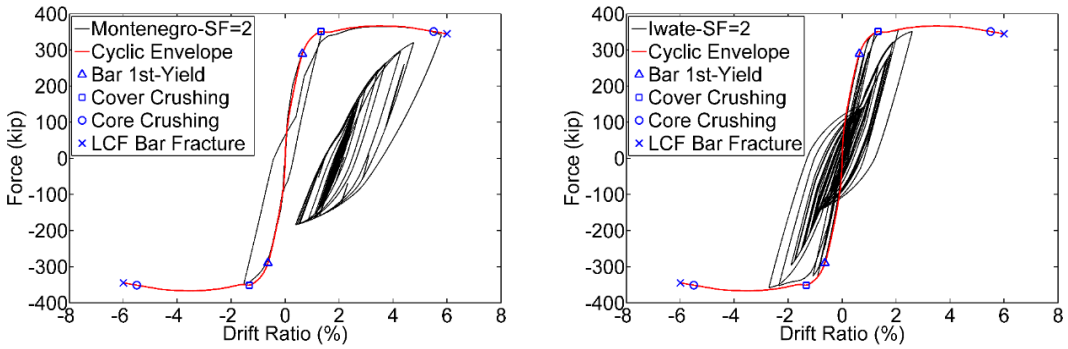

(b)

Fig. 6.29. Force-Drift response of Precast-2 to uniformly scaled ground motions: (a) scale factor of 1.5; (b) scale factor of 2.0.

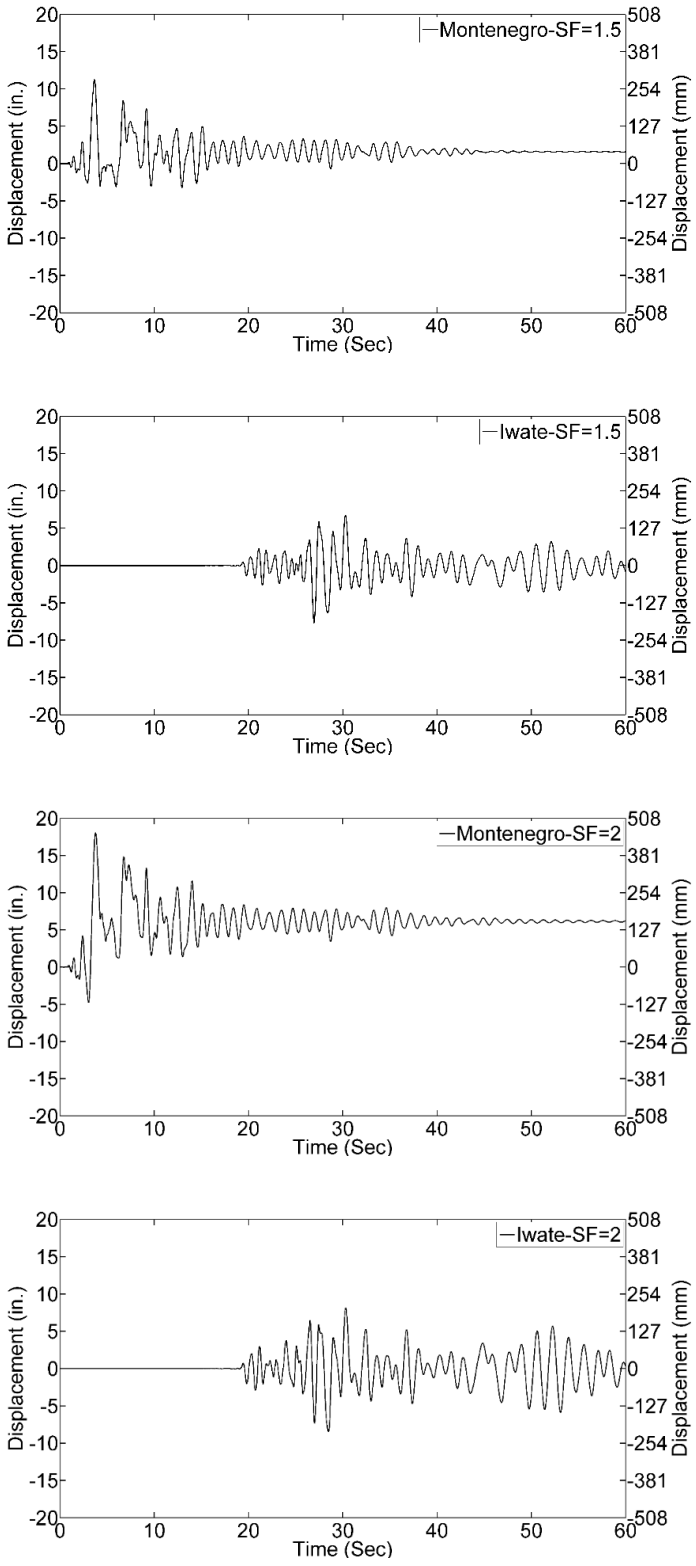

Fig. 6.30. Precast-2 displacement response to uniformly scaled ground motions.

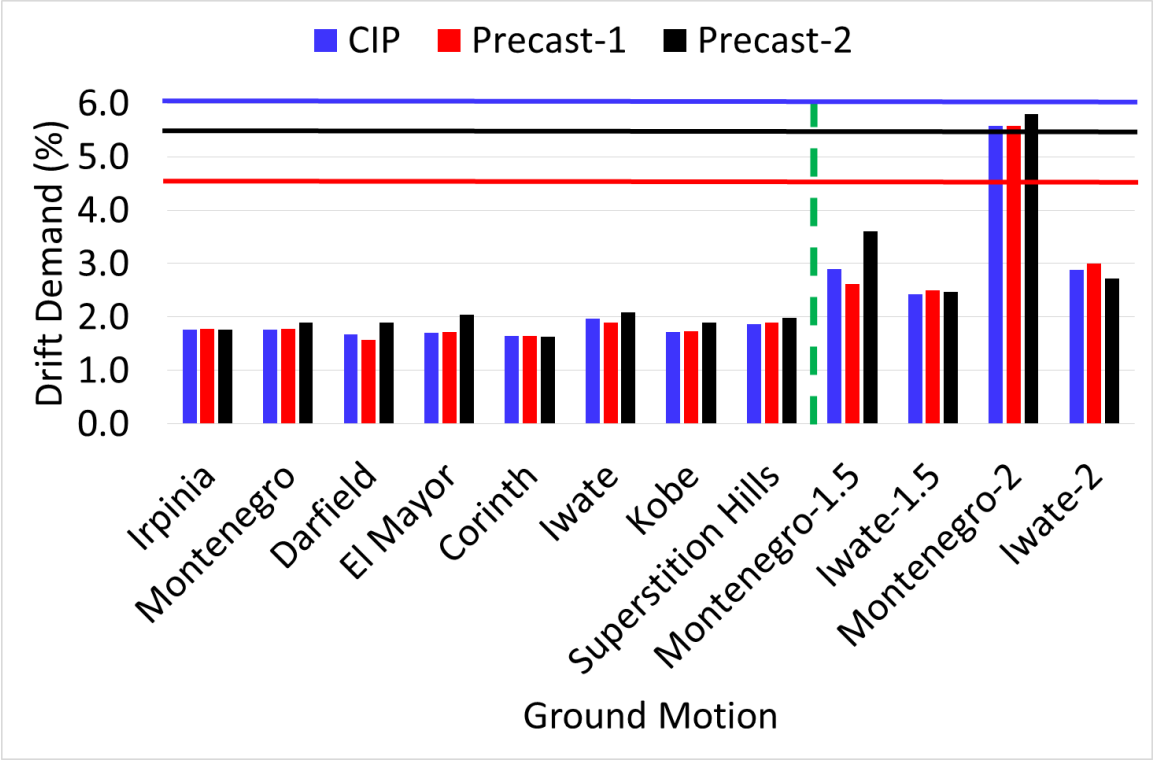

Fig. 6.31. Comparison of drift demands for all bridge bents (horizontal lines indicate drift capacity of respective bents).

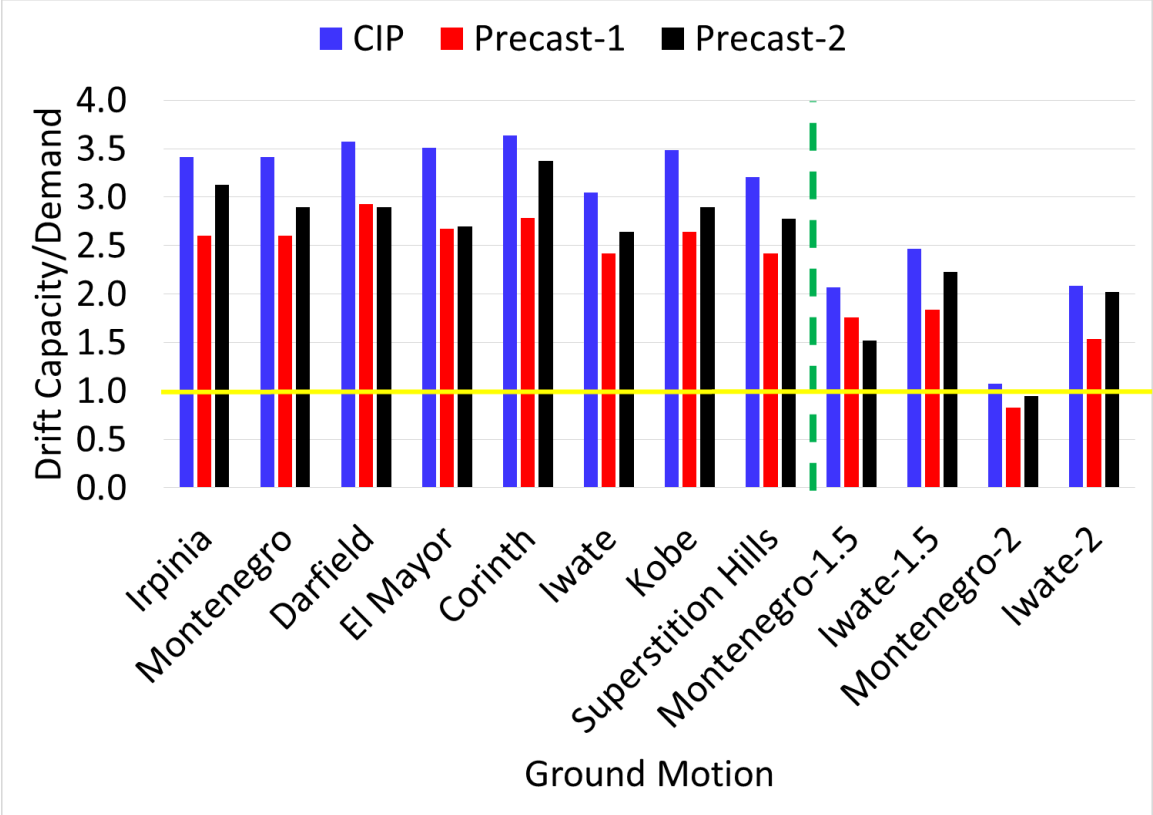

Fig. 6.32. Comparison of drift capacity-to-demand ratios for all bridge bents.

CHAPTER 7

CONCLUSIONS

The grouted splice sleeve connection was studied for accelerated bridge construction in high-seismic regions. The research program described in this dissertation was executed to ascertain the performance of two proprietary grouted splice sleeve connectors used in different configurations within the bridge substructure. It was found that the strength properties of all half-scale test subassemblies were comparable indicating a moment-resisting connection type; however, the specimens had distinct displacement capacities when the location of the connectors was changed.

Experiments

The experimental data analysis provided both qualitative and quantitative measures to study the performance of the specimens under quasi-static cyclic loads. The summary of the findings from the experimental data analysis is presented separately for each category of specimens. The conclusions for the column-to-cap beam subassemblies with FGSS connectors are as follows:

- A reduced displacement capacity was achieved for the precast subassemblies. The cast-in-place control specimen had a ductile response up to a 10% drift ratio when column bars fractured due to low-cycle fatigue. The precast subassembly with FGSS

connectors in the column end (FGSS-1) failed during the 6% drift ratio because of bar pullout, while the precast specimen with FGSS connectors in the cap beam (FGSS-2) failed during the 7% drift ratio when a column bar fractured prematurely due to low-cycle fatigue.

- A localized damage was noted for FGSS-1 with few flexural cracks along the column, whereas FGSS-2 had a similar damage state to the control specimen.
- A displacement ductility capacity of 9.9, 4.9, and 5.8 was obtained for the control specimen, FGSS-1, and FGSS-2, respectively, which is greater than the minimum component displacement ductility capacity of 3.0 specified in the Caltrans SDC. The displacement ductility capacity obtained for FGSS-2 is greater than the maximum displacement ductility demand of 5.0 for single column bents specified in the AASHTO Guide Specifications.

The findings for the column-to-footing connections which incorporated GGSS connectors are as follows:

- All of the subassemblies failed due to low-cycle fatigue bar fracture. The precast subassemblies failed prematurely because of strain concentration in dowel bars outside the connectors adjacent to the column-footing interface.
- The precast subassembly with GGSS connectors in the column end (GGSS-1), along with the precast subassembly with GGSS connectors in the column end and debonded bars in the footing (GGSS-3), had a localized damage near the column-footing interface. Bond-slip rotation comprised at least 60% of the column displacement capacity for GGSS-1 and GGSS-3. The precast subassembly with GGSS connectors in the footing (GGSS-2) had a distributed damage state which was similar to the

control specimen.

- A displacement ductility capacity of 8.9, 5.4, 6.1, and 6.8 was obtained for the control specimen, GGSS-1, GGSS-2, and GGSS-3, respectively, which exceeds the minimum component displacement ductility capacity of 3.0 specified in the Caltrans SDC, as well as the maximum displacement ductility demand of 5.0 for single column bents specified in the AASHTO Guide Specifications.

Computational Study

A simplified computational modeling strategy was developed for seismic assessment of precast bridge columns connected to precast footings using GGSS connectors. The computational model was developed and validated using three half-scale bridge subassemblies tested to failure. Force-based beam-column elements with fiber sections were used to construct the proposed model based on plastic hinge weighted integration; the model included low-cycle fatigue and bond-slip. A summary of findings is offered:

- The one-dimensional idealization of a bar grouted inside a GGSS connector which included both the bar elongation component and bond-slip component was able to determine the overall response of the connector under monotonic tensile loads.
- Results from the column computational models were in close agreement with both the global and local response of the test subassemblies implying that the modeling strategy was capable of addressing the reduced displacement capacity of the precast columns. The largest absolute error between the models and experiments was 6% and 11% in terms of peak lateral force and peak curvature, respectively.

- The plastic hinge length of the cast-in-place control specimen (CIP) which was obtained iteratively is in close agreement with empirical relationships. The fictitious plastic hinge length determined for Precast-1 (GGSS in footing) and Precast-2 (GGSS in column end and debonded bars in footing) was found to be 4/6 and 5/6 times that of CIP, respectively.

Parametric Study

A parametric study was conducted on actual size bridge columns to assess the accuracy of the proposed modeling strategy introduced in Chapter 4. The objective was to ascertain the applicability of the proposed model to both cast-in-place monolithic columns and precast bridge columns with grouted splice sleeve connectors. Two alternatives were considered: a cast-in-place column with monolithic details (CIP) and a precast column with grouted splice sleeves in the column end and debonding of dowel bars in the footing (Precast-2). The findings of this parametric study are summarized as follows:

- Results from the analyses are in good agreement with the anticipated behavior of reinforced concrete columns, based on mechanics, under changing parameters.
- For the Precast-2 column model, sectional curvature was magnified when reduced plastic hinge lengths compared to the assumed plastic hinge length were incorporated.
- The displacement ductility capacity of the Precast-2 column model remained relatively unchanged for values of the assumed plastic hinge length above the value established based on the half-scale experiments.
- The parametric study showed that the proposed model was capable of capturing the

reduced displacement capacity of precast columns as a result of an increased sectional demand.

Prototype Bridge Bents

In the absence of experiments on full-scale precast bridge substructures connected with grouted splice sleeves, a prototype multicolumn bridge bent was designed and detailed in accordance with current recommendations of bridge seismic design codes to achieve a ductile performance. Three bent systems were considered, one cast-in-place bridge bent with monolithic details (CIP), one precast bent composed of precast columns with grouted splice sleeves in the footings and the cap beam (Precast-1), and one precast bent made of precast columns with grouted splice sleeves in the column and debonded footing and cap beam dowel bars (Precast-2). Nonlinear time-history analysis was performed using eight spectrally matched records to obtain the demand levels. The findings are summarized as follows:

- The static cyclic analysis showed that the displacement capacity of the precast bridge bent models was smaller than that of bent model CIP.
- The nonlinear time-history analysis revealed that displacement demands due to the spectrally matched ground motions were smaller than the displacement capacity for both CIP and precast bridge bent models.
- Potential damage to the columns of the bent models consisted of yielding of column longitudinal bars and spalling of the cover under the spectrally matched ground motion records.

- A drift capacity-to-demand ratio of 3.1, 2.4, and 2.6 was achieved for bent models CIP, Precast-1, and Precast-2, respectively, using the maximum drift demand.

CHAPTER 8

RECOMMENDATIONS FOR FUTURE RESEARCH

Further research should be conducted to improve the existing knowledge on precast connections with grouted splice sleeve connectors for bridge substructures. This includes further experiments on large-scale subassemblies or tests on the connectors using improved grout properties and under various loading protocols, in addition to improvements to the computational model and the constitutive laws.

Based on the experimental results of the subassemblies with FGSS connectors along with the FGSS connector tensile test results, it is apparent that an improved high-strength grout can be utilized to prevent pullout failure of the dowel bars, thus achieving the tensile strength of the spliced bars. The one-dimensional bond-slip model developed in Chapter 4 of this dissertation shows that if the compressive strength of the grout were 12.2 ksi (instead of the actual strength of 9.4 ksi), it would be possible to achieve bar fracture instead of pullout failure. Considering that the fastening capability (using the threaded end) is a viable feature of this specific type of splicing devices, further experiments should be carried out using grouts with a higher compressive strength. Three precast alternatives were studied in Chapter 3 of this dissertation. It is informative to experiment another alternative with GGSS connectors inside the footing and debonding of bars in the column plastic hinge region. However, since the high-strength

confined grout inside the footing will postpone and decrease the yield penetration which is advantageous to column displacement capacity, it would be more effective to make a recess at the top of the footing and debond the column dowel bars in the recessed region. Debonding of reinforcing bars has become a popular method for enhancing the deformability of precast connections. Even though existing experiments, including GGSS-3 which was discussed in Chapter 3, justify the usefulness of debonding, further research is needed to ascertain the effect of debonding on the response in more depth. In particular, it is important to understand the relationship between the debonded length and the reduction in bar strain, and subsequently the increase in displacement capacity.

The application of the GGSS connection could be investigated in a hybrid setting. That is, mild steel is spliced by means of GGSS connectors while high-strength bars or tendons are utilized to achieve self-centering effects to reduce the residual drift and damage levels. If this is combined with mechanisms to increase the low-cycle fatigue life of the reinforcing bars, the resulting system will be resilient and suitable for applications in high seismic zones.

A proposed analytical modeling strategy which includes a predefined plastic hinge length for precast columns with GGSS connectors was developed; currently empirical relationships are not available due to a very small number of experiments on such components. Given the current design procedure required by the bridge seismic design codes which uses an analytical plastic hinge length, it is useful to conduct a series of experiments with a sole objective of deriving an empirical plastic hinge relationship as a function of the effective parameters.

The one-dimensional bond-slip model discussed in Chapter 4 was developed

based on experiments on bars grouted in ducts. Experiments are needed to be performed on bars grouted in GGSS or FGSS connectors to derive more accurate constitutive laws for the unconfined and confined regions of the embedded bars in sleeve connectors. Another level of improvement can be achieved by conducting cyclic tests in addition to monotonic tests. Therefore cyclic effects could be included.

Although the tested columns had an octagonal cross section, the computational model used an equivalent circular column because of a simpler fiber discretization available for circular sections in OpenSees. Even though this has a relatively minor effect on the overall response of the model, an automated discretization of typical concrete sections can result in higher level of accuracy.

Lumped plasticity models can be used to simulate the response of bond-critical structural components such as the subassemblies that incorporated FGSS connectors. These particular models are especially useful when all the deterioration modes are to be investigated including pinching as a result of bond-slip effects. In addition, more accurate simulation of bond-slip effects may be possible by combining the distributed plasticity models (to include flexural response) and the lumped plasticity models (to include the bond-slip response).